MEASUREMENT OF THE W AND Z CROSS SECTIONS IN THE ELECTRON CHANNEL FOR $p\bar{p}$ COLLISIONS AT $\sqrt{s} = 1.96$ TeV AND EXTRACTION OF THE W TOTAL WIDTH FROM THE RATIO

By

JOHN MICHAEL GARDNER

Submitted to the Department of Physics and Astronomy
and the Faculty of the Graduate School of the University of Kansas
in partial fulfillment of the requirements
for the degree of Doctor of Philosophy

Professor Philip Baringer
Committee CoChair

Assistant Professor Graham Wilson
Committee CoChair

Professor Dave Besson
Committee Member

Professor David Lerner
Outside Committee Member

Professor Douglas McKay
Committee Member

Date defended: _____

The Dissertation Committee for John Gardner certifies that this is the approved version of the following dissertation:

MEASUREMENT OF THE W AND Z CROSS SECTIONS IN THE ELECTRON CHANNEL FOR $p\bar{p}$ COLLISIONS AT $\sqrt{s} = 1.96$ TeV AND EXTRACTION OF THE W TOTAL WIDTH FROM THE RATIO

Committee:

Professor Philip Baringer
Committee CoChair

Assistant Professor Graham Wilson
Committee CoChair

Professor Dave Besson
Committee Member

Professor David Lerner
Outside Committee Member

Professor Douglas McKay
Committee Member

Date approved _____

ABSTRACT

MEASUREMENT OF THE W AND Z CROSS SECTIONS IN THE ELECTRON CHANNEL FOR $p\bar{p}$ COLLISIONS AT $\sqrt{s} = 1.96$ TeV AND EXTRACTION OF THE W TOTAL WIDTH FROM THE RATIO

Name: John Michael Gardner
Department: Department of Physics and Astronomy
Term Degree Awarded: Fall 2005
University of Kansas

This dissertation presents measurements of the inclusive production cross sections for W and Z gauge bosons decaying through the electron channel with $p\bar{p}$ collisions at a center-of-mass energy of 1.96 TeV. The ratio of these cross sections is then used to extract the W total width.

The Standard Model (SM) of electroweak and strong interactions is a collection of theories which together encompass what is currently known about the elementary particles that make up matter and the forces through which they interact. Experimentalists are constantly searching for violations of the Standard Model by making precision measurements of predicted interactions. The decay of the W boson is one such interaction. The rate of its decay is reflected in its width which is predicted to high precision using Standard Model-based calculations. Therefore, a high precision experimental width measurement would be very sensitive to any such violation. In principle the W and Z boson production cross sections could also be good Standard Model tests. However, a precise knowledge of integrated luminosity is required which is unfortunately difficult to obtain at the Tevatron. In fact, the W and Z cross section results can be used to obtain a more precise luminosity measurement.

The data set consists of a total integrated luminosity of 177 pb^{-1} collected from September 2002 to September 2003 using the DØ detector at Fermilab.

From this, 97757 $W \to e\nu$ and 7928 $Z \to ee$ candidates are found where at least one electron having a matched track is present within the central region of the detector ($|\eta_{det}| < 1.05$). The inclusive cross sections and their ratio are found to be

$$\sigma_W \times B(W \to e^{\pm}\nu) = 2929 \ \pm \ 9 \ (stat) \pm 57 \ (sys) \ ^{\mathbf{+56}}_{\mathbf{-28}} \ (pdf) \pm 190 \ (lumi) \text{ pb},$$

$$\sigma_Z \times B(Z \to e^+e^-) = 267.7 \pm 3.0 \ (stat) \pm 4.8 \ (sys) \ ^{\mathbf{+4.0}}_{\mathbf{-3.3}} \ (pdf) \pm 17.4 \ (lumi) \text{ pb},$$

and

$$R \equiv \frac{\sigma_W \times B(W \to e^{\pm}\nu)}{\sigma_Z \times B(Z \to e^+e^-)} = 10.94 \pm 0.13 \ (stat) \pm 0.16 \ (sys) \ ^{\mathbf{+0.12}}_{\mathbf{-0.08}} \ (pdf).$$

Sources of uncertainty arise from limited statistics (stat), systematic effects (sys), parton distribution function parameters (pdf) and integrated luminosity (lumi).

Indirect measurements of the branching ratio, $Br(W \to e^{\pm}\nu)$, and the W total width, Γ_W, are extracted from the ratio, R:

$$Br(W \to e^{\pm}\nu) = (10.89 \pm 0.13 \ (stat) \pm 0.16 \ (sys) \ ^{\mathbf{+0.12}}_{\mathbf{-0.08}} \ (pdf) \pm 0.16 \ (ext) \ )\%$$

and

$$\Gamma_W = 2.080 \pm 0.024 \ (stat) \pm 0.030 \ (sys) \ ^{\mathbf{+0.023}}_{\mathbf{-0.015}} \ (pdf) \pm 0.031 \ (ext) \text{ GeV}$$

where an additional uncertainty arises from the use of external parameters (ext). Results are consistent with Standard Model (SM) predictions [1]:

(SM) $Br(W \to e^{\pm}\nu) = (10.822 \pm 0.016)\%$ and $\Gamma_W = 2.0936 \pm 0.0022$ GeV.

To my parents
Robert and Sharon Gardner

ACKNOWLEDGEMENTS

I would like to thank all those who have given me advice and assistance during my years of graduate study. The list of everyone who has contributed in some way to the work presented in this thesis is too large to state here and rightly should include everyone in the DØ experiment.

First of all, I would like to thank Philip Baringer, Graham Wilson and Alice Bean for acting as my advisors during my time at DØ. I would like to thank the Kansas folks in the DØ trailers for helping me get started and their friendship during my stay there: Don Coppage, Len Christofek, Shabnam Jabeen, Tanya Moulik, Carsten Hansel and last but not least Christina Hebert.

I would like to thank everyone in the W/Z group for their assistance, helpful suggestions and constructive criticism which has kept the analysis on the right track. In particular, I would like to thank Junjie Zhu, Harald Fox and Doug Chapin who have all made major contributions to the work presented in this thesis and the W/Z conveners Marco Verzocchi, Terry Wyatt, Ia Iashvili and Dmitri Denisov for helping to keep this analysis moving along.

CONTENTS

LIST OF TABLES

LIST OF FIGURES

OUTLINE

Chapter 1) Introduction

This chapter begins with a brief description of the elementary particles and forces of the Standard Model. Then the W and Z boson production cross sections and decay processes along with methods for measuring the W width are given. Finally W and Z cross sections and W width measurements from previous experiments are summarized.

Chapter 2) Fermilab and the DØ Detector

The Tevatron accelerator complex at Fermilab and the Run II DØ detector are described with an emphasis on detector subsystems important to this analysis.

Chapter 3) Data Acquisition

The triggering system, offline reconstruction of the data and finally data quality issues involving the calorimeter after the reconstruction are described.

Chapter 4) Event Selection

Variables used in identifying electrons are described. Selection cuts based on these variables, along with geometric and kinematic cuts, are used to obtain the W and Z candidate samples.

Chapter 5) Monte Carlo

An introduction is given for the event generators and PDFs used to produce the Monte Carlo event samples needed for this analysis. Monte Carlo events

are needed in order to calculate a theoretical value for the ratio of total cross sections, to check the validity of measurement methods, and finally to model acceptance.

Chapter 6) Acceptance

PMCS is used to measure the acceptances for W and Z candidate events. These acceptances are defined as the fraction of all events producing $W \rightarrow e\nu$ and $Z/\gamma^* \rightarrow ee$ interactions in the selected data sample obtained from the DØ detector which are successfully identified as W and Z candidate events. This is after surviving all geometric, kinematic and electron selection cuts. The efficiencies for an electron to pass each of the electron selection cuts are found and the procedure used for modeling these efficiencies in PMCS is described.

Chapter 7) Backgrounds

The levels of contamination in the W and Z candidate samples from significant sources of background are estimated here.

Chapter 8) Results and Conclusions

This is where the W and Z electronic decay cross sections and the W total width are calculated. All inputs and uncertainties are summarized.

CHAPTER 1

INTRODUCTION

1.1 The Standard Model

The Standard Model of electroweak and strong interactions is the currently accepted description of particle physics. It is based on a collection of related quantum field theories and the requirement of local gauge invariance. In quantum field theories, forces are mediated by the exchange of particles. These particles are known as the quanta of the field. The indivisibility of these quanta limits the strength of the field to discrete units and in this way the force is said to be quantized.

The theory of Quantum Chromodynamics [2] describes interactions involving the strong force and the electroweak model of Glashow, Weinberg and Salam describes interactions involving the electromagnetic and weak forces [1, 3]. The gauge symmetry groups of the Standard Model are $SU(3)_C$, $SU(2)_L$ and $U(1)_Y$ describing the strong, weak and electromagnetic forces respectively. Absent from the Standard Model, is a description of the gravitational force which at the scale of fundamental particle interactions is negligible.

In the Standard Model there are several elementary particles which are the fundamental building blocks of all matter. These particles are divided into two groups according to spin: the fermions with spin-$\frac{1}{2}$ of which matter is composed and the gauge bosons with spin-1 which act as the mediators for the forces

between particles.

Unlike bosons, fermions must obey the Pauli exclusion principle dictating that no two particles can share the same state. This gives fermions the properties, such as structure and volume, generally attributed to "matter". They are grouped into three generations with particles in each successive generation increasing in mass, but otherwise sharing similar properties to previous generations. Fermions are also divided into leptons and quarks. The main distinction is that leptons do not interact with the strong force while quarks do. Also quarks have fractional electric charge and can only be found in bound states with other quarks.

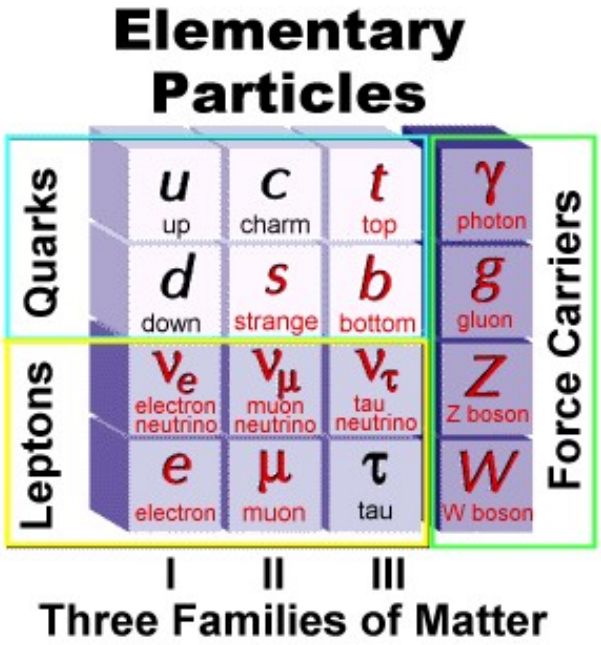

Fig. 1.1: Elementary particles of the Standard Model.

1.1.1 Leptons

There are two leptons in each generation: one lepton with an electric charge of -1 and a corresponding neutrino with no charge. The units of electric charge used in the text and the tables are with respect to the charge of a proton (1.602×10^{-19}

Generation	Lepton	Mass	Charge
1	Electron (e^-)	0.5110 MeV/c^2	-1
	Electron Neutrino (ν_e)	< 3 eV/c^2	0
2	Muon (μ^-)	105.66 MeV/c^2	-1
	Muon Neutrino (ν_μ)	< 0.19 MeV/c^2	0
3	Tau (τ^-)	1777.0 MeV/c^2	-1
	Tau Neutrino (ν_τ)	< 18.2 MeV/c^2	0

Tab. 1.1: The three generations of leptons in the Standard Model.

Coulomb). The charge -1 leptons, listed in order of successive generation, are the electron, muon and tau. Ignoring gravity, these can interact through the weak and electromagnetic forces while the neutrinos only interact through the weak force. Neutrinos interact very weakly with other particles and until recently were thought to be massless. Strong evidence of massive neutrino eigenstates was found in 1998 through the observation of neutrino oscillations [4]. See Table 1.1 for a summary of lepton properties [5].

1.1.2 Quarks

There are two quarks in each generation: one with charge $+2/3$ and the other with charge $-1/3$. Listed in order of successive generation, the quarks with $+2/3$ charge are named up, charm and top. The quarks with $-1/3$ charge are named down, strange and bottom. Quarks interact through the weak and electromagnetic forces and, unlike leptons, they also experience strong interactions which bind quarks together to form hadrons. Single quarks have never been observed, which leads to the concept of "quark confinement"; quarks only appear in combinations as hadrons. See Table 1.2 for a summary of quark properties [5].

Generation	Quark	Mass	Charge
1	Up (u)	1.5 - 4 MeV/c^2	+2/3
	Down (d)	4 - 8 MeV/c^2	−1/3
2	Charm (c)	1.15 - 1.35 GeV/c^2	+2/3
	Strange (s)	80 - 130 MeV/c^2	−1/3
3	Top (t)	175 GeV/c^2	+2/3
	Bottom (b)	4.1 - 4.9 GeV/c^2	−1/3

Tab. 1.2: The three generations of quarks in the Standard Model.

1.1.3 Antiparticles

The lists of leptons and quarks stated above are only half complete. For every particle there exists an antiparticle with identical mass but all other properties reversed. For example, the antiparticle of the electron is the positron (e^+) with +1 charge. Another property is chirality which is indicated by the sign of the projection of a particle's spin along its direction of motion. For neutrinos this is always left handed while for anti-neutrinos this is always right-handed. Antiparticles of charged leptons are written by replacing the '−' with a '+': e^+, μ^+ and τ^+. Antiparticles of quarks and neutrinos are written with a line on top: $\bar{u}$, $\bar{d}$, $\bar{c}$, $\bar{s}$, $\bar{t}$, $\bar{b}$, $\bar{\nu_e}$, $\bar{\nu_\mu}$ and $\bar{\nu_\tau}$. Given that the universe is matter dominated and that a particle and antiparticle pair will annihilate each other if they come into contact, antiparticles are not typically found in nature. This is the main distinction for assigning which is the particle and which is the antiparticle. Gauge bosons also have corresponding antiparticles. The photon and Z^0 turn out to be their own antiparticle while the W^+ is the antiparticle of the W^-.

Force	Gauge Boson	Mass	Charge
Electromagnetic	Photon (γ)	0	0
Weak	W Boson ($W^{\pm}$)	80.43 GeV/c^2	± 1
	Z Boson (Z^0)	91.19 GeV/c^2	0
Strong	Gluon (g)	0	0

Tab. 1.3: Gauge bosons in the Standard Model.

1.1.4 Gauge Bosons and the Fundamental Forces

Each of the fundamental forces between particles is mediated by the exchange of gauge bosons. The photon is the mediator of the electromagnetic force, the W^+, W^- and Z^0 are mediators of the weak force and the gluons are mediators of the strong force. See Table 1.3 for a summary of gauge boson properties [5].

The electromagnetic and weak force have been unified into the electroweak force by the Glashow, Weinberg and Salam model. The electromagnetic force interacts with charged particles and can be attractive or repulsive. The photon is stable and therefore the range of the electromagnetic force is infinite. The weak force affects all leptons and quarks, but its range is very short due to the short lifetimes of the W and Z bosons. Weak interactions involving the uncharged Z^0 are referred to as "neutral currents" and interactions involving the charged W^+ or W^- are referred to as "charged current" interactions. Only charged current weak interactions have the ability to change the flavor of quarks. The Cabibbo-Kobayashi-Maskawa (CKM) matrix,

$$\begin{pmatrix} d' \\ s' \\ b' \end{pmatrix} = V_{CKM} \begin{pmatrix} d \\ s \\ b \end{pmatrix} = \begin{pmatrix} V_{ud} & V_{cd} & V_{td} \\ V_{us} & V_{cs} & V_{ts} \\ V_{ub} & V_{cb} & V_{tb} \end{pmatrix} \begin{pmatrix} d \\ s \\ b \end{pmatrix}, \tag{1.1}$$

characterizes the strength with which these flavor changing charged current in-

teractions occur. Flavor changing weak interactions occur between charge $+2/3$ quarks and $-1/3$ quarks with the strongest couplings occurring between quarks in the same generation. The experimentally determined values for these matrix elements are [6]

$$\begin{pmatrix} V_{ud} & V_{cd} & V_{td} \\ V_{us} & V_{cs} & V_{ts} \\ V_{ub} & V_{cb} & V_{tb} \end{pmatrix} = \begin{pmatrix} 0.9739 - 0.9751 & 0.221 - 0.227 & 0.0029 - 0.0045 \\ 0.221 - 0.227 & 0.9730 - 0.9744 & 0.039 - 0.044 \\ 0.0048 - 0.014 & 0.037 - 0.043 & 0.9990 - 0.9992 \end{pmatrix}. \tag{1.2}$$

Only quarks are influenced by the strong force which confine them into bound states called hadrons. Quarks have an internal degree of freedom referred to as color which governs how they can be bound together. They have one unit of either red, blue or green while antiquarks will have -1 units. The rule governing hadron formation is that quarks can only be bound together in colorless combinations. Baryons are colorless in that they contain one each of red, blue and green quarks to make 'white'. Mesons are composed of a quark and antiquark whose color sum adds to zero. The gluons contain 1 unit of one color and -1 units of another enabling them to transfer color and therefore act as mediators of the strong force.

1.1.5 Feynman Diagrams

Feynman diagrams are a way of representing interactions among particles. These diagrams can be a useful tool for describing complex processes and determining interaction strengths. Particles are represented as lines and fundamental interactions are represented as primitive vertices connecting these lines. For all Feynman diagrams shown in this thesis positive time is represented going from left to right. Leptons and quarks are represented by solid lines with an arrow pointed in the direction of positive time flow for particles and negative time flow

for antiparticles. For example, the left diagram in Figure 1.2 shows a weak interaction in which the u and $\bar{d}$ quarks annihilate to form the W^+ boson. More complex processes can be represented by joining together more than one primitive vertex. For example, the left diagram in Figure 1.3 describes the process $u + g \rightarrow W^+ + d$ through a combination of strong and weak interactions.

1.2 W and Z Production

For inclusive W and Z production in $p\bar{p}$ collisions,

$$p\bar{p} \rightarrow W^{\pm} + X \quad \text{or} \quad p\bar{p} \rightarrow Z^0 + X, \tag{1.3}$$

most commonly a valence quark or gluon from the proton and a valence antiquark or gluon from the antiproton annihilate in a hard scattering process. The remnants of the proton and antiproton continue down the beam pipe and can be safely ignored. Since this is an inclusive measurement, additional decay products, denoted by 'X', are allowed.

The dominant method of production is through the weak Drell-Yan process in which a quark and antiquark collide to form a single W or Z boson as shown in Figure 1.2. In this case, the boson is produced with negligible momentum transverse to the beam. However, in higher order processes the boson can recoil off of additional decay products. For example, in Figure 1.3 a quark is produced through Compton scattering and Figure 1.4 shows the initial state radiation of a gluon. An important source of background is the electromagnetic Drell-Yan process in which a massive virtual photon acts as the force mediator. This is indistinguishable from the weak Drell-Yan process and its effect must be accounted for. The diagrams only show W^+ production, but W^- is easily represented by swapping each particle with its anti-particle.

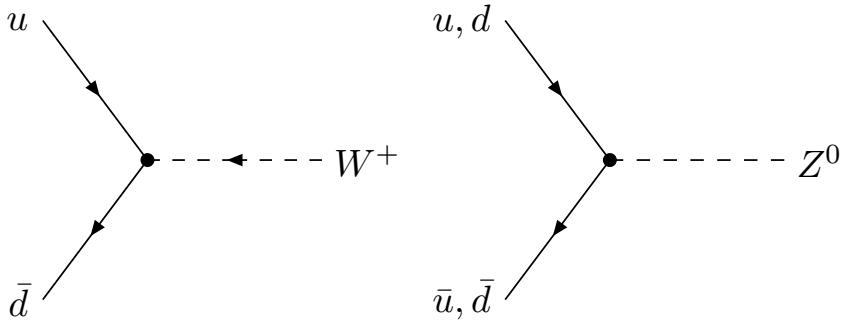

Fig. 1.2: Lowest order diagrams for W^+ and Z^0 production.

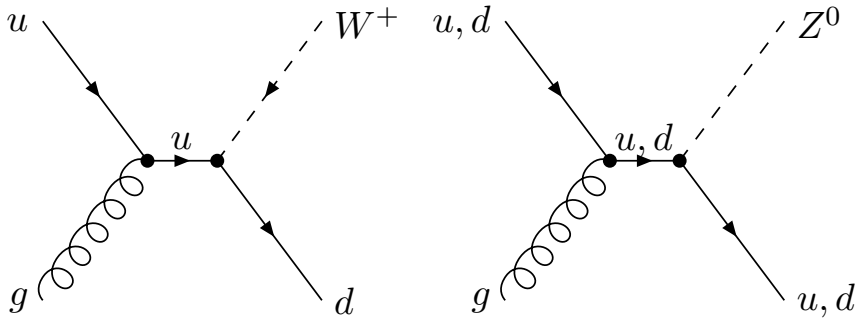

Fig. 1.3: Compton scattering in W^+ and Z^0 production.

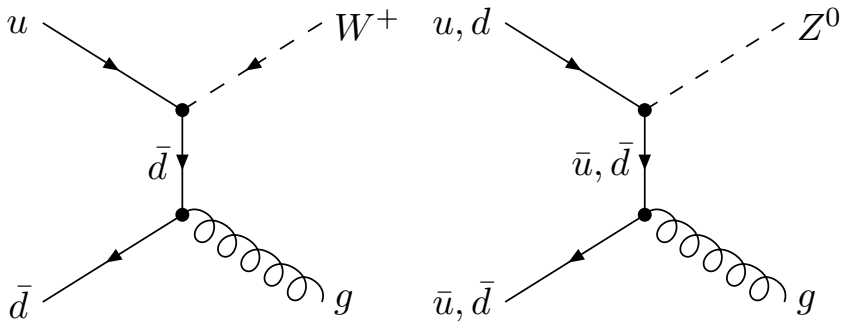

Fig. 1.4: Initial state gluon radiation in W^+ and Z^0 production.

1.2.1 The Production Cross Sections

The W and Z boson production cross sections describe the strength of the interactions resulting in their production and therefore predict the number of bosons produced over time for a given flux of incident particles. Ever since the discovery of the W and Z Bosons in 1983 at CERN [7], the cross sections have been an important early measurement at new experiments.

The subprocess cross section for $q\bar{q}' \to W^+$ is [8]

$$\hat{\sigma}(q\bar{q}' \to W^+) = 2\pi |V_{qq'}|^2 \frac{G_F}{\sqrt{2}} \; M_W^2 \; \delta(\hat{s} - M_W^2) \tag{1.4}$$

where $V_{qq'}$ is the CKM matrix element, G_F is the Fermi constant and $\sqrt{s}$ is the center-of-mass energy of the collision. A Dirac delta function is used as an approximation to the Breit-Wigner W mass distribution with width Γ_W shown in Equation 1.8. See Section 1.3 for a description of the W width, Γ_W.

The subprocess cross section for $q\bar{q} \to Z^0$ is [8]

$$\hat{\sigma}(q\bar{q}' \to Z^0) = 8\pi \frac{G_F}{\sqrt{2}} \; [(g_V^q)^2 + (g_A^q)^2] \; M_Z^2 \; \delta(\hat{s} - M_Z^2) \tag{1.5}$$

where g_V and g_A are the vector and axial-vector quark coupling strengths respectively. The total cross sections are found by convolving these subprocess cross sections with the appropriate parton distribution functions (PDF's) [8]:

$$\sigma(p\bar{p} \to B + X) = \frac{K(\alpha_s)}{3} \int_0^1 dx_a \int_0^1 dx_b \; \sum_{q,\bar{q}'} \; f_q(x_a, Q^2) \; f_{\bar{q}'}(x_b, Q^2) \; \hat{\sigma} \tag{1.6}$$

where B is the W^+, W^- or Z^0 boson and $K(\alpha_s)$ is a correction factor for higher order QCD processes. A color factor of $1/3$ is required to take into account that the quarks must have the same color. The PDF's, $f_q(x_a, Q^2)$ and $f_{\bar{q}'}(x_b, Q^2)$,

describe the probability of obtaining a quark and anti-quark with momentum fractions x_a and x_b of the proton and anti-proton at an energy scale of Q^2 where Q is set to the boson mass. See [8] for more information.

1.2.2 W and Z Boson Decay

The electronic decay of W and Z bosons occurs only a small percent of the time. These electronic branching ratios are $B(W \rightarrow e\nu) = 10.822\%$ and $B(Z \rightarrow ee) = 3.3655\%$ [1]. The principal W and Z decay modes allowed in the Standard Model are shown in Figure 1.5. Approximately 68% of the time, they decay hadronically into one of the pairs of quarks shown in this figure. Unfortunately study of W and Z bosons through the hadronic channels at the Tevatron is made practically impossible due to the overwhelmingly large background from QCD processes with final states indistinguishable from those of the bosons. This is not a problem for leptonic final states since they are not produced through strong interactions. Ignoring the possibility of particle misidentification, only very small backgrounds from other weak or electromagnetic decays must be considered. The electron, muon and tau have identical branching ratios, but electrons and muons are most commonly used since, unlike taus, they are long lived, and can be easily identified.

1.3 The W Total Width

W bosons are produced at masses which can differ quite noticeably from the "on-shell" mass stated in Table 1.3. Given that the W boson has an extremely short lifetime, one explanation for this variation can be taken from the uncertainty principle,

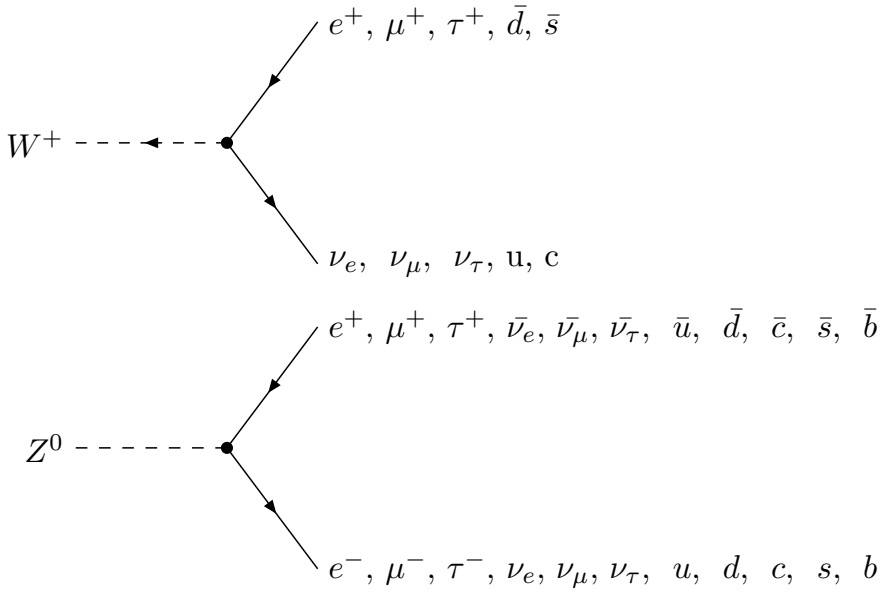

Fig. 1.5: Principal W and Z boson decay modes

$$\Delta E \times \Delta t \approx \frac{h}{2\pi}. \tag{1.7}$$

As the lifetime, Δt, decreases the uncertainty on the mass, $\Delta E/c^2$, increases. This produces a Breit-Wigner shaped distribution described by

$$P_{BW} \equiv \frac{\Gamma_W^2/4}{(\sqrt{s} - M_W)^2 + \Gamma_W^2/4} \tag{1.8}$$

which is peaked at the on-shell mass. The W total width is defined as the parameter, Γ_W, in this distribution.

A W boson decays much too rapidly to be measured directly. Instead, its mass is inferred from its decay products. This invariant mass is defined as

$$M^2 \equiv (E_1 + E_2)^2 - (\overrightarrow{p}_1 + \overrightarrow{p}_2)^2 \tag{1.9}$$

where E_1 and E_2 are the energies and $\overrightarrow{p}_1$ and $\overrightarrow{p}_2$ are the momenta of the decay products. In practice, measuring the width is not nearly so straightforward as plotting this distribution and observing its width. For example, particle detectors suffer from imperfect energy resolution which will widen the peak. This is also assuming the decay product's momenta can be fully reconstructed. As described in Section 1.3.1 below, this is not the case for $W \to l\,\nu$ decays.

The $W \to e\,\nu$ partial width can be derived as [8]

$$\Gamma(W \to e\,\nu) = \frac{G_F}{\sqrt{2}} \frac{M_W^3}{6\pi} \equiv \Gamma_W^0 \tag{1.10}$$

where the electron mass is neglected. An equation for the total width can be derived in terms of Γ_W^0 [9],

$$\Gamma_W = [1 + \delta(M_t, M_H)] \times \left[3 + 6\left(1 + \frac{\alpha_S(M_W)}{\pi}\right)\right] \times \Gamma_W^0. \tag{1.11}$$

The factor of 3 in this equation comes from the three leptonic channels where lepton universality is assumed [10], while the factor of 6 is from the 2 primary hadronic decays times 3 color combinations. The δ term is for radiative corrections which are dependent upon the top quark (M_t) and Higgs (M_H) masses while the α_S term accounts for gluon radiation.

Since, the radiative corrections are dependent on M_H, the W width could potentially be used as a constraint for the Higgs mass. However, the level of precision required is much higher than has been attained so far. Also, since the W width is dependent upon the rate of decay, additional decay modes not predicted by the Standard Model would lead to a higher than predicted width. Since the Standard Model prediction, 2.0936 ± 0.0022 GeV [1], is quite well known, a precision measurement of the W width would be sensitive to any disagreement.

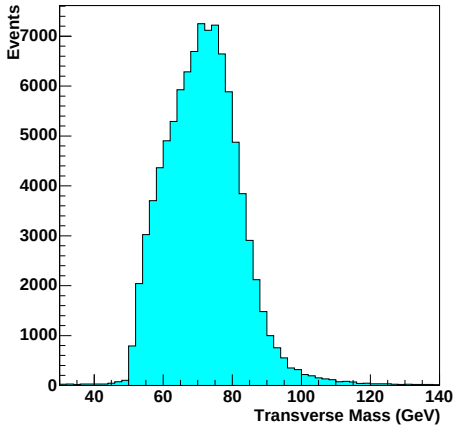

Fig. 1.6: $W \rightarrow e\,\nu$ data sample transverse mass

1.3.1 Direct Measurement Method

In principle, the strategy here is to measure the width directly from the shape of the invariant mass distribution. However, this can not be measured for $W \rightarrow l\,\nu$ decays. Since the neutrino leaves no trace as it passes through the detector, its momentum can't be measured directly and can only be inferred by noting the resulting energy imbalance left in the detector. Energy lost along the beam pipe is left undetected and spoils the reconstruction of the longitudinal component of momentum. This prevents the reconstruction of the invariant mass and an incomplete invariant mass using only the transverse component of momentum must be used instead. This is referred to as the transverse mass:

$$M_T^2 \equiv (|\overrightarrow{p}_{e\,T}| + |\overrightarrow{p}_{\nu\,T}|)^2 - (\overrightarrow{p}_{e\,T} + \overrightarrow{p}_{\nu\,T})^2 \tag{1.12}$$

where $\overrightarrow{p}_{e\,T}$ and $\overrightarrow{p}_{\nu\,T}$ are the transverse momenta of the electron and neutrino. Here the lepton masses are negligible. An example of this distribution can be seen in Figure 1.6.

The sharp drop in the peak at M_W is referred to as a Jacobian edge. At

transverse masses below this there is significant smearing caused by detector energy resolution effects which will widen the peak according to a Gaussian distribution. Only at higher transverse masses do the detector effects become small enough for the distribution to be dominated by the Breit-Wigner shape from the W width. However, placing a high M_T requirement on W events severely limits available statistics. In general the M_T cut is selected somewhat above M_W with the exact choice made to balance higher systematic error with a lower M_T cut against higher statistical error with a higher M_T cut.

1.3.2 Indirect Measurement Method

The ratio, R, of the W and Z cross sections times electronic branching fractions can be used to find the W width. R can be expressed as

$$R \equiv \frac{\sigma(p\bar{p} \rightarrow W + X) \times Br(W \rightarrow e\nu)}{\sigma(p\bar{p} \rightarrow Z + X) \times Br(Z \rightarrow ee)} = \frac{\sigma_W}{\sigma_Z} \times \frac{Br(W \rightarrow e\nu)}{Br(Z \rightarrow ee)} \tag{1.13}$$

and therefore

$$Br(W \rightarrow e\nu) = R \times \frac{[Br(Z \rightarrow ee)]}{[\sigma_W/\sigma_Z]} \tag{1.14}$$

and

$$\Gamma_W \equiv \frac{[\Gamma(W \rightarrow e\nu)]}{Br(W \rightarrow e\nu)} \quad = \quad \frac{1}{R} \times \frac{[\Gamma(W \rightarrow e\nu)] \times [\sigma_W/\sigma_Z]}{[Br(Z \rightarrow ee)]}. \tag{1.15}$$

The ratio of the production cross sections, σ_W/σ_Z, the leptonic partial width, $\Gamma(W \rightarrow e\nu)$, and the leptonic Z boson branching fraction, $Br(Z \rightarrow ee)$, can be calculated to high precision from the boson couplings and parton distribution functions described in Sections 1.2 and 1.2.2.

An advantage of the indirect method is a more precise experimental measure-

ment due to the ability to use the entire W and Z data set, as compared to the direct method where only around 1% of W statistics are used. The main disadvantage is a dependence on external inputs. In this analysis, the R measurement is the dominant source of uncertainty. However in future measurements, as the amount of data available continues to grow, uncertainty from external inputs will begin to dominate and place a limit on the precision attainable. Additionally, this measurement is sensitive to the assumption that the theoretical inputs are correctly described by the Standard Model. Both methods are important since they have very few common sources of systematic error and therefore complement each other quite well.

1.4 Previous Measurements

Figures 1.7 and 1.8 summarize measurements for the inclusive W and Z cross sections times leptonic branching fraction obtained from the DØ and CDF experiments for Run I and Run II [11, 12, 13, 14, 15, 16, 17]. These results are compared to the Standard Model with uncertainty ranges estimated as described in Section 5.3. The cross sections for Run II at 1960 GeV are expected to increase by approximately 10% compared to Run I. Figure 1.9 compares results obtained for the W total width by combining Run I results [18] to Run II and other experimental results. Measurements obtained using the direct and indirect methods are compared to the Standard Model.

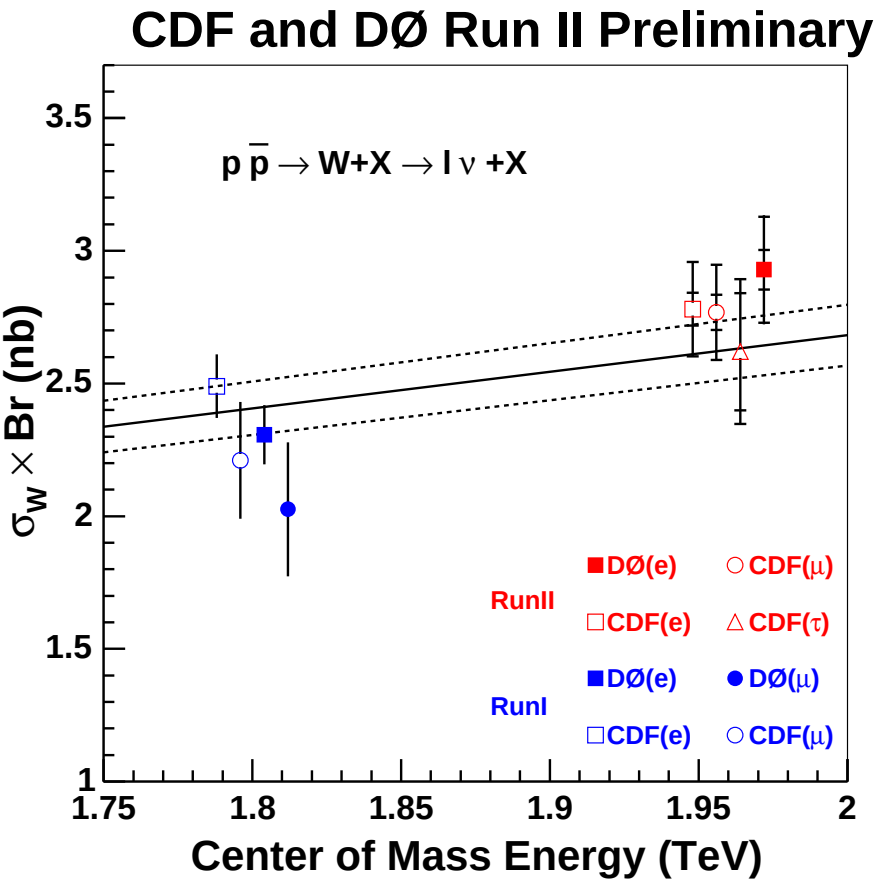

	$\sigma(W \to l\nu)$ (pb)	$\mathcal{L}(\text{pb}^{-1})$	$\sqrt{s}$ (TeV)
CDF Run I, $W \to e\nu$ [12]	2490 ± 120	19.7	1.80
CDF Run I, $W \to \mu\nu$ [14]	2210 ± 220	3.5	1.80
DØ Run I, $W \to e\nu$ [11]	2310 ± 112	84.5	1.80
DØ Run I, $W \to \mu\nu$ [13]	2090 ± 253	82	1.80
CDF Run II, $W \to e\nu$ [15]	2780 ± 178	72	1.96
CDF Run II, $W \to \mu\nu$ [15]	2768 ± 179	72	1.96
CDF Run II, $W \to \tau\nu$ [16]	2620 ± 273	72	1.96
DØ Run II, $W \to e\nu$	2929 ± 206	177	1.96

Fig. 1.7: A comparison of experimental results for the lepton channel W cross section as a function of center-of-mass energy. Experimental results for CDF and DØ are given for Run I with $\sqrt{s} = 1800$ GeV and Run II with $\sqrt{s} = 1960$ GeV. The solid middle line represents the Standard Model prediction and the dashed lines represent uncertainty.

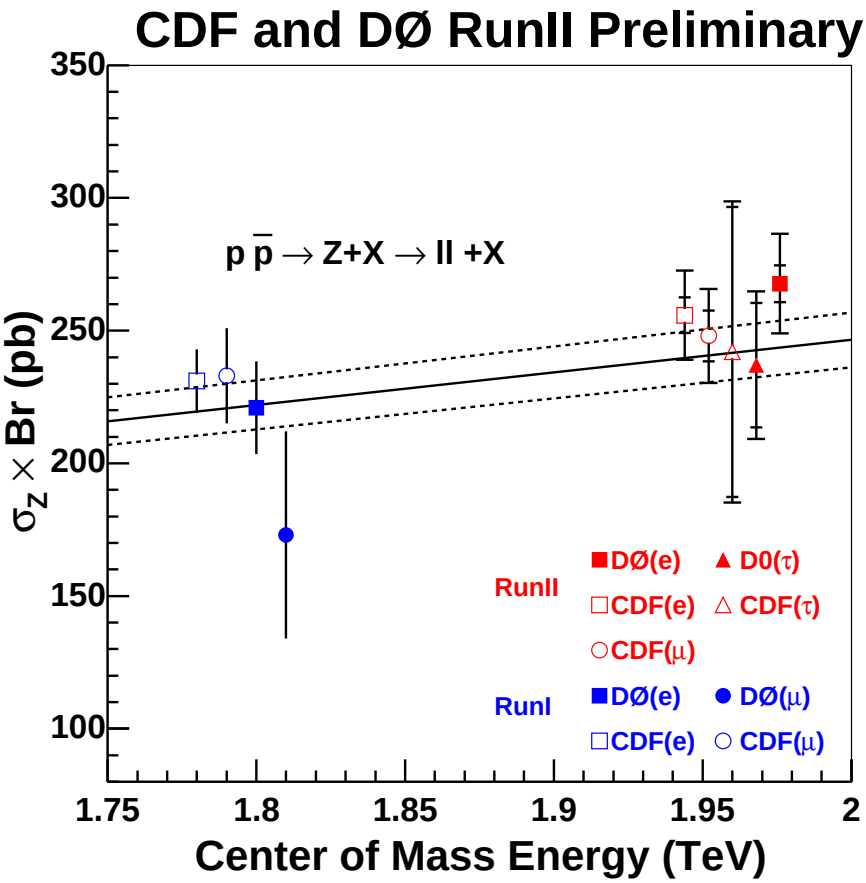

	$\sigma(Z \rightarrow l\nu)$ (pb)	$\mathcal{L}$(pb^{-1})	$\sqrt{s}$ (TeV)
DØ Run I, $Z \rightarrow ee$ [11]	221 ± 11	84.5	1.80
DØ Run I, $Z \rightarrow \mu\mu$ [13]	178 ± 39	82	1.80
CDF Run I, $Z \rightarrow ee$ [12]	231 ± 12	19.7	1.80
CDF Run I, $Z \rightarrow \mu\mu$ [14]	214 ± 23	3.5	1.80
CDF Run II, $Z \rightarrow ee$ [15]	256 ± 17	72	1.96
CDF Run II, $Z \rightarrow \mu\mu$ [15]	248 ± 18	72	1.96
CDF Run II, $Z \rightarrow \tau\tau$ [16]	242 ± 57	72	1.96
DØ Run II, $Z \rightarrow \tau\tau$ [17]	237 ± 28	226	1.96
DØ Run II, $Z \rightarrow ee$	268 ± 19	173	1.96

Fig. 1.8: A comparison of experimental results for the Z lepton channel cross section as a function of center-of-mass energy. Experimental results for CDF and DØ are given for Run I with $\sqrt{s} = 1800$ GeV and Run II with $\sqrt{s} = 1960$ GeV. The solid middle line represents the Standard Model prediction and the dashed lines represent uncertainty.

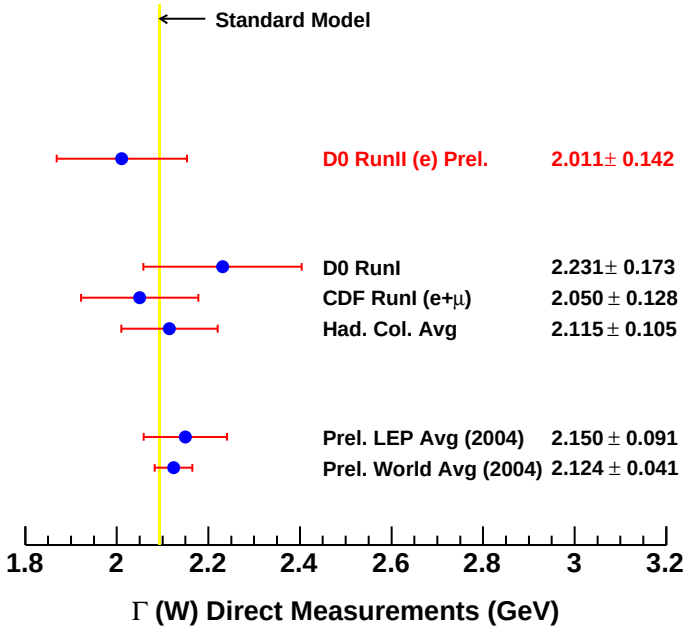

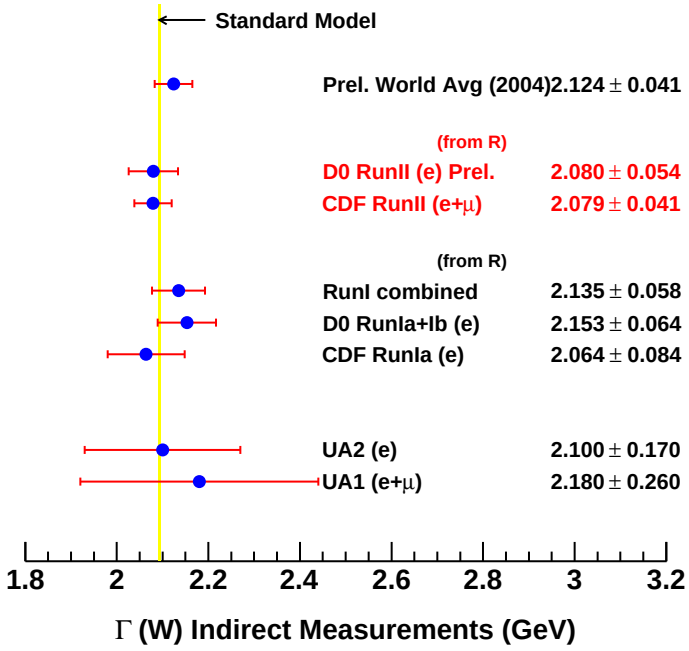

Fig. 1.9: A comparison of the Standard Model prediction of Γ_W to Run I and II results at the CDF and DØ detectors [18, 19], LEP [20], UA1 [21], UA2 [22] and combined averages using the direct measurement method (top) and indirect (bottom). For 'Prel. World Avg (2004)', direct and indirect methods are combined.

CHAPTER 2

FERMILAB AND THE DØ DETECTOR

The Fermi National Accelerator Laboratory, located near Chicago, Illinois, is currently home to the highest energy particle accelerator in the world. Protons and antiprotons collide with a center-of-mass energy of 1.96 TeV at one of the two general purpose detectors located along the Tevatron ring. One of these detectors is our DØ experiment, named after its position on the Tevatron, and the other is CDF, short for 'Collider Detector at Fermilab'. Figure 2.1 shows the arrangement of the accelerator system and detectors.

During Run I, between 1989 and 1996, collisions took place at a center-of-mass energy of 1.8 TeV with one of the highlights being the joint discovery of the top quark at DØ [23] and CDF [24]. Many improvements were made to both the detectors and the accelerator system in preparation for the start of Run II in 2001.

2.1 The Tevatron

The Tevatron is the last in the series of accelerators needed to produce the 980 GeV beams of protons and antiprotons used in collisions at DØ. In order of energy, these accelerators are the Cockroft-Walton, the Linac, the Booster, the Main Injector and the Tevatron. A chain of accelerators is necessary because each individual accelerator is only able to operate efficiently within a limited

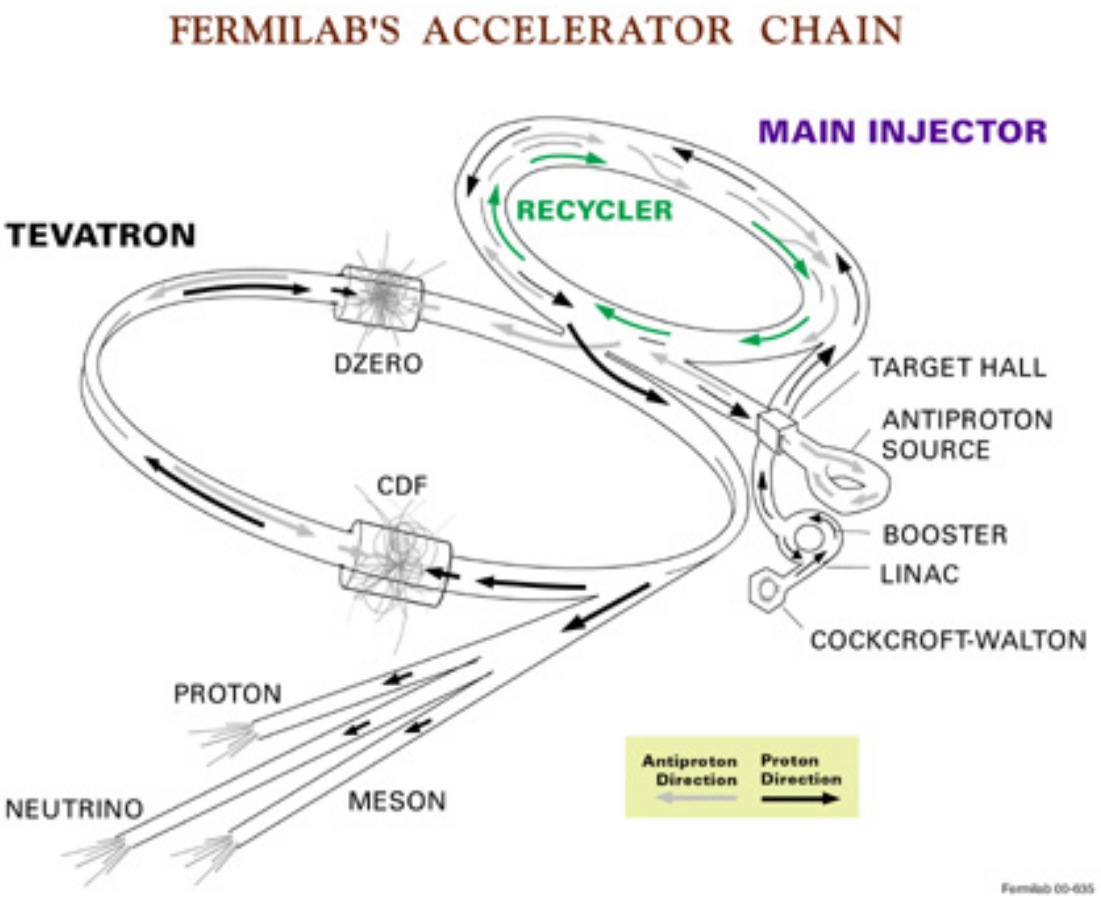

Fig. 2.1: The Tevatron Accelerator Chain.

energy range.

For the first step, hydrogen ions consisting of two electrons and one proton (H^-) are produced inside the Cockroft-Walton accelerator. This is a linear device which accelerates the ions across several constant voltage steps to a kinetic energy of 750 keV. Then the ions are bunched together and accelerated further using the Linac linear accelerator where they obtain a kinetic energy of 400 MeV.

The final three accelerators are synchrotrons which confine particles to circular orbits using dipole magnets. Radio frequency (RF) electric fields give the particles an energy boost at specific positions along the ring. At the same time the magnetic field must be increased to keep the particles within the ring. Quadrupole magnets are also necessary to stabilize the beam during this process.

The first synchrotron is the Booster with a radius of 75 meters. Here the beam is directed through a thin carbon foil which strips off the electrons and accelerates the bare protons to a kinetic energy of 8 GeV. The beam then enters the Main Injector where one of two things can occur: either the protons are accelerated to 150 GeV and transferred to the Tevatron or they are accelerated to 120 GeV and transferred to the antiproton source. Antiprotons are produced by colliding these protons into a nickel target. In approximately one out of every 10,000 collisions an antiproton is produced. These are stored in the accumulator until enough (roughly 10^{11}) have been collected to fill the Tevatron. The antiprotons are bunched and then inserted back into the Main Injector where they are accelerated to 150 GeV and inserted into the Tevatron.

The main advantage of synchrotrons over linear accelerators is the ability to send particles through the same potential difference many times. Disadvantages include increases to both energy loss from synchrotron radiation and magnetic field strength requirements as the beam energy increases. This can be offset by an increased radius of curvature which is why the Tevatron has a relatively large

one kilometer radius with a 4.2 Tesla superconducting magnetic field.

A Tevatron store consists of 36 bunches of protons and 36 bunches of antiprotons spaced 396 ns apart. The protons travel clockwise and the antiprotons counter-clockwise until they are made to collide at either the DØ or CDF interaction points. The preparation of a store typically takes several hours with a majority of that time spent in the antiproton accumulator. Once started, the instantaneous luminosity, described in Section 3.1, continues to decrease due to the interaction of the beams with each other, bunch emittance growth and other effects. A typical store lasts around 20 to 25 hours before luminosity drops below an acceptable level. When this occurs, the beam is dumped and a new store is prepared [25].

Major additions to the accelerator for Run II include the Main Injector which acts as an intermediate accelerator as described above and the antiproton recycler which improves luminosity by providing highly reliable antiproton storage with the largest boost in luminosity coming from its ability to retain antiprotons from old stores for reuse. These additions along with improvements to the Tevatron and antiproton production scheme allow for the production of a more stable supply of protons and antiprotons at greater luminosity and higher energy.

2.2 Introduction to the DØ Detector

The DØ Run II Detector is made up of several different types of specialized subdetectors layered one after the other around the expected beam interaction point. By combining measurements from all these subdetectors, the DØ Detector gains the flexibility to distinguish a wide variety of particles. Typically only neutrinos are able to escape undetected. In tracing the path of a particle produced in the collision, the first layers encountered are those of the inner tracking

system. The purpose of the tracking system is to precisely locate the paths of charged particles. This is important for locating where the particles of interest were produced. Also, a solenoid magnet provides a 2 Tesla uniform magnetic field within the tracking system. This magnetic field allows momentum to be measured based on the resulting curvature of the charged particle tracks. The bulk of the magnet can cause particles to "shower" so a preshower detector is placed immediately after it to provide energy and position measurements before much showering can occur in order to aid in particle discrimination. The next detector is the calorimeter which absorbs all particles except for muons and neutrinos and provides a precise energy measurement of these particles. Finally, muons are identified by the muon detector system. The presence of a neutrino can be inferred indirectly by a detector momentum imbalance. The entire DØ Detector is shown in Figure 2.2 and a zoomed in drawing of the inner layers is shown in Figure 2.3.

2.3 Work for the DØ Run II Upgrade

The time period between Run I and Run II has been taken advantage of to provide several improvements to the DØ Detector. Some major upgrades for Run II include a completely new inner tracking system for better track and vertex finding, a solenoid for measuring the momentum of charged particles and preshower detectors to compensate for energy loss from the solenoid. All systems make use of new electronics to take advantage of the increased flow of collision data [26]. For a detailed description of the Run I detector see [27] and for the Run II upgrade see [28].

Upgrading the DØ Detector for Run II has been a massive undertaking requiring the contribution of several institutions and hundreds of people over a

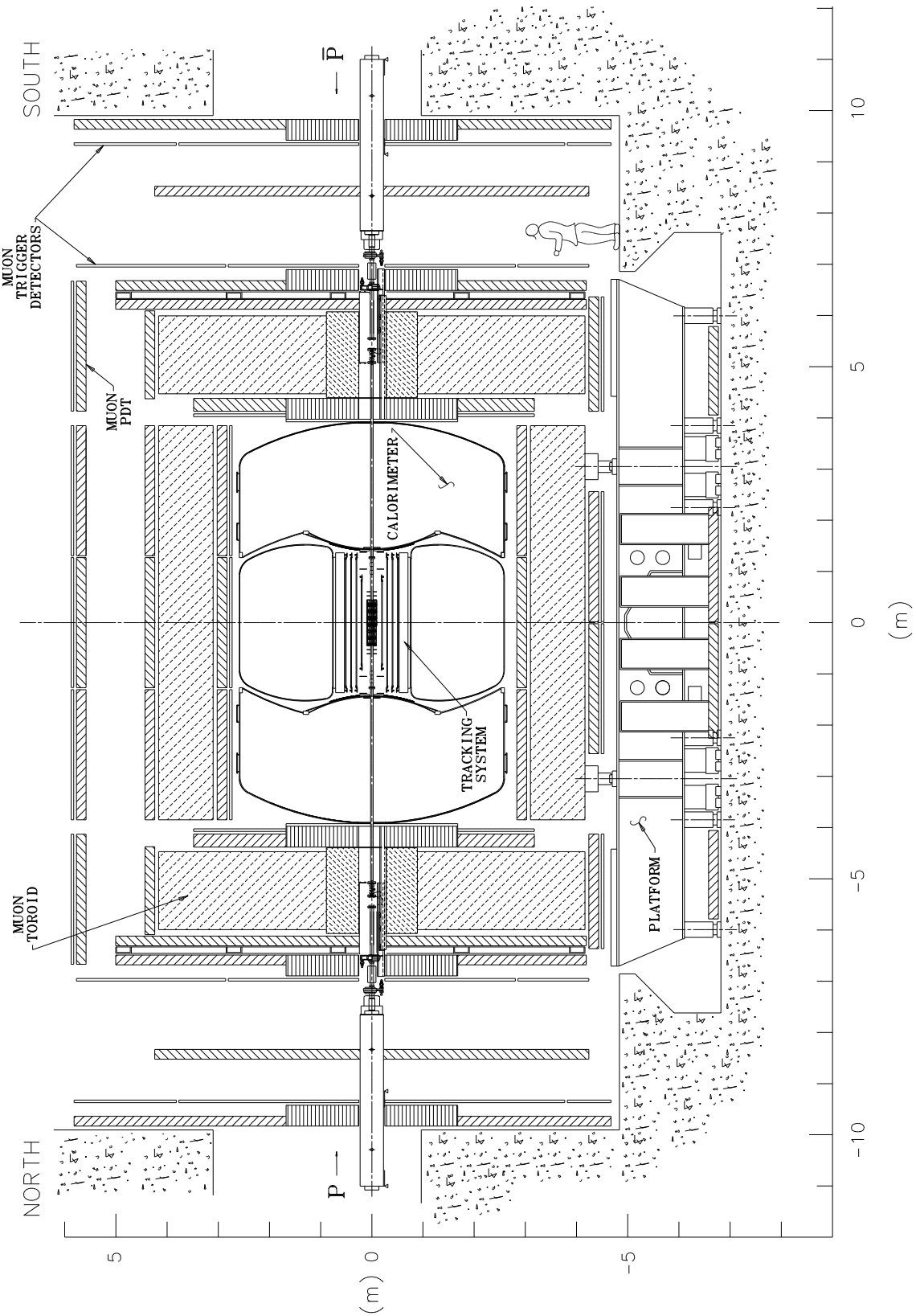

Fig. 2.2: Side view of the DØ Detector.

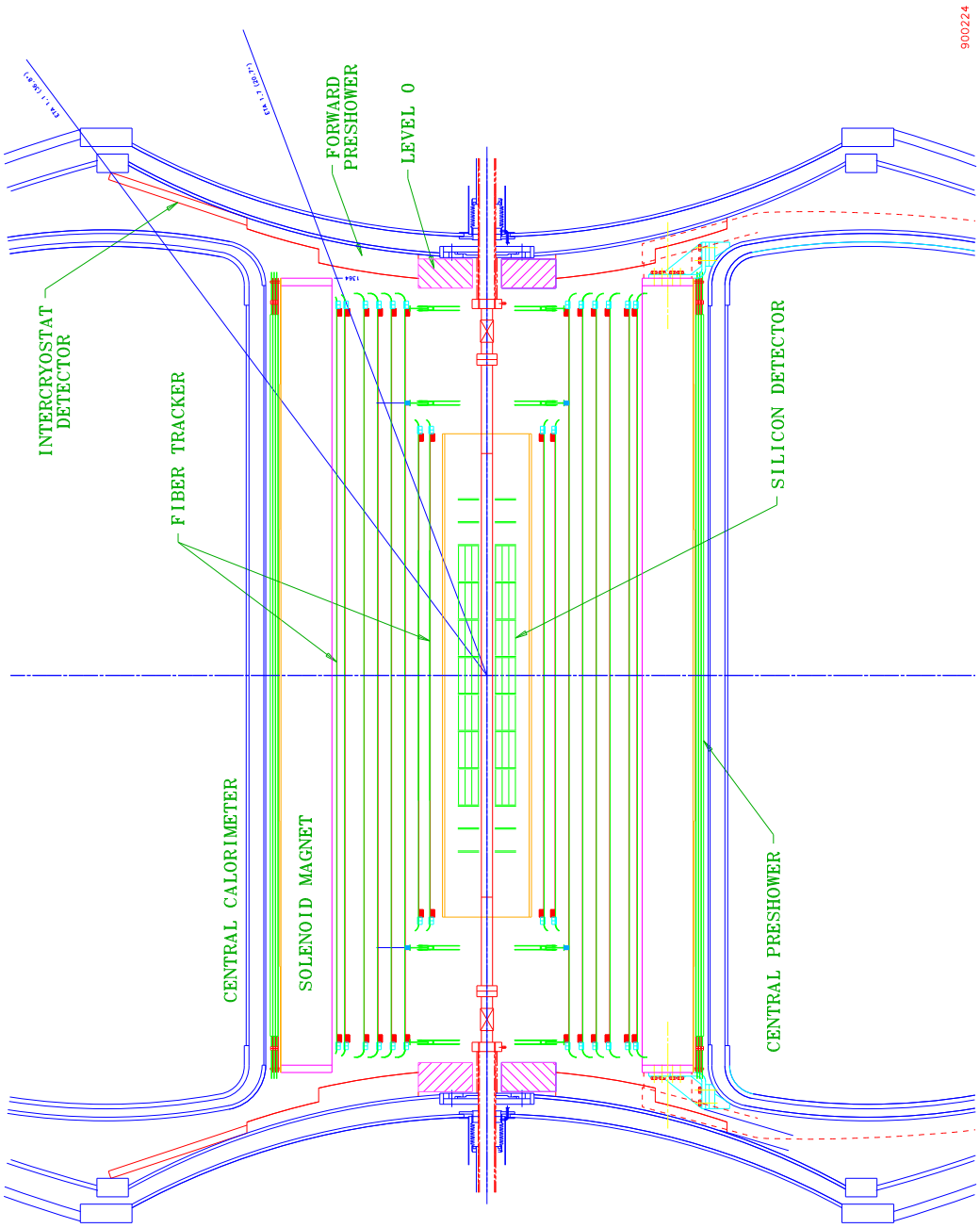

Fig. 2.3: Side view of the inner DØ Detector systems.

number of years. Therefore a large fraction of the time for an experimentalist at DØ must be devoted toward developing, testing and maintaining the hardware and software needed to run the experiment. Some of the work that I have contributed to, which is not directly relevant to this thesis, includes materials and hardware testing for the Silicon Microstrip Tracker and software development for the Central Preshower.

Before being installed in the detector, each of the 793,000 readout channels in the SMT must be thoroughly tested over extended periods of time to make sure they are not defective. Initial tests included a visual inspection to make sure wire bonds properly connected the silicon strips to the readout electronics and examination of each channel to identify dead or unreliable channels. To ensure long-term reliability, checks for dead or unreliable channels were again performed after a 72 hour burn-in [29].

The inner tracking detectors, especially those layers closest to the beam, are exposed to much more radiation than in Run I. Therefore consideration must be given to the effects of this radiation on the detectors and electronics over the expected life of the experiment. This is done by simulating the effects of exposure over time with a beam from a linear accelerator. Effects after exposure such as increased leakage current which can reduce the size of the depletion region are measured. This was carried out for Run II silicon modules [30] and also for a proposed silicon detector upgrade for Run IIb [31].

The preshower detectors have great potential to improve the quality of electron identification, but unfortunately they were not quite ready in time to be used in this analysis. One of the software projects I have worked on for the Central Preshower involved optimizing the parameters governing the formation of 3-D clusters in the CPS reconstruction code [32]. Another involved developing an algorithm to remove the false clusters often produced in busy events when several

particles pass through the CPS in close proximity to each other [33].

2.4 Detector Coordinates

A right-handed coordinate system is defined with the origin at the center of the detector along the beam path. The positive z-axis points in the direction of the proton beam, the y-axis directly up and the x-axis away from the center of the Tevatron ring. In spherical coordinates, the polar angle $\theta = 0$ corresponds to the positive z-axis and $\phi = 0$ corresponds to the x-axis. For cylindrical coordinates, r and r-ϕ are used to refer to distance from the beam line and around the beam line respectively.

Of the many elementary particles within the colliding proton and antiproton, typically only two of these partons will collide. The remaining 'spectator' partons will continue down the beam pipe undetected. This loss of momentum prevents a measurement of the magnitude of the boost along the z-axis for the interacting pair. Because of this, a useful variable to use in place of θ is rapidity, defined as

$$y \equiv \frac{1}{2}\, ln\left(\frac{E + p_z}{E - p_z}\right), \tag{2.1}$$

since it is invariant under Lorentz transformations along the z-axis; therefore differences in rapidity between two particles will be unchanged by such transformations. A useful approximation to rapidity that can be applied when a particle's rest mass is much smaller than its energy is pseudorapidity, η, defined as

$$\eta \equiv -\, ln\left(tan\,\frac{\theta}{2}\right). \tag{2.2}$$

This is often more convenient since it can be expressed as a function of θ and is

more easily measured than rapidity.

Collisions do not occur at exactly the same position each time, but rather the distribution of the interaction point is approximated by a Gaussian shape. While the widths along the x and y axes are only around 30 μm, the 28 cm width along the z-axis makes two definitions of pseudorapidity necessary. The first is the true pseudorapidity, $\eta_{physics}$ or simply η, which is defined with respect to the vertex from which the particle originated. The other, η_{det}, is defined with respect to the center of the detector at (x,y,z) = 0. This is the most convenient choice when the location through which a particle passes a layer of the detector is desired. η_{det} should be specified with respect to a particular layer since it will vary slightly from layer to layer. For this thesis, η_{det} will always be given with respect to the third EM layer of the calorimeter unless otherwise indicated.

It is convenient to define conical regions for the purpose of clustering together nearby objects in a detector subsystem and for matching these objects between different subsystems:

$$\Delta R_{det} \equiv \sqrt{(\Delta\eta_{det})^2 + (\Delta\phi)^2} \tag{2.3}$$

and

$$\Delta R_{physics} \equiv \sqrt{(\Delta\eta_{physics})^2 + (\Delta\phi)^2}. \tag{2.4}$$

Here $\Delta\eta_{det}, \Delta\eta_{physics}$ and $\Delta\phi$ are distances between the objects being compared for each respective variable. For clustering, ΔR_{det} is normally used while it is best to use $\Delta R_{physics}$ for matching physics objects between layers.

Pair annihilation is a hard-scattering process leading to the creation of new particles with high transverse momentum,

$$p_T \equiv p \, sin \, \theta. \tag{2.5}$$

With the ability of the calorimeter to measure energy up to $|\eta_{det}| = 4.5$, the transverse momenta of the spectator particles which escape undetected down the beam pipe are negligible and conservation of transverse momentum can be applied. Similarly a "transverse energy" term can be defined as

$$E_T \equiv E \, sin \, \theta \tag{2.6}$$

where E is the energy found in the calorimeter. Since, for particles traveling through the detector, mass is typically negligible compared to energy, these two variables can be treated as equivalent quantities measured with different detector systems: p_T with the tracking system and E_T with the calorimeter.

The central calorimeter EM layers are physically assembled from 32 individual wedge shaped modules. Each module subtends $\pi/16$ radians in ϕ and extends the entire length of the central calorimeter in z [34]. Due to this, small cracks between modules are unavoidable. It is important to know where a particle passes through the calorimeter with respect to these cracks since they will affect particle reconstruction. For this reason, the variable *phimod* is introduced:

$$phimod \equiv \left(32 \times \frac{\phi}{2\pi} \right) \; mod \; 1. \tag{2.7}$$

In terms of *phimod*, a value of 0 or 1 indicates the particle traveled directly through a crack while 0.5 indicates it traveled through the center of a module with respect to ϕ.

2.5 The Inner Tracking System

The inner tracking system is designed to precisely measure the position of charged particles as they pass through the inner detector layers. The tracks left by these particles can be extrapolated, from the detector hits, back to their point of origin. For particles produced directly from the $p\bar{p}$ collision, this point of origin is called the primary vertex. Many of these high energy particles will decay very near the primary vertex. To distinguish these secondary vertices from the primary vertex, detectors capable of very precise position measurements are used. The most precise measurements are needed nearest the beam for vertex reconstruction, which is why the innermost part of the tracking system employs a Silicon Microstrip Tracker (SMT). The silicon detectors are far too expensive and bulky to be used for the entire inner tracker so a majority of the volume is occupied by the Central Fiber Tracker (CFT). Another advantage of the CFT is a faster response time which is necessary for low level triggering. With the combined tracking systems, the primary vertex can be located to within a resolution of 35 μm along the beam line and, for high transverse momentum particles, the r-ϕ impact parameter resolution can be better than 15 μm. The paths of charged particles are curved by the solenoid magnet which surrounds the inner tracking system. Based on the level and direction of curvature, a particle's momentum and charge sign can be determined.

2.5.1 The Silicon Microstrip Tracker (SMT)

The SMT is built extremely close to the beam pipe with as little as 2.6 cm of separation. Its central part is composed of alternating barrel and F-disk type detector segments, as shown in Figure 2.4, which is extended to $\pm$50 cm to cover most of the interaction region. The barrel faces are parallel to the beam and are

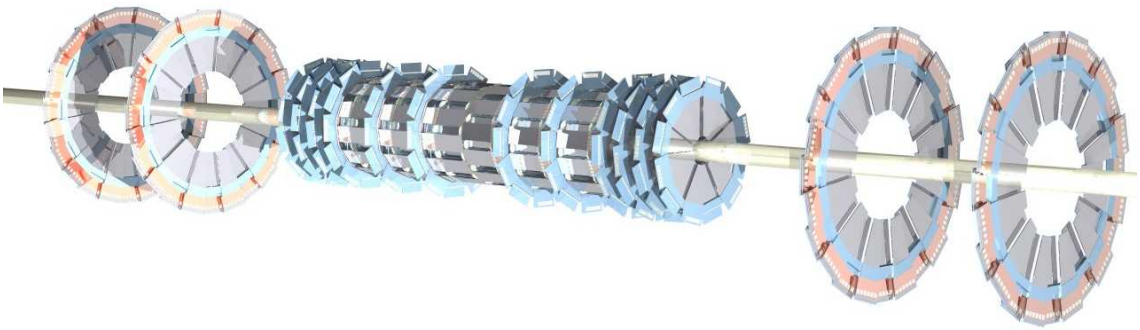

Fig. 2.4: The Silicon Tracker. At the ends are the four H-disks and in the middle are the twelve F-disks. Placed parallel to the beam, between the F-disks, are the barrels.

designed for particles traveling at low η while the F-disks face perpendicular to the beam and are designed for particles traveling at high η. There are also four larger H-disks spaced further away at $\pm$94 cm and $\pm$126 cm from the interaction region whose purpose is to provide additional high η coverage up to $|\eta_{det}| = 3$.

The silicon is segmented into strips which direct the electrons and "holes", freed by the passage of charged particles, to the appropriate readout channel. There are a total of 793,000 channels which are read out using SVX-IIe chips [35]. The SMT is designed to be capable of position resolutions up to 30 μm although in practice resolution is closer to 50 μm. 3-D track hit positions are made possible through the use of double-sided silicon modules which are present in most of the SMT layers. For the construction of the bulkhead which holds the detectors in place, beryllium was chosen due to its high rigidity and long radiation length (radiation length is described in Section 2.7).

There are six barrels, each 12.4 cm long and containing four layers spaced out evenly from the beam with layer 1 at a radius of 2.6 cm to layer 4 at 10 cm. They are composed of rectangular ladder type detectors which are staggered to provide full ϕ coverage as shown in Figure 2.5. Layers 1 and 3 contain double-

sided detectors for the four central barrels with a 90^o difference in strip direction. Layers 1 and 3 are single sided for the two end barrels. Layers 2 and 4 are double-sided with a 2^o angle difference in strip direction between sides for all barrels. All layers have a side with silicon strips running parallel to the beam for an r-ϕ hit measurement with a strip pitch (the center-to-center distance between adjacent strips) of 50 μm, while the strips angled at 90^o have a pitch of 156 μm and at 2^o 62.5 μm. Position resolutions are expected to be approximately equal to strip pitch divided by $\sqrt{12}$, however the ability to share charge between strips improves this. With the 50 μm pitch of the axial layers, an $r - \phi$ resolution of 7 μm has been obtained. Z resolution is approximately 25 μm with the 90^o stereo detectors and 250 μm with the 2^o stereo detectors [36].

The F-disks, shown in Figure 2.5, are formed from twelve F-wedge type detectors which are double-sided with a radial coverage of 2.5 to 9.8 cm from the beam and a strip pitch of 50 μm. Each of the four H-disks has a radial coverage of 9.6 to 23.6 cm from the beam and a strip pitch of 80 μm. H-wedges are composed of single sided detectors which are glued back to back to mimic a double-sided detector. The F-wedge strips are angled at $\pm 15^o$ from perpendicular to the beam on either side while the H-wedges are at $\pm 7.5^o$, yielding a 30^o difference in strip direction for the F-wedge and 15^o for the H-wedge [37][38].

2.5.2 The Central Fiber Tracker (CFT)

The CFT is used in conjunction with the SMT to provide track reconstruction up to $|\eta_{det}| < 2.0$. It consists of 76,800 scintillating fibers over eight cylinders with a radius ranging from 20 to 52 cm. Most of the cylinders are 2.5 m in length, however the two innermost are cut to 1.7 m in order to make room for the SMT H-disks. This layout is shown in Figure 2.6

As a charged particle passes through a scintillating fiber, the material is ex-

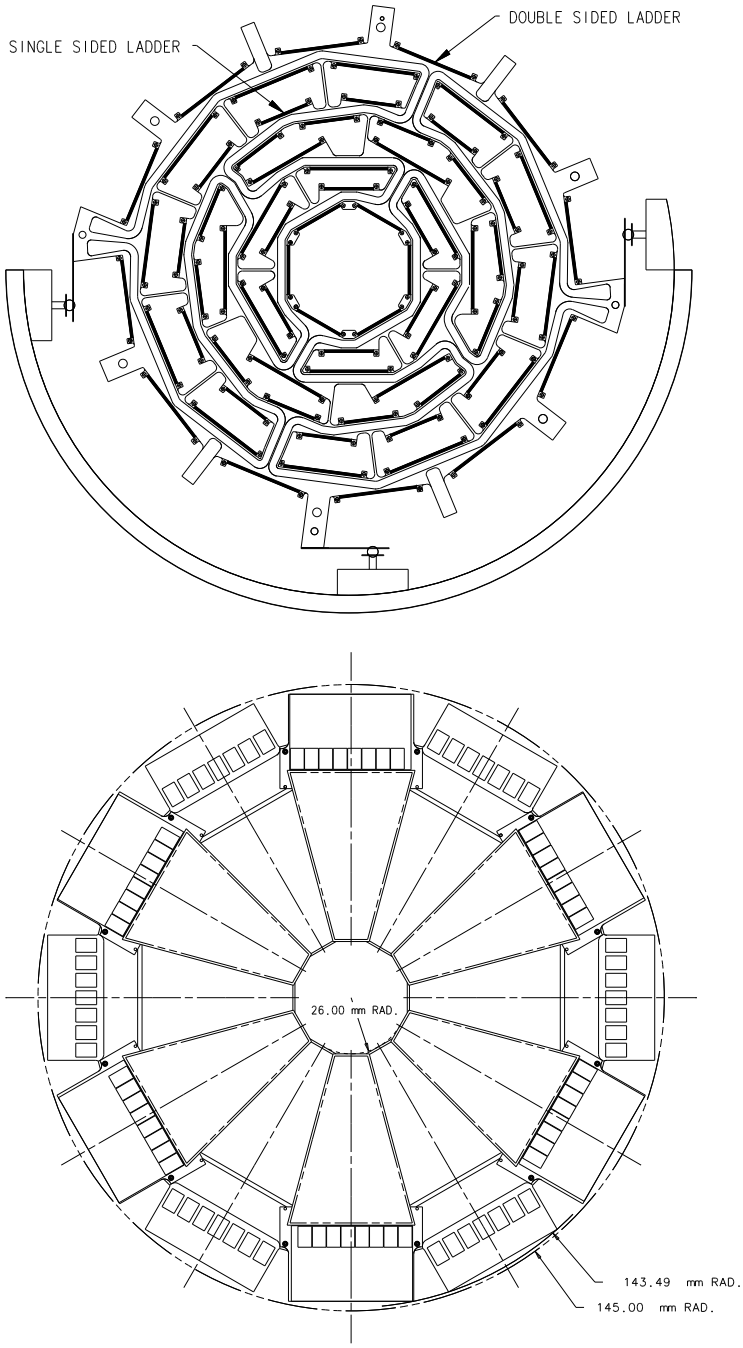

Fig. 2.5: Diagrams showing an end view of the arrangement of the ladder detectors in a barrel (top). The detectors, represented by the thick shaded lines, are held in place by bulkheads made of beryllium. The arrangement of the F-wedges and the SVXII readout electronics is shown in a F-disk (bottom).

cited and, in the process of returning to its original state, yellow-green light is emitted. This light is transported through fiber optic wave guides attached at the ends of the CFT to the visible light photon counters (VLPCs). The conversion of the analog VLPC current into digital readout is handled by SVXIIe chips.

Each cylinder is composed of two doublet layers with strips in one doublet oriented parallel to the beam (z), and strips in the other doublet at an angle of $+3^o$ (u) or -3^o (v) in order to enable 3-D hit finding. Starting with the inner cylinder, the orientation of doublets is $zu - zv - zu - zv - zu - zv - zu - zv$. Scintillating fibers have a diameter of 835 μm and, with the two layers in each doublet staggered, an effective strip spacing of just under 500 μm is obtained. This allows a doublet resolution of about 100 μm [39][40].

2.5.3 The Solenoid Magnet

One of the major additions to the detector for Run II is the 2 Tesla superconducting magnet which makes possible the measurement of charged particle momenta in the inner tracking system. The relative momentum resolution is approximately $\Delta p_T/p_T = 0.002\, p_T$ (in GeV/c), where the relative momentum resolution gets worse for higher p_T tracks due to a decreased level of curvature. The solenoid has a length of 2.8 m, a mean radius of 60 cm and a total thickness of 67 cm. With this thickness, there is approximately one radiation length (described in Section 2.7) of material through which particles must pass. In addition to reducing energy loss, the radiation length is kept at approximately one in order to optimize the amount of showering for the Central Preshower located just outside the solenoid. The superconducting coils, through which a 4825 A current travels, are composed of strands of Cu + NbTi and stabilized inside a tube of pure aluminum. In order to maintain a uniform magnetic field, the current density is increased near the ends of the magnet by narrowing the coil [41].

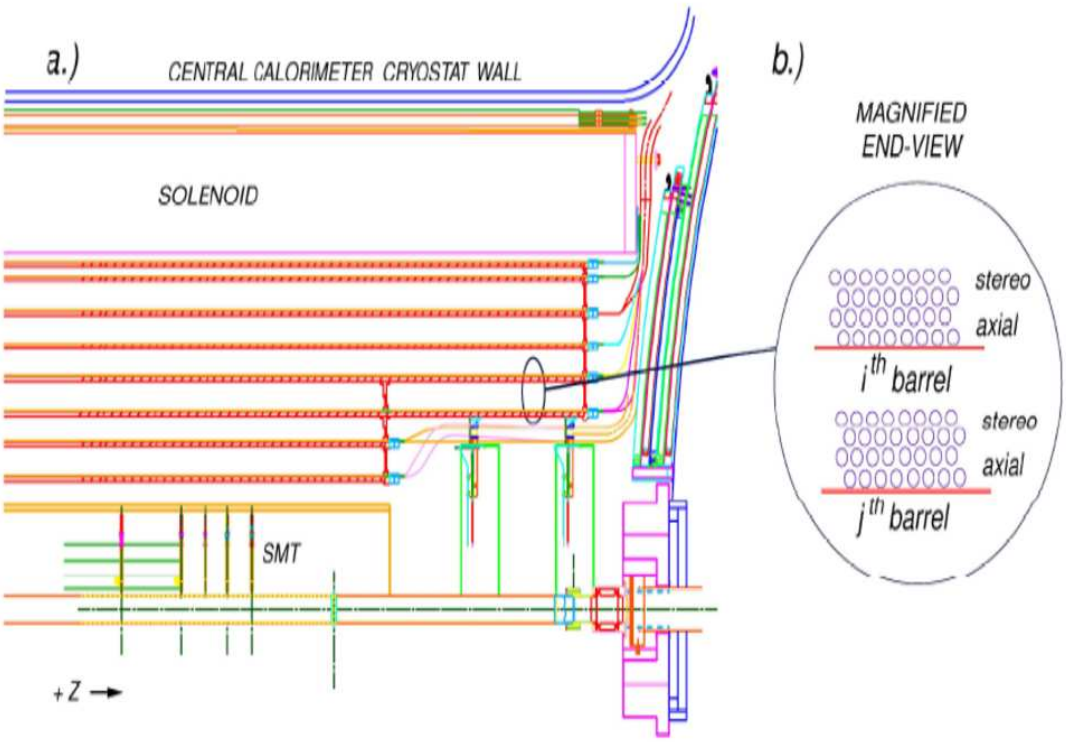

Fig. 2.6: a) Side view of one quadrant of the inner detector showing the eight cylinders of the CFT layered between the SMT and solenoid. b) A magnified view showing the arrangement of scintillating fibers within two of the cylinders.

2.6 The Preshower Detectors

The preshower detectors have been added for Run II to counter energy loss and showering effects caused by interactions with the material in the solenoid and the inner tracker. They are composed of scintillating fibers which can be used to measure both the position and energy of charged particles. This will help compensate for the expected degradation in position and energy resolution in the calorimeter. Identification of particles such as the electron, photon and π^0 can be improved by taking advantage of differences in their showering characteristics as observed in the preshower. Also, the fast response of the scintillating fibers enables the CPS to be used in low level electron trigger conditions. The preshower is composed of the Central Preshower (CPS) covering $|\eta_{det}| < 1.2$ and the Forward Preshower (FPS) covering $1.5 < |\eta_{det}| < 2.5$. Light is emitted as charged particles pass through triangular-shaped scintillator strips. This light is collected in a fiber that goes through the middle of the strip and transferred through waveguides at the edge of the detector to the VLPCs. Diagrams of the scintillator strips are shown in Figure 2.7.

The Central Preshower is placed immediately after the solenoid to provide position and energy measurements before the resulting particle showers have had a chance to spread out. It is composed of three layers with strips in the inner x layer aligned parallel to the beam and strips in the u and v layers angled at $+$ and $-$ 23^o with respect to the x layer. While only two layers are necessary to provide 3-D hit finding, an extra layer is important in multiple particle events to locate the correct strip intersection for each hit. The three layers must fit in a very tight space between the solenoid and calorimeter cryostat with the x layer starting at 72 cm and the v layer ending at 75 cm. Each layer is divided into two halves split at z = 0 with each half read out at the corresponding detector

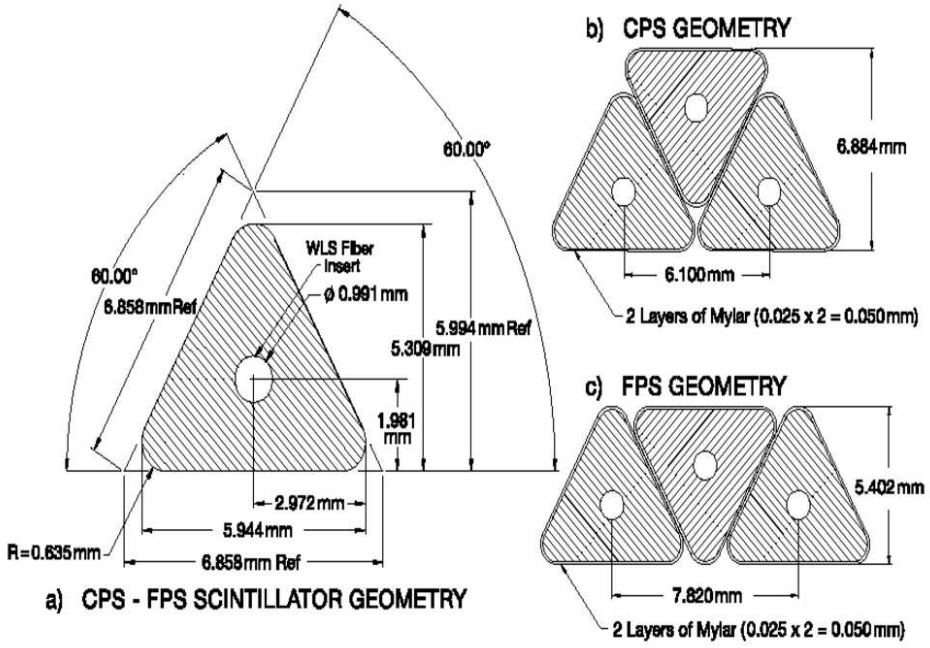

Fig. 2.7: Geometry of the scintillator strips used in the CPS and FPS..

end. Each half is composed of 1280 strips with an average strip separation of 3.5 mm for a total of 7680 strips [42]. Position resolution is approximately 1.0 mm along $r - \phi$ and 2.0 mm along z.

The Forward Preshowers are mounted directly in front of the end calorimeter cryostats at either end of the detector. Each FPS has two layers in z with each layer composed of two stereo planes, u and v, of scintillator strips. The two layers are separated by two radiation lengths of lead absorber. The purpose of this lead layer is to induce showering similar to that of the solenoid. Each layer is divided into two sublayers in z with each sublayer divided into sixteen wedge segments covering 22.5^o each in ϕ. However, only every other wedge contains active scintillator while the other wedge spaces are needed for cabling. The active wedges are staggered between sublayers in order to keep full azimuthal coverage. Each wedge contains both a u and a v plane, with scintillator strips aligned perpendicular to one radial edge for the u plane and to the other radial

edge for the v plane. This results in a 22.5^o stereo angle between the u and v planes [43].

2.7 The Calorimeter

The DØ calorimeter is composed of a central calorimeter (CC) providing coverage up to $|\eta_{det}| < 1.05$ and two end cap calorimeters (EC) providing coverage for $1.5 < |\eta_{det}| < 4.5$. In order of distance from the beam, each calorimeter subsystem is divided into three sets of layers: electromagnetic (EM), fine hadronic (FH) and coarse hadronic (CH). These divisions can be seen in the view of the entire calorimeter shown in Figure 2.8. With a total of 150 radiation lengths and 7.2 nuclear interaction lengths (definitions below), practically all the energy from electrons, photons and hadronic jets is absorbed by the calorimeter. Its main purpose is to precisely measure the energy of these particles while providing a decent position measurement. The calorimeter energy resolution varies with type of particle and energy. For example, at an energy of 25 GeV, an electron in the CC has a resolution of approximately 1.5 GeV and at 50 GeV resolution is approximately 2.5 GeV. For high p_T electrons in the CC, position resolution is approximately 0.007 in both η and ϕ. Energy and position resolutions are discussed in detail in Chapter 6.

The calorimeters are composed of many individual cells which are represented in Figure 2.9 by the alternating shaded and unshaded boxes. Most of these cells have a size of 0.1×0.1 in η and ϕ. One exception is the third EM layer where cell size is reduced to 0.05×0.05 in order to improve resolutions where the largest percentage of energy from electrons and photons is expected to be deposited. Also, cell size is increased to 0.2×0.2 for all cells where $|\eta_{det}| > 3.2$ to prevent the physical cell size from becoming too small. Cells are grouped into readout

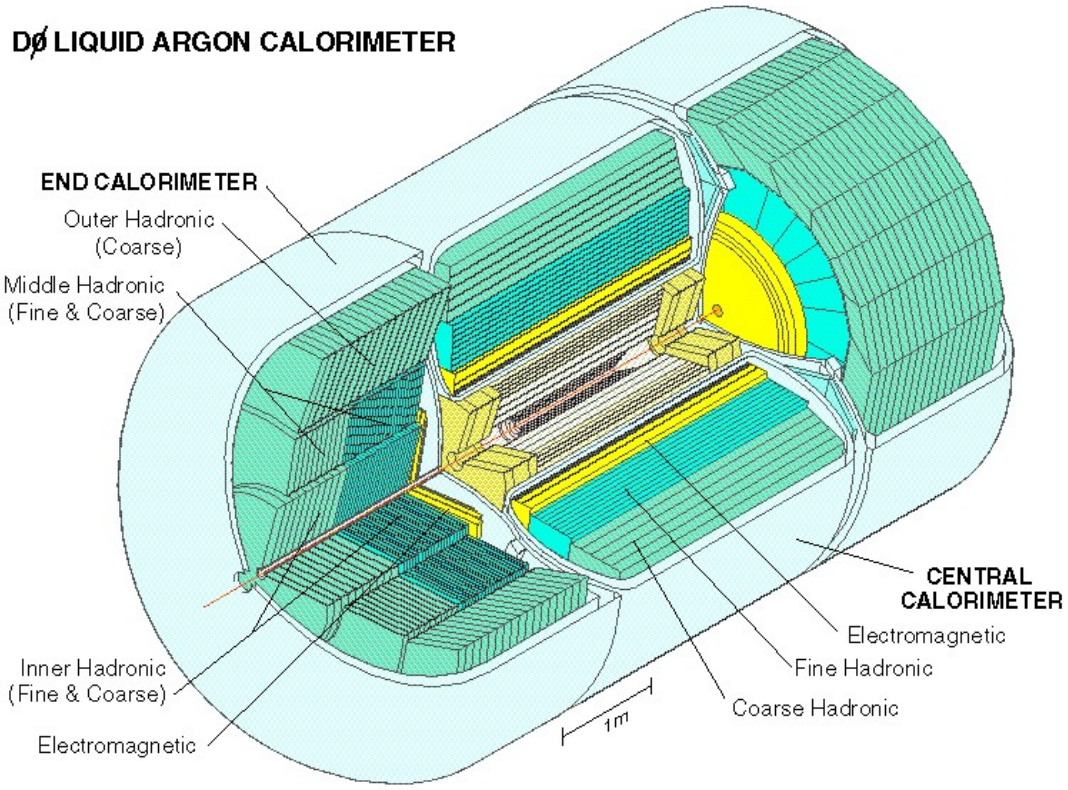

Fig. 2.8: The calorimeter.

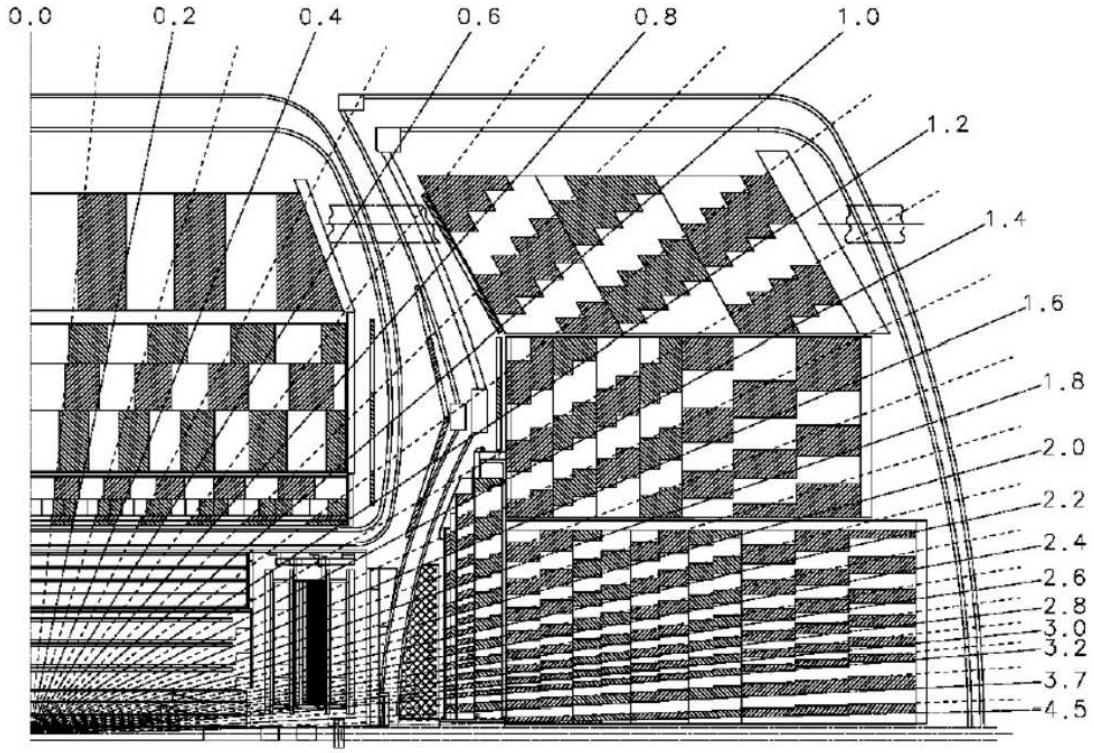

Fig. 2.9: Side view of one quarter of the calorimeter showing calorimeter towers and the corresponding η_{det} coordinates.

towers of size 0.1 $\times$ 0.1 and into trigger towers of size 0.2 $\times$ 0.2 containing all cells in all layers within these η and ϕ ranges. It can be seen in Figure 2.9 that the cells in a tower are arranged so that they line up in terms of η_{det}.

The layers of the calorimeter are designed to take advantage of the smaller distance of penetration of electrons and photons compared to hadronic jets. Almost all energy from EM objects, electrons and photons, will be deposited in the EM layers while much of the energy from hadronic jets will make it into the hadronic layers. This is due to the differences in the way EM objects and hadronic jets interact with the material in the calorimeter. EM objects will interact through electromagnetic processes: bremsstrahlung radiation ($e \rightarrow e\gamma$) and pair production ($\gamma \rightarrow e^+e^-$). The rate of electromagnetic interactions falls off rapidly with

the mass of the particle and can therefore be ignored for hadrons. This is also why muons can pass through the calorimeter with very little energy loss. Due to showering caused by multiple interactions, the energy of the original electron is expected to fall off exponentially:

$$E(x) = E_0 \; e^{-x/X_0} \tag{2.8}$$

where X_0 is the radiation length. With a total of 20 radiation lengths in the EM layer, a low η electron will deposit almost all of its energy here while much of the energy from hadronic jets will make it into the hadronic layers. Showering for hadronic jets occurs in the calorimeter through strong interactions with the nuclei of the atoms in the material. The nuclear interaction length, λ_0, describes the probability, over a given distance traveled, for a nuclear interaction to occur.

The EM cells, in each of the four EM layers of the calorimeter, make use of an absorber plate made of depleted uranium with a thickness of 3 mm per layer to cause particles to shower. Following the absorber plates is liquid-argon which ionizes as the charged particles in the shower pass through it. This released charge is made to travel to copper pads through a high positive voltage where it is read out. The calorimeters are enclosed in cryostats and kept at around 90 K so that liquid-argon can be used as the active medium. There are three fine hadronic layers in the CC and four in the EC which also use depleted uranium as the absorber. There is one coarse hadronic layer in the CC and up to three in the EC which make use of stainless steel and copper absorber plates [34][44].

The region between the CC and EC calorimeters, $1.05 < |\eta| < 1.5$, is referred to as the intercryostat region. There is no energy sampling for the calorimeter and a large amount of material from the cryostat in this region. An Intercryostat Detector (ICD) is introduced to help compensate by providing some energy

sampling in this region. It is composed of a single layer of 384 scintillating tiles of size 0.1×0.1 arranged into sixteen wedges [45].

2.8 The Muon Detector

Since muons will typically experience very little energy loss while passing through the calorimeter, they can be distinguished from other particles through the use of a tracking system placed outside the calorimeter. For the muon detector, tracking is carried out through the use of drift chambers and scintillation counters. With a much larger area to be covered than for the inner tracking system, these are more appropriate since they are relatively low-cost. Drift chamber tubes are filled with a gas which ionizes as charged particles pass through it. The freed charge is made to travel toward the high voltage chamber wires where it is read out. A disadvantage of drift tubes is that they do not provide a very precise measure of the time of a particle's passage. To offset this, layers of scintillation counters, which provide very good timing but poor position resolution, are placed both before the innermost and after the outermost drift tube layers. This improved timing is important for ensuring that the drift tube readout is matched to the correct bunch crossing and for the identification of cosmic ray muon background.

The Muon Detector is divided into central and forward systems. These are the Wide Angle Muon System [46] for $|\eta_{det}| < 1.0$ and the Forward Angle Muon Systems [47][48] at either end for $1.0 < |\eta_{det}| < 2.0$. The central muon system makes use of Proportional Drift Tubes while the forward muon system makes use of Mini-Drift Tubes. Both the central and forward systems are divided into three major layers designated A, B and C. A 2 Tesla toroidal magnet is placed between the A and B layers. This enables a momentum measurement independent of the inner tracking system by matching up hits from the curved path in the A layer

to the hits from the B and C layers outside the magnet. In comparison to the inner tracker, the momentum measurement is rather poor with $\Delta p/p \approx 0.25$, but it can be useful for matching muons to tracks. The muon system is surrounded by shielding material which reduces contamination from backgrounds such as scattered $p\bar{p}$ fragments. In Figure 2.2, the muon drift chambers are represented by the thin boxes with solid diagonal lines and the toroid by the dashed diagonal lines [49].

2.9 The Forward Proton Detector

The forward proton detector (FPD) was added to the DØ Detector to study hard diffraction physics. Accelerator magnets and position detectors are used to measure the position and scattering angle of very high rapidity protons and antiprotons. Position detectors are placed inside roman pots which are moved to a distance of just a few millimeters away from the beam during stable beam conditions. These position detectors use scintillating fibers to measure the x and y coordinates of the deflected proton or antiproton. Thin steel windows at the entrance and exit of each roman pot allow protons and antiprotons to pass through it while keeping the position detectors inside the pot from being exposed to the ultra-high vacuum of the accelerator. There are a total of 18 roman pots housing position detectors: 16 are contained within the two quadrupole castles positioned at both sides of the detector at ± 23 m and ± 31 m, and one each is placed inside the two dipole castles at -58 m and -59 m, in the direction of the outgoing antiproton beam. The quadrapole castles arrange the position detectors so that most of the area surrounding the beam is covered while the dipole castles are positioned after the dipole magnet to intercept scattered antiprotons diverted into it [28, 50].

CHAPTER 3

DATA ACQUISITION

3.1 Luminosity

The number of events expected to be produced for a particular process in $p\bar{p}$ collisions is given by its production cross section, σ (units of area), times the integrated luminosity, $\mathcal{L}$ (units of area^{-1}):

$$\text{events} = \sigma\mathcal{L}. \tag{3.1}$$

The basic unit of area used to express cross sections and integrated luminosities is the barn, where 1 barn = 10^{-24} cm^2. For this analysis, the picobarn is most convenient with 1 pb = 10^{-12} barns. The integrated luminosity is found by integrating the instantaneous luminosity over time. A simplified relation for the integrated luminosity collected over the time interval t_1 to t_2 for a Tevatron store is

$$\mathcal{L} = \int_{t_1}^{t_2} fn\frac{N_p N_{\bar{p}}}{A} dt \tag{3.2}$$

where f is the revolution frequency, n is the number of bunches in either beam, N_p is the number of protons in a bunch, $N_{\bar{p}}$ is the number of antiprotons in a bunch and A is the cross sectional area of the beam interaction region [51].

Luminosity is measured at DØ with the aid of Luminosity Monitors which are

placed 1.35 m away from the center of the detector at either end. A luminosity monitor consists of 24 wedge shaped scintillation counters surrounding the beam pipe. They cover a pseudorapidity range of $2.7 < |\eta| < 4.4$. The luminosity monitors detect the passage of very high rapidity particles produced in inelastic processes. With knowledge of the inelastic cross section and the acceptance for these processes to be identified by the monitors, the luminosity can be determined by counting the number of events found [52].

During Run I, the Tevatron was designed to run with an instantaneous luminosity of 1×10^{31} $\mathrm{cm}^{-2}\mathrm{s}^{-1}$ while currently luminosity rates have exceeded 1×10^{32} $\mathrm{cm}^{-2}\mathrm{s}^{-1}$ and continue to increase. A total integrated luminosity of several fb^{-1} is expected in the next few years.

The data sample used in this analysis consists of an integrated luminosity of 177 pb^{-1} collected between September 2002 and September 2003. Continuous data taking periods are identified by a run number. Whenever data taking must be stopped, upon resuming the run number is incremented by one and assigned to the new data taking session. Data used in this analysis consists of run numbers between 161973 to 180956. Not all of the run numbers in this range are used. Many are just test runs and some are removed because they are declared bad due to problems such as hardware failures or excess noise [53]. A 6.5% total uncertainty on the luminosity is obtained by combining in quadrature the uncertainty on the inelastic cross section (4%) and the uncertainty on the efficiency and acceptance for the detector to successfully identify an inelastic process (5%) [54]. Thus, a value of 177 ± 12 pb^{-1} for integrated luminosity is used in this analysis.

3.2 The Trigger System

The rate of collisions at the DØ Detector, 1.7 MHz, is far too great for every event to be reconstructed and written to tape. Limited computing power and storage space restricts the final recorded event rate to only around 50 Hz. Fortunately, it is possible to drastically reduce the number of events kept while retaining most of the interesting physics. This task is accomplished through the use of a triggering system divided into three levels: Level 1 (L1), Level 2 (L2) and Level 3 (L3). The L1 trigger decision making process must keep up with the collision rate and therefore must rely on the limited information that can be gathered fast enough. Subsequent levels have extra time to make use of more detailed selection information in order to better determine what events to keep. In this way, a multi-level triggering system allows much better event selection than would be possible with just one level. The event output rate is typically around 1400 Hz for L1 triggers, 800 Hz for L2 triggers, and finally 50 Hz for L3 triggers [28].

Triggers are defined as a combination of L1, L2 and L3 trigger conditions. For a trigger to fire, trigger conditions for all three levels must be satisfied. Some triggers are designed to fire on more common physics events which occur too often to be kept every time. To lower the event rate produced by these triggers to an acceptable level, prescales are defined. Prescaled triggers are only tested once out of every 'prescale' number of events. For example, a prescale of one means the trigger is always considered while a prescale of two means only every other event is considered and luminosity is effectively halved. There is no middle ground between a prescale of one (unprescaled) and two and therefore much effort is made to fine tune important borderline triggers so that they can be run unprescaled. The prescale of a trigger may change on a run to run basis

depending on the luminosity at the time. The most extreme prescaling occurs for 'zero_bias' events, useful for studying other triggers, with the only trigger condition being a beam crossing. The zero_bias prescale setting usually exceeds 3,000,000.

Many different triggers are defined for use in data taking with each one designed to fire on a specific type of event. All triggers used in a data taking period are grouped together into a trigger list. If any trigger in the list fires, the event is kept along with information about which triggers were fired. New versions of the standard data taking trigger list are constantly being created in order to add new and improved triggers. As the average instantaneous luminosity continues to increase, revisions to important triggers are necessary so that they can remain unprescaled. In the last trigger list version used to collect data for this analysis, global_CMT 12.30, there are a total of 223 triggers. Here, global refers to the global configuration where trigger conditions may be defined using multiple subsystems and CMT indicates that the calorimeter, muon and tracker trigger subsystems are all used.

The triggers used in this analysis are designed to fire on detection of a single high E_T electron. These triggers are based entirely on calorimeter information. Therefore, in the individual trigger level subsections below, only the calorimeter based triggering subsystems are described in any detail.

3.2.1 The Level 1 Trigger

The L1 trigger subsystem takes as input all events produced at DØ at a rate of 1.7 MHz and outputs selected events at a rate of around 1400 Hz. To operate at this speed, trigger decisions must be based solely on hardware. Only the fastest readout electronics are capable of a quick enough response time. All events awaiting L1 trigger decisions are pipelined in order to prevent dead time which

would otherwise occur in cases where a trigger decision couldn't be made in time before the next beam crossing. The three main detectors used at L1 are the calorimeter, muon and CFT subsystems. Additional L1 information comes from the luminosity monitor, forward proton detector, CPS and FPS subsystems. The L1 trigger has limited information available for decision making and therefore relatively limited discrimination ability. An emphasis is placed toward ensuring interesting physics events are saved at the expense of keeping many that are not. The L1 trigger framework manages the collection of information from all subsystems. It checks if any of the L1 triggers have fired or, if prescaled, whether the trigger should be ignored for the event. The trigger framework is capable of handling a maximum of 128 L1 trigger conditions.

The L1 calorimeter trigger subsystem makes use of information gathered from the 1280 calorimeter trigger towers of size 0.2×0.2 in η and ϕ as defined in Section 2.7. Information from each tower includes the η and ϕ position of the tower along with total transverse tower energy and EM only transverse tower energy. Two of the L1 trigger conditions used in this analysis are CEM(1,10), one tower with EM only energy > 10 GeV, and CEM(2,5), two towers with EM only energy > 5 GeV. The intention of the CEM(2,5) trigger condition is to save events in which an electron's energy is shared by two adjacent towers, however the trigger condition does not actually require the towers to be adjacent. The efficiency for these trigger conditions to keep events where there is at least one electron with $E_T > 25$ GeV, as needed for this analysis, is extremely high.

3.2.2 The Level 2 Trigger

In practice, the level 2 trigger subsystem inputs events from L1 at a rate of around 1400 Hz and outputs events to L3 at a rate of around 800 Hz. It consists of preprocessor subsystems for the tracker, calorimeter, preshower and muon de-

tectors and a global processor which combines data across the detectors. First, the L1 information from each subsystem is read out and sent to the corresponding L2 preprocessor where it is, for some subsystems, combined with additional information. The preprocessors analyze this information separately for each subsystem to form basic physics objects such as clusters and tracks. Results from all preprocessors are sent to the L2 global preprocessor where they are combined. Here, advanced physics objects are formed by matching up the basic physics objects between subsystems.

The L2 calorimeter preprocessor combines the trigger towers together to form clusters. The L2 jet algorithm is especially important for hadronic jets which can spread out over several towers. The jet algorithm starts by defining all towers with a total $E_T > 2$ GeV as seeds and orders them according to E_T. Clustering is carried out in order starting out with the highest E_T seed. Seeds which are too close to higher E_T seeds are dropped. Jet candidate clusters are formed by adding up all towers in a 5×5 grid centered at the seed towers. The L2 EM algorithm works in a similar manner using the EM-only tower energies. Here seed towers must have an EM-only $E_T > 1$ GeV and EM candidate clusters are formed from a 3×3 grid centered at the seed towers. Most of the triggers used in this analysis do not have a L2 trigger component. Those that do use the L2 trigger condition EM(1,12), defined as one EM candidate cluster with $E_T > 12$ GeV.

3.2.3 The Level 3 Trigger

If the L2 global processor passes the event, the entire detector is read out into a buffer which waits for the next available processor in the L3 computer 'farm'. The farm is capable of analyzing many events in parallel through the use of large numbers of standard x86-based processors. The events are partially re-

constructed using a simplified version of the offline reconstruction code. This reduces the 800 Hz L2 input rate to the 50 Hz needed for recording and offline analysis.

The L3 calorimeter reconstruction makes use of higher precision readout with information available at the calorimeter cell level. For EM objects, the clustering method uses a a simplified cone of width $\Delta R_{det} = 0.25$. Discriminants for electron identification are defined including EM energy fraction and transverse shower shape. EM fraction is simply the fraction of the total energy of the cluster found in the EM layers. The transverse shower shape compares the relative widths of the cluster in each of the EM layers to that expected from an electron. A couple of the L3 algorithms used in this analysis are ELE_LOOSE(1,30) and ELE_LOOSE_SH_T(1,20). The first trigger requires one $E_T > 30$ GeV cluster satisfying EM fraction > 0.9 while the second requires one $E_T > 20$ GeV cluster satisfying EM fraction > 0.9 and transverse shower shape cuts. The shower shape cuts place maximum width restrictions on the electron shower in the first three EM layers. For ELE_LOOSE_SH_T(1,20), these widths are $\Delta R_{det} < 0.09$ for EM layer 1, $\Delta R_{det} < 0.08$ for EM layer 2 and $\Delta R_{det} < 0.05$ for EM layer 3.

3.3 Offline Reconstruction

Events which have fired one or more triggers are stored on tape and sent to a farm containing hundreds of standard x86-based Linux computers for reconstruction. At this point the data are stored as 'raw' electronic digital readout. The offline reconstruction program, DØReco [55], converts this raw information into physical objects such as electrons, muons and hadronic jets. To fully reconstruct one event takes approximately 15 to 30 seconds on a 1 GHz machine.

In the first step of the reconstruction process, the digital readout channels

for detector components such as silicon strips, scintillator fibers and calorimeter cells are converted into particle 'hits'. If minimum threshold requirements are surpassed, the readout of the hit channel is converted to a definite position and energy. In the next step these hits are grouped together. For the tracking system hits from different layers are used to extrapolate the paths of charged particles. For the calorimeter, adjacent energetic cells are grouped together to form a cluster. In the last step these tracks and clusters are matched together to form the basic physics objects. At this stage, particle identification cuts are placed with an emphasis on maximizing efficiency. This gives individual analyzes greater flexibility in defining their own cuts.

3.3.1 EM Object Reconstruction

Both electrons and photons entering the calorimeter are identified by the formation of EM objects. The reconstruction of EM objects is handled by the EMReco component of D0Reco. There are three different clustering algorithms included in EMReco: the Nearest Neighbors, Simple Cone and CellNN algorithms. For this analysis, only the Simple Cone algorithm is used. For this method, rough initial clusters are created using tower information only in order to reduce computation time. These then become seeds for the formation of final clusters which make use of all available information. The initial clusters are defined by a cone of radius $\Delta R_{det} = 0.2$ and are rejected unless they satisfy the following requirements: $E_T > 1.5$ GeV, EM fraction > 0.9 and isolation < 0.2. The isolation variable, f_{iso}, is defined as:

$$f_{iso} = \frac{E_{total}(0.4) - E_{EM}(0.2)}{E_{EM}(0.2)} \tag{3.3}$$

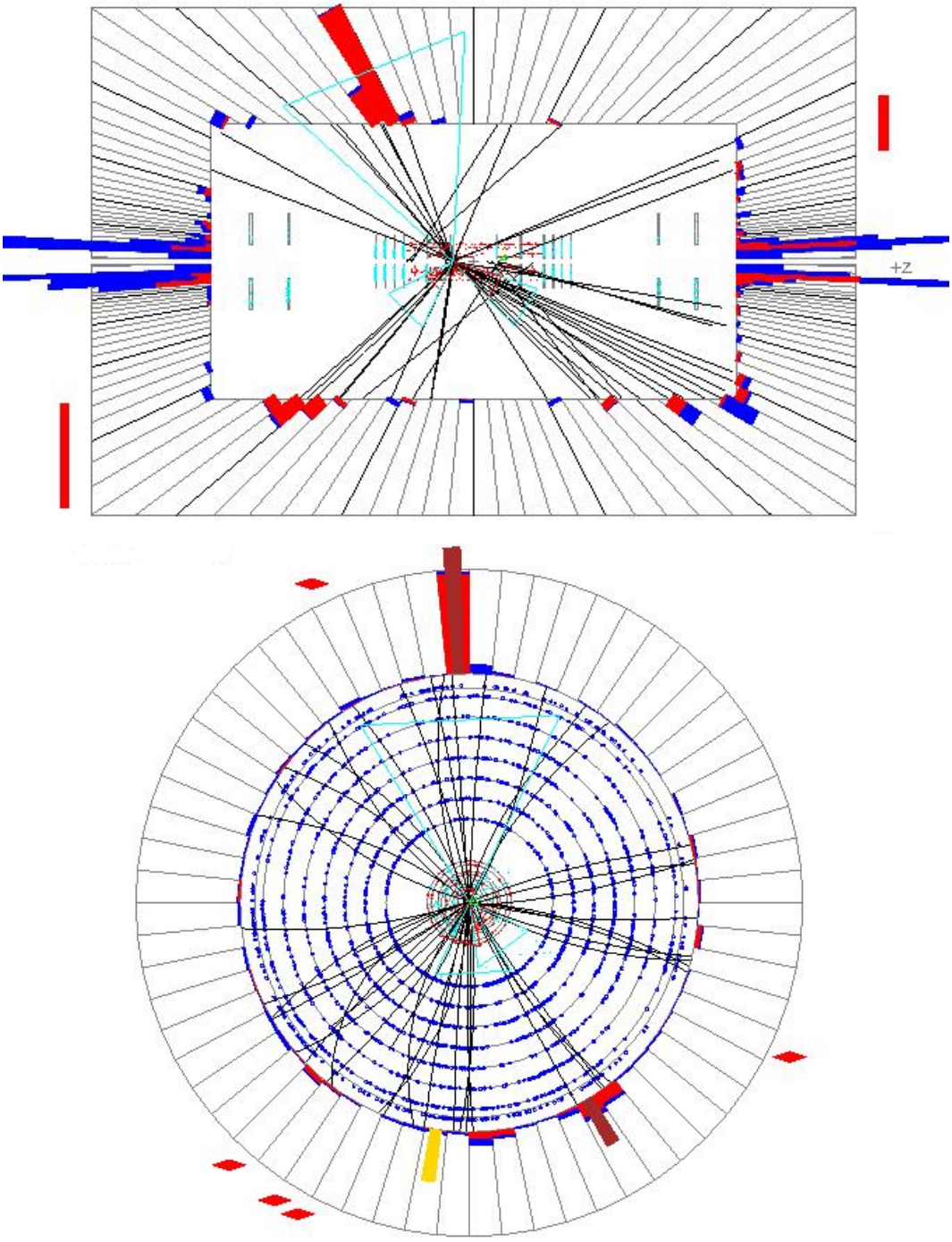

Fig. 3.1: Side and end views of an event containing E_T = 35 and 14 GeV EM objects with nearby tracks and 15 GeV missing E_T. Also, a large amount of hadronic energy can be seen in the calorimeter at very high rapidity. (The color scheme for the calorimeter is red for EM energy, blue for hadronic energy and yellow for missing E_T.)

where $E_{tot}(\Delta R_{det})$ and $E_{EM}(\Delta R_{det})$ are the total energy and EM energy within a cone of radius ΔR_{det}. Initial clusters passing these requirements are used as seeds for final cluster formation. Quantities are defined for the final clusters which make use of information from all the cells within a cone of radius $\Delta R_{det} = 0.2$ centered at the highest E_T tower in the initial clusters [56].

3.3.2 Track Reconstruction

The track reconstruction code attempts to extrapolate the trajectories of charged particles passing through the tracker layers using the hits left behind in the detector. These hits are formed by clustering together groups of readout channels in a single layer which are determined to have been produced by a single particle. The extrapolation of tracks is then carried out using a road following algorithm [57]. The basic principle of this algorithm is to start with a track segment composed of three hits and iteratively build up the track by matching to hits in adjacent layers. The track + hit combination is fit to a curve defined by six parameters. In cylindrical coordinates, these parameters are

- r, ϕ and z for position,
- α for track direction in the x-y plane,
- tan λ for track direction along the polar angle ($\lambda = \pi/2 - \theta$),
- and q/p_T for the charge of the track over p_T (defines the direction and level of curvature of the path in ϕ).

A χ^2 test is performed for the track + hit combination, using the best curve fit, in order to determine if the hit should be added. If no hit is matched in a layer then it is referred to as a miss. Due to the possibility of a particle traveling through an inactive region in a layer, the occasional miss is allowed.

To reduce computation time, tracks are propagated to the next layer and only hits reasonably near the expected track position are considered. A final list of candidate tracks is produced and ordered according to track quality based on number of hits, fewest misses and best χ^2 value. Information defining the path and momentum of these final tracks is obtained from the parameters used in the curve fits [58].

3.3.3 Vertex Reconstruction

Measuring the position of the primary vertex, where the $p\bar{p}$ collision occurred, is very important. It is needed for many purposes such as the reconstruction of EM objects, hadronic jets and missing E_T. The primary vertex is expected to be very close to the beam line, although position varies considerably along the z-axis. For this reason, only tracks with an impact parameter significance less than three are used for primary vertex reconstruction. Here, impact parameter significance is defined as the distance of closest of approach with respect to the beam line divided by the uncertainty. All remaining tracks are fit to a single vertex and removed one by one based on which increases the χ^2 the most. This is repeated until none of the remaining tracks increase the χ^2 by over a certain amount. More vertices are searched for by applying the same method to tracks not already included in a vertex. If more than one vertex is found, the primary vertex is chosen using

$$F_{vertex} \equiv \sum_j log(p_T^j). \tag{3.4}$$

where $\sum_j$ runs over all tracks included in the vertex. The vertex with the highest value of F_{vertex} is chosen. This method is designed to select the hard scattering $p\bar{p}$ collision as the primary vertex, while rejecting any secondary interactions,

expected to produce high rapidity and low p_T tracks, which may occur along the beamline. After this, secondary vertices from long lived particles are searched for. Secondary vertices are not used in this analysis, because W and Z bosons have extremely short lifetimes and can always be treated as decaying at the primary vertex [59].

3.3.4 Missing E_T

A momentum imbalance is produced by a neutrino passing through the detector without leaving a trace. By applying the law of momentum conservation, a neutrino's momentum could in principle be inferred as equal in magnitude to the momentum imbalance and pointing in the opposite direction. This is spoiled however by high rapidity particles escaping down the beam pipe undetected. This energy loss can lead to large imbalances in the longitudinal component of momentum. However, losses in the transverse direction should be negligible and therefore conservation of transverse momentum can still be applied.

Assuming particle masses are negligible with respect to energy, $E_T \approx |\vec{p}_T|$, the momentum imbalance can be calculated by adding up the calorimeter cell transverse energy vectors. These vectors are defined as $\vec{E}_T = E_T\ \hat{\phi}$ where $\hat{\phi}$ points from the z-axis to the cell. The missing transverse energy, $\not{E}_T$, is found using

$$\not{E}_x = -\sum_i E_{Ti} \cos\phi_i \ , \quad \not{E}_y = -\sum_i E_{Ti} \sin\phi_i \tag{3.5}$$

$$\text{and} \quad \not{E}_T = \sqrt{\not{E}_x^2 + \not{E}_y^2} \tag{3.6}$$

where the sum runs over all calorimeter cells except for those from the coarse hadronic layer. Corrections can then be applied to account for energy scale dif-

ferences based on particle type. For this analysis, only electron corrections are applied. Jet corrections are not applied because they are not well understood for the low E_T recoil jets and because of problems caused by misidentified jets. The value for missing E_T which is used for all data analysis in this thesis is calculated using the component of DØReco named 'missingET' [60]. This calculation includes the electron corrections.

3.4 Calorimeter Issues

After the offline reconstruction is finished, there are still a number of data quality issues involving the calorimeter which must be addressed. These include: inconsistent energy calibrations across calorimeter modules, cluster shifting in ϕ caused by energy loss in the cracks between modules, and problematic calorimeter regions.

3.4.1 Calibration

Several parameters are used to model the detector in our Parameterized Monte Carlo Simulation (PMCS) [61] described in Chapter 6. For most parameters, a single value is used over the entire central calorimeter. However, due to an inconsistent calibration in the central calorimeter, it is necessary to model two of the most affected of these parameters in greater detail. The electron energy scale, described in Section 5.6.1, is not consistent from module to module in ϕ. Also, missing E_T is found to differ significantly between the positive and negative central calorimeter η_{det} halves. The PMCS parameter describing the amount of hadronic energy lost to the region surrounding the electron cluster, $u_{\parallel}$ (see Section 5.6.7 for details), has a direct effect on missing E_T and is found to vary with both ϕ and η_{det}.

In order to account for these variations, both relative electron energy scale and $u_{\parallel}$ are measured for each of the ϕ modules and both halves of the central calorimeter as shown in Figure 3.2. Relative electron energy scale is measured as the peak in the ratio of calorimeter E_T to track p_T distribution for the W candidate sample. For $u_{\parallel}$, a correction factor is chosen which equally divides the W candidate sample based on measured $u_{\parallel}$.

3.4.2 EM Cluster Shifting in ϕ

There are cracks in the central calorimeter between the azimuthal module boundaries. A particle entering the calorimeter near these boundaries can lose a portion of its energy to these cracks which will shift its ϕ cluster centroid toward the center of the module. Since the energy scale in the region around the cracks is not well understood, it must be excluded from the good fiducial region. For consistency, fiducial cuts must be made based on position using calorimeter only information since not all electrons are required to have a matched track. Therefore, there will be a tendency for particles whose true ϕ position falls within a cut region to have a measured ϕ position shifted into the good fiducial region. This causes a significant increase in our acceptance and therefore must be accurately modeled in PMCS.

Electrons with a track match are used to measure the calorimeter ϕ shift with the track position treated as the true position of the electron. The data sample is identical to that used in measuring preselection efficiency (see Section 6.2.2). Units of *phimod*, defined in Section 2.4, are used. In *phimod* units, 0.0 is at one module boundary and 1.0 is at the other. The EM object is cut if the *phimod* position, using calorimeter-only information, is less than 0.1 or greater than 0.9. Figure 3.3 compares the track and calorimeter *phimod* positions of our electron sample. For the track, ϕ is extrapolated to the calorimeter EM3 layer. It can

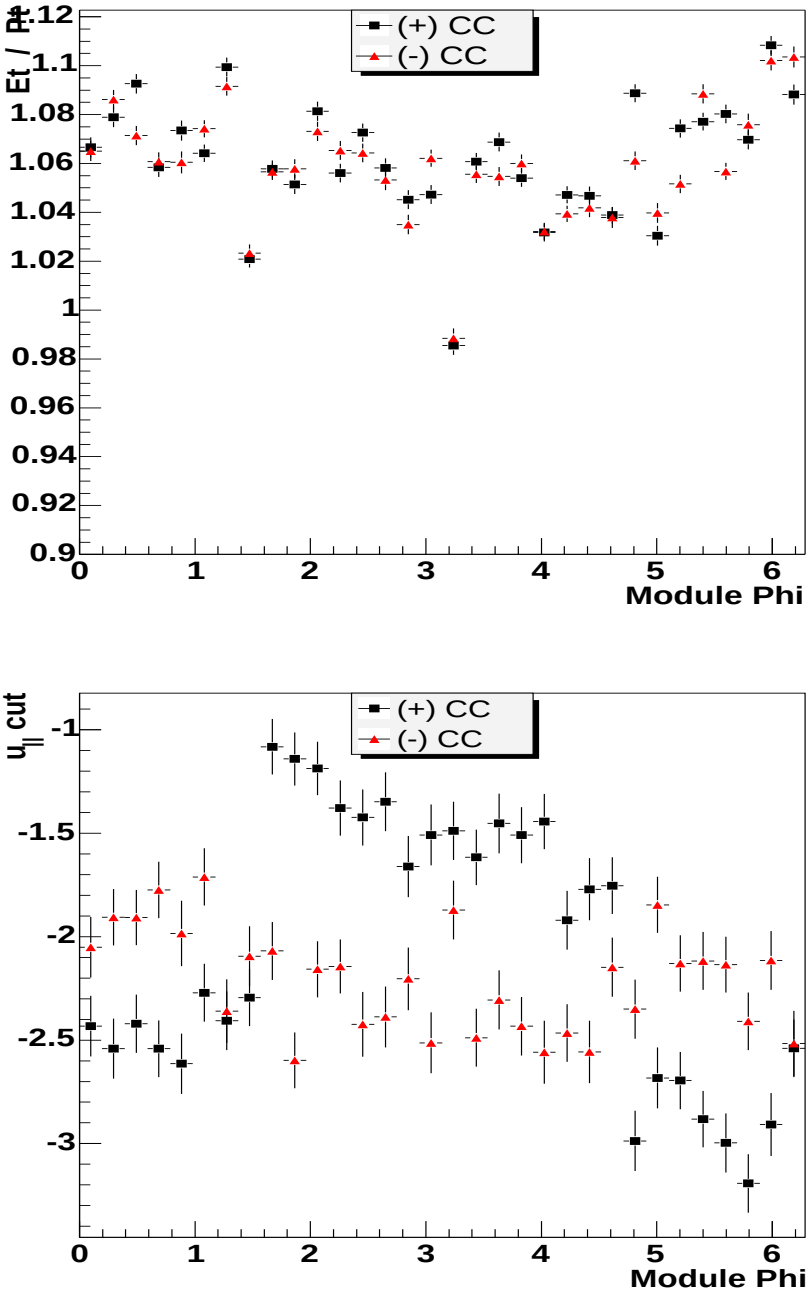

Fig. 3.2: Calorimeter E_T over track p_T (top) and the $u_{\parallel}$ correction factor (bottom). Data points show the averages of these values in each region as found using the W candidate sample. Regions are divided into the 32 ϕ modules and the positive and negative η_{det} halves.

be seen by comparing the track and calorimeter *phimod* distributions that many electrons are shifted out of the cracks. Figure 3.4 is a scatter plot of *phimod* shift as a function of track *phimod* measured by plotting calorimeter *phimod* − track *phimod*. The tendency for calorimeter *phimod* to be shifted toward module centers is quite noticeable at the tower edges and also at the cell boundary at 0.5.

The amount electrons are shifted is found to be dependent not only on *phimod* position but also p_T and $|\eta_{physics}|$. To see this, the electron sample is divided into four bins for each quantity and plotted as a function of *phimod* as shown in Figure 3.5. For PMCS, shifting is modeled as a function of *phimod*, p_T and $|\eta_{physics}|$. Statistics limitations necessitate coarse binning: 50 uniform bins from 0 to 1 for *phimod* and for p_T and $|\eta_{physics}|$, the number of bins is further reduced to three each. The bins used for PMCS are ($<$ 36, 36 to 43, $>$ 43 GeV) for p_T and ($<$ 0.35, 0.35 to 0.65, $>$ 0.65) for $|\eta_{physics}|$. This is described further in Section 5.6.4.

3.4.3 Problematic Regions

The calorimeter has a number of regions which have, for all or part of the data set, unreliable acceptance or efficiency. These regions must be cut out in the data and the reduced acceptance accounted for in the calculation. Problem areas are identified by both the relative number and quality of EM objects falling within each of the calorimeter readout towers in η_{det} and ϕ. Affected cells are removed by cutting everything within a box centered on the cells and extending slightly beyond the cell boundaries in η_{det} and ϕ to account for effects on neighboring cells. For an example, see Figure 3.6.

Since many problems occur for only a fraction of the data, run ranges are assigned to all of these boxes. An electron is cut if its η_{det} and ϕ position fall

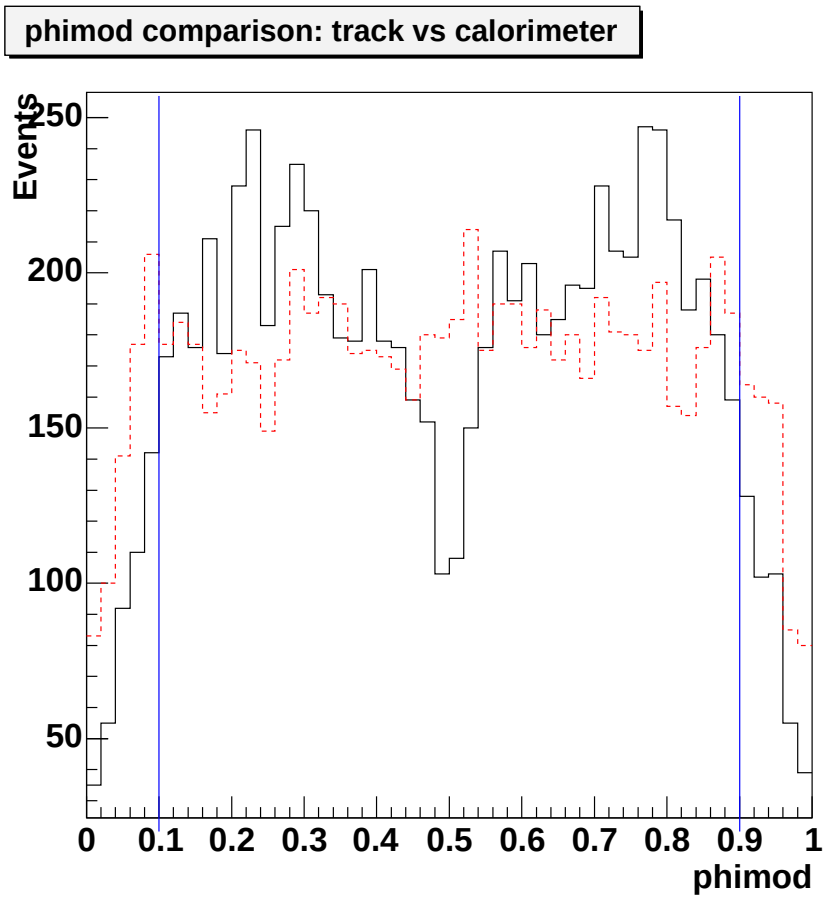

Fig. 3.3: Comparison of *phimod* positions for electrons passing preselection cuts. The red dashed histogram is track *phimod*, the black solid histogram is calorimeter *phimod* and the blue vertical lines at 0.1 and 0.9 are fiducial ϕ crack cut boundaries. This plots shows that the number of electrons left in the cracks is greatly reduced after the calorimeter ϕ shift due to energy loss in the cracks.

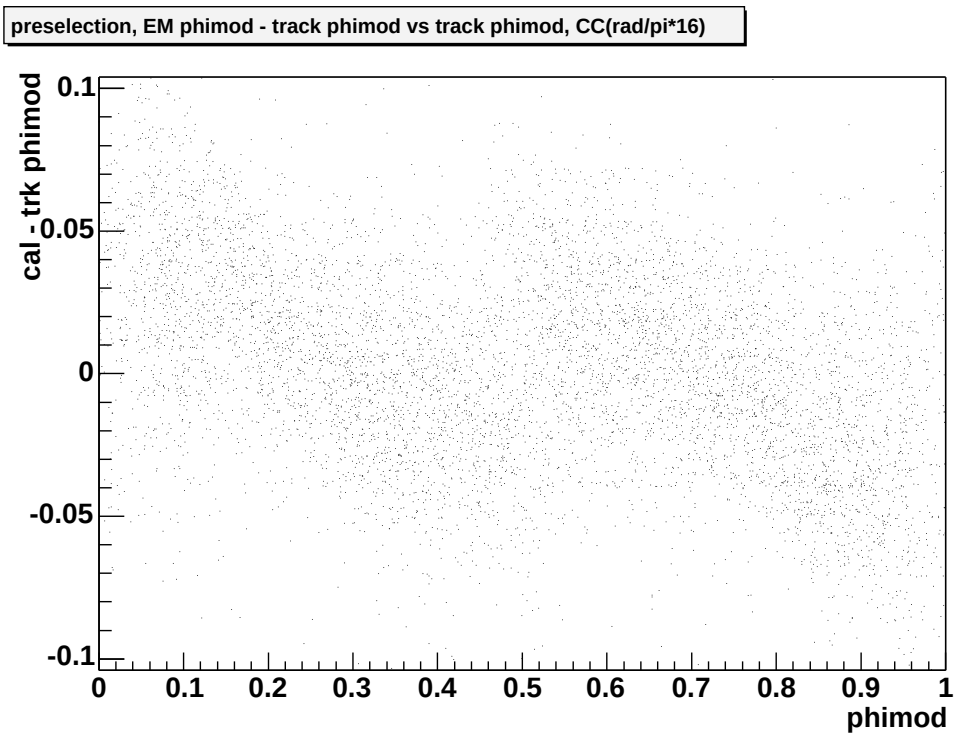

Fig. 3.4: Scatter plot showing shift of calorimeter *phimod* with respect to track *phimod*

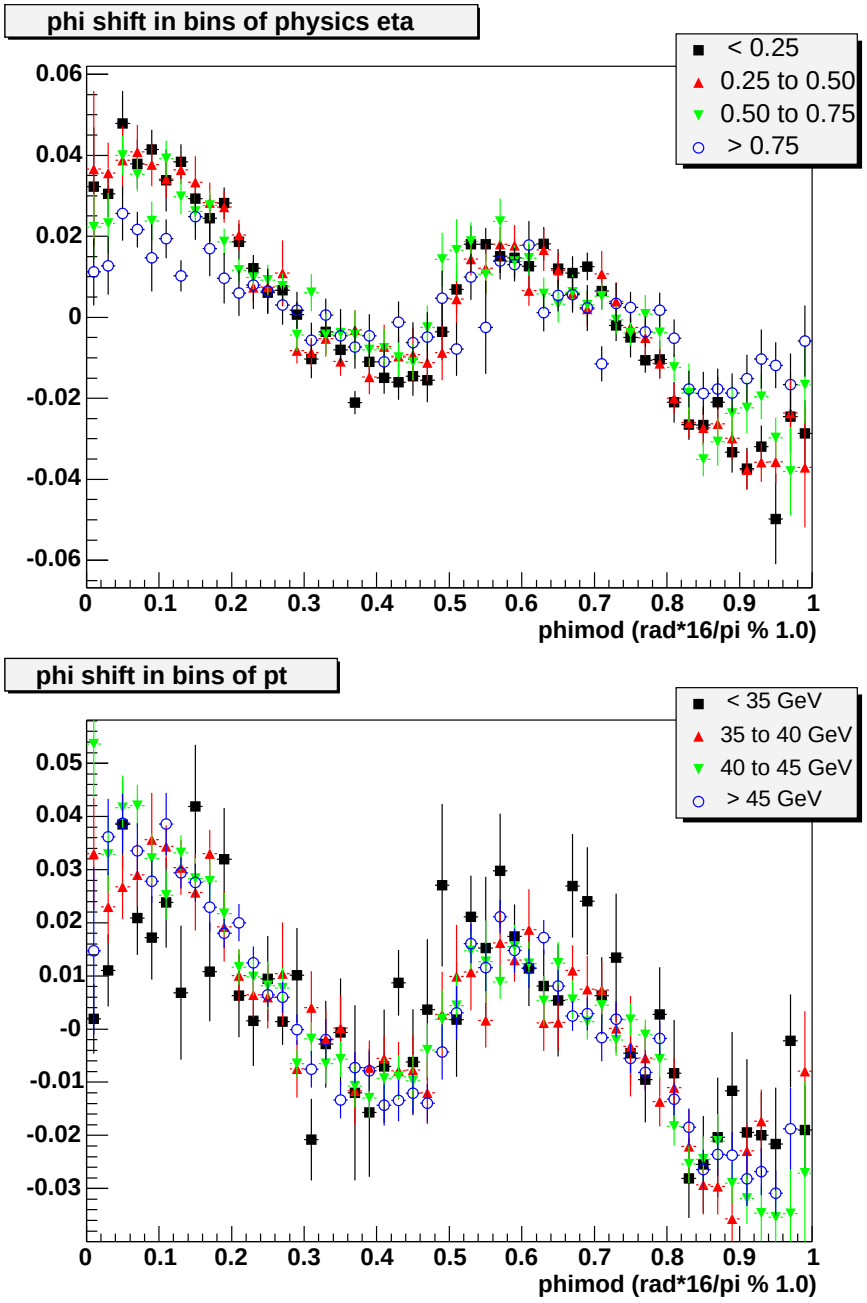

Fig. 3.5: Scatter plots vs. *phimod* showing dependence of calorimeter *phimod* shift on $\eta_{physics}$ (top) and p_T (bottom). The binning for each quantity is shown on the legends.

within one of these boxes and its run number is within the corresponding box's run range. To model this in PMCS, luminosity weighted random run numbers are generated for each event. This, along with the generated η_{det} and ϕ, is applied in exactly the same way as data to determine if a generated electron should be cut. PMCS comparisons with and without these cuts indicate an acceptance loss of 8% for W candidate events and 20% for Z candidate events.

By comparing the number of EM objects formed in a calorimeter cell to the average number for all cells at that ϕ, low efficiency "holes" can be identified. Figure 3.7 shows these low efficiency cells for a particular range of runs. Low efficiency cells are identified by solid blue boxes, with the lightest blue boxes less than 60% efficient down to the darkest blue with less than 20% efficiency. Also, cells with over twice the average acceptance are marked as bright orange solid boxes.

Hollow boxes represent regions cut out. They are color coded based on the reason for their removal. For example, the violet boxes represent the 'tower 2' problem [62] which prevents EM objects from forming in the surrounding regions. For each trigger tower, there are four readout towers (2×2) which are referred to as towers 0, 1, 2 and 3. The problem is that the information in tower 2 is read out a second time in place of the information for tower 3. Therefore, if an electron falls within tower 2 it will appear as if an identical electron fell within tower 3. This will cause the electron cluster to fail the isolation requirement resulting in its rejection.

The light blue hollow box represents central calorimeter ϕ module 17 which extends the length of the central calorimeter in η_{det} and from $\frac{1}{2}\pi < \phi < \frac{17}{16}\pi$. This module is removed because its energy scale is approximately 8% lower than the rest as can be seen in Figure 3.2. 2D plots like that in Figure 3.7 are useful as a check. However, to more precisely locate problem areas, 1D projections

along η_{det} and ϕ are made both of all EM objects with p_T over 25 GeV and of EM objects satisfying electron id cuts. For example, Figure 3.6 shows electron id efficiency vs η_{det} and ϕ for regions with the 'tower 2' problem.

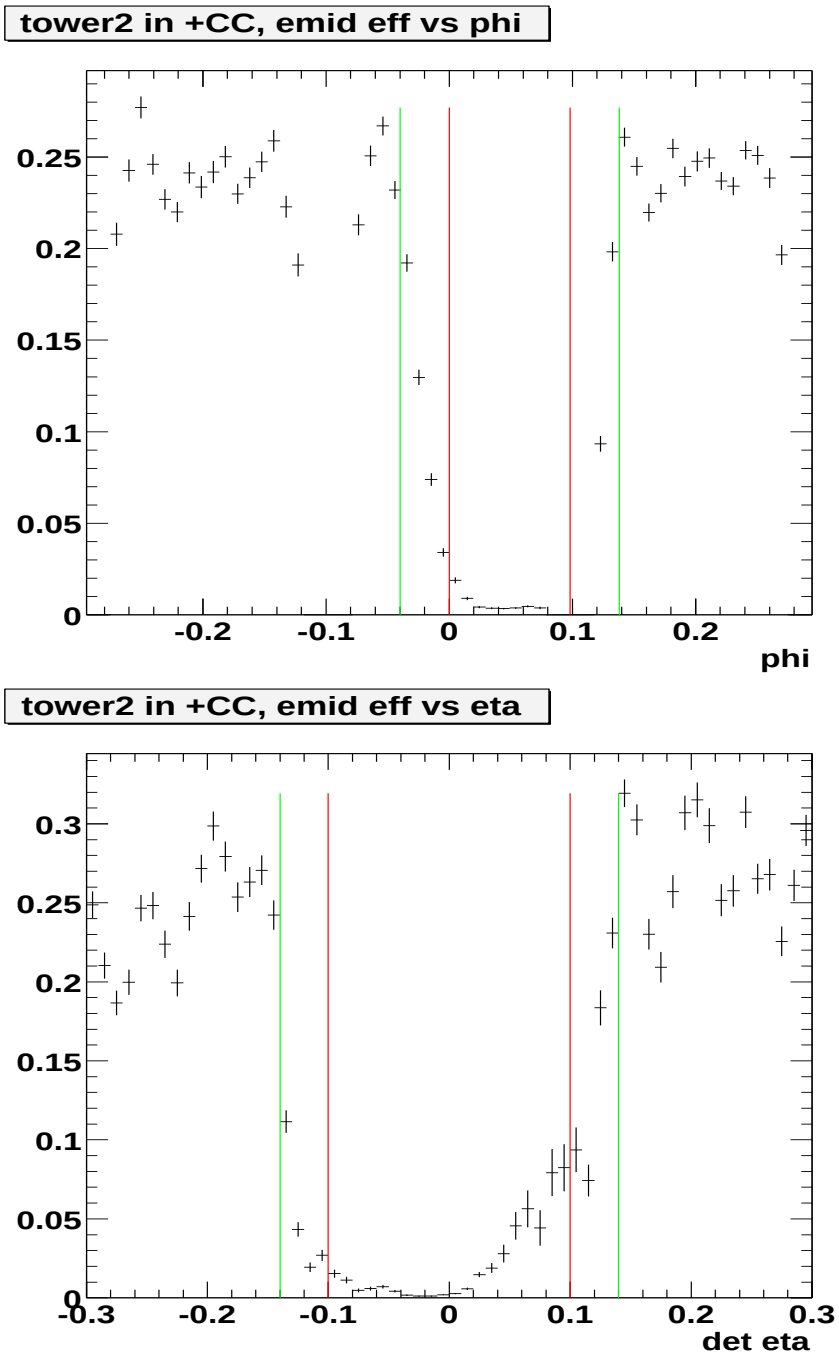

Fig. 3.6: Projections along ϕ (top) and η_{det} (bottom) of electron id efficiency vs. position relative to the tower 2 cells. The red lines at $\phi = 0$ and 0.1 (top) and $\eta = -0.1$ and 0.1 (bottom) indicate cell boundaries and the green lines extended beyond the cell boundaries on either side by 0.04 in η or ϕ indicate where data are cut.

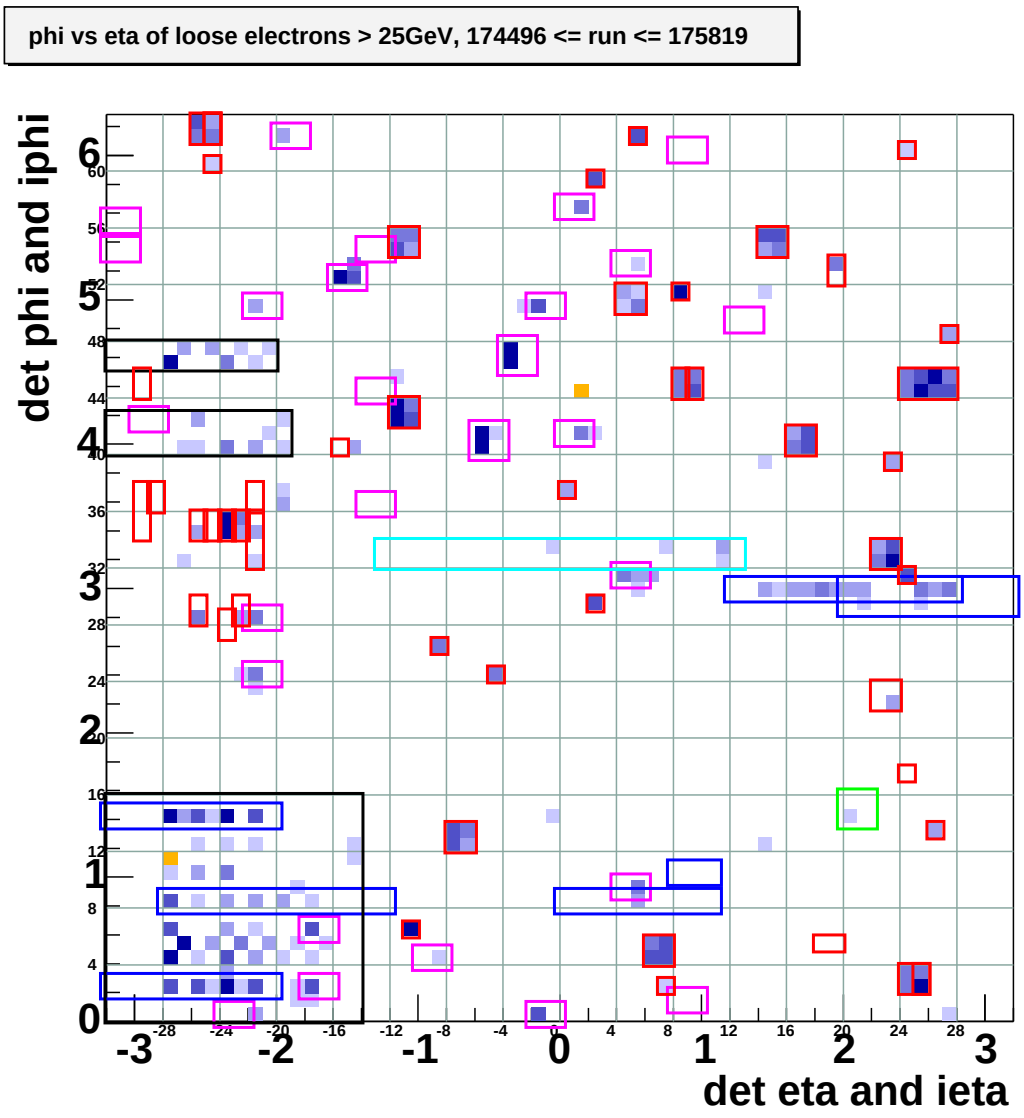

Fig. 3.7: Calorimeter quality cuts shown as a function of η_{det} and ϕ. A light gray grid indicates regions 4×4 readout towers in size. Hollow boxes represent regions removed from the analysis. Solid boxes represent either highly inefficient regions of the calorimeter (blue) or regions with much greater than normal acceptance (orange). The level of inefficiency is indicated by the shade of blue with the darkest boxes the most inefficient.

CHAPTER 4

EVENT SELECTION

The events used in this analysis consist of an integrated luminosity of 177 ± 12 pb^{-1} of data collected between September 2002 and September 2003 (runs 161973 to 180956) using triggers designed to fire on the detection of a single high E_T electron (See Section 3.2). The data set has been processed using the p14 version of DØReco (See Section 3.3). In order to reduce processing time, events that have at least one EM object with $E_T > 15$ GeV are skimmed from the full data set and stored in a compact form known as the thumbnail format [63]. To further reduce processing time and disk storage space, ROOT-tuples containing only the information needed for this analysis are produced from this skim. This is a more convenient final format since the ROOT data analysis framework [64] is also used to produce all histograms and efficiency plots shown from here on.

The W and Z candidate samples are selected from this data set. Basic descriptions of the types of events selected are given below:

- W Candidates

  Events are expected to have at least one electron with $E_T > 25$ GeV and also, in order to select a high E_T neutrino, missing E_T for the event must be greater than 25 GeV.

- Z Candidates

  Events are expected to have two electrons with $E_T > 25$ GeV. The invariant

mass of the two electrons is expected to be close to the mass of the Z (between 70 and 110 GeV).

Additional samples are obtained from this data set for the study of electron efficiencies and QCD background. For electron efficiencies, di-EM event samples with a high $Z/\gamma^* \rightarrow ee$ signal purity are chosen (see Chapter 6.2). The QCD background samples are described in Chapter 7.

The criteria for selecting electrons and a detailed description of the selection cuts used in obtaining the W and Z candidate samples are given in this chapter. These selection cuts include

- Preselection Cuts

  cuts placed on EM clusters which must be satisfied in order for the cluster to be kept as an electron candidate

- Fiducial Cuts

  cuts restricting the regions of the detector allowed for use in data collection

- Kinematic Cuts

  cuts on the allowed energy and mass ranges ($E_T > 25$ GeV for electrons, missing $E_T > 25$ for W candidates and invariant mass within 70 and 110 GeV for Z candidates)

- Trigger Selection

  requires one of the electrons to have fired a trigger used in the event

- Track Matching

  background can be reduced greatly by requiring an electron to have a track match

- Electron Likelihood

  applying an electron likelihood cut after the track match reduces background

even further.

4.1 Electron Preselection

In data reconstruction, EM objects in the calorimeter are only kept if they meet a minimum set of requirements. These requirements are referred to as preselection cuts since EM objects are automatically rejected if they are not met.

4.1.1 EM Fraction

Most of the energy from electrons and photons will be deposited in the electromagnetic (EM) layers of the calorimeter while much of the energy in hadronic jets will continue until reaching the hadronic layers. This makes a cut based on the fraction of total energy deposited in the EM layers an effective method of discriminating between electrons and QCD background. The EM clustering algorithm requires EM fraction > 0.9 for EM object identification.

4.1.2 Shower Isolation

Electrons originating from W and Z events are expected to be isolated since they are not produced in conjunction with other nearby particles. The purpose of the isolation requirement is therefore not to identify electrons but rather to select a particular physics process. This will help to discriminate against such particles as the π^0 and η which decay into two photons. These particles will shower electromagnetically, but have poor isolation.

The isolation variable is defined as:

$$f_{iso} = \frac{E_{total}(0.4) - E_{EM}(0.2)}{E_{EM}(0.2)} \tag{4.1}$$

where $E_{tot}(\Delta R_{det})$ and $E_{EM}(\Delta R_{det})$ are the total energy and EM energy within

a cone of radius ΔR_{det}. A cone of radius 0.2 is chosen for the EM energy since it is usually large enough to fully contain an electromagnetic shower. This is subtracted from the total energy within a 0.4 radius cone. The EM clustering algorithm requires $f_{iso} < 0.15$ for EM object identification.

4.1.3 EM object ID

EM objects with an ID of 10 or ± 11 are selected. Electromagnetic clusters from EMReco are assigned an ID of 10 if they satisfy $E_T > 1.5$ GeV, EM fraction > 0.9 and $f_{iso} < 0.15$. These requirements are quite loose and result in very little efficiency loss. If the cluster also has a track loosely matched to it, it is given an ID of ± 11 depending on the sign of the track: $+11$ for electrons and -11 for positrons.

4.2 Fiducial Cuts

The fiducial requirements are defined so that only well understood instrumented regions of the DØ detector are used. The positions of EM objects, based on calorimeter information only, must fall within the good fiducial region. The following fiducial cuts are defined:

- η_{det} cuts:
  - central (CC): $|\eta_{det}| < 1.05$
  - end cap (EC): $1.5 < |\eta_{det}| < 2.3$
- in_phi_fiducial:

  This refers to the removal of the cracks between ϕ modules in the central region of the calorimeter.

- problematic regions:

  This refers to the removal of regions in the calorimeter due to unreliable acceptance or efficiency as described in Section 3.4.3. This also includes the removal of calorimeter ϕ module 17 due to an energy scale which is significantly lower than the other modules.

4.3 Trigger Selection

The data samples are acquired using triggers designed to fire upon the detection of a single high E_T electron entering the calorimeter. An identical trigger selection is used for both W and Z candidate events. The triggers come from the trigger list versions global_CMT 8 to 12 (see Section 3.2). Massive changes were made to the trigger list for global_CMT 12; previous triggers were removed and new triggers defined making it necessary to split the sample into two sets for trigger study. For an event to be used one of the following triggers must have fired and be unprescaled:

- global_CMT 8 to 11 triggers:

  EM_HI_SH, EM_HI, EM_MX_SH or EM_MX

- global_CMT 12 triggers:

  E1_SHT20, E2_SHT20, E3_SHT20 or E1_SH30

All of these triggers use calorimeter only information. The primary requirement at L1 is a single calorimeter EM tower with E_T over a certain threshold which varies between 10 and 15 GeV depending on the trigger condition. A very small gain in statistics is produced by the inclusion of triggers allowing two lower E_T EM towers. L2 trigger conditions were not required for a majority of the data taken. For only a portion of the time, a few of the triggers use a L2 trigger condition requiring one 12 GeV EM candidate cluster.

All of the L3 trigger conditions require EM fraction > 0.9. Additionally, shower shape cuts are placed on all but one L3 trigger condition. These shower shape cuts place restrictions on the maximum width of the electron shower in each of the first three EM layers. These shower shape cuts are necessary in order to reduce the L3 output rate while keeping the E_T threshold below the 25 GeV cut used in this analysis. The L3 trigger condition ELE_LOOSE(1,30) does not have shower shape cuts and must therefore have a 30 GeV E_T threshold while ELE_LOOSE_SH_T(1,20), with shower shape cuts, has the threshold reduced to 20 GeV. Due to increasing luminosity, the CMT 12 trigger condition ELE_NLV_SH(1,30), which has loose shower shape cuts, must also have a 30 GeV E_T threshold while ELE_NLV_SHT(1,20), with tighter shower shape cuts, has the threshold reduced to 20 GeV. Ideally, the threshold should be a few GeV below the 25 GeV cut used in the analysis. This is because the offline E_T used in the analysis is recalculated using more detailed information and may differ somewhat from the L3 value.

An additional requirement for W and Z candidate event selection is that one of the electrons used in the selection 'fires' a trigger used in the event. For an electron to fire a trigger, the corresponding EM object must satisfy the trigger's requirements. This means that the EM object must have a matching trigger object at each level which passes all cuts for the corresponding trigger level condition. The electron EM to trigger object matching requirements are:

- L1: $\Delta\phi < 0.4$ (L1 η information not available)
- L2: $\Delta R_{det} < 0.4$
- L3: $\Delta R_{det} < 0.4$.

Table 4.1 summarizes the trigger conditions which make up all the triggers used in this analysis.

trigger	L1	L2	L3
EM_HI_SH	CEM(1,10)	EM(1,12)	ELE_LOOSE_SH_T(1,20)
EM_HI_2EM5_SH	CEM(2,5)	EM(1,12)	ELE_LOOSE_SH_T(1,20)
EM_HI	CEM(1,10)	EM(1,12)	ELE_LOOSE(1,30)
EM_MX_SH	CEM(1,15)	none	ELE_LOOSE_SH_T(1,20)
EM_MX	CEM(1,15)	none	ELE_LOOSE(1,30)
E1_SHT20	CEM(1,11)	none	ELE_NLV_SHT(1,20)
E2_SHT20	CEM(2,6)	none	ELE_NLV_SHT(1,20)
E3_SHT20	CEM(1,9)CEM(2,3)	none	ELE_NLV_SHT(1,20)
E1_SH30	CEM(1,11)	none	ELE_NLV_SH(1,30)

L1 trigger conditions

CEM(1,10)	one EM trigger tower with $E_T > 10$ GeV
CEM(2,5)	two EM trigger towers with $E_T > 5$ GeV
CEM(1,15)	one EM trigger tower with $E_T > 15$ GeV
CEM(1,11)	one EM trigger tower with $E_T > 11$ GeV
CEM(2,6)	two EM trigger towers with $E_T > 6$ GeV
CEM(1,9)CEM(2,3)	one EM trigger tower with $E_T > 9$ GeV, another EM trigger tower with $E_T > 3$ GeV

L2 trigger conditions

EM(1,12)	one EM candidate with $E_T > 12$ GeV (not present for runs below 169524)

L3 trigger conditions

ELE_LOOSE_SH_T(1,20)	one electron with $\lvert\eta_{det}\rvert < 3.0$, $E_T > 20$ GeV, EM fraction > 0.9 and passing shower shape cuts
ELE_LOOSE(1,30)	one electron with $\lvert\eta_{det}\rvert < 3.0$, $E_T > 30$ GeV and EM fraction > 0.9
ELE_NLV_SHT(1,20)	one electron with $\lvert\eta_{physics}\rvert < 3.6$, $E_T > 20$ GeV, EM fraction > 0.9 and passing tight shower shape cuts
ELE_NLV_SH(1,30)	one electron with $\lvert\eta_{physics}\rvert < 3.6$, $E_T > 30$ GeV, EM fraction > 0.9 and passing loose shower shape cuts

Tab. 4.1: A summary of the single EM triggers used in W and Z event selection. The top part lists the triggers used along with the names of the trigger conditions at each level. Below this are descriptions of all the trigger conditions used.

4.4 Track Matching

All W and Z candidate events must have a central EM object with a matched track. Additionally, track matching in both the central and end cap regions is needed when measuring the electron identification efficiencies. The following algorithms are used to match a track to an EM object in the central and end cap regions:

$$\text{for CC, } \chi^2 = \left(\frac{\Delta z}{\sigma(z)}\right)^2 + \left(\frac{\Delta\phi}{\sigma(\phi)}\right)^2 + \left(\frac{E_T/p_T - 1}{\sigma(E_T/p_T)}\right)^2 \quad (4.2)$$

$$\text{for EC, } \chi^2 = \left(\frac{\Delta z}{\sigma(z)}\right)^2 + \left(\frac{\Delta\phi}{\sigma(\phi)}\right)^2. \quad (4.3)$$

In the above expressions, Δz and $\Delta\phi$ are the differences between the track position and the EM cluster position at the third floor of the calorimeter, and E_T/p_T is the transverse energy of the EM cluster as measured by the calorimeter divided by the transverse momentum of the track. The σ values are the resolutions for the experimental measurements of each quantity. The E_T/p_T requirement is dropped for the EC region due to a poor p_T reconstruction. For a good track match, the track matching χ^2 probability cut is $P(\chi^2) > 10^{-2}$. To give an idea of the level of matching this cut requires, for $P(\chi^2) > 10^{-2}$ this equates to roughly $\Delta z < 2.4$ cm, $\Delta\phi < 0.02$ rad or $|E_T/p_T - 1| < 0.6$ when the other terms are zero.

4.5 Electron Likelihood

The electron likelihood provides excellent discrimination between electrons and various sources of background. It is built from several variables with good discriminating power:

- EM fraction
- H-Matrix(8) (see Section 4.6)
- Calorimeter E_T / Track P_T
- Track DCA (distance of closest approach to the beam axis)
- Track spatial χ^2 match probability
- Number of tracks in an 0.05 radius cone around (and including) the candidate track
- Total P_T of tracks in an 0.4 radius cone around the candidate track, but excluding the candidate track.

The likelihood algorithm inputs histograms for the distributions of these seven variables produced using both a high purity electron sample and a fake electron sample. By comparing these histograms on a bin by bin basis, it is able to optimize the combined discriminating power of these variables in a much more flexible manner than by simply defining hard cut values. More information about the likelihood method and the variables used can be found in [65]. The distribution of the likelihood variable runs from 0 to 1 with 1 being the tightest possible cut. Tight electrons require likelihood to be greater than 0.9.

4.6 H-Matrix(8) and H-Matrix(7)

Although not used directly in electron selection for this analysis, the H-Matrix is used in the electron likelihood and for background checks. The purpose of the H-Matrix method is to discriminate between electrons and hadronic jets through differences in shower shape and energy distribution. Variables distinguishing electrons from jets are used in a covariance matrix,

$$M_{ij} = 1/N \sum_{n=1}^{N} (x_i^n - \bar{x}_i)(x_j^n - \bar{x}_j) \quad i,j = 1...dim, \tag{4.4}$$

where x_i^n is the value of the i^{th} variable for the n^{th} particle in the electron sample used for tuning. The H-Matrix χ^2 is then defined as the inverse of the covariance matrix

$$H = M^{-1} \tag{4.5}$$

and the χ^2 defining the likelihood that a particle shower is consistent with that of an electron is [66]

$$\chi^2 = \sum_{ij}^{N} (x_i - \bar{x}_i) H_{ij} (x_j - \bar{x}_j). \tag{4.6}$$

For H-Matrix(8), the variables used are [67]:

- the energy fractions in the EM1, EM2, EM3 and EM4 calorimeter layers (four variables),
- cluster size in z for CC or r for EC in EM3,
- cluster size in r $\times$ ϕ in EM3,
- total calorimeter energy in the shower,
- and primary vertex z position.

For H-Matrix(7), the variable describing cluster size in z for CC or r for EC in EM3 is removed.

4.7 The Decay Vertex

One of the main reasons for requiring all events to have a matched track is that, without this requirement, approximately 4% of events do not have a primary

vertex. Requiring a matched track reduces this to under 0.4%. For the W and Z bosons, the difference in position between the primary vertex and decay vertex should be negligible. However, comparing the z position of the track at the point of closest approach to the beam (track z0) to the primary vertex indicates that the primary vertex is biased towards z=0 as shown in Figure 4.1. For this reason, track z0 of the highest p_T electron is used in place of the primary vertex for all plots dependent on the decay vertex. Checks comparing the z0 position of both electrons in Z candidates show excellent consistency. The z position of the decay vertex is referred to as vertex z or $zvtx$ from here on.

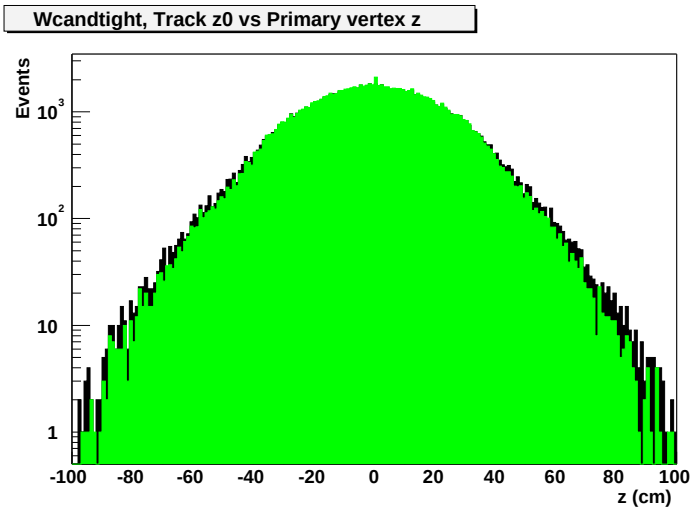

Fig. 4.1: W candidate tight sample track z0 (black) vs primary vertex z (green) showing bias of vertex z toward zero.

4.8 Electron candidate selection criteria

All EM objects used as electron candidates must pass preselection, fiducial and kinematic cuts.

- Preselection Cuts (see Section 4.1):
  - EM Fraction > 0.9

  - $f_{iso} < 0.15$
  - EM object ID = 10 or $\pm$ 11

- Fiducial Cuts (see Section 4.2):
  - η_{det} in CC or EC
  - 'is_phi_fiducial'
  - Not in a problematic calorimeter region

- Kinematic Cut:
  - $E_T > 25$ GeV

Additional requirements are defined for when higher electron purity is needed.

- Loose electron requirements:
  - EM object passing all preselection, fiducial and kinematic cuts
  - Track match with $P(\chi^2) > 0.01$ (see Section 4.4)

- Tight electron requirements:
  - Loose electron requirements
  - Electron likelihood > 0.9 (see Section 6.2.5)

4.9 W candidate selection criteria

The criteria for W candidate selection are:

- W candidate (loose):
  - At least one loose central electron
  - The electron candidate must have 'fired' a trigger (see Section 4.3).
  - Missing $E_T > 25$ GeV (for the neutrino)

The highest E_T electron candidate is selected if there is more than one.

A tighter sample is also required for background subtraction:

- Tight W candidate:
  - W candidate (loose)
  - The electron must also satisfy tight electron requirements.

In total, 97,757 W candidates and 85,947 tight W candidates have been selected. Figure 4.2 shows the distributions of the W candidate electron E_T and missing E_T distributions.

4.10 Z candidate selection criteria

The criteria for Z candidate selection are:

- At least two electron candidates passing preselection, fiducial and kinematic cuts
- At least one tight central electron.
- One of the electron candidates must have 'fired' a trigger (see Section 4.3).
- di-EM invariant mass between 70 and 110 GeV (see Equation 1.9).

If there are more than two electron candidates, the two with the highest E_T are selected.

In total, 5174 Z candidates with both electrons in the central region (CC-CC) and 2754 with one electron in the central region and one in the end cap (CC-EC) have been selected for a total of 7928 Z candidates. Figures 4.3 and 4.4 show the Z candidate electron E_T and invariant mass distributions separately for (CC-CC) and (CC-EC) events.

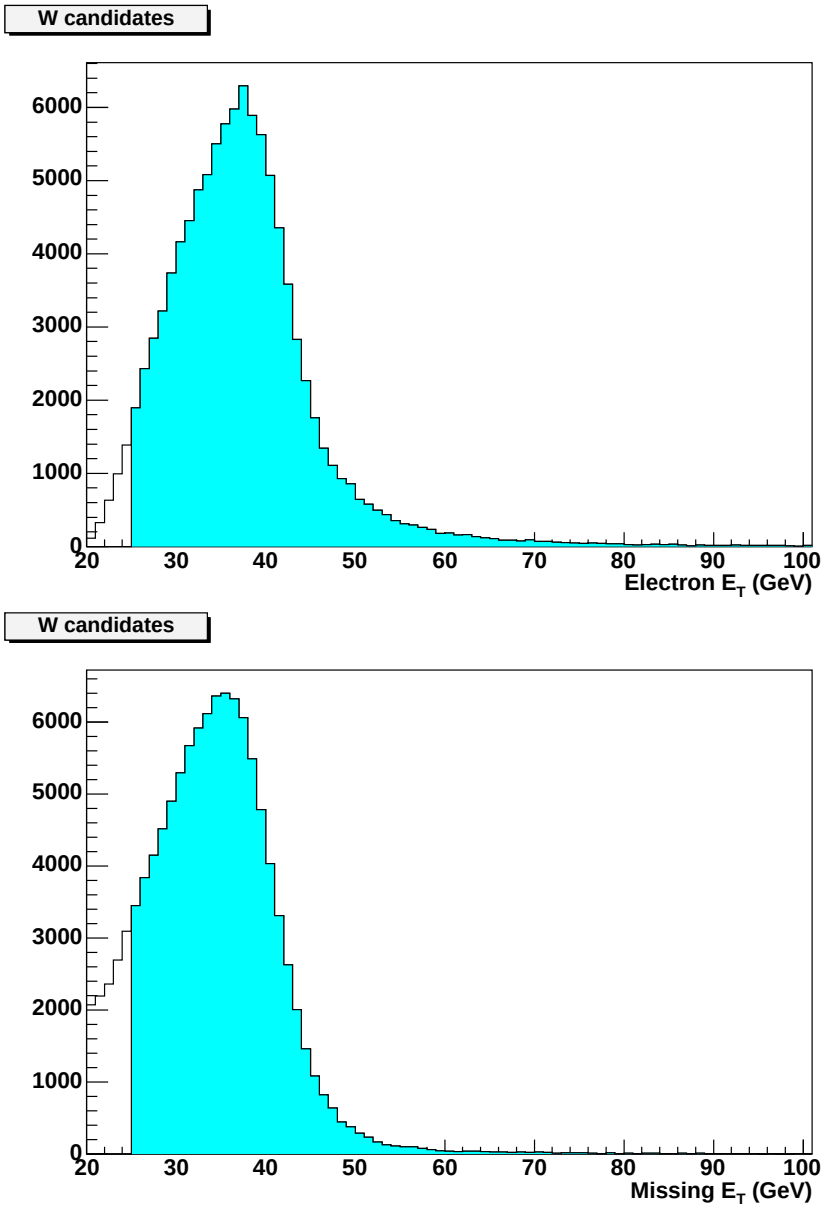

Fig. 4.2: W candidate electron E_T (top) and MET (bottom). Distributions are extended beyond kinematic cut boundaries. Only candidates in the shaded regions are used.

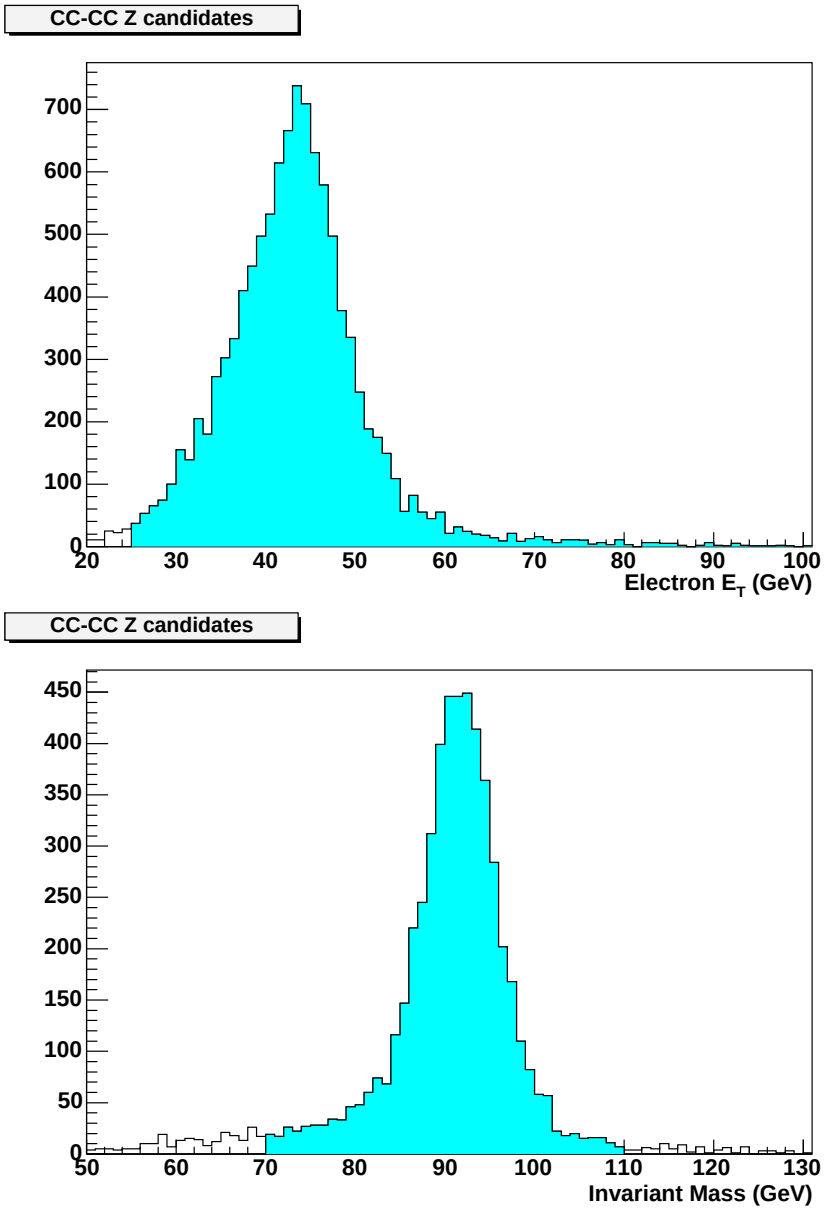

Fig. 4.3: Z (CC-CC) candidate electron E_T (top) and invariant mass (bottom). Distributions are extended beyond kinematic cut boundaries. Only candidates in the shaded regions are used.

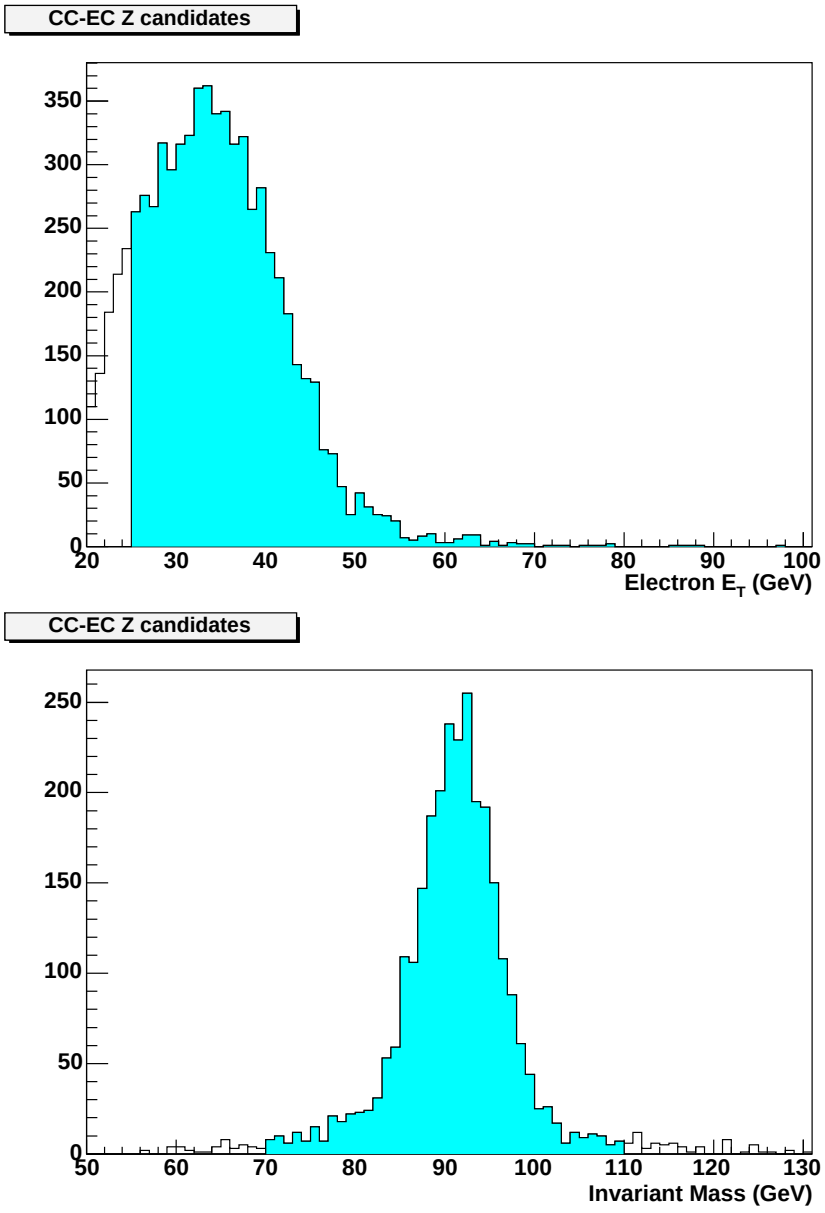

Fig. 4.4: Z (CC-EC) candidate electron E_T (top) and invariant mass (bottom). Distributions are extended beyond kinematic cut boundaries. Only candidates in the shaded regions are used.

4.11 Remaining Steps in the Cross Sections Calculations

The W and Z cross sections, decaying through the electron channel, are calculated using the following equations:

for $W \rightarrow e\nu$,

$$\sigma_W \times B(W \rightarrow e^{\pm}\nu) = \frac{N_W}{\mathcal{L}} \frac{1}{A_W}(1 - f_\tau^W - f_Z^W) \tag{4.7}$$

and for Z, first a physical $Z/\gamma^* \rightarrow ee$ cross section is found,

$$\sigma_{Z/\gamma^*} \times B(Z/\gamma^* \rightarrow e^+e^-) = \frac{N_Z}{\mathcal{L}} \frac{1}{A_{Z/\gamma^*}}, \tag{4.8}$$

which includes the contribution from the electromagnetic Drell-Yan process, $\gamma^* \rightarrow ee$, along with Z-γ^* interference terms. This is multiplied by a correction factor to obtain the pure Z cross section,

$$\sigma_Z \times B(Z \rightarrow e^+e^-) = R_\sigma \times [\sigma_{Z/\gamma^*} \times B(Z/\gamma^* \rightarrow e^+e^-)] \tag{4.9}$$

where N_W and N_Z are the number of W and Z candidates which remain after QCD background subtraction is performed, $\mathcal{L}$ is the integrated luminosity defined in Section 3.1 which is 177 ± 12 pb^{-1}, A_W and A_{Z/γ^*} are the $W \rightarrow e\nu$ and $Z/\gamma^* \rightarrow ee$ event acceptances, f_τ^W and f_Z^W are background fraction terms for the W candidate sample and R_σ is a conversion factor used to obtain the pure Z cross section.

The acceptance values, A_W and A_{Z/γ^*}, which are defined as the fraction of all events producing $W \rightarrow e\nu$ and $Z/\gamma^* \rightarrow ee$ interactions which make it into the candidate samples, are determined in Chapter 6. Acceptance is calculated using Monte Carlo which is tuned to account for detector effects using various input parameters. An overview of the Monte Carlo samples and the tuning procedure

used is given in Chapter 5.

QCD background subtraction is performed on the W and Z candidate samples to find N_W and N_Z in Chapter 7. Other sources of background are also estimated in this chapter. f_τ^W and f_Z^W are the fraction of events in the W candidate sample arising from $W \to \tau\nu$ and $Z \to ee$ backgrounds. R_σ is defined as the ratio of the pure $Z \to ee$ cross section to the $Z/\gamma^* \to ee$ cross section and is used to remove the contribution to the cross section coming from the electromagnetic Drell-Yan process.

Finally, in Chapter 8 the cross sections are calculated using the equations above and the values obtained in Chapters 4 to 7. The cross sections are then used to extract the branching ratio, $Br(W \to e\nu)$, and the W total width, Γ_W, using the procedure outlined in Section 1.3.2.

CHAPTER 5

MONTE CARLO

Monte Carlo simulating real physical processes is needed for several parts of this analysis. It is used for the calculation of a theoretical value of the ratio of total cross sections, σ_W/σ_Z, which is needed in order to extract the final results: $Br(W \to e\nu)$ and Γ_W. The amount of contamination from sources of background with final states which look very similar to the $W \to e\nu$ or $Z \to ee$ final states can only be estimated with Monte Carlo. It is necessary for the calculation of the kinematic and fiducial components of the acceptance and is very convenient for determining the total acceptance which includes event identification efficiency modeled from data. It is also useful as a crosscheck for the methods used in data for determining the electron identification efficiencies.

5.1 Physics Generators

Resbos [68] is a next-to leading order event generator made specifically for the simulation of W and Z boson production in a hadron collider with a subsequent decay into leptons. While it includes initial state QCD and electromagnetic corrections, it does not simulate electromagnetic final state radiation. For this purpose, Photos [69] is run on the output of Resbos to simulate the final state radiation of photons. This is very important for the acceptance calculation since radiated photons can escape detection therefore lowering measured electron E_T.

This combination of Resbos and Photos is used for the generation of the Monte Carlo used in the acceptance calculations.

A different event generator is necessary for the calculation of uncertainty due to choice of PDF. This is because the extra PDF sets needed for this calculation were unavailable for Resbos at the time. Pythia is a general purpose generator capable of simulating a wide variety of processes [70]. It is used in conjunction with TAUOLA [71] for the generation of the $W \rightarrow \tau\nu$ Monte Carlo needed for background estimation. The primary reason it was not used for the acceptance calculation is that is a leading order generator (LO) which makes the NLO Resbos generator a preferable choice.

5.2 PDFs

Parton Distribution Functions (PDFs) are needed by the event generators to predict how the partons in the proton and anti-proton will interact with each other. As described in Section 1.2.1, PDFs describe the probability of each pair of partons interacting with each other along with what momentum fraction they will carry with them in the event of a collision. For event generation in Resbos and Pythia, the CTEQ6.1 next-to leading order (NLO) [72] PDF set is used. An advantage of this PDF set is that it includes extra PDF sets designed for calculating the uncertainty due to choice of PDF.

5.2.1 PDF uncertainty

The PDF uncertainty calculation makes use of the 20 pairs of error PDFs included with CTEQ6.1. Each pair of error PDFs tests, for one of 20 free parameters, the effect on an observable, X, when the parameter is displaced 'up'(S^+) and 'down'(S^-) by its uncertainty. The total PDF uncertainty is found by following

Order	σ_W nb	σ_Z nb	σ_W/σ_Z
LO	19.66	5.770	3.407
NLO	23.78	7.006	3.394
NNLO	24.27	7.179	3.381

Tab. 5.1: Standard Model predictions of the W and Z inclusive boson cross sections at $\sqrt{s} = 1.96$ TeV obtained using ZWPROD.

the prescription given by the CTEQ collaboration [73]:

$$\Delta X_{\pm} = \left(\sum_{i}^{pairs} [X(S_i^{\pm}) - X(S_0)]^2 \right)^{1/2} \tag{5.1}$$

where the uncertainty on the observable X is $\Delta X_{\pm}$, the sum runs over all pairs of PDFs, $X(S_i^{\pm})$ are the values of X determined using the PDF pairs $S_i^{\pm}$, and $X(S_0)$ is the value of X using the nominal PDF. If $[X(S_i^{\pm}) - X(S_0)]$ is positive, the term is added to ΔX_+ and, if negative, to ΔX_-. In cases where both S^- and S^+ increase X the term [$\{X(S_i^-) + X(S_i^+)\}/2 - X(S_0)$] is added to ΔX_+ and, if both decrease X, to ΔX_-.

5.3 Theoretical Calculation of σ_W/σ_Z

For an inclusive cross section calculation, the contributions from an infinite number of possible subprocesses must be considered. Fortunately, each additional vertex in a process introduces another factor of α_s which can reduce the magnitude of its contribution. Additionally, most of the higher order contributions cancel out in a calculation of the ratio of inclusive total cross sections, σ_W/σ_Z. The program ZWPROD [74] is used for this purpose with the CTEQ6.1 NLO PDF set to obtain the results summarized in Table 5.1. The result for σ_W/σ_Z is 3.381 ± 0.051.

Uncertainty is estimated in a manner similar to Run I [75] which takes into account input parameter uncertainties. The change in σ_W/σ_Z is recorded as each input parameter is varied both 'up' and 'down' by its uncertainty. Table 5.2 summarizes these results for all significant sources. One change to this procedure is the computation of PDF uncertainty through the method described in Section 5.2.1 with σ_W/σ_Z assigned to X in Equation 5.1.

5.4 Full Monte Carlo Simulation Using DØgstar

The simulation package, DØgstar [76], is referred to as a full Monte Carlo Simulation, because it attempts to simulate every aspect of the DØ Detector. The full Monte Carlo simulates the entire reconstruction process in a manner similar to the reconstruction of real data passing through the detector. Therefore, all parameters used as selection criteria in this analysis are able to be defined in the same way as data. Although the simulation is not necessarily able to make absolute predictions about particular quantities, it is very useful for understanding what the relative effects will be when altering these quantities. This makes it a very useful tool for studying the validity of a measurement method or for understanding how systematic effects can bias the result.

5.5 Parameterized Monte Carlo Simulation (PMCS)

A Monte Carlo Simulation program called PMCS [61] (Parameterized Monte Carlo Simulation) is used to simulate the response of the detector, the effect of the geometric and kinematic cuts, and the effect of the electron identification and trigger efficiencies. Initially, Resbos is used with the CTEQ6.1 NLO PDF set to generate

Input Parameter	σ_W/σ_Z	$\Delta(\sigma_W/\sigma_Z)$
PDF uncertainty		
$\Delta(\sigma_W/\sigma_Z)_-$		-0.022
$\Delta(\sigma_W/\sigma_Z)_+$		$+0.015$
$M_W = 80.425 \pm 0.038\text{GeV/c}^2$		
$M_W = 80.387\text{GeV/c}^2$	3.3831	$+0.002$
$M_W = 80.463\text{GeV/c}^2$	3.3797	-0.002
Factorization Scale (Mean = M_W)		
Factorization Scale = M_W / 2	3.3791	-0.002
Factorization Scale = $M_W \times 2$	3.3823	$+0.001$
Renormalization Scale (Mean = M_W)		
Renormalization Scale = M_W / 2	3.3784	-0.003
Renormalization Scale = $M_W \times 2$	3.3834	$+0.002$
$sin^2_{\theta_W}$(effective Born approx. = 0.23124)		
$sin^2_{\theta_W}(on - shell) = 0.22267$	3.3357	-0.046
Total symmetric uncertainty = ± 0.051		

Tab. 5.2: A summary of the major uncertainties on σ_W/σ_Z arising from varying input parameters by their uncertainties. For PDF uncertainty, $\Delta(\sigma_W/\sigma_Z)_-$ and $\Delta(\sigma_W/\sigma_Z)_+$ represent the asymmetric uncertainty calculated using Equation 5.1. A symmetric total uncertainty is obtained by combining in quadrature the largest $\Delta(\sigma_W/\sigma_Z)$ for each input parameter.

for $W \to e\nu$:

- 40 million $W^{\pm} \to e\nu$ events

and for $Z/\gamma^* \to ee$:

- 20 million $Z^0 \to ee$ events,
- 2 million $\gamma^* \to ee$ events,
- and 2 million Z/γ^* interference events.

All Z/γ^* events are generated within the mass range 50 to 130 GeV. The sets of events for Z/γ^* are weighted to represent equal relative integrated luminosities so that Z/γ^* acceptance can be found by running over all three samples at once. These samples are used in PMCS to determine W and Z candidate event acceptances.

To each sample, PMCS applies the measured detector responses, selection efficiencies, and cuts on an event-by-event basis in order to obtain a single acceptance value for the sample.

5.6 PMCS Detector Response

The detector response (or *smearing*) parameters and input vertex distribution are described below. The smearing parameters are summarized in Table 5.3.

5.6.1 Electron Energy Scale

The electron energy scale is determined by comparing the invariant mass peak of the $Z/\gamma^* \to ee$ Monte Carlo to that of a pure $Z/\gamma^* \to ee$ data sample obtained by requiring both electrons to pass tight electron cuts. The electron energy scale and energy offset are applied to the Monte Carlo as $E_{final} = E_0 \times$ [energy scale] + [energy offset]. Altering the energy scale will therefore adjust the width of

Descriptor	Value
EM Energy Scale (CC)	1.0054 ± 0.0020
EM Energy Offset (CC)	(0.191 ± 0.048) GeV
EM Sampling Term (CC)	0.15 $\text{GeV}^{1/2}$
EM Constant Term (CC)	$(4.08 \pm 0.30)\%$
EM Energy Scale (pEC)	0.9990 ± 0.0066
EM Energy Offset (pEC)	(0.574 ± 0.300) GeV
EM Energy Scale (nEC)	0.9600 ± 0.0129
EM Energy Offset (nEC)	(0.070 ± 0.499) GeV
EM Sampling Term (EC)	0.206 $\text{GeV}^{1/2}$
EM Constant Term (pEC)	$(4.00 \pm 0.50)\%$
EM Constant Term (nEC)	$(1.10 \pm 0.70)\%$
Calorimeter Position Resolution $\sigma_{\eta^{det}}$ (CC)	0.0070 ± 0.0035
Calorimeter Position Resolution σ_{ϕ} (CC)	(0.0068 ± 0.0034) rad
Calorimeter Position Resolution $\sigma_{\eta^{det}}$ (EC)	0.0029 ± 0.0015
Calorimeter Position Resolution σ_{ϕ} (EC)	(0.0041 ± 0.0021) rad
HAD Energy Scale	0.67 ± 0.02
HAD Sampling Term	(0.80 ± 0.20) $\text{GeV}^{1/2}$
HAD Constant Term	0.05 ± 0.01
$u_{\parallel}$ Correction (CC)	(-1.78 ± 0.01) GeV
$\Delta R_{det}(e\gamma)$	0.2 ± 0.1

Tab. 5.3: Parameters used in PMCS

the peak and altering the energy offset will adjust the position of the peak. The optimal pair is determined by systematically varying both values and picking the pair which results in the best data-MC fit. The method for determining the best fit is the binned likelihood method. In this method, the peak between 75 and 105 GeV is divided into 30 bins and a binned likelihood is calculated using

$$L = -\sum_{bins}[x_i \times ln(y_i) - y_i - ln(x_i!)] \tag{5.2}$$

where x_i is the number of data points in bin i and y_i is the number of Monte Carlo events in bin i. The results for L as a function of both energy scale and offset are fit to a cubic polynomial to obtain the minimum value for L. An example of this for the central region is shown in Figure 5.1. More detailed information about this procedure along with a description of cross checks is given in [77].

The electron energy scale is determined to be 1.0054 ± 0.0020 for CC, 0.9990 ± 0.0066 for positive EC and 0.9600 ± 0.0129 for negative EC. The energy offset is determined to be 0.191 ± 0.048 GeV for the CC, 0.574 ± 0.300 GeV for positive EC and 0.070 ± 0.499 GeV for negative EC. The errors are determined from a 0.5 change in the likelihood from the minimum value (see Figure 5.1).

The electron energy scale is calibrated further in the central region. A histogram is made by taking the plot shown in Figure 3.2, of peak calorimeter E_T over track p_T as a function module ϕ and η_{det} half, and dividing by the CC average peak value. The CC electron energy scale is then multiplied by the value in the corresponding (η_{det}, ϕ) bin in this histogram which is shown in Figure 5.2.

5.6.2 Electron Energy Resolution

Energy resolution effects will result in an increased $Z/\gamma^* \rightarrow ee$ invariant mass peak width. However, the manner in which the peak is widened can be distin-

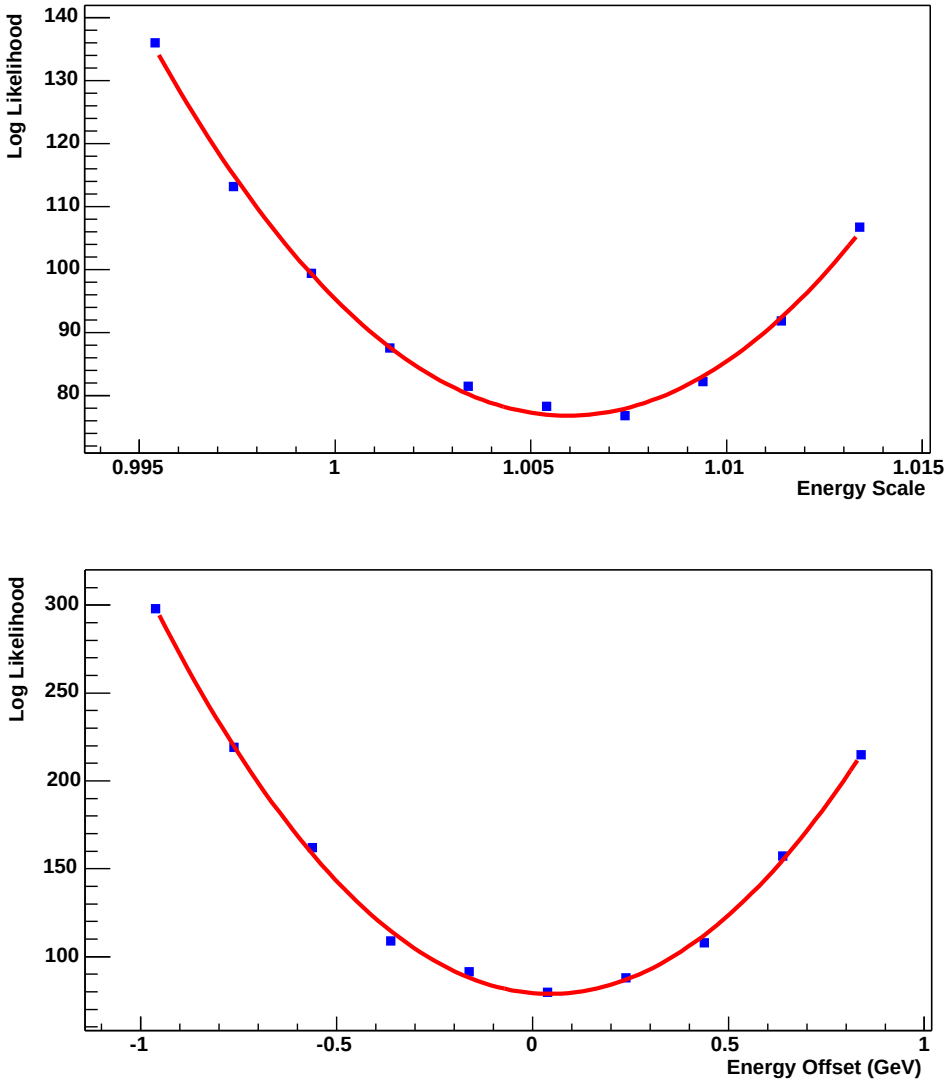

Fig. 5.1: Maximum Likelihood vs CC energy scale and energy offset

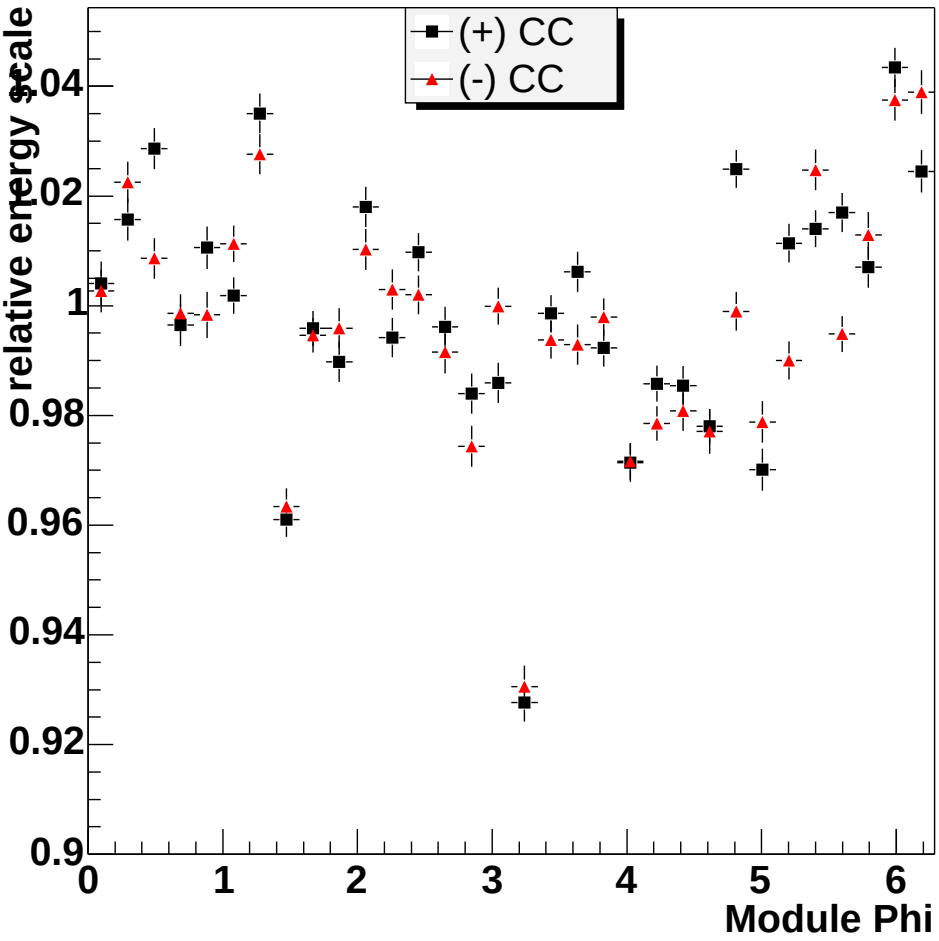

Fig. 5.2: Relative electron energy scale as a function of ϕ and divided into halves in η_{det}

guished from that of the energy scale. The energy scale directly scales the width of the Breit-Wigner shape of the peak (Equation 1.8) while the effect from energy resolution is to smear out the peak in the form of a Gaussian distribution. Compared to the Breit-Wigner, Gaussian smearing will widen the center of the peak much more while leaving the tail relatively unaffected.

The electron energy resolution is parameterized as

$$\frac{\Delta E}{E} = \sqrt{C^2 + \frac{S^2}{E} + \frac{N^2}{E^2}} \tag{5.3}$$

where the terms are called the constant, sampling, and noise terms, respectively. The sampling term is determined from test beam data and has values of 0.15 $\text{GeV}^{1/2}$ for the CC calorimeter and 0.206 $\text{GeV}^{1/2}$ for the EC calorimeter. The noise term is very small relative to the other terms for the energy range encountered in this analysis. It has been set to 0.29 GeV for CC and 0.125 for EC.

The value of the constant term in the simulation is determined using the binned likelihood method comparing the $Z/\gamma^* \rightarrow ee$ Monte Carlo to the same pure $Z/\gamma^* \rightarrow ee$ data sample described in the Section 5.6.1. The top plot in Figure 5.3 shows the binned likelihood versus the CC constant term. This is fit to a quadratic function to get the minimum value and the statistical error.

The plot shown in the bottom of Figure 5.3 shows a crosscheck which directly compares the width of the peak, obtained from a Gaussian fit, in the Monte Carlo to that of the pure $Z/\gamma^* \rightarrow ee$ data sample. A line fit of width vs. constant term is used with the value of the constant term at the intersection with the horizontal line representing the width measured from data determined to be the best constant term. Additional horizontal lines obtained from the data Gaussian fit error are used for an uncertainty estimate. Agreement between the binned

likelihood and Z width comparison methods is quite good.

The constant term using the binned likelihood method is determined to be $(4.08 \pm 0.30)\%$ for CC, $(4.00 \pm 0.50)\%$ for positive EC and $(1.10 \pm 0.70)\%$ for negative EC. For more information see [77].

5.6.3 Electron Position Resolution

Position resolutions for the EM calorimeter are determined from data using a sample of electrons required to pass preselection cuts (see Section 6.2.2). The resolution is measured by fitting a Gaussian shape to histograms of the track − calorimeter position residuals as shown in Figure 5.4. Here, the track position is treated as the true position of the electron since it is known to much greater precision. Values for the η_{det} and ϕ resolutions are measured separately for CC and EC and assigned a conservative relative uncertainty of 50%. This uncertainty is an overestimation which could be reduced with study. However, even with variations of this magnitude, acceptance results are found to be quite insensitive to assigned position resolution. The η resolutions are $\sigma_\eta = 0.0070 \pm 0.0035$ for CC and $\sigma_\eta = 0.0029 \pm 0.0015$ for EC. The ϕ resolutions are $\sigma_\phi = 0.0068 \pm 0.0034$ rad for CC and $\sigma_\phi = 0.0041 \pm 0.0021$ rad for EC. For CC, however, σ_ϕ is found to be highly dependent on the position of the electron with respect to the EM tower boundaries and must be modeled more carefully (See Section 5.6.4).

5.6.4 Electron *phimod* Shift

As is described in Section 3.4.2, the measured electron calorimeter-only ϕ positions tend to shift away from module boundaries and toward cell centers. Scatter plots of *phimod* shift vs track *phimod* position, as shown in Figure 3.4, are used directly in PMCS to determine the amount to shift the CC electrons. The plot shown in Figure 3.4 is actually divided into three bins in both p_T and $|\eta_{physics}|$

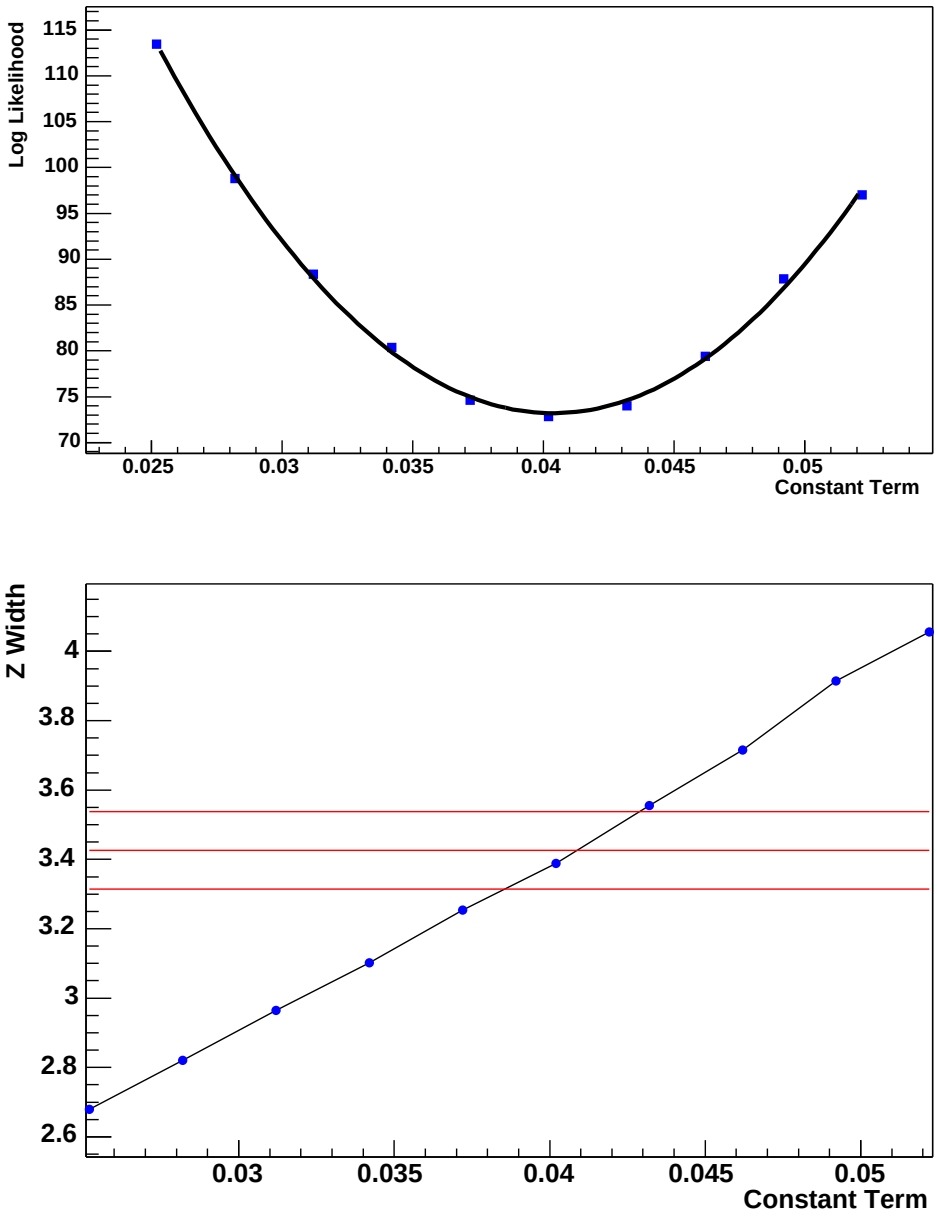

Fig. 5.3: Binned Likelihood vs CC constant term (Top) and Z width vs CC constant term (Bottom)

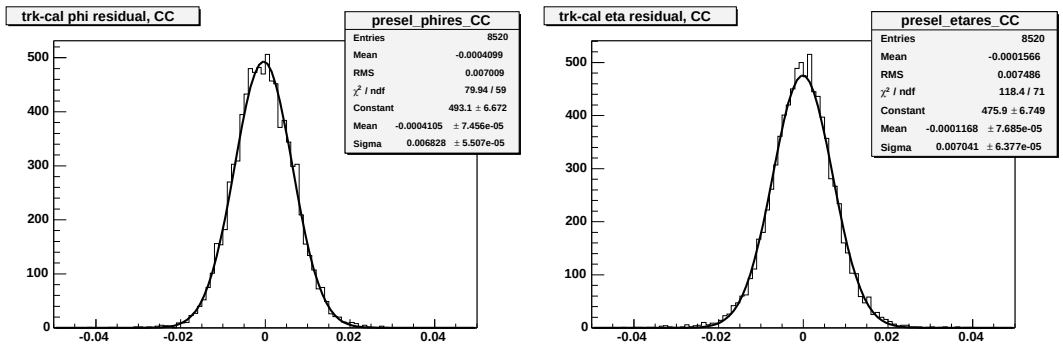

Fig. 5.4: ϕ (left) and η (right) track−calorimeter residuals for CC.

for PMCS. There are a total of 50 uniform bins from 0 to 1 for *phimod*, bins of ($<$ 36, 36 to 43, $>$ 43 GeV) for p_T and ($<$ 0.35, 0.35 to 0.65, $>$ 0.65) for $|\eta_{physics}|$. Figures 5.5 and 5.6 are PMCS to data comparisons of W and Z candidate electron *phimod* position after this correction is applied.

5.6.5 Hadronic Energy Scale

Of particular importance is the response of the detector to the recoil jet in W and Z production. The energy scale of the measured recoil momentum differs from the electron energy scale because the recoil measurement also includes energy from hadronic showers and suffers from the loss of energy in uninstrumented regions of the calorimeter. The response of the hadronic calorimeter relative to the response of the electromagnetic calorimeter was determined from $Z \rightarrow ee$ events. In $Z \rightarrow ee$ events the transverse momentum of the Z boson, p_T^Z, can be obtained from either the measurement of the transverse momenta of the two electrons $\vec{p_T^{ee}}$ or from the recoil activity in the event $-\vec{p_T^{rec}}$. To minimize the effects of the hadronic energy scale relative to the electromagnetic energy scale, the momentum imbalance was measured with respect to the (η, ξ)-coordinate system. The η axis is defined as the bisector of the two electron transverse directions. In the plane of the electrons, the axis orthogonal to the η axis is the

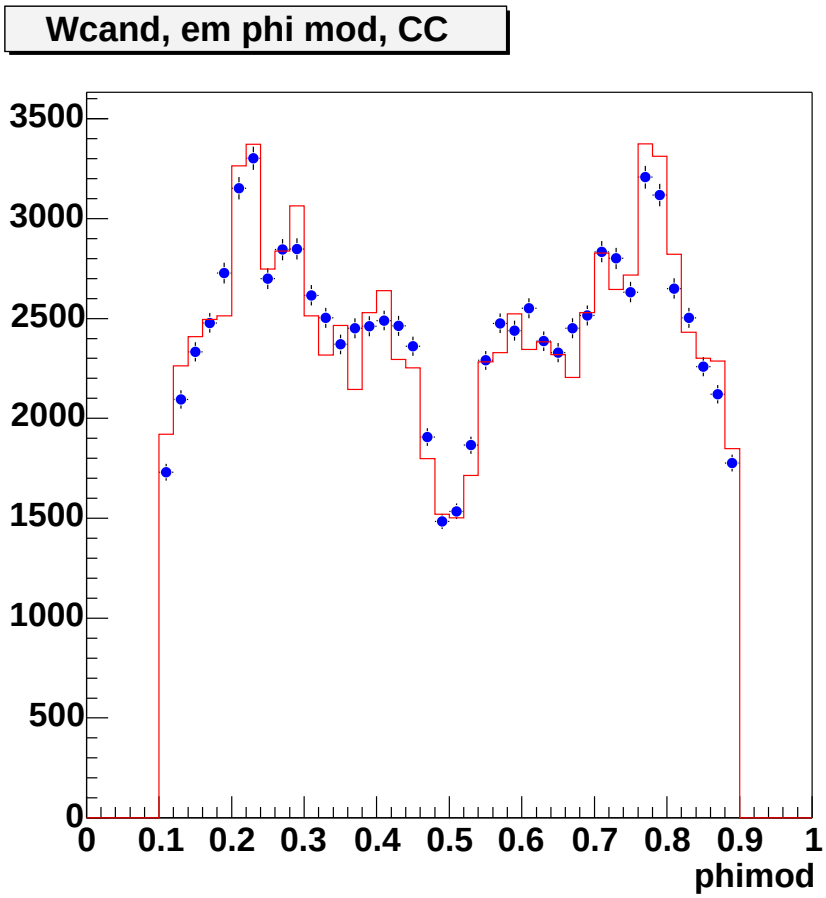

Fig. 5.5: *phimod* for W candidates in the central region. PMCS (the red histogram) is compared to data (the dots).

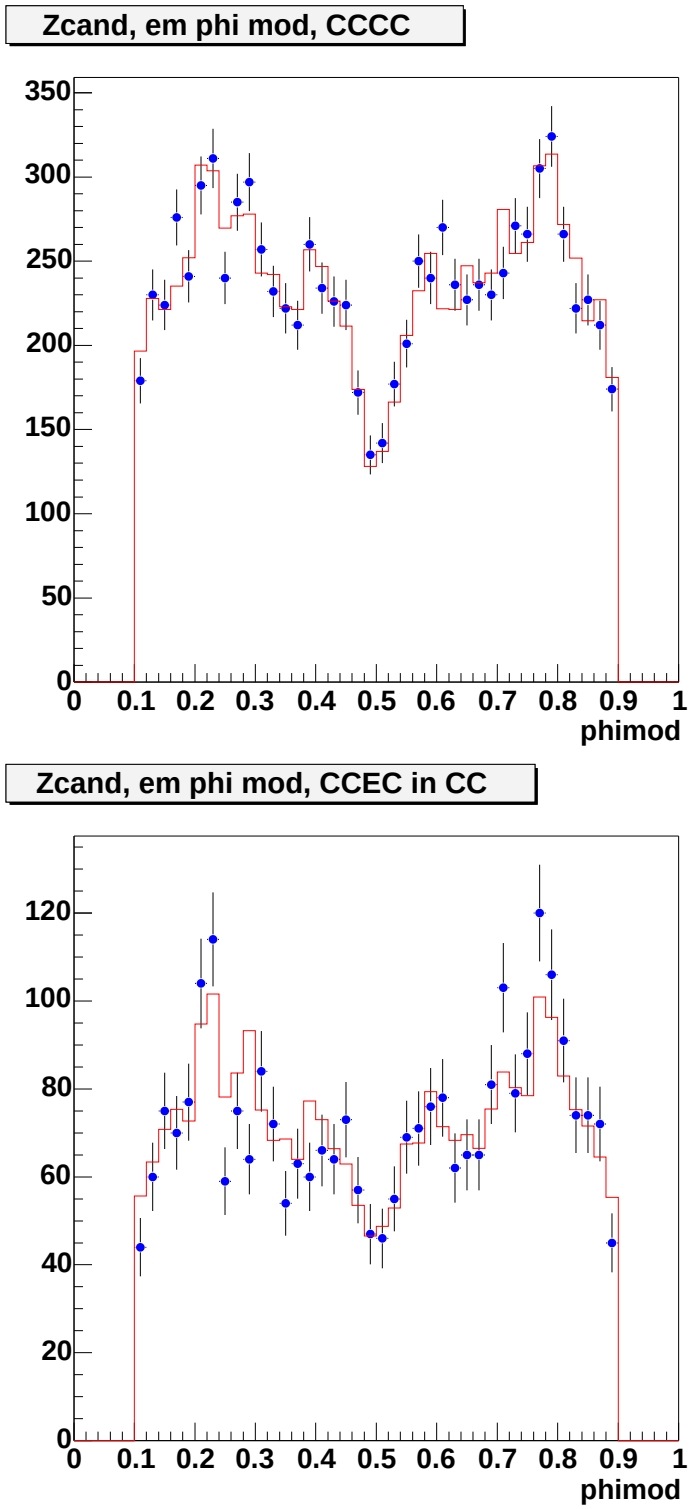

Fig. 5.6: Z candidate *phimod* for CC-CC electrons (top) and CC-EC electrons in the CC (bottom). PMCS (the red histogram) is compared to data (the dots).

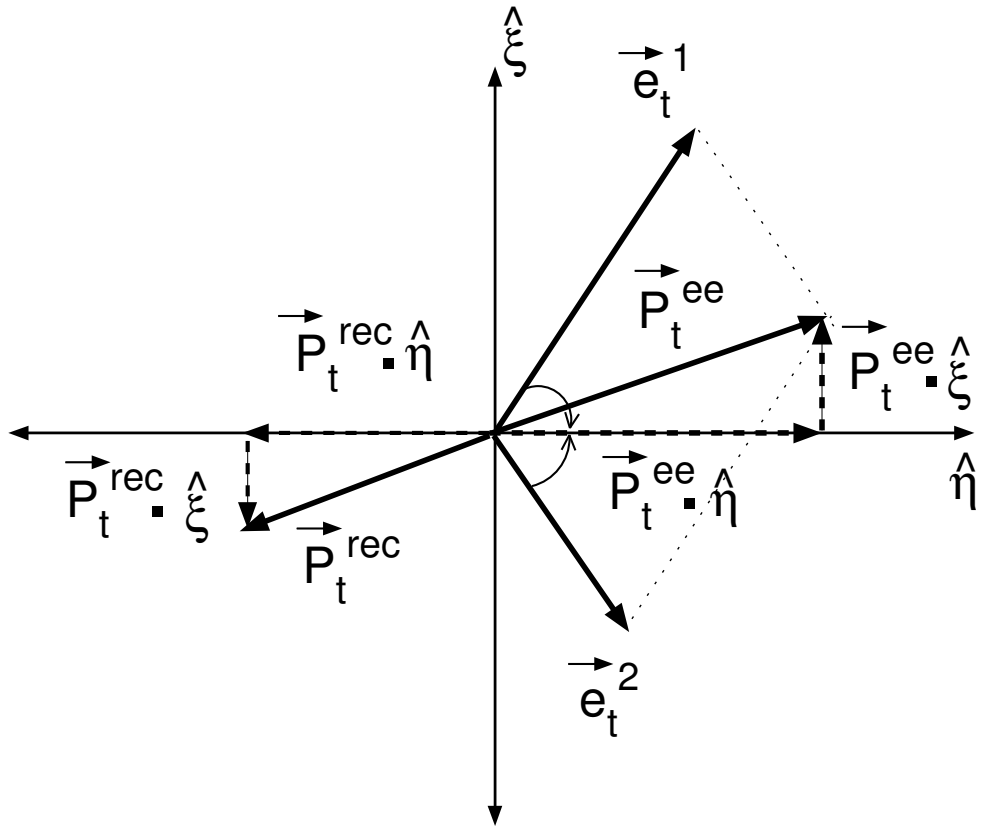

Fig. 5.7: Diagram of the η-ξ coordinate system for a $Z \rightarrow ee$ event. The $\hat{\eta}$ axis is defined as the bisector of the angle between electron directions and $\hat{\xi}$ is defined as the axis perpendicular to $\hat{\eta}$.

ξ axis. See Figure 5.7.

The hadronic response, defined as the relative hadronic energy scale with respect to the electron energy scale, is obtained by plotting $< \vec{p_T^{rec}} \bullet \hat{\eta} >$ versus $< \vec{p_T^{ee}} \bullet \hat{\eta} >$ as shown in Figure 5.8. The hadronic response is the absolute value of the slope in this plot which is found to be $\kappa = 0.67 \pm 0.02$. The offset of the response, obtained from the intercept of the fit, is 0.10 ± 0.10 GeV which is consistent with zero.

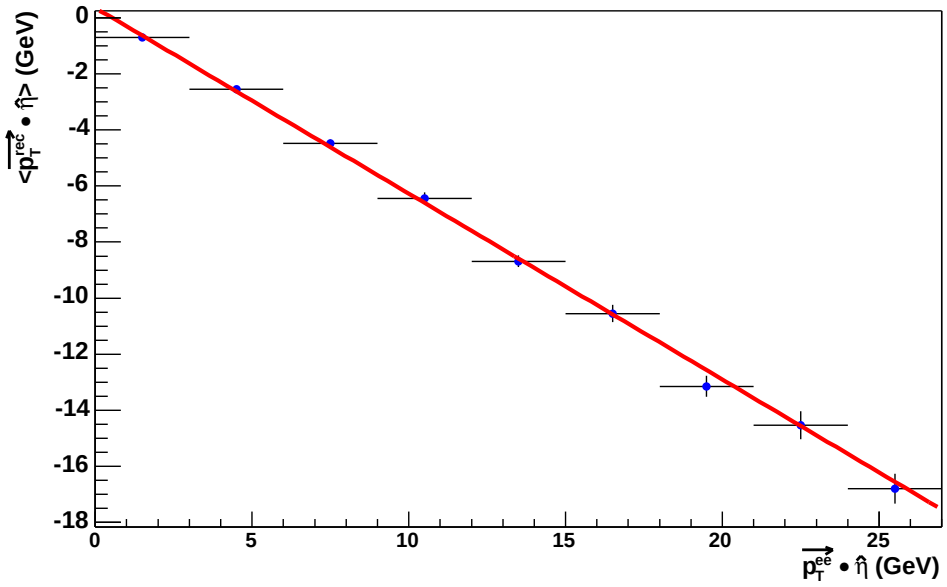

Fig. 5.8: Average value of $\vec{p_T^{rec}} \bullet \hat{\eta}$ vs $\vec{p_T^{ee}} \bullet \hat{\eta}$ for $Z \rightarrow ee$ events, the line is obtained from a linear fit to the data

5.6.6 Imbalance and Recoil

The η and ξ imbalance in Z events are defined as:

- $\eta_{imb} = (\vec{p_T^{ee}} + \vec{p_T^{rec}}) \bullet \hat{\eta}$
- $\xi_{imb} = (\vec{p_T^{ee}} + \vec{p_T^{rec}}) \bullet \hat{\xi}$

where $\hat{\eta}$ and $\hat{\xi}$ are unit vectors along the η and ξ axis respectively. Figure 5.9 compares the η and ξ imbalance for data and PMCS. Agreement is reasonable enough to prevent any significant systematic error from arising in the modeling of the hadronic energy resolution and energy scale.

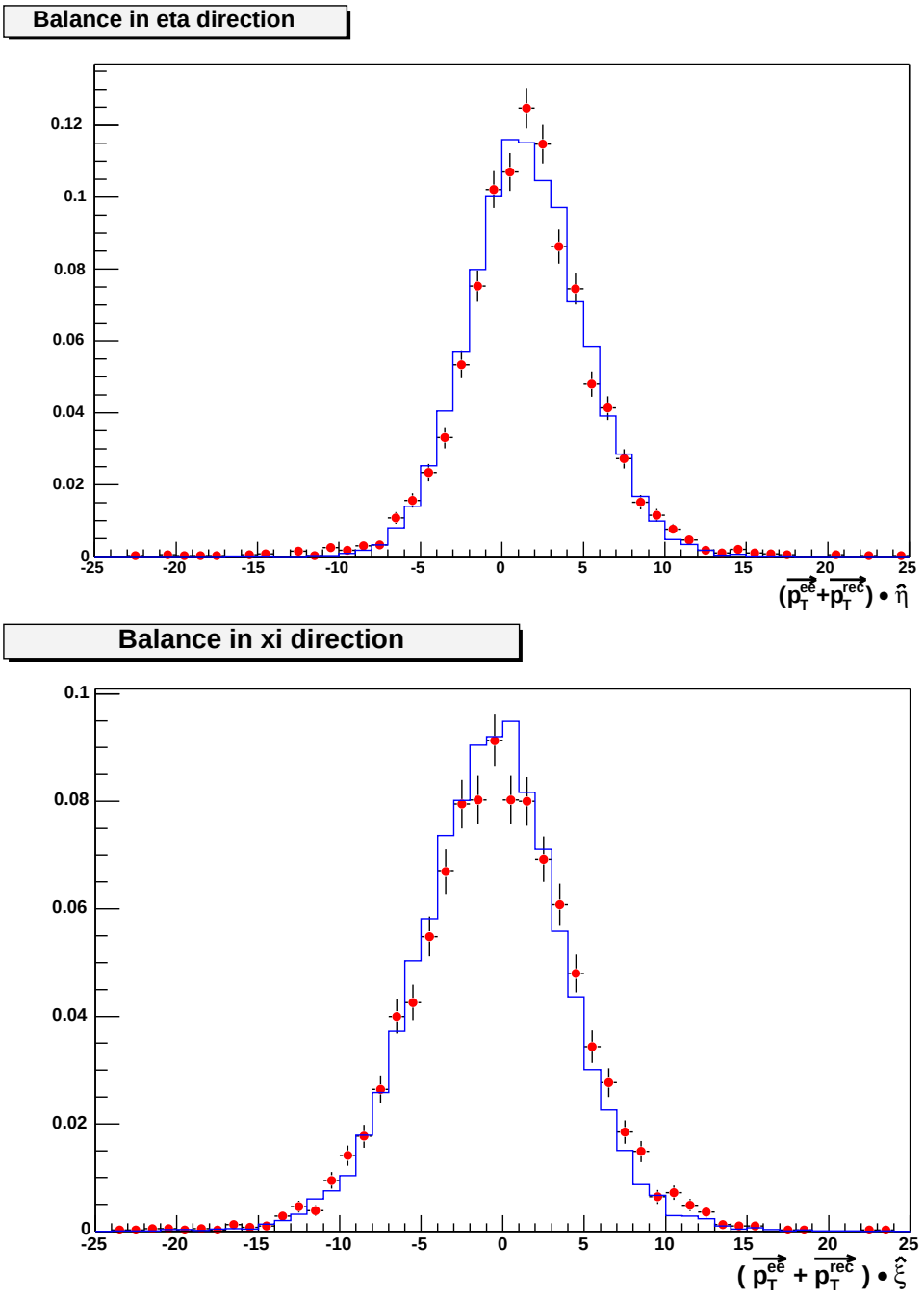

Fig. 5.9: η and ξ balance for $Z \rightarrow ee$ events, Red dots for data, Blue histograms for PMCS, the total entries are normalized to 1

5.6.7 $u_{\parallel}$ correction

The electron energy is measured as the energy within a window of 5×5 readout towers centered at the highest E_T tower; this region is excluded from the computation of missing E_T. The size of the window is selected so that leakage of the electron shower out of the window is negligible, however, leakage of energy from the underlying event into the electron window can not be avoided. The underlying event energy in the electron window will bias the recoil measurement.

We must correct the recoil momentum, u_T, for the momentum that is lost by excluding the electron window. The momentum that is lost always points in the direction of the electron and therefore biases the component of the recoil momentum parallel to the electron, $u_{\parallel}$, towards negative values.

Since for $p_T^W \ll M_W$

$$\text{missing } E_T \approx p_T(e) + u_{\parallel} \quad \text{and} \quad m_T \approx 2p_T(e) + u_{\parallel} \tag{5.4}$$

any $u_{\parallel}$ bias directly propagates into a bias on missing E_T and the transverse mass, we call this bias $\Delta u_{\parallel}$ and have to apply a correction for it in the MC simulation. This correction is applied to the component of the missing E_T parallel to the direction of the electron. Transverse mass can then be calculated using the corrected missing E_T.

The $u_{\parallel}$ correction is very sensitive to the ratio of W events with $u_{\parallel} > 0$ and $u_{\parallel} < 0$, we change the $u_{\parallel}$ correction in the Monte Carlo simulation until MC gives the same ratio as data. From Figure 5.10, we can determine the $u_{\parallel}$ correction to be -1.78 ± 0.01 GeV for the central region.

The $u_{\parallel}$ correction is calibrated further in the central region. A histogram is made by taking the plot shown in Figure 3.2, of the $u_{\parallel}$ cut equally dividing the W candidate sample as a function of ϕ module and η_{det} half, and subtracting the

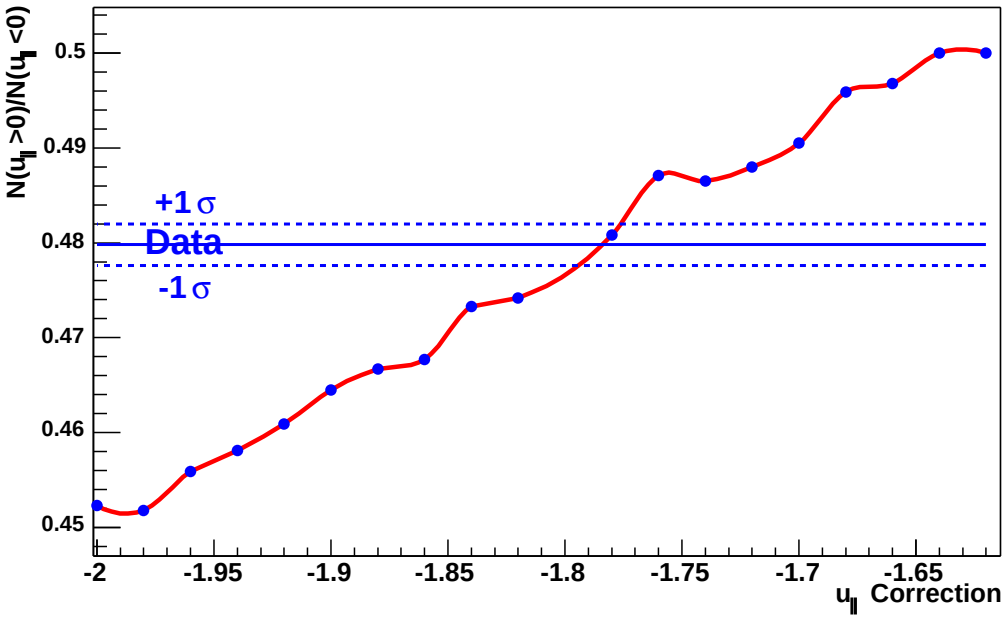

Fig. 5.10: Determination of the $u_{\parallel}$ correction $\Delta u_{\parallel}$ for the CC region. The curved red line connecting the Monte Carlo points shows the correlation between the $u_{\parallel}$ correction vs $N(u_{\parallel} > 0)/N(u_{\parallel} < 0)$ from Monte Carlo. The horizontal solid line shows the ratio $N(u_{\parallel} > 0)/N(u_{\parallel} < 0)$ measured from data and the horizontal dashed lines the uncertainty on $N(u_{\parallel} > 0)/N(u_{\parallel} < 0)$. From the intersection of the data line with the curved line we determine the $u_{\parallel}$ correction..

CC average cut. The corresponding (η_{det},ϕ) bin in this histogram, shown in Figure 5.11, is then added to the CC region $u_{\parallel}$ correction. Agreement between data and PMCS is good for the W candidate $u_{\parallel}$ distribution after these corrections are applied as shown in Figure 5.12.

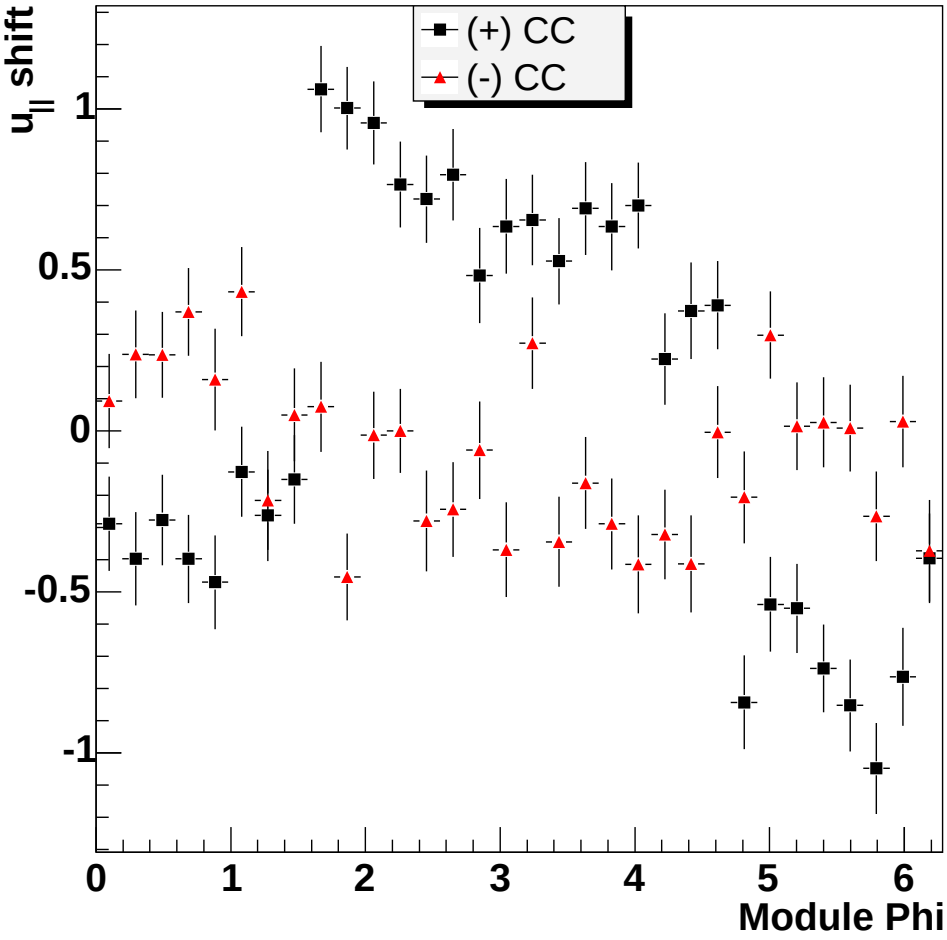

Fig. 5.11: Relative $u_{\parallel}$ shift as a function of ϕ_{det} and divided into halves in η_{det} for CC

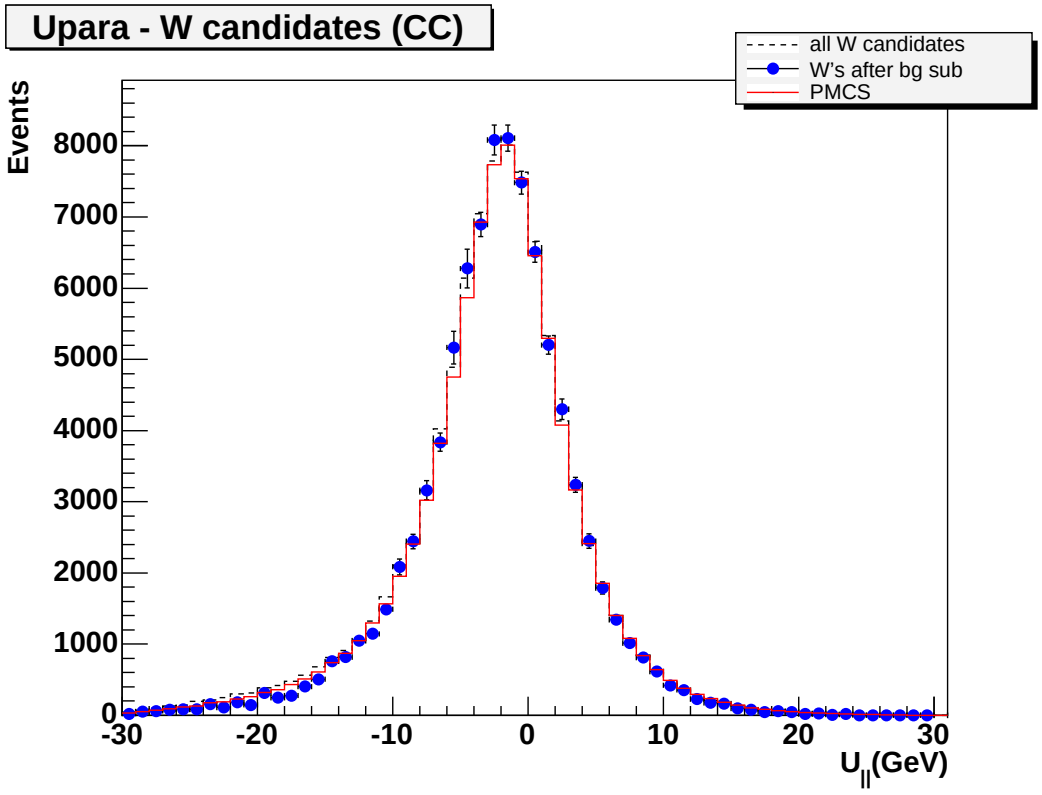

Fig. 5.12: $u_{\parallel}$ distribution for all $W \rightarrow e\nu$ events (after subtracting QCD background using the Matrix method), Blue dots for data, Red histograms for PMCS

5.6.8 Hadronic Energy Resolution

The hadronic energy resolution is parameterized in the same way as the electron energy resolution, and results are taken from a group at DØ which specializes in the study of jets [78]. A constant term of 0.05 ± 0.01 and a sampling term of 0.80 ± 0.20 GeV$^{1/2}$ have been obtained.

5.6.9 Underlying Event

The underlying event refers to everything in the event which does originate from the hard scattering process from which the W or Z are produced. It is modeled by randomly selecting an event from a sample of over 1,000,000 minimum bias events. These events are obtained from a trigger only requiring the luminosity monitor be hit and should simulate the underlying event well. A 2-D scatter plot of the x and y components of the missing E_T for these events are input into PMCS and added to the recoil. Applying the underlying event correction smears the missing E_T distribution resulting in a 1.1% decrease in the W candidate acceptance.

5.6.10 Vertex Distribution

The decay vertex distribution is generated as a Gaussian with a width of 28 cm to match the observed distribution. Figures 5.13 and 5.14 show the z vertex distributions for Z CC-CC and CC-EC candidates and Figure 5.15 shows the z vertex distribution for W candidates in the central calorimeter. For data, the decay vertex, defined in Section 4.7, uses the highest E_T electron track z0 (z position at the point of closest approach to the beam). Although treating track z0 as the vertex lowers the percent of events with no vertex to 0.4%, there is still an issue with the primary vertex z bias toward zero. The main concern is the use of an incorrect primary vertex when reconstructing missing E_T for W

candidate events and E_T for an electron with no track match in Z candidate events. Including events with no primary vertex (assigned $z = 0$), nearly 4% of W candidates have a primary vertex that is more than 20 cm away from the high E_T electron track z0. To model this in PMCS, a plot of W candidate (primary vertex z - track z0) vs. track z0, shown in Figure 5.16, is input into PMCS. This shift is applied to EM particles to alter E_T at the point in the PMCS code where missing E_T is calculated. E_T is only smeared in this way for the missing E_T calculation since track z0 is used in electron measurements. The change in acceptance with this smearing is less than 0.1%. The other concern is Z electrons with no track match. However, this is considered negligible since a much smaller percentage, at only 0.6%, of Z events have both an electron without a track match and poor agreement with the primary vertex.

The number of z vertex bins used is limited by statistics, especially at high vertex z where the greatest track match efficiency dependence is found. The nominal vertex z set has ten bins: $<$ -39, -39 to -30, -30 to -23, -23 to -10, -10 to 0, 0 to 10, 10 to 23, 23 to 30, 30 to 39 and $>$ 39 cm. To check that the number of vertex z bins is adequate, the cross sections are found using two alternate z vertex bin sets. The first set has five bins: $<$ -39, -39 to -10, -10 to 10, 10 to 39 and $>$ 39 cm, and the second has six bins: $<$ -30, -30 to -10, -10 to 0, 0 to 10, 10 to 30, and $>$ 30 cm. Agreement is very good with all three vertex bin sets. Compared to the nominal binning, the Z (CCCC) cross section decreases by 0.04% using the first set and 0.15% using the second. For the W (CC) cross section, the result decreases by 0.19% for the first set and 0.26% for the second.

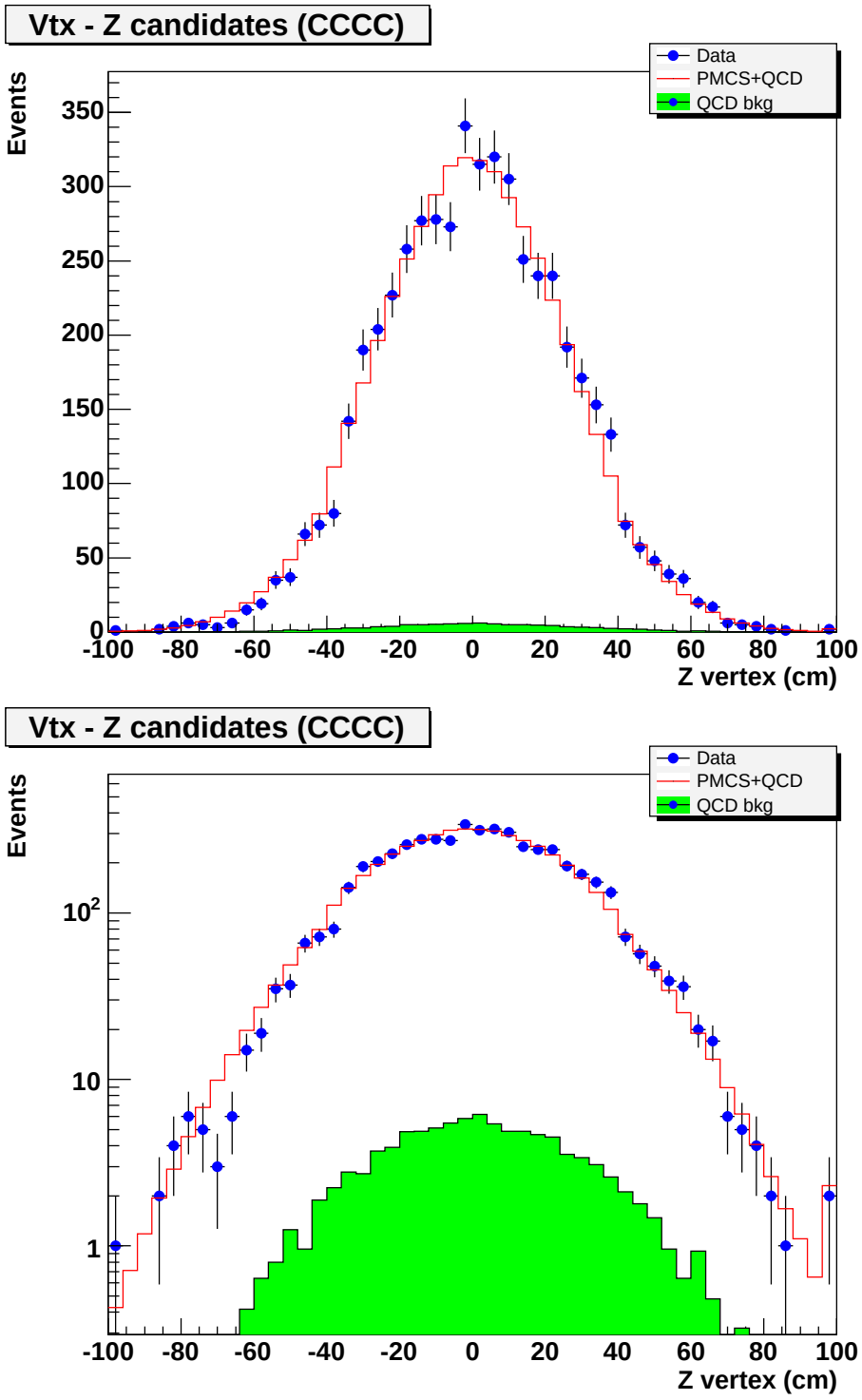

Fig. 5.13: PMCS to data comparison of Z candidate vertex z for CC-CC events shown with a linear scale (top) and log scale (bottom)

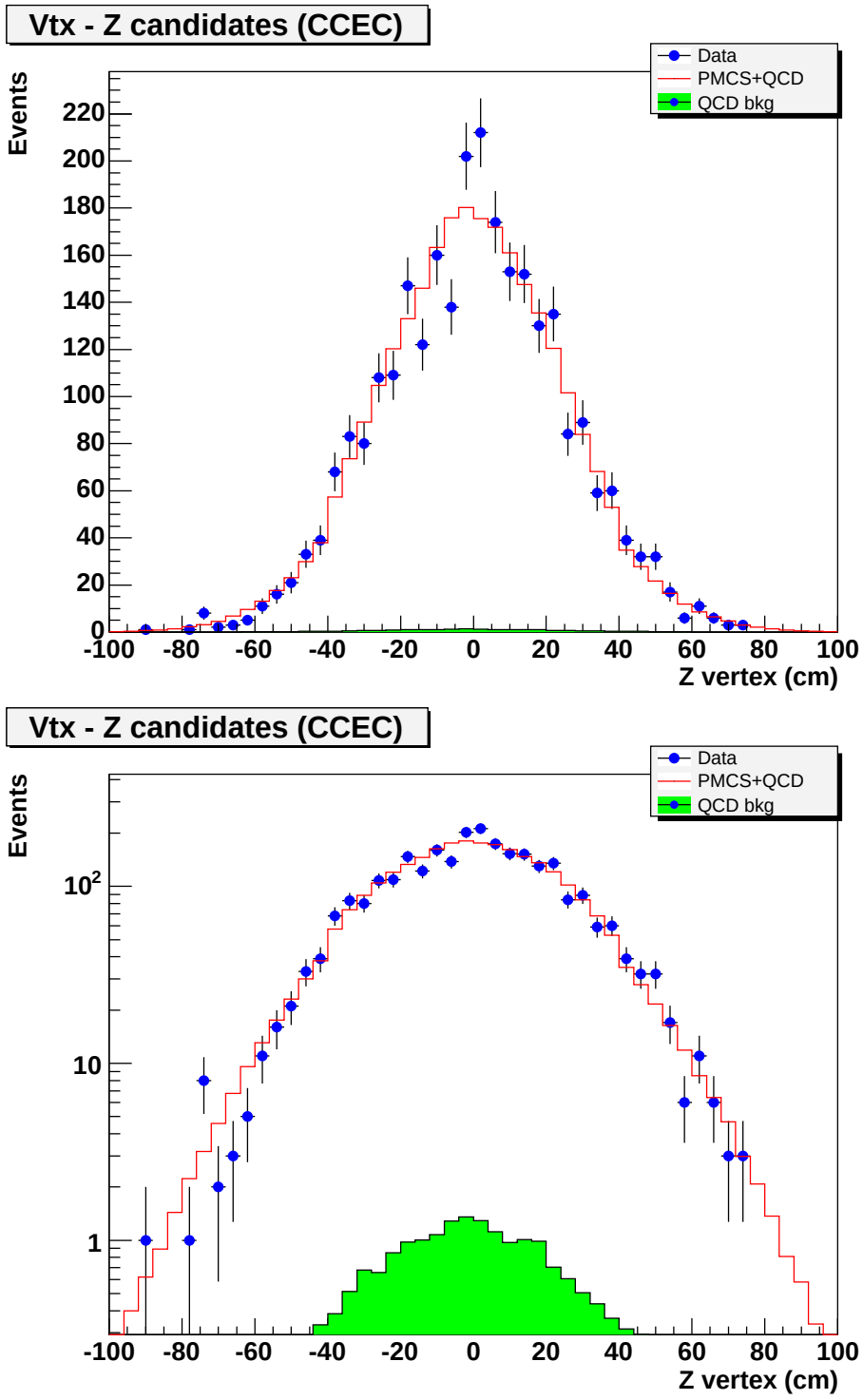

Fig. 5.14: PMCS to data comparison of Z candidate vertex z for CC-EC events shown with a linear scale (top) and log scale (bottom)

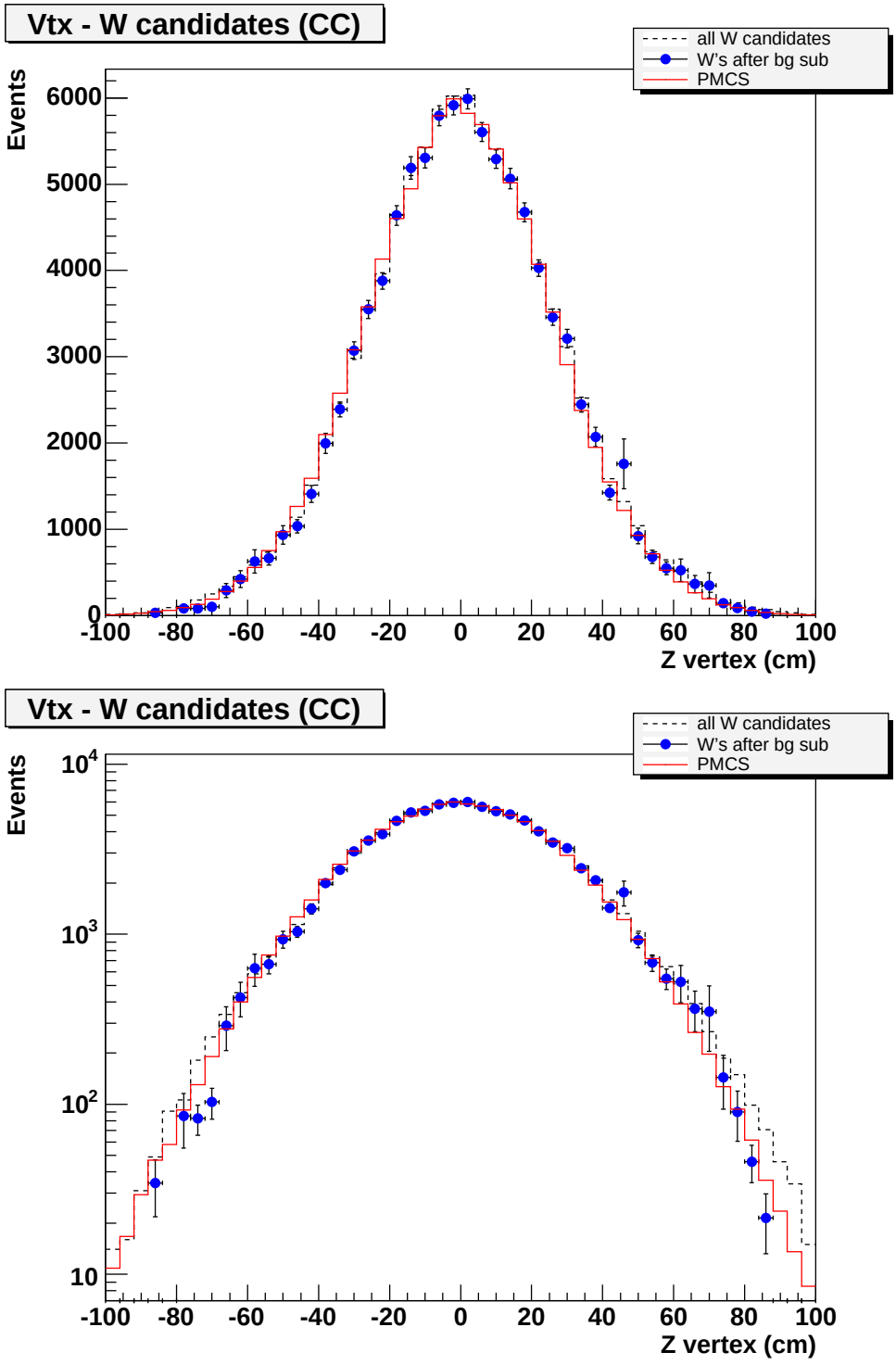

Fig. 5.15: PMCS to data comparison of W background subtracted vertex z for CC using a linear scale (top) and log scale (bottom). W candidates before background subtraction are represented by the black dashed histogram.

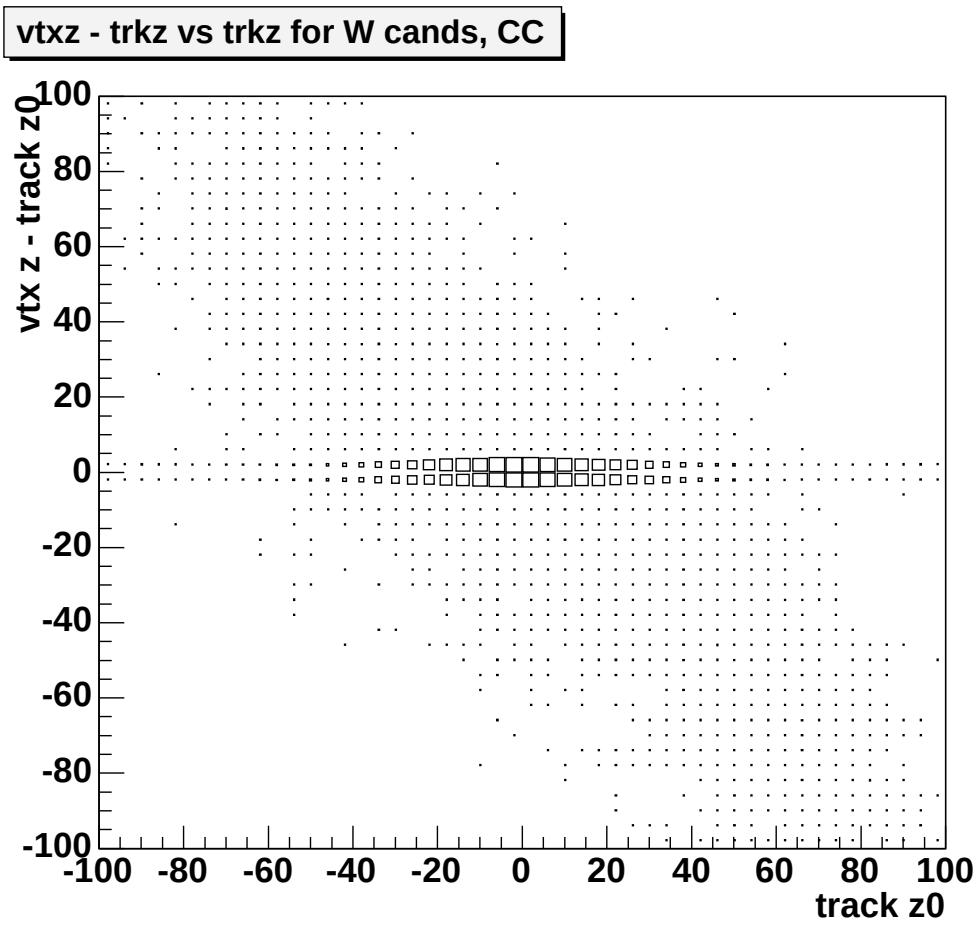

Fig. 5.16: W candidates in CC (primary vertex z - track z0) vs track z0 (cm) used to smear the z vertex in PMCS.

CHAPTER 6

ACCEPTANCE

The W and Z candidate acceptances are defined as the fraction of all events producing $W \rightarrow e\nu$ and $Z/\gamma^* \rightarrow ee$ interactions in the selected data sample obtained from the DØ detector which are successfully identified as W and Z candidate events. This chapter describes the procedure used to obtain these acceptances.

6.1 Acceptance Determination Procedure

For each generated event the following steps are applied in PMCS. First, final-state radiated photons within 0.2 in ΔR_{det} of an electron are added via four-vector addition into the generated electron. The radius of 0.2 very roughly corresponds to the reach of the EM clustering algorithm used in the data. A systematic uncertainty is estimated by varying this radius from 0.1 to 0.3. Using the generated event vertex, the known magnetic field, and the known calorimeter geometry, the η and ϕ position of each generated electron and photon at the third-layer of the EM calorimeter is determined.

Efficiencies are simulated using a uniformly distributed random run number between 0 and 1. For a given cut, if this random number is greater than the corresponding efficiency then the electron is said to have failed the cut. This efficiency is read from one of the bins in the corresponding efficiency input his-

Efficiency	Binned according to..	shown in figure(s)
Preselection (CC)	track *phimod*	6.2
Preselection (EC)	track η_{det}	6.2
Track	η_{det} and z vertex	6.6
Trigger (runs $\leq$ 178721)	p_T, η_{det} and z vertex	6.11 and 6.12
Trigger (runs $\geq$ 178722)	p_T, η_{det} and z vertex	6.13 and 6.14
Electron Likelihood	η_{det} and z vertex	6.15

Tab. 6.1: Efficiency Input Histogram Summary

togram. The bin to read the efficiency from is selected based upon the value of the dependencies, summarized in Table 6.1, for the generated electron.

Preselection is the first efficiency applied to the electrons. Those that fail are removed from consideration. For electrons in the CC region, the preselection efficiency is applied as a function of *phimod* position. In the EC region it is applied as a function of η_{det} only.

After the preselection efficiency is applied, the ϕ and η_{det} positions of the remaining electrons are smeared. For CC electrons, the *phimod* shift described in Section 5.6.4 is applied. For electrons in the EC region the ϕ position is smeared by the measured resolution. For all electrons, the η_{det} position is smeared by the measured η_{det} resolution.

A random run number (weighted by luminosity) from the list of runs used in the data sample is then assigned to the event. Electrons are rejected if they have an $\eta_{det} - \phi$ position that falls into a bad calorimeter region that is active for the associated run.

The generator-level energy of each electron and photon is shifted and smeared by the measured electron energy scale and resolution, respectively. The transverse recoil energy (all energy except missing E_T and electrons) is shifted and smeared by the measured hadronic energy scale and resolution, respectively. The adjusted transverse recoil energy, along with the adjusted electron energies, is

used to recalculate the missing E_T. The underlying event energy is then added to the missing E_T, and the $u_{\parallel}$ correction is applied.

The geometric acceptance cuts (pseudorapidity cut and the is_in_fiducial requirement) and E_T cut are applied and the remaining efficiencies are simulated. W and Z event selection cuts are then applied in a manner similar to data.

The total Z (or W) acceptance is then given by the ratio of the number of accepted Z (or W) candidate events to the total number of generated events.

6.2 Electron Identification and Trigger Efficiencies

The efficiencies, for electrons to pass each of the selection cuts: preselection, track matching, trigger and electron likelihood, are needed in PMCS to calculate the W and Z acceptance. It is important to understand what efficiency dependencies the selection cuts have and to model them in PMCS. A tag & probe method is used to study efficiencies as a function of the following variables:

- electron η_{det},
- electron $\eta_{physics}$,
- electron E_T,
- electron ϕ,
- electron *phimod*,
- *zvtx* (the Z position of the decay vertex),
- run number (dependence on time),
- instantaneous luminosity (dependence on activity in the detector),
- tick number (dependence on the bunch in which the collision occurred),

- and number of jets in the event.

If a dependency is not accounted for, it can bias the result. For example, many of the efficiencies drop at high $zvtx$ and there is a higher proportion of W candidate events at high $zvtx$ than in the tag & probe electron sample. If not accounted for, this will lead to an overestimation of W candidate efficiency.

6.2.1 The Tag & Probe Method

Efficiencies are found with a tag & probe method using a high purity sample of $Z/\gamma^* \rightarrow ee$ events. An electron becomes a 'tag' if it satisfies the requirements of a tight electron and has fired the trigger. The other electron in the event can then be used as a 'probe'. The tag requirement is necessary both to remove QCD background and to ensure that the probe is selected in an unbiased manner. For all efficiencies found with the tag & probe method, both electrons can be used as a probe if the other electron satisfies tag requirements. Efficiencies are applied in the following order:

- Preselection
- Track Matching
- Trigger
- Electron Likelihood

The probe electron must satisfy cut requirements of all previous efficiencies. Cuts and efficiencies must be applied in this order to remove any concerns over correlations between selection cuts. Although this method allows efficiency to be studied as a function of various variables, a disadvantage is that background subtraction can be difficult. This is mainly a concern for preselection and track matching efficiencies. For trigger and electron likelihood efficiencies, background is extremely small since the probe must already have a track match.

6.2.2 Preselection Efficiency

The preselection efficiency is defined as the efficiency for an electron satisfying the fiducial and kinematic requirements to form an EM object passing the preselection cuts:

- EM fraction > 0.9
- isolation < 0.15
- ID $= 10$ or $\pm$ 11

An unbiased method not using calorimeter information needs to be employed to study the preselection efficiency. Fiducial cuts similar to those used for determining geometric acceptance are made with the exception of the central ϕ fiducial cut. For PMCS, efficiency in the central calorimeter is measured as a function of *phimod* and must include the ϕ crack regions. For the study of dependence on other variables, it is desired to only measure efficiency of electrons in the ϕ fiducial region. For this, the probe track is required to be an additional 0.025 *phimod* units away from the ϕ module boundaries. The extension to this cut is necessary to ensure the matching EM object is within the fiducial region. For all tracks except the tag, η_{det} and ϕ positions are found by extrapolating to the third floor of the calorimeter. For an event to be included in the probe sample, there must be a good tag electron and a second track with the following properties:

- $27 < p_T < 80\ GeV$
- $|\eta_{physics}| < 3.2$
- $\chi^2 < 8$ and DCA < 0.3 cm
- no muon within $\Delta R_{physics} < 0.02$
- $\Delta zvtx$ of the two tracks < 4 cm

- $\Delta\phi$ of the two tracks > 2 rad
- invariant mass of tag electron and probe track within $70 < M < 105\ GeV$.

The track with the highest p_T is selected as the probe track if more than one fulfills the above requirements.

EM objects are successfully matched to the probe track if they are within $\Delta R_{physics} < 0.1$ of the extrapolated track position. Background subtraction is based on the expectation that signal events will have opposite sign tracks while the relative sign of tracks in background will be random. Events which are matched to two tracks with the same sign are therefore used for background studies. However, some signal will remain in the background sample due to the possibility of charge sign misidentification. Before matching, the same sign track sample contains mainly background events whereas after matching the same sign track sample contains mainly signal events. Therefore, events with same sign tracks are counted as signal if an EM object match is found and background if not.

The efficiency is defined as

$$\epsilon_{presel} = \frac{\text{probes with a matching EM object}}{\text{total probe tracks}} \tag{6.1}$$

Defining opposite sign tracks passing the EM match requirement as P_O, failing as F_O, passing with same sign tracks as P_S and failing same sign as F_S gives the background subtracted preselection efficiency:

$$\epsilon_{presel} = \frac{P_O + P_S}{(P_O + P_S) + (F_O - F_S)}. \tag{6.2}$$

Figure 6.1 shows the invariant mass distributions for these four samples. The uncertainty on ϵ_{presel} can be calculated by writing it in terms of the statistically independent samples P defined as $P_O + P_S$ and F defined as $F_O - F_S$:

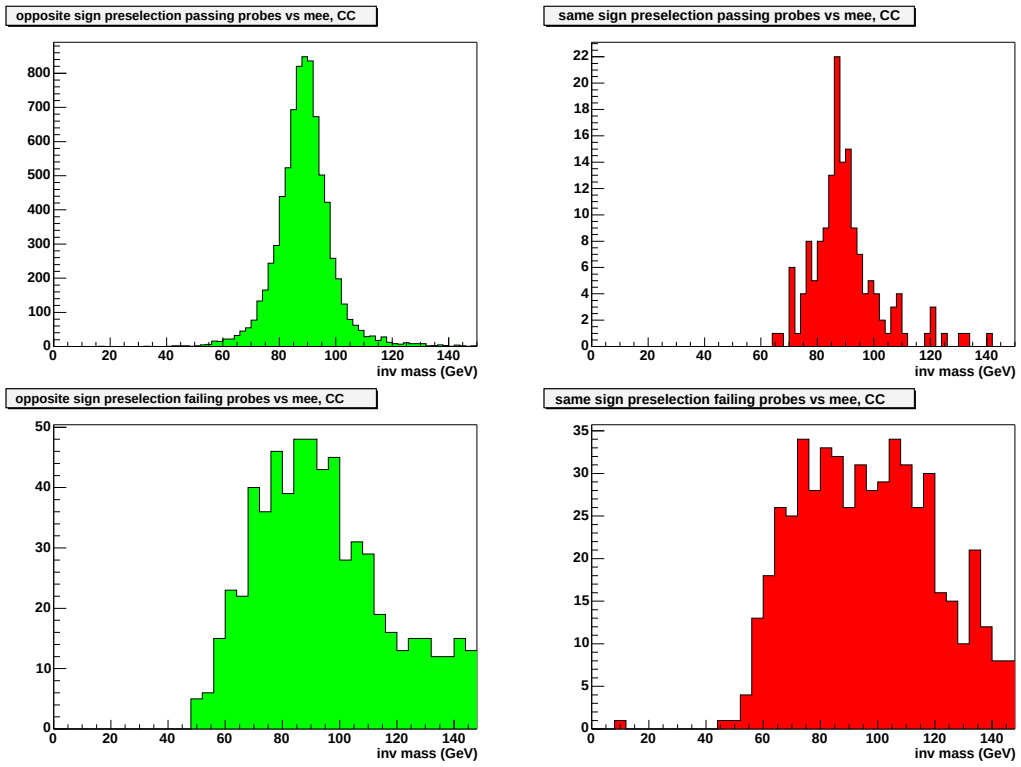

Fig. 6.1: Invariant mass of the tag electron and probe track for the independent samples used in determining efficiency for CC. Plots are of opposite sign tracks (left side), same sign (right side), passing preselection cuts (top half) and failing cuts (bottom half).

$$\epsilon_{presel} = \frac{\mathrm{P}}{\mathrm{P+F}}. \tag{6.3}$$

The uncertainty is then:

$$\delta\epsilon_{presel} = \sqrt{\frac{(F\delta P)^2 + (P\delta F)^2}{(F+P)^4}}, \tag{6.4}$$

where δP and δF are the statistical uncertainties of the samples P and F:

$$\delta P = \sqrt{P_0 + P_S}\ , \quad \delta F = \sqrt{F_0 + F_S}. \tag{6.5}$$

Using all statistics yields for the CC region $P_O = 6692$, $P_S = 76$, $F_O = 132$ and $F_S = 72$ and for EC: $P_O = 1298$, $P_S = 45$, $F_O = 56$ and $F_S = 41$. Using these to calculate an average preselection efficiency per electron, one gets:

$$\epsilon_{pre}^{CC} = (99.1 \pm 0.2)\% \tag{6.6}$$

$$\epsilon_{pre}^{EC} = (98.9 \pm 0.7)\% \tag{6.7}$$

Figure 6.2 shows the histograms input into PMCS. For PMCS, preselection efficiency as a function of *phimod* is needed in order to model the shifting of calorimeter clusters away from the ϕ module cracks in the central region. It is quite possible to measure an efficiency in some bins greater than 100% due to the way background is subtracted.

One source of systematic uncertainty for preselection efficiency is estimated based on variations found in regions where it is expected to be constant and very close to 100%. These include distributions in ϕ, shown in the bottom plot of Figure 6.3, and in η_{det}, shown in the top plot of Figure 6.2, away from the edges of the central calorimeter ($|\eta_{det}| < 0.7$). From these variations, a relative uncertainty of 0.5% is estimated.

Additionally, full Monte Carlo checks indicate an upward bias of 0.4% from the use of a track in the tag & probe method. This is based on the observed increase in average CC efficiency when a track is required as described in Section 6.2.6. This upward bias is assigned a systematic error and for simplicity treated as symmetric.

An additional check is based on a possible systematic error due to the treatment of events with same sign tracks as signal if a matched EM object is found. However, it is found that throwing these events out results in a negligible change in preselection efficiency and therefore it can be ignored.

Another check was made for a possible systematic error arising from the number of jets in the event not being modeled in PMCS. Preselection efficiency does appear to drop with the presence of jets as shown in Figure 6.4. This is expected because it is possible for particles in a jet to fall near an electron which will cause it to be less isolated. There are not enough statistics available in data to adequately model preselection efficiency as a function of number of jets along with the other dependencies. Therefore, full Monte Carlo, which is first compared to data to ensure good agreement, is used to check for any bias from failing to model number of jets in PMCS. Fortunately, negligible bias is indicated by the full Monte Carlo check.

Combining the 0.5% uncertainty based on variations in ϕ and η_{det} and the 0.4% bias from the use of a track as the probe yields a total systematic uncertainty of 0.7% for preselection efficiency.

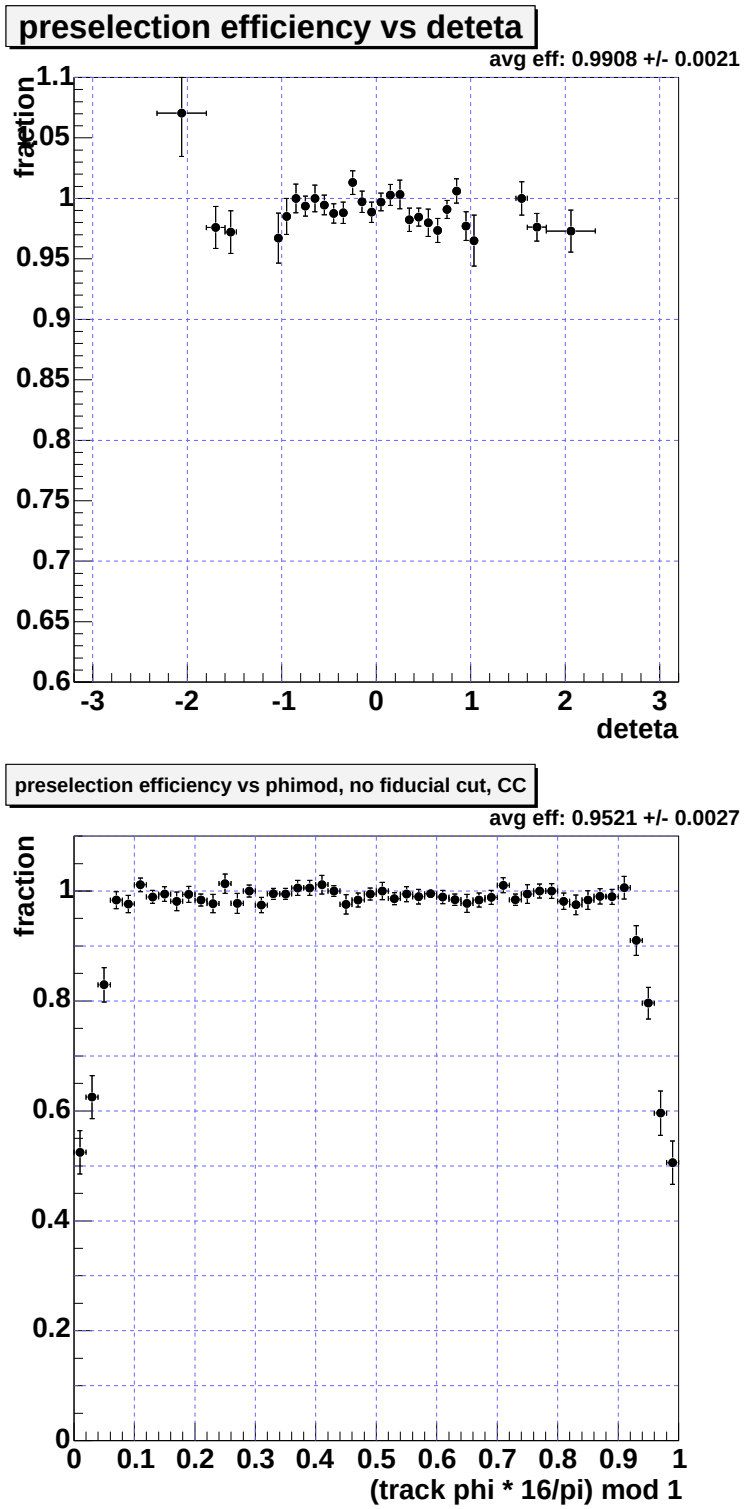

Fig. 6.2: Preselection efficiency after background subtraction as a function of η_{det} (top) and, for CC, *phimod* (bottom).

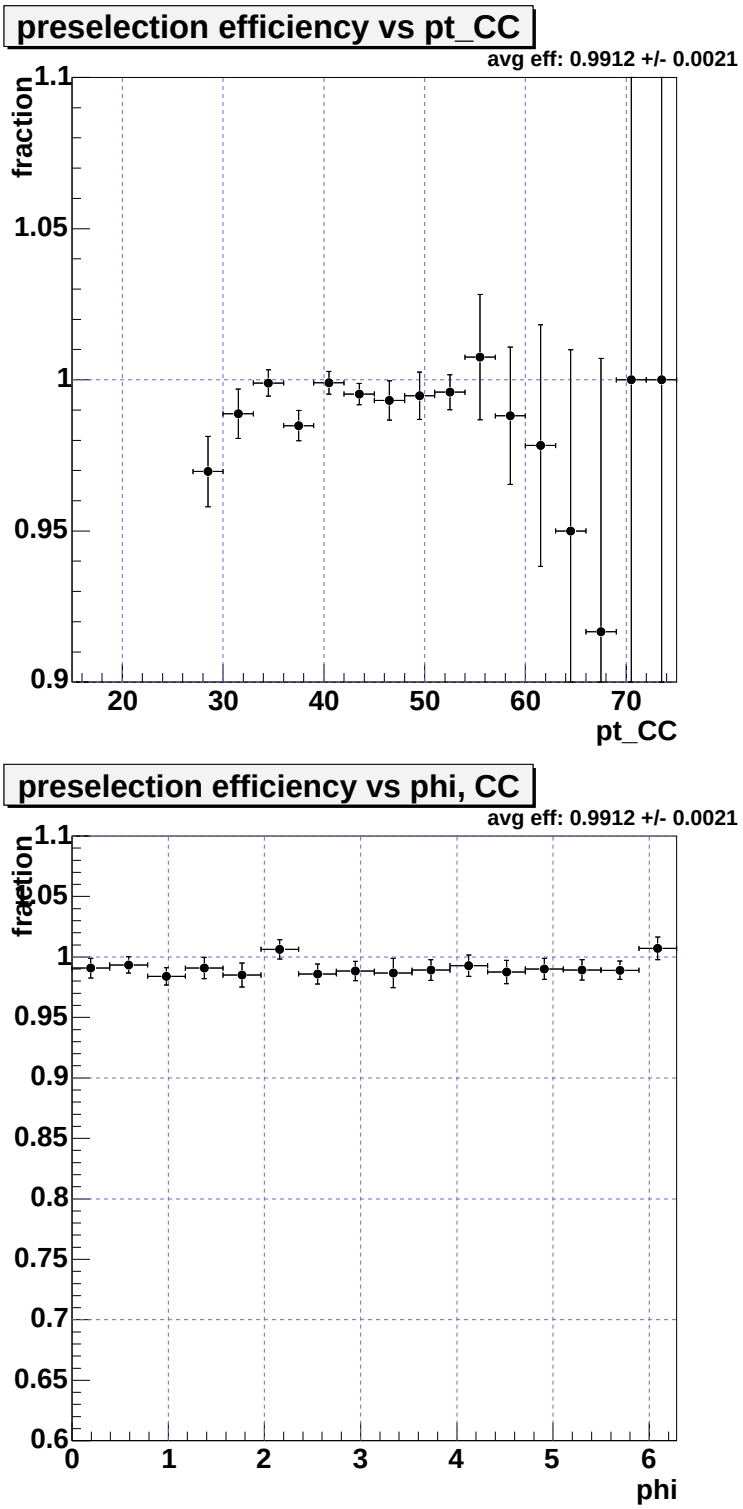

Fig. 6.3: Preselection efficiency after background subtraction in the central region as a function of E_T (top) and ϕ (bottom)

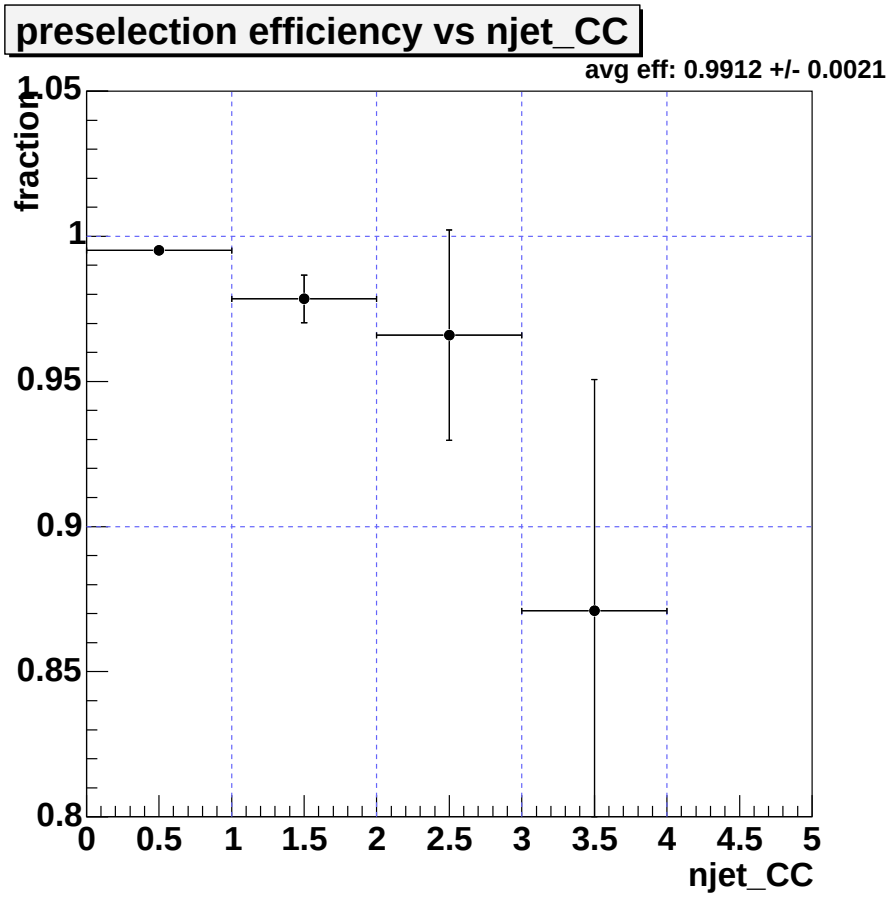

Fig. 6.4: Preselection efficiency after background subtraction in the central region as a function of number of jets

6.2.3 Track Match Efficiency

The tag & probe method is used with the probe electron required to pass preselection cuts in order to be considered. The efficiency for the probe electron to also have a matched track, as defined in Section 4.4, is measured. Background is too large to be ignored in the probe sample so its contribution must be carefully taken into account. The invariant mass, based on the tag and probe electrons, is fit to the QCD background shape estimated from data plus a signal shape estimated from the tuned PMCS $Z/\gamma^* \rightarrow ee$ sample. Fitting is done separately for CC-CC and CC-EC events as shown in Figure 6.5 resulting in background fractions of 1.3% and 2.3% respectively. The background invariant mass distribution is estimated using the QCD background shape defined in Section 7.3.2.

The track match efficiency is then the ratio of the number of probes having a track match to the total number of probes after background subtraction. The track matching efficiencies are input into PMCS as a function of η_{det} and $zvtx$. Figure 6.6 shows track match efficiency as a function of η_{det} split into ten histograms according to $zvtx$. In the central region, the track match efficiency is fairly stable with an average value of $(77.4 \pm 0.4)\%$. As can be seen in Figure 6.6, track match efficiency varies greatly in the EC dropping to practically nothing for high $zvtx$ when the electron is on the same side. This is one of the reasons why no EC track requirements are made.

The main source of systematic uncertainty for track match efficiency arises from the relatively large background in the probe sample, before track matching is applied, compared to the negligible background remaining after the track match. Neglecting to account for this background would therefore result in the underestimation of efficiency by an amount approximately equal to the background percentage. The uncertainty on the background in the probe sample is therefore assigned as the track match systematic uncertainty. The method of

background subtraction and error estimation is described in Section 7.3.3. Estimated uncertainty is 0.42% for CC-CC, 0.51% for CC-EC and 0.45% for all CC probes combined. This combined uncertainty is rounded up to 0.5% for use in the acceptance calculation.

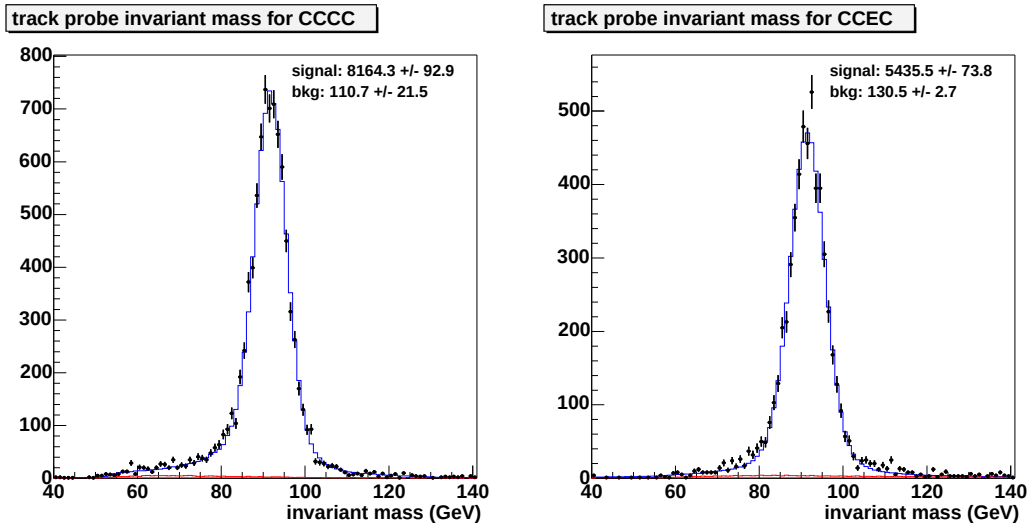

Fig. 6.5: Invariant mass distribution of probes before the track match requirement for CC-CC (left) and CC-EC (right).

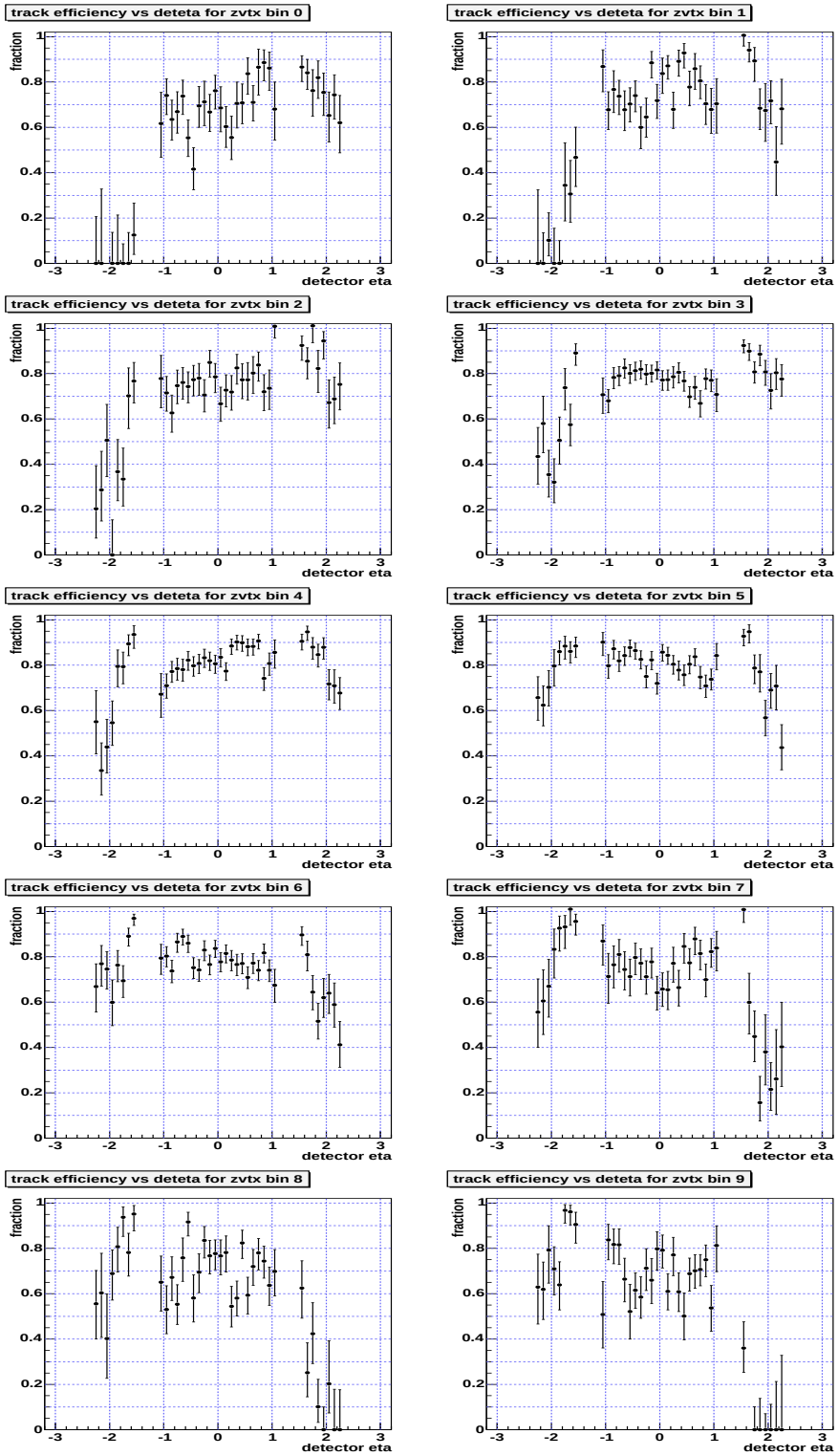

Fig. 6.6: Track matching efficiency vs η_{det} using $zvtx$ bins as input into PMCS. $zvtx$ bins are, going left to right from top to bottom: $<$ -39, -39 to -30, -30 to -23, -23 to -10, -10 to 0, 0 to 10, 10 to 23, 23 to 30, 30 to 39, and $>$ 39 cm.

6.2.4 Trigger Efficiency

The efficiency for an electron to satisfy trigger requirements for at least one trigger used in the analysis (see Section 4.3) is studied using the tag & probe method with the probe required to pass preselection and track match requirements. For this efficiency, the requirement that the tag electron passes trigger requirements for at least one unprescaled trigger is especially important. This ensures the probe is not biased by the event trigger requirement.

As described in Section 4.3, the data sample is divided into two sets based on run range for the purpose of the trigger efficiency study. This is because major changes were made to the trigger definitions starting at run 178722. Therefore the sample is split up into runs $\leq$ 178721 and runs $\geq$ 178722. This results in some significant statistical limitations, especially for the runs $\geq$ 178722 sample. There are a total of 8285 probes for runs $\leq$ 178721 and only 2949 for runs $\geq$ 178722. A total of 8180 probes for runs $\leq$ 178721 and 2896 for runs $\geq$ 178722 pass trigger requirements, yielding average trigger efficiencies of 98.7% and 98.2% respectively. Since either electron in Z events has the capability of firing the trigger, Z event trigger efficiency is extremely high at over 99.9%. Since W event electrons tend to have slightly lower E_T than the probe sample and efficiency tends to drop at low E_T, W event efficiency is slightly lower than the average efficiency, at around 97.5 to 98.0%

Trigger efficiency is highly dependent on E_T. Figures 6.7 and 6.8 show trigger efficiency for both run ranges as a function of electron E_T in the calorimeter CC region. Figure 6.9 shows the η_{det} dependence for both run ranges. Separating this into two parts for $zvtx > 0$ and $zvtx < 0$ shows also a z vertex dependence as can be seen in Figure 6.10. Limited statistics prevent more than two bins for $zvtx$, however binning checks described below indicate that this bin choice is adequate. This results in four dependencies which must be taken into account for

the electron trigger efficiencies used in PMCS. These are electron E_T with eight bins (including overflow), electron η_{det} with ten bins, $zvtx$ with two bins and run range with two bins. PMCS input histograms are displayed in Figures 6.11 to 6.14. There are four figures: two for run range $\times$ two for $zvtx$ sign. Each figure contains ten histograms based on η_{det} with each histogram displaying trigger efficiency as a function of electron E_T. See [79] for a more thorough examination of trigger efficiency dependencies.

A systematic uncertainty for the Z trigger efficiency enters from the use of a track requirement on the probe since only one of the Z candidate electrons must have a track. A conservative estimate is made by measuring the change in acceptance from using a trigger efficiency with no track requirement on the probe. Acceptance increases by 0.05% for CC-CC and drops by 0.29% for CC-EC for a combined change of -0.07%.

A systematic uncertainty for the W trigger efficiency is estimated based on the difference in cross sections measured using runs ≤ 178721 (CMT 8 to 11 triggers) vs. runs ≥ 178722 (CMT 12 triggers). The cross sections are 2924 pb^{-1} for runs ≤ 178721 and 2946 pb^{-1} for runs ≥ 178722. The systematic is determined to be 0.38% by taking the relative difference divided by two.

Due to the large number of dependencies, rather large bin sizes are necessary in order to have a reasonable number of statistics for every bin. These large bin sizes can result in large jumps from bin to bin, especially at low E_T. To check the stability of the result with bin size, changes in W and Z acceptances are recorded when different binning choices are made. See Table 6.2 for a summary of results from binning tests.

binning test	change in Z acceptance	change in W acceptance
double E_T bin size	-0.02%	-0.6%
halve E_T bin size	-0.12%	-0.3%
don't use zvtx bins	-0.15%	-0.3%
use 2 CC deteta bins	+0.04%	-0.2%

Tab. 6.2: A check of acceptance result dependence on choice of trigger efficiency bin size.

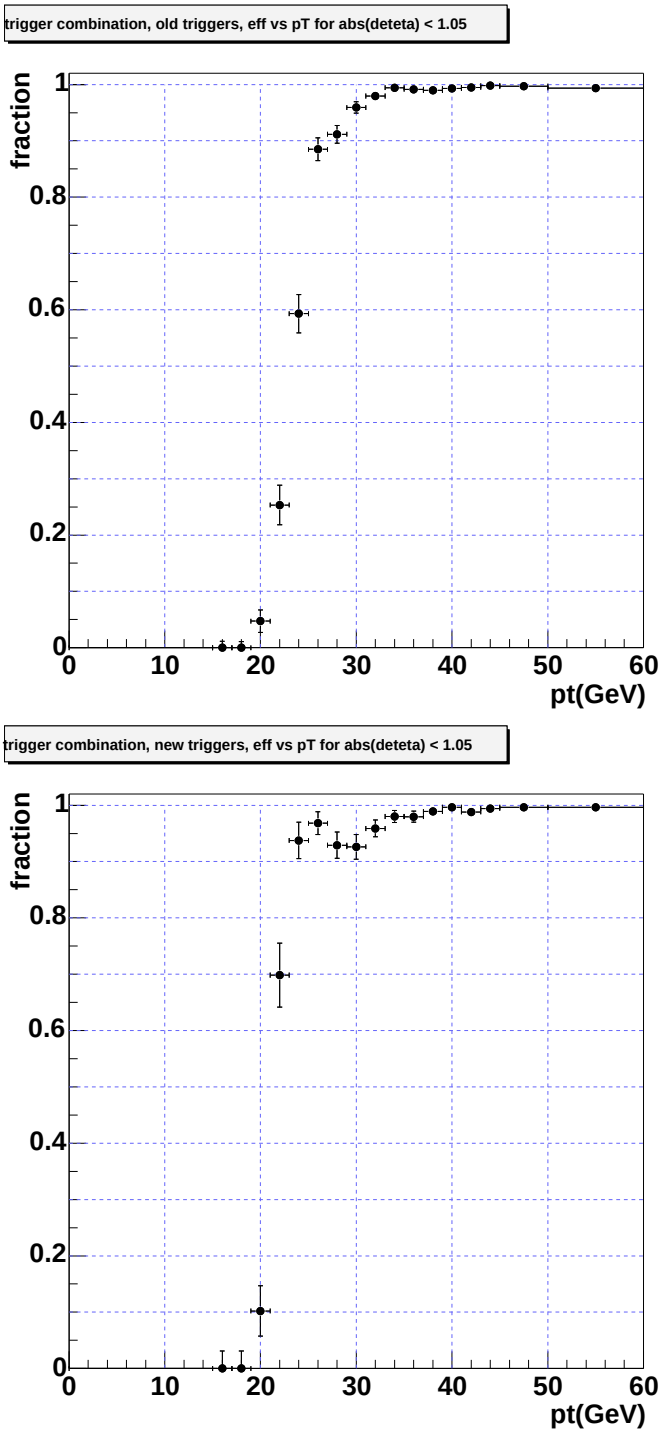

Fig. 6.7: Electron trigger efficiency with respect to electron E_T in the CC region for runs $\leq$ 178721 (top) and runs $\geq$ 178722 (bottom). The bottom plot shows an odd bump around 25 GeV. This bump is produced by the combination of the two level 3 triggers used in this run range. These level 3 triggers, ELE_NLV_SH and ELE_NLV_SHT, are shown in Figure 6.8.

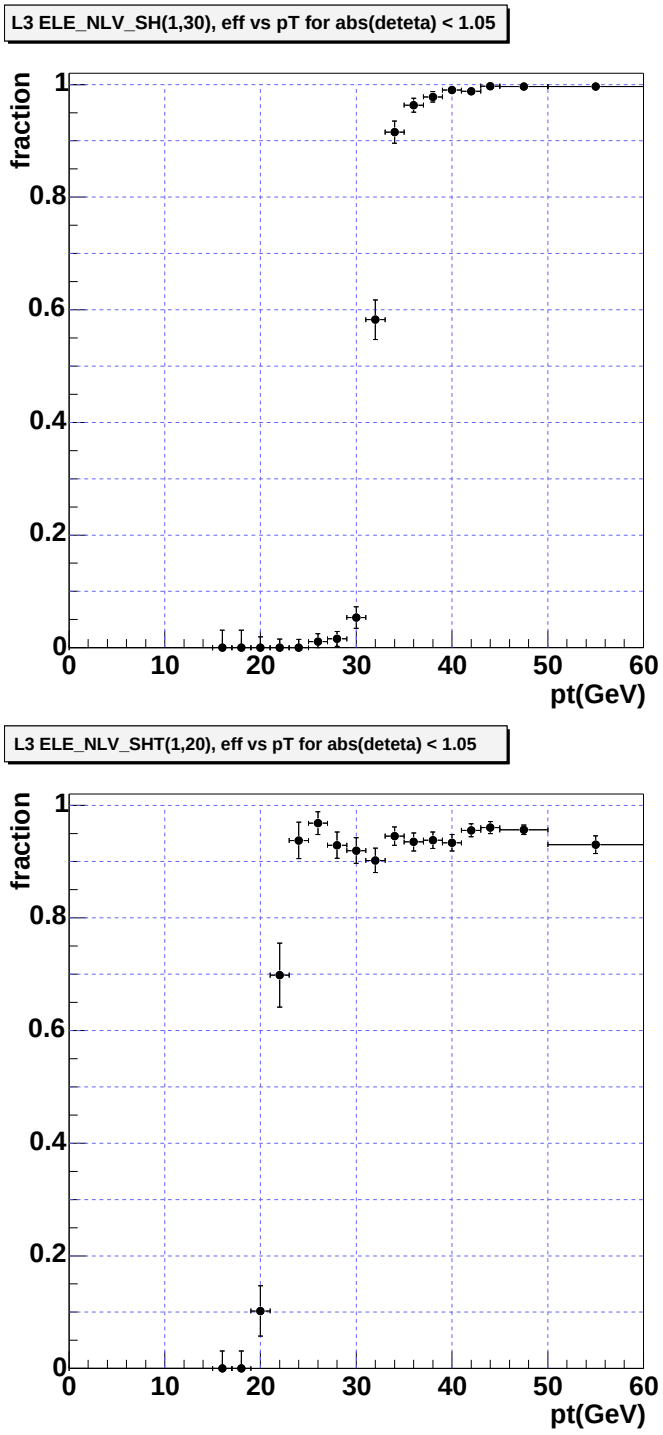

Fig. 6.8: Electron trigger efficiency for L3 triggers used in runs $\geq$ 178722 with respect to electron E_T in the CC region. Although not statistically significant, the plot for ELE_NLV_SHT(1,20) (bottom) appears to have a small peak at around 25 GeV. This is responsible for the odd bump in the bottom plot of Figure 6.8 when combined with ELE_NLV_SH(1,30) (top).

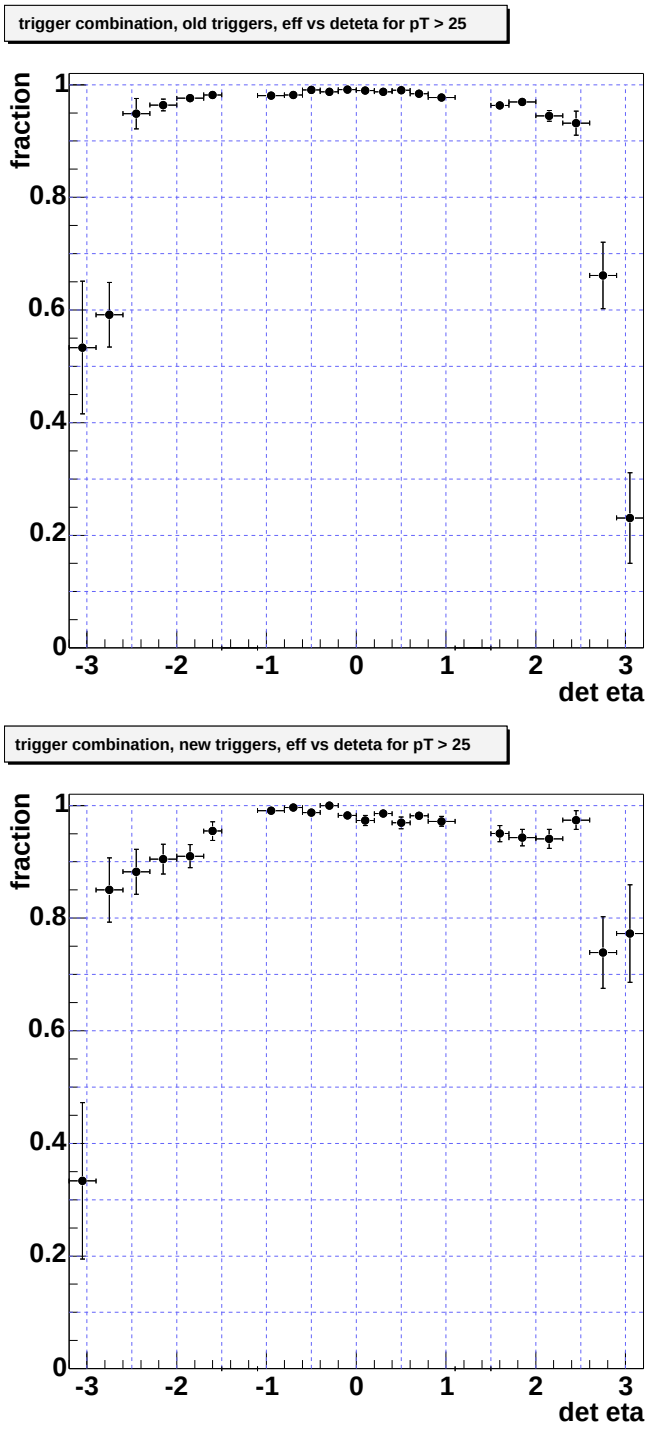

Fig. 6.9: Electron trigger efficiency with respect to electron η_{det} for runs ≤ 178721 (top) and runs ≥ 178722 (bottom).

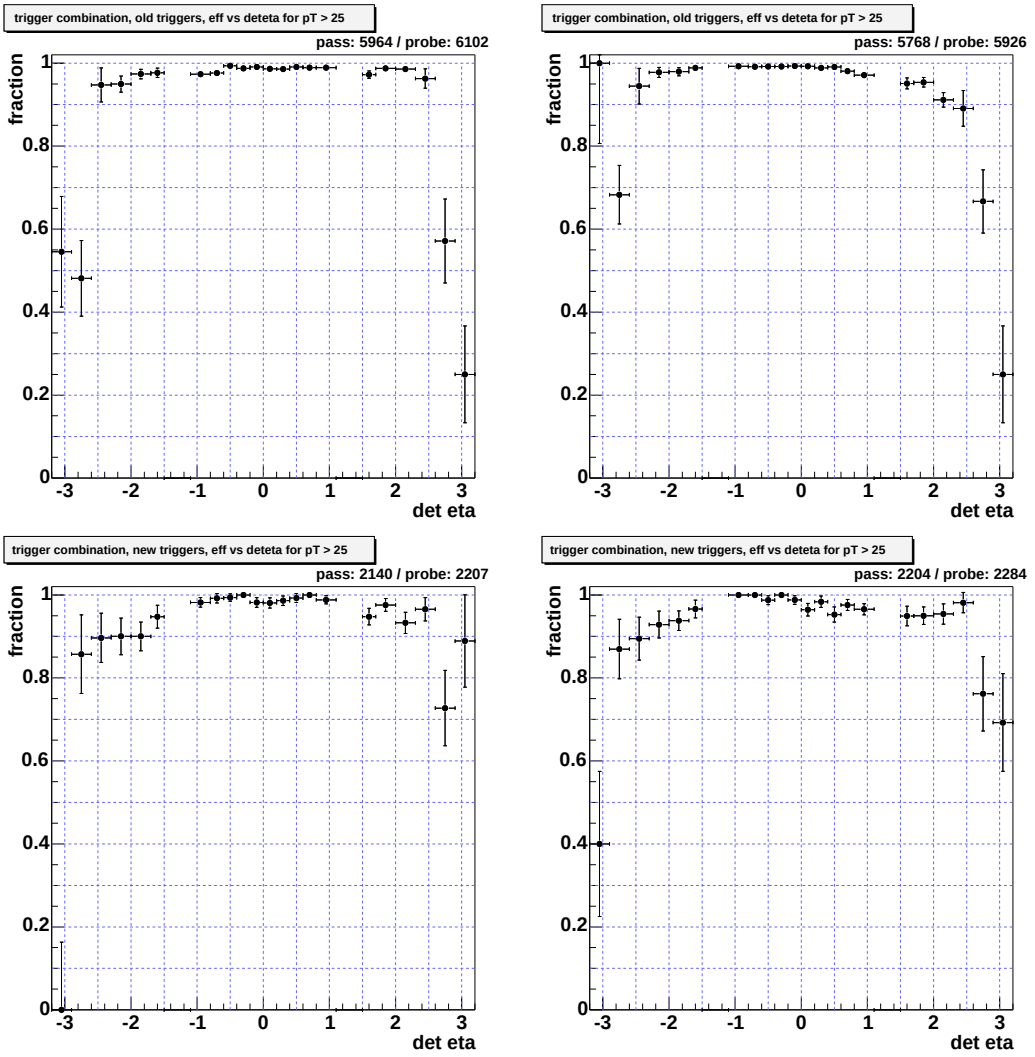

Fig. 6.10: Electron trigger efficiency with respect to electron η_{det} for runs $\leq$ 178721 (top), runs $\geq$ 178722 (bottom), $zvtx < 0$ (left) and $zvtx > 0$ (right). An η_{det} asymmetry can be seen in the bottom right plot.

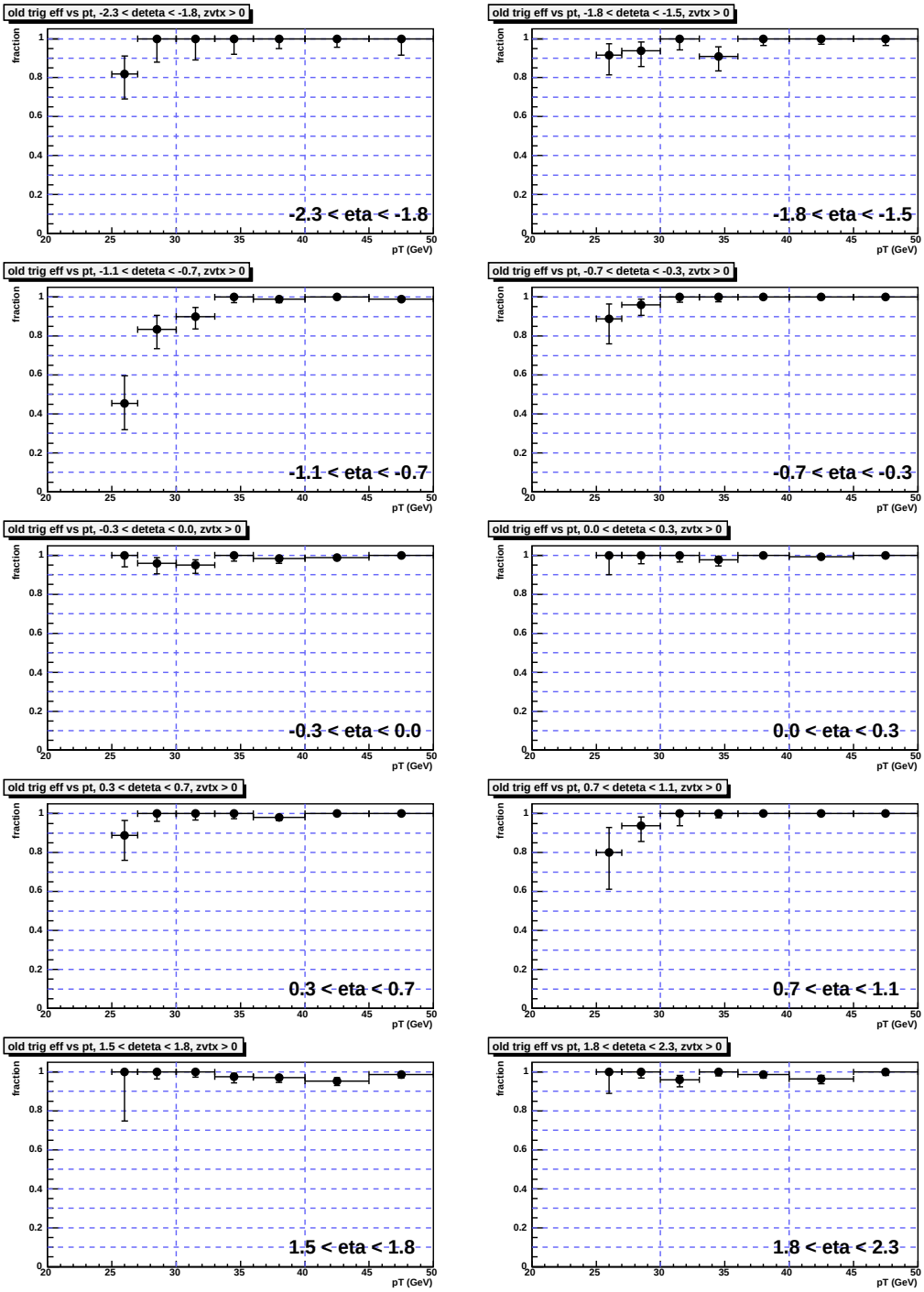

Fig. 6.11: Summary of electron trigger efficiency in bins used in PMCS for runs $\leq$ 178721 and $zvtx < 0$. Plots are shown as a function of electron E_T (GeV) with η_{det} range displayed on each plot.

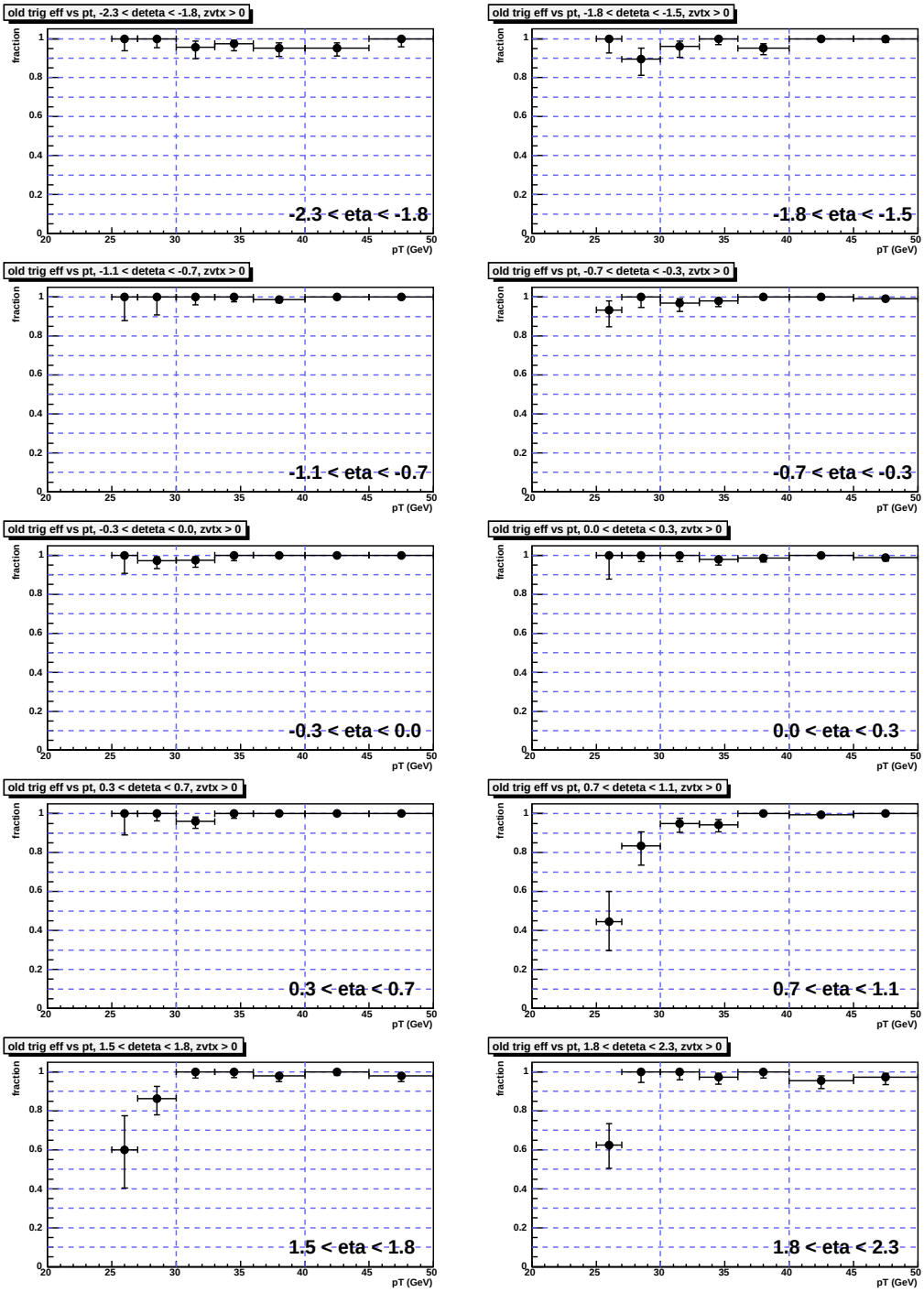

Fig. 6.12: Summary of electron trigger efficiency in bins used in PMCS for runs $\leq$ 178721 and $zvtx > 0$. Plots are shown as a function of electron E_T (GeV) with η_{det} range displayed on each plot.

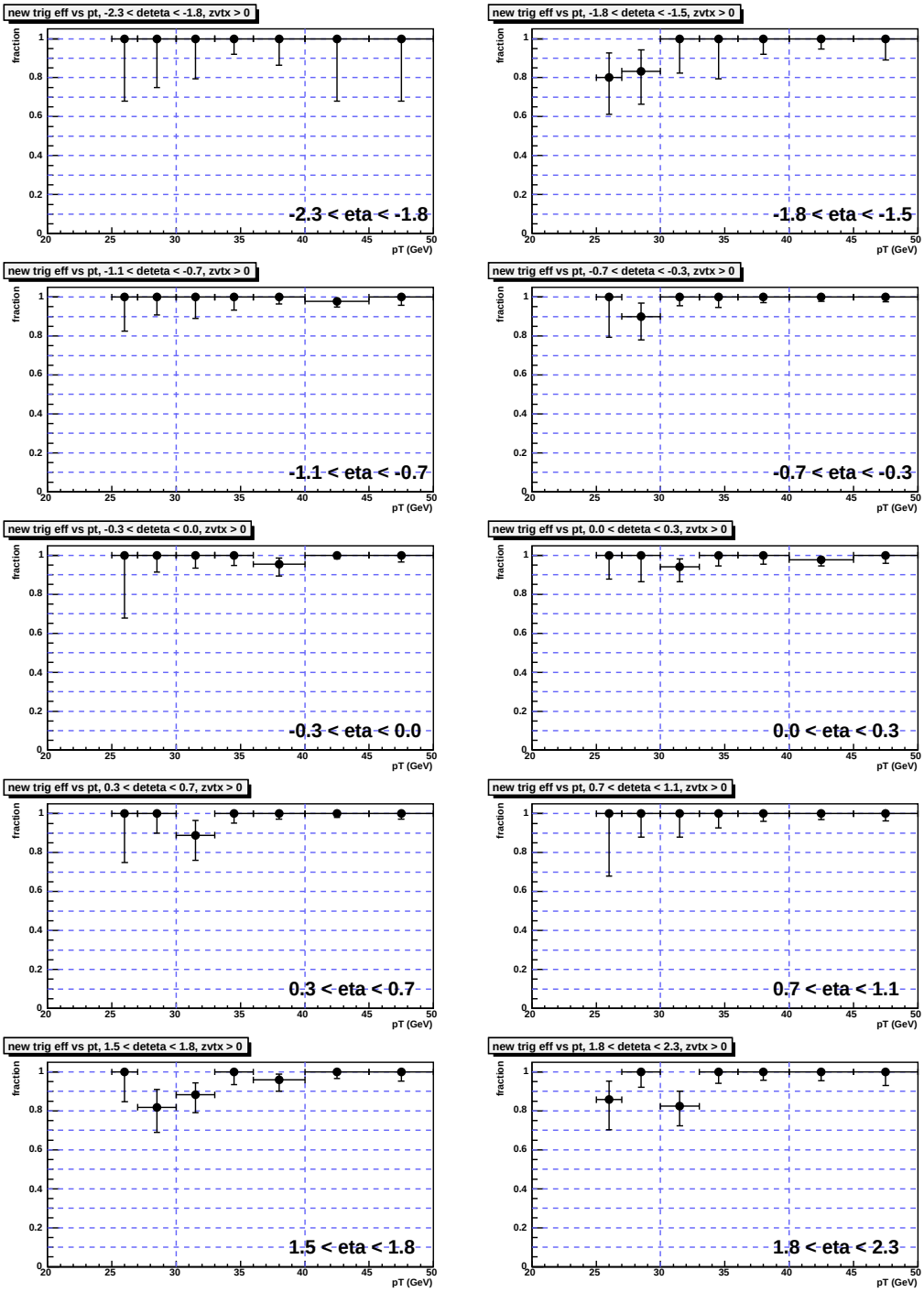

Fig. 6.13: Summary of electron trigger efficiency in bins used in PMCS for runs $\geq$ 178722 and $zvtx < 0$. Plots are shown as a function of electron E_T (GeV) with η_{det} range displayed on each plot.

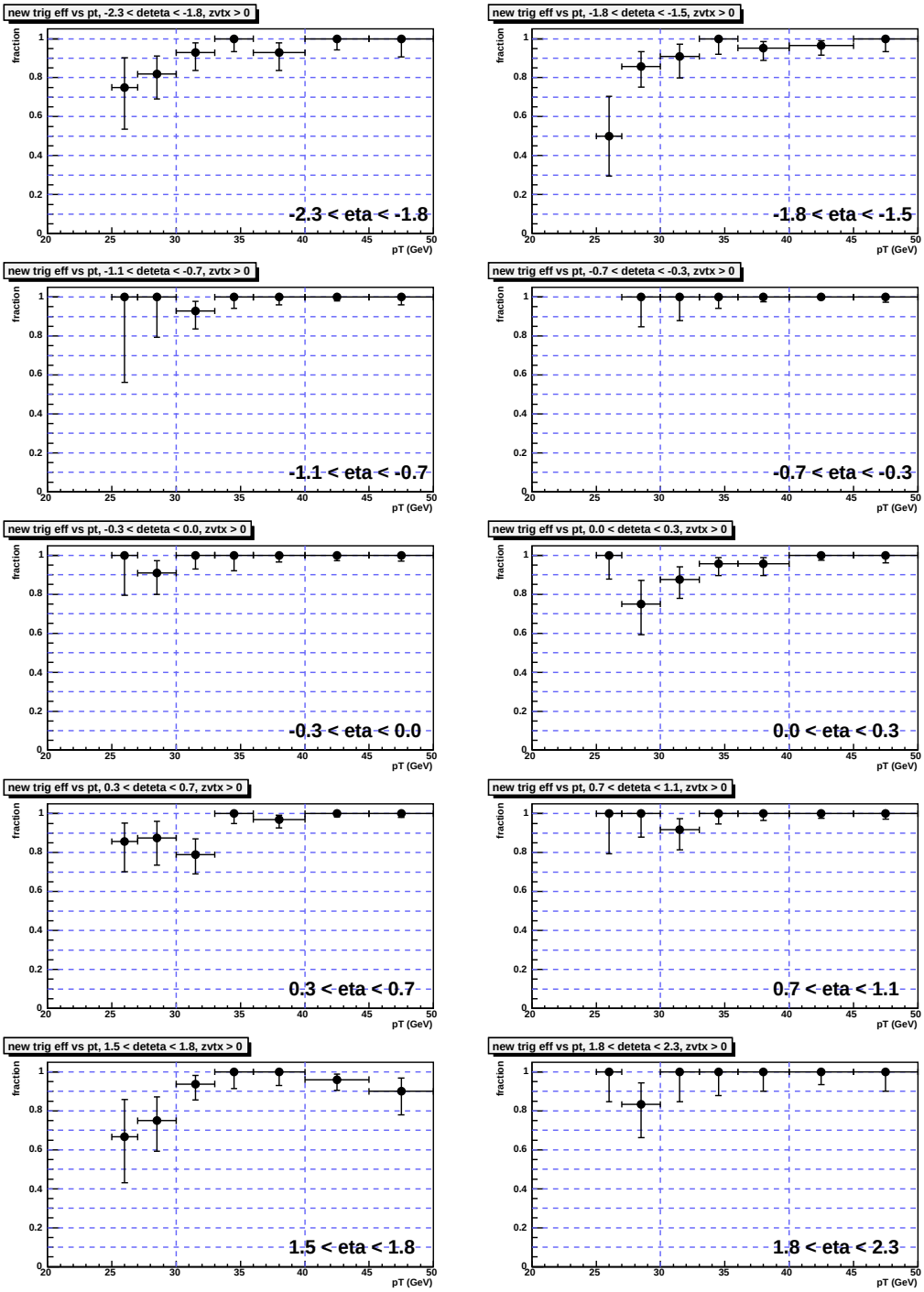

Fig. 6.14: Summary of electron trigger efficiency in bins used in PMCS for runs $\geq$ 178722 and $zvtx > 0$. Plots are shown as a function of electron E_T (GeV) with η_{det} range displayed on each plot.

6.2.5 Electron Likelihood Efficiency

The electron likelihood efficiency is defined as the fraction of events with the probe electron passing the likelihood cut over the total number of probes. See Section 4.5 for an explanation of the electron likelihood. The tag & probe method is used with the probe electron required to pass preselection, track match and trigger cuts to be considered. The average efficiency is $(90.7 \pm 0.3)\%$ for CC.

For the PMCS simulation and W candidate background subtraction, likelihood efficiency uses the same η_{det} and $zvtx$ binning as track match efficiency. The efficiency is fairly steady except for when $zvtx$ is far from zero. See Figure 6.15 for plots vs η_{det} for all z vertex bins.

Background is negligible in the tag & probe sample used in finding electron likelihood efficiency since the probe must already satisfy all other cuts. However, a conservative systematic error of 0.5% is assigned to the efficiency due to variations in the central E_T distribution and at the ϕ module boundaries. The likelihood efficiencies are shown as a function of electron E_T and *phimod* in Figure 6.16.

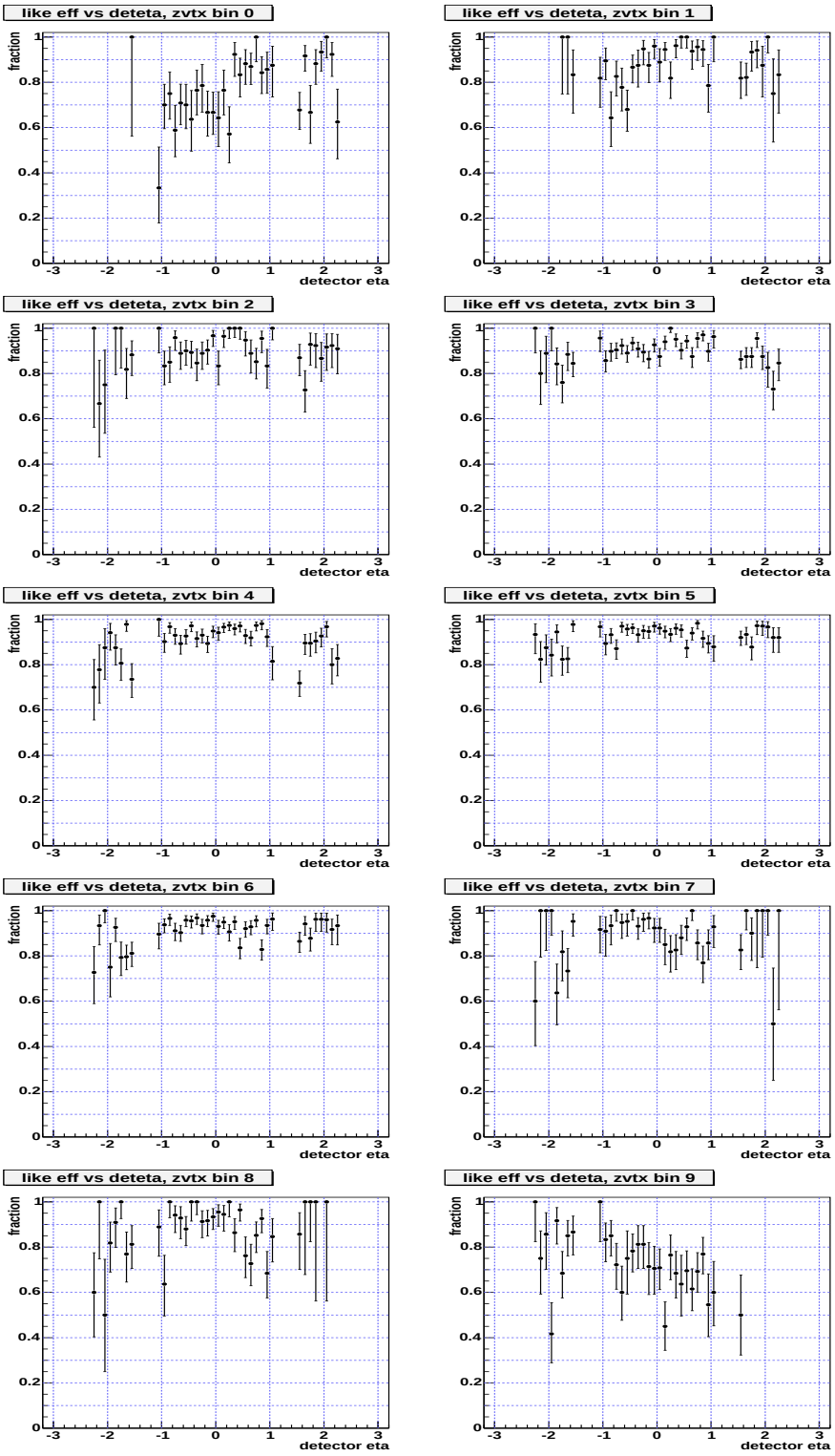

Fig. 6.15: Likelihood efficiency vs η_{det} in bins of $zvtx$ as used for W background subtraction and input into PMCS. Z vertex bins are, going left to right from top to bottom: $<$ -39, -39 to -30, -30 to -23, -23 to -10, -10 to 0, 0 to 10, 10 to 23, 23 to 30, 30 to 39, and $>$ 39 cm.

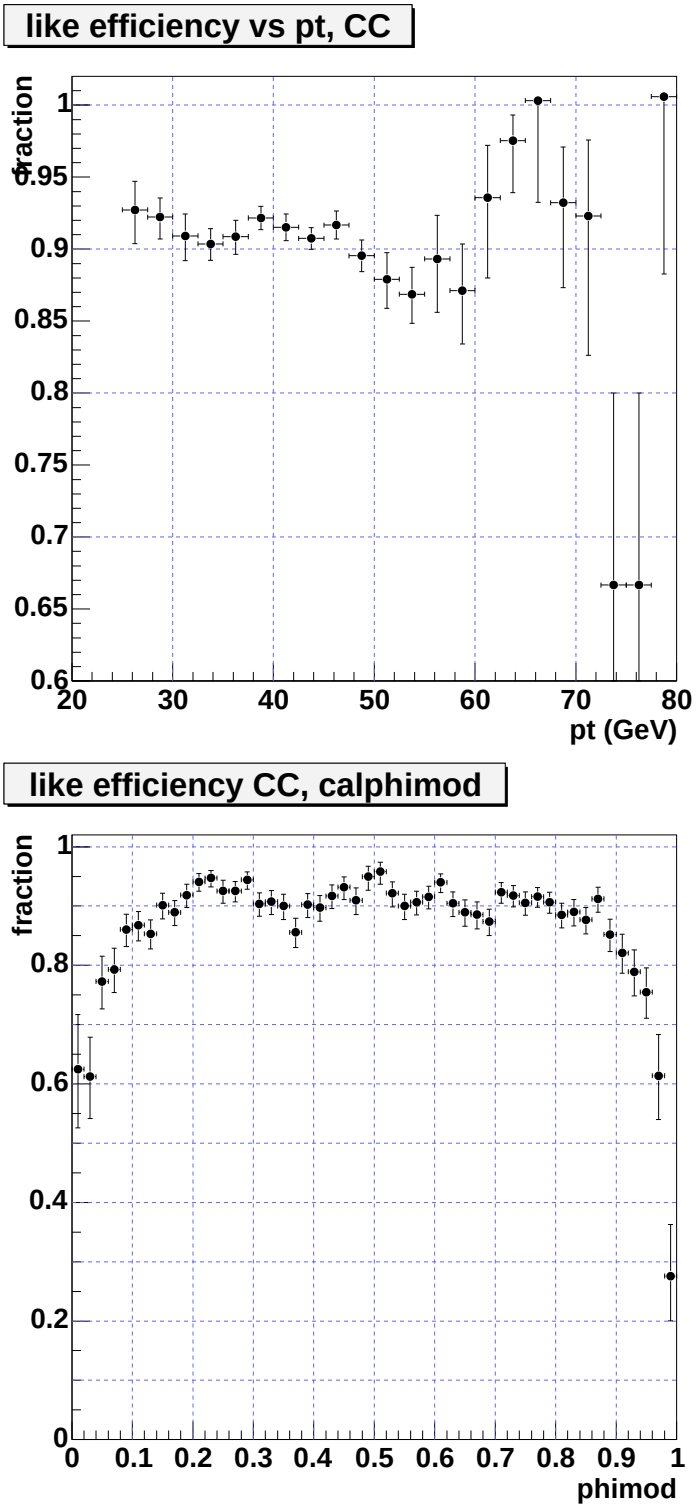

Fig. 6.16: Likelihood efficiency vs. E_T (top) and *phimod* (bottom) for the central region.

6.2.6 Full Monte Carlo Checks of Tag & Probe Method

To check our tag & probe method of determining efficiency we use 247,000 $Z/\gamma^* \rightarrow ee$ full Monte Carlo events generated using dØgstar (described in Section 5.4). There is a potential for the tag & probe method of calculating the efficiency of a cut in data to bias the result due to both electrons sharing the same decay vertex and their tendency to be separated by very nearly 180 degrees in ϕ. This bias can be checked by comparing the efficiency obtained using the tag & probe method in the full Monte Carlo to the 'actual' efficiency of the generated electrons. The 'actual' efficiency is defined as the fraction of all generated electrons satisfying the requirements of the probe which also pass the cut requirement of the efficiency.

Figures 6.17 and 6.18 are comparisons for preselection efficiency vs. η_{det} and *phimod*. The full Monte Carlo suggests a small upward bias due to the requirement of a track near the probe in our tag & probe method as indicated by the blue dashed line in the Figures. The actual efficiency drops off in the bins (-1.05,1.00) and (1.00,1.05) much more than with our preselection efficiency method. The cause of this disagreement appears to be from the necessity of having a tight electron as a tag. If at least one tight electron is required in an event, these drops disappear. With this requirement, the efficiency as seen in Figure 6.19 is consistent with our method although biased slightly higher due to the tight electron requirement. Combining the requirement of a tag electron and the requirement of a track near the probe indicates an upward bias of 0.4% in the tag & probe method for preselection efficiency.

Shown in Figure 6.20, is a comparison of the tag & probe method for calculating the track matching efficiency and the actual electron efficiency divided into bins of η_{det} and $zvtx$ (see Section 6.2.3). In bins of $zvtx$, agreement is quite good. Plotting track matching efficiency as a function of η_{det} only, shown in Fig-

ure 6.21, indicates a measured efficiency greater than the actual value for EC. This is due to the bias caused by the tag and probe electrons sharing the same decay vertex and illustrates one reason why z vertex binning is important. With z vertex binning, as input into PMCS, no bias in the tag & probe method for track match efficiency is indicated.

Figure 6.22 shows good agreement for our tag & probe method for likelihood efficiency divided into bins of η_{det} and $zvtx$ (see Section 6.2.5). Likelihood efficiency as a function of η_{det} only, shown in Figure 6.23, also shows no bias in the tag & probe method for electron likelihood efficiency.

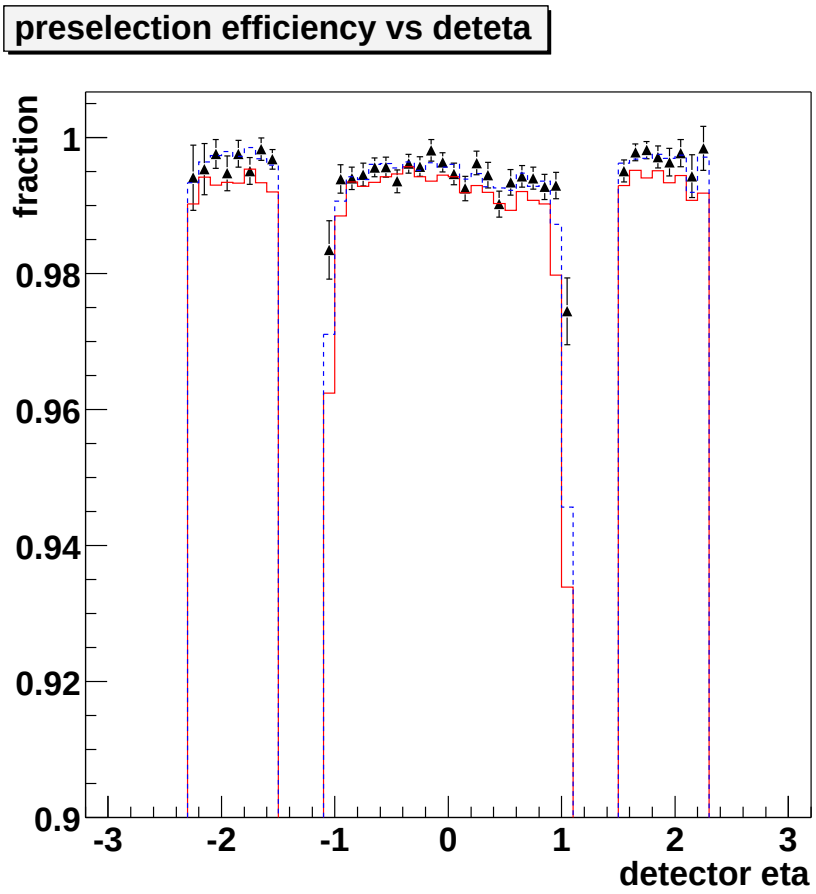

Fig. 6.17: A comparison of preselection efficiency vs η_{det} using the full Monte Carlo simulation. The points are for the preselection efficiency tag & probe method and the histograms are actual efficiencies. The blue dashed histogram is with a track match with $p_T > 27$ and the red is with no track required.

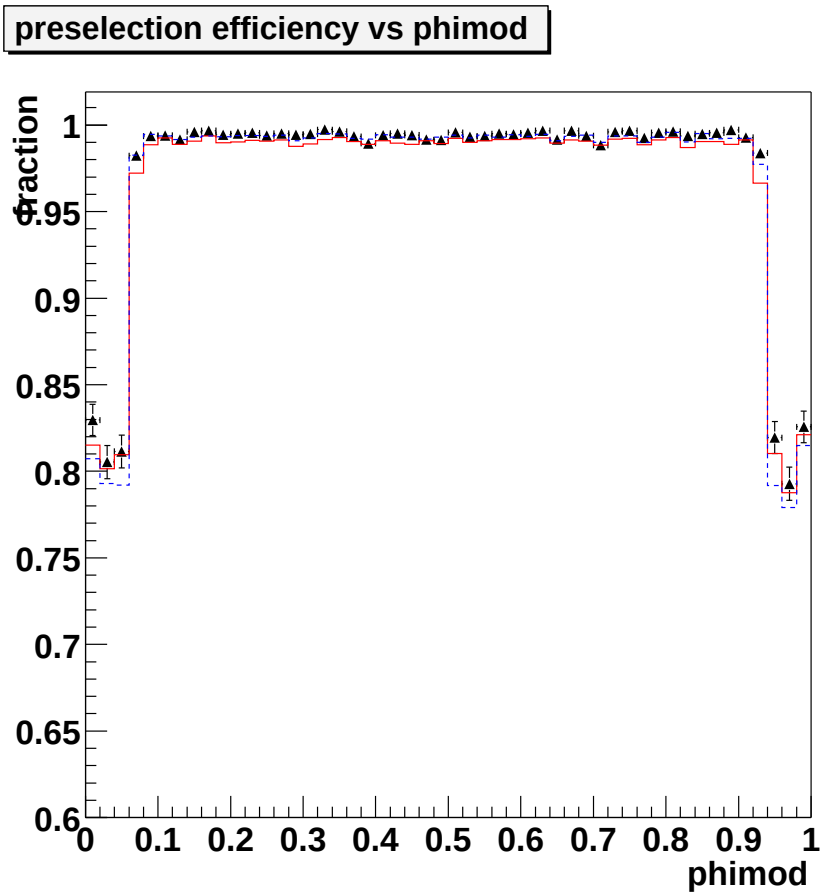

Fig. 6.18: A comparison of preselection efficiency vs *phimod* using the full Monte Carlo simulation. The points are for the preselection efficiency tag & probe method and the histograms are actual efficiencies. The blue dashed histogram is with a track match with $p_T > 27$ and the red is with no track required.

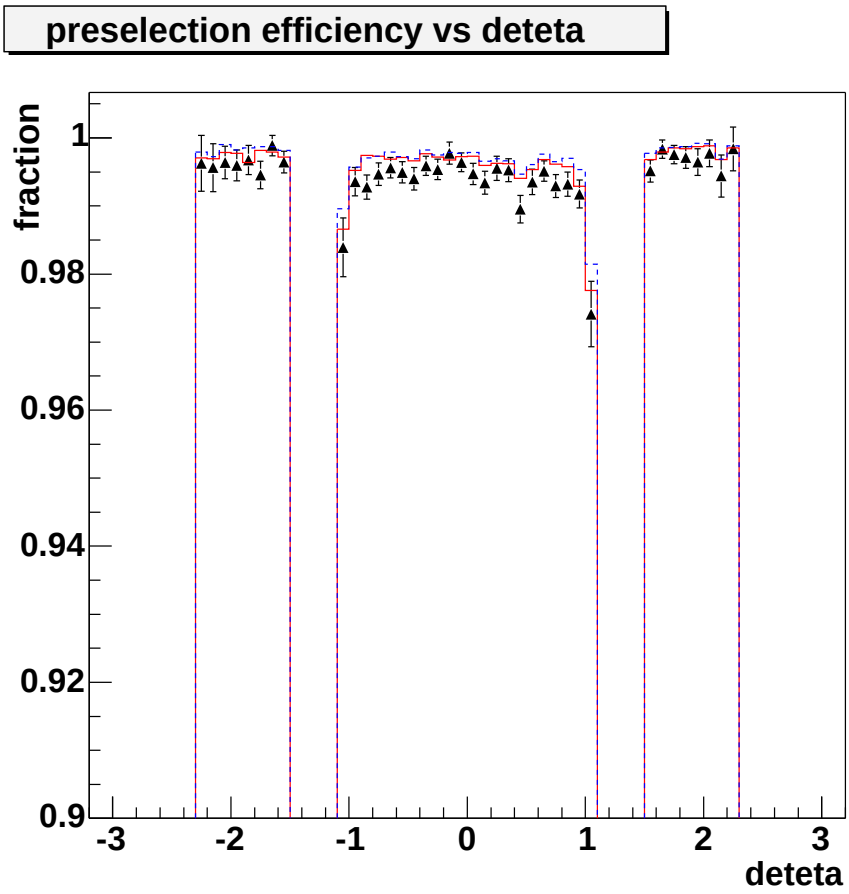

Fig. 6.19: A comparison of preselection efficiency vs η_{det} using the full Monte Carlo simulation. The points are for the preselection efficiency tag & probe method and the histograms are actual efficiency with an additional requirement of at least one tight electron in the event. The better agreement at high CC η_{det}, compared to Figure 6.17, suggests the tag & probe method is biased by the requirement of a tight electron for the tag.

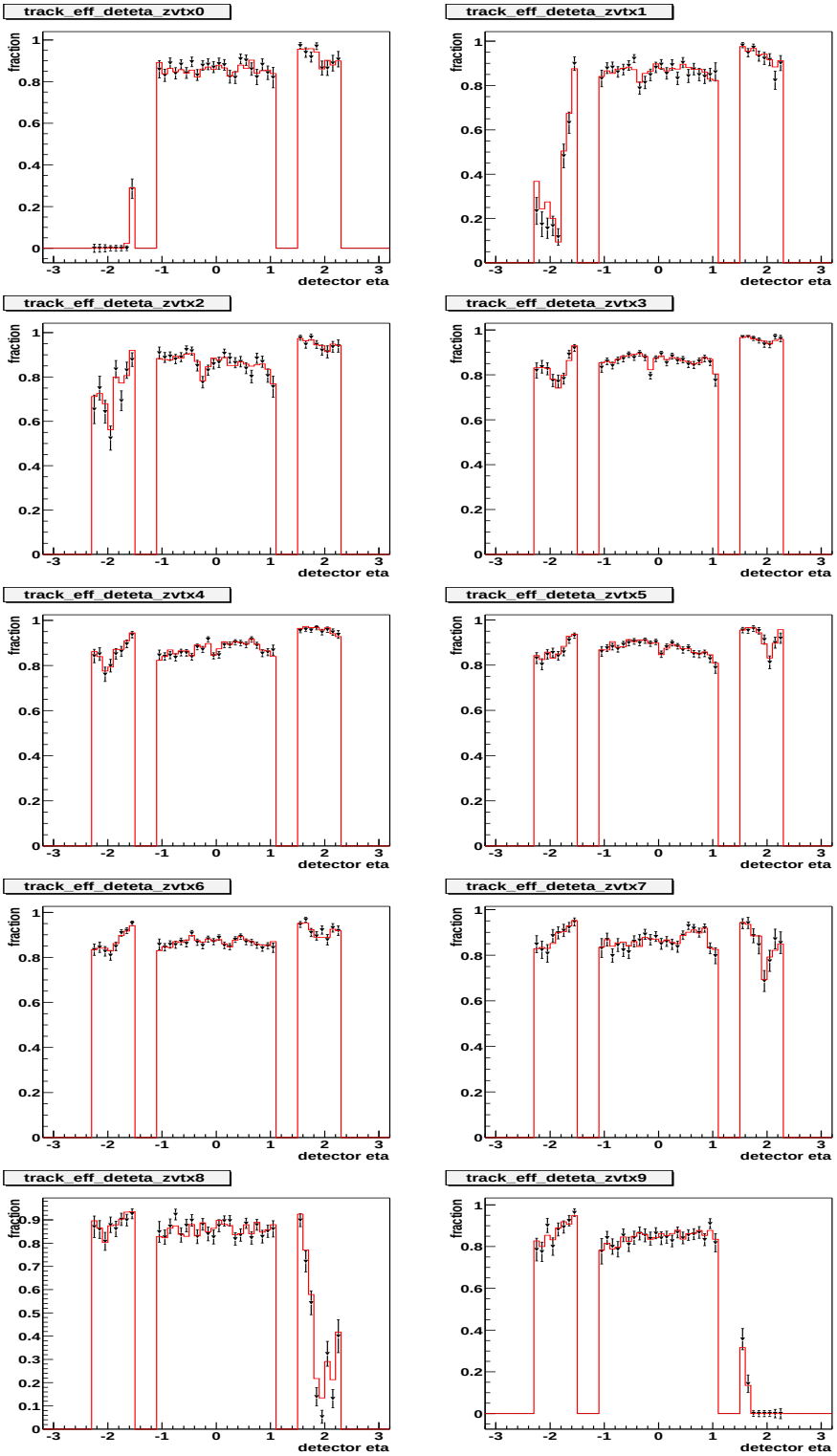

Fig. 6.20: A comparison for track matching efficiency vs η_{det} in $zvtx$ bins using the full Monte Carlo simulation. The points are for the track efficiency tag & probe method and the histograms are actual efficiencies. Z vertex bins are, going left to right from top to bottom: $<$ -39, -39 to -30, -30 to -23, -23 to -10, -10 to 0, 0 to 10, 10 to 23, 23 to 30, 30 to 39, and $>$ 39 cm.

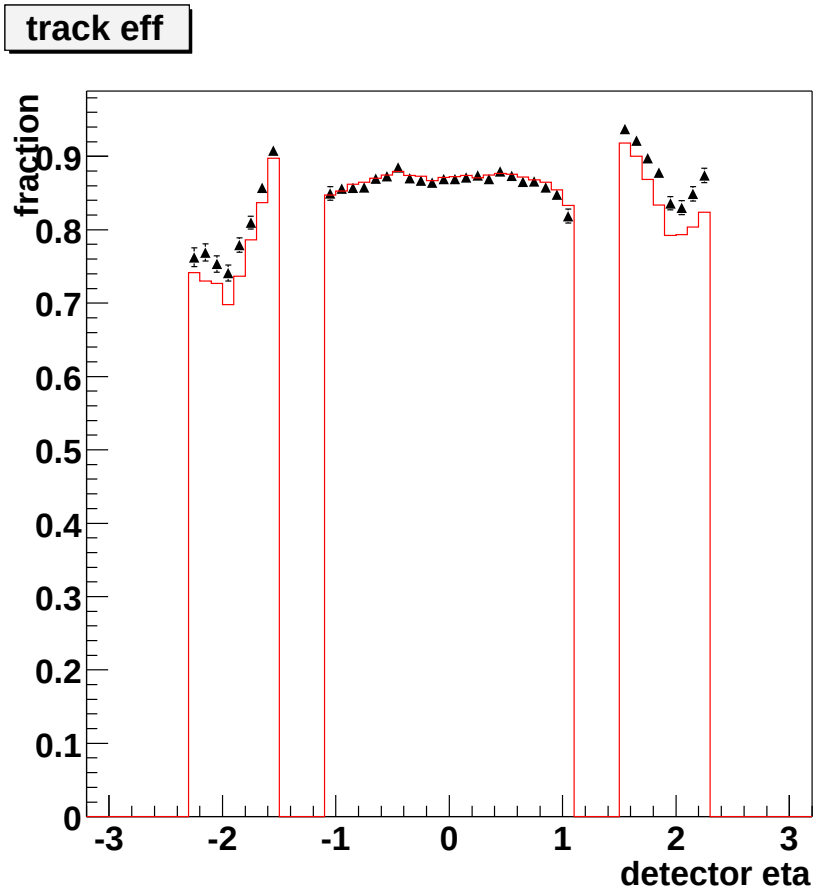

Fig. 6.21: A comparison of track matching efficiency vs electron η_{det} for all $zvtx$ using the full Monte Carlo simulation. The points are for the track efficiency tag & probe method and the histogram is actual efficiency. Disagreement in EC is from $zvtx$ bias.

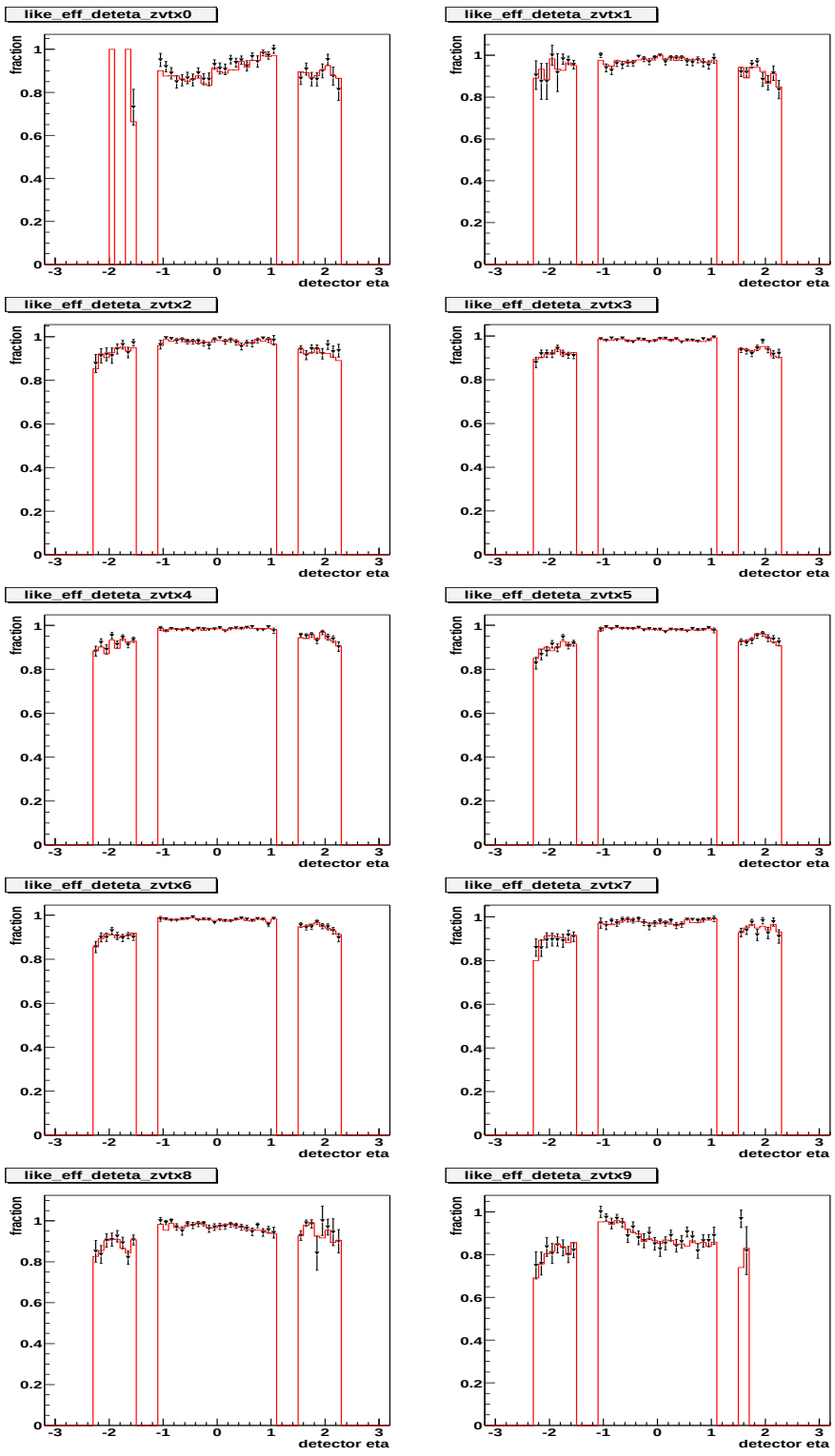

Fig. 6.22: A comparison for likelihood efficiency vs η_{det} in $zvtx$ bins using the full Monte Carlo simulation. The points are for the track efficiency tag & probe method and the histograms are actual efficiencies. Z vertex bins are, going left to right from top to bottom: < -39, -39 to -30, -30 to -23, -23 to -10, -10 to 0, 0 to 10, 10 to 23, 23 to 30, 30 to 39, and > 39 cm.

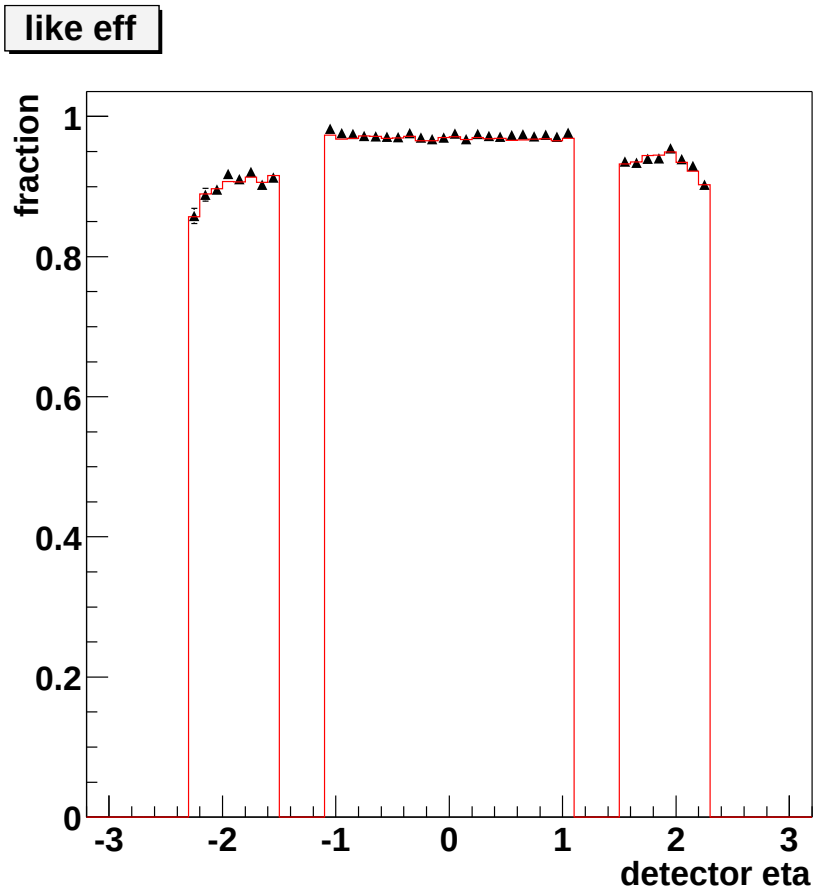

Fig. 6.23: A comparison of likelihood efficiency vs η_{det} for all vertex z using the full Monte Carlo simulation. The points are for the likelihood efficiency tag & probe method and the histogram is actual efficiency.

6.3 Data-PMCS Comparisons

PMCS is compared to data after acceptance and efficiency effects are applied. Z candidates are compared to a sum of PMCS and QCD background estimations with the amount of background for each bin indicated by the green shaded histogram. Agreement with data in the central region is quite good overall. For W candidates, plots are arranged differently; plots compare the number of W events after QCD background subtraction directly to PMCS. To get an idea of the amount of background present, all W candidates before background subtraction are also shown in the plot. This representation for W events is preferable because it is possible for background estimation to be negative in some bins where there is a large error due to the dependence of the calculation on the likelihood efficiency derived from Z data statistics. For W candidates, the agreement is good in the central region with the possible exceptions of transverse mass and missing E_T.

For Z candidate data to PMCS comparisons of invariant mass, electron E_T, electron η_{det} and electron $\eta_{physics}$, see Figures 6.24 to 6.26 for CC-CC and Figures 6.27 to 6.29 for CC-EC. For W candidate comparisons of electron E_T, missing E_T, transverse invariant mass, electron η_{det} and electron $\eta_{physics}$ see Figures 6.30 to 6.33. Dots are for the data being compared, solid lines are for PMCS and dashed lines are for W candidates before background subtraction.

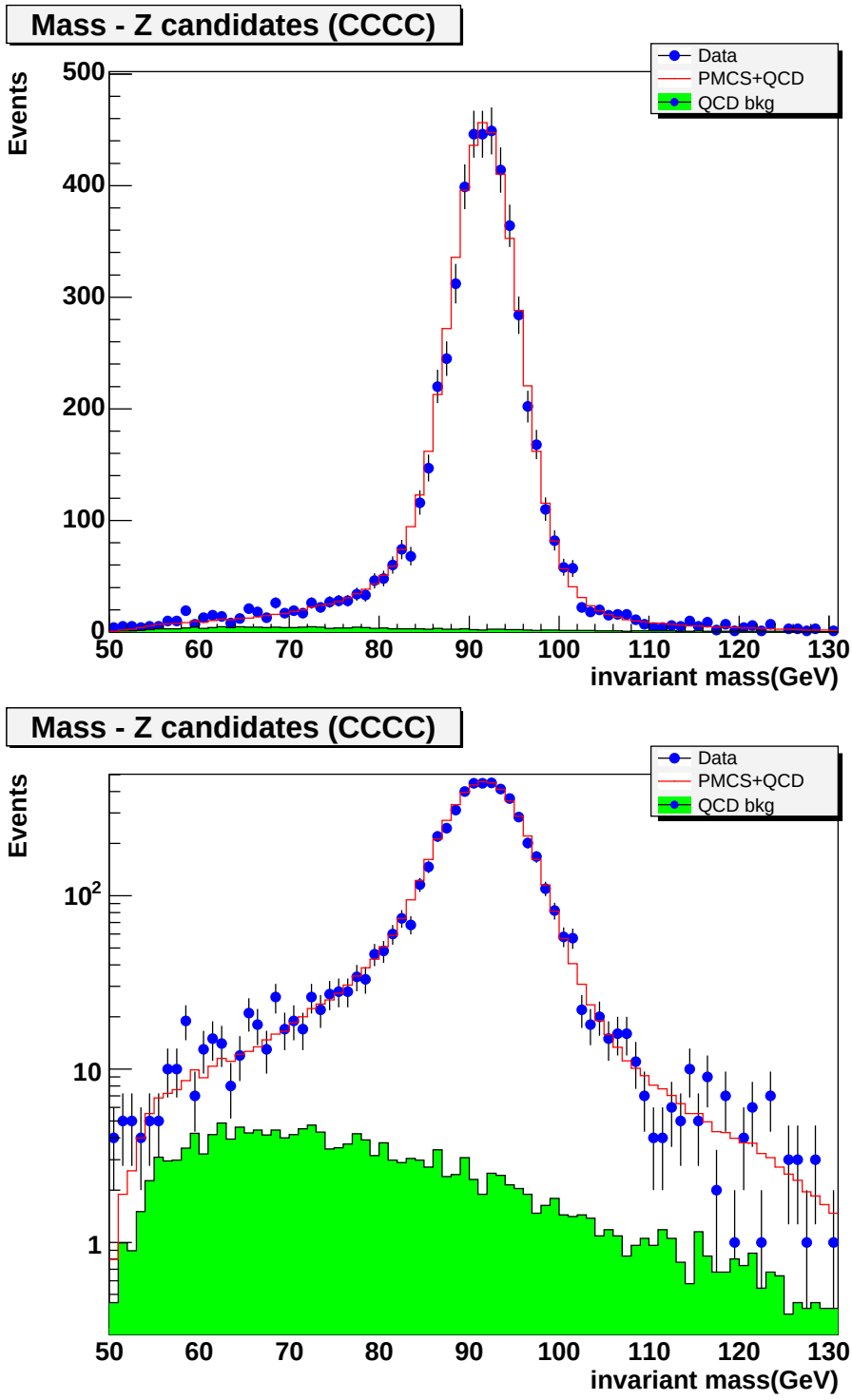

Fig. 6.24: PMCS to data comparison of Z candidate invariant mass for CC-CC events shown with a linear scale (top) and log scale (bottom)

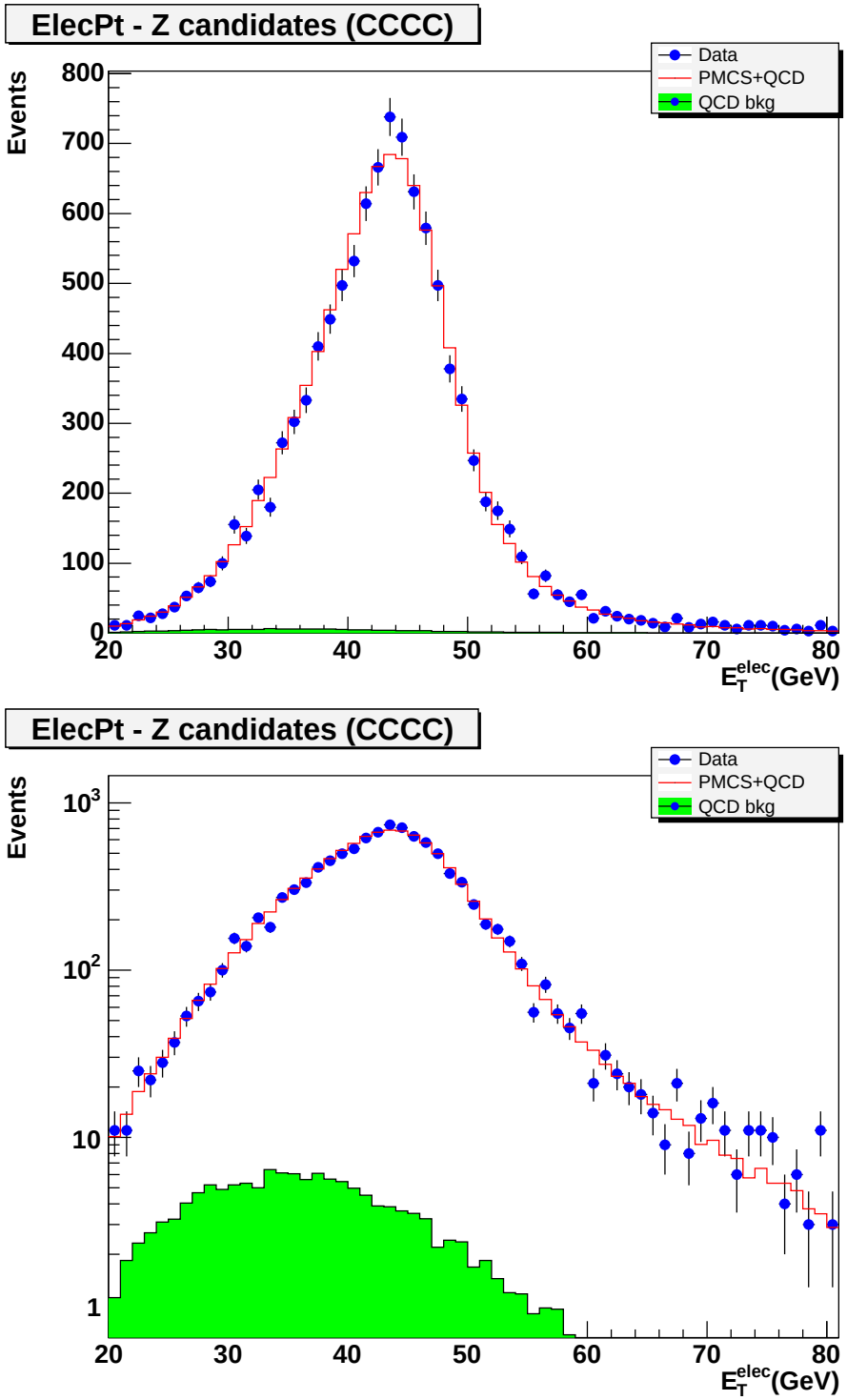

Fig. 6.25: PMCS to data comparison of Z candidate electron E_T for CC-CC events shown with a linear scale (top) and log scale (bottom) The E_T cut is extended down to 20 GeV for this plot only in order to ensure reasonable behavior.

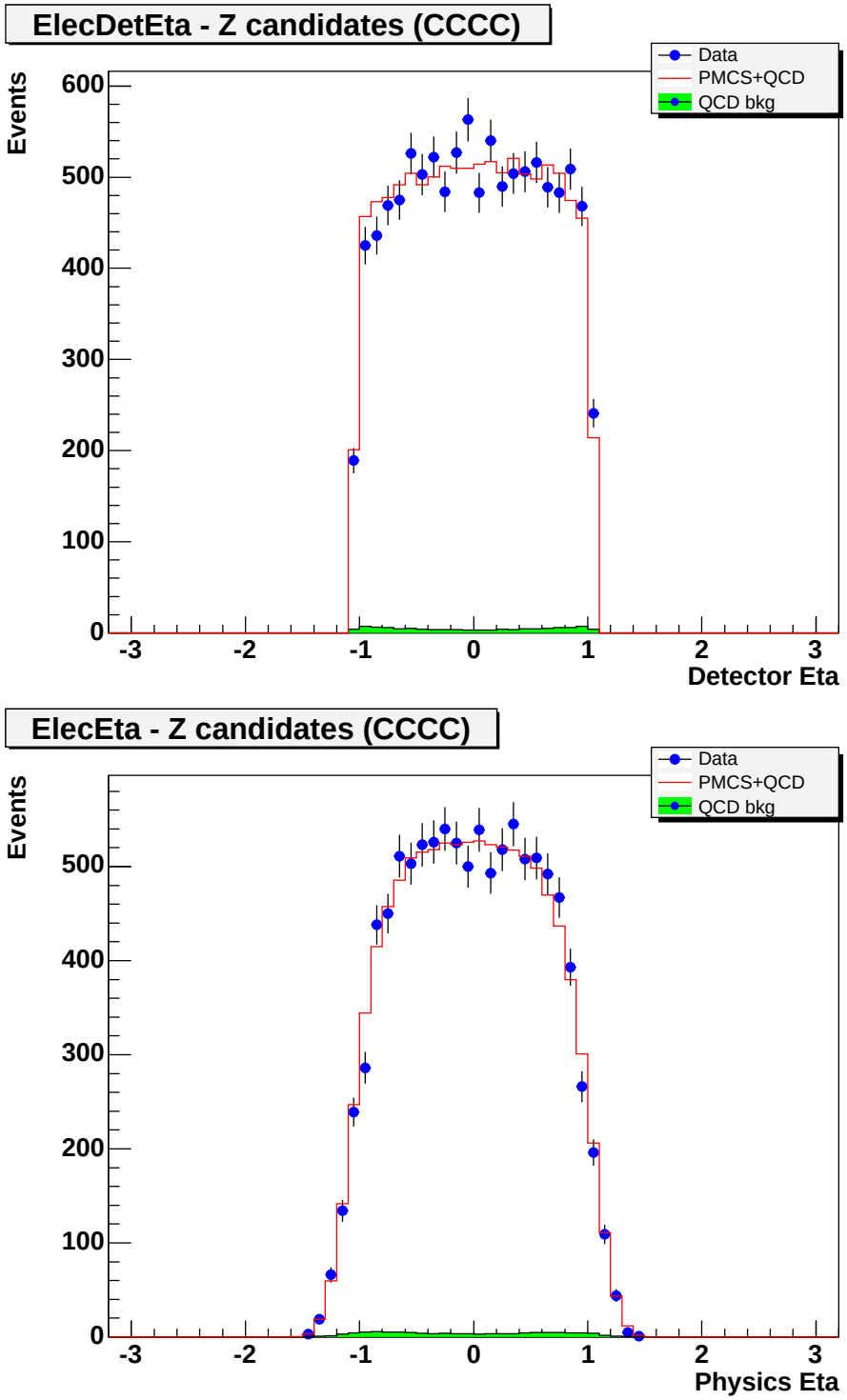

Fig. 6.26: PMCS to data comparison of Z candidate CC-CC electron η_{det} (top) and $\eta_{physics}$ (bottom) .

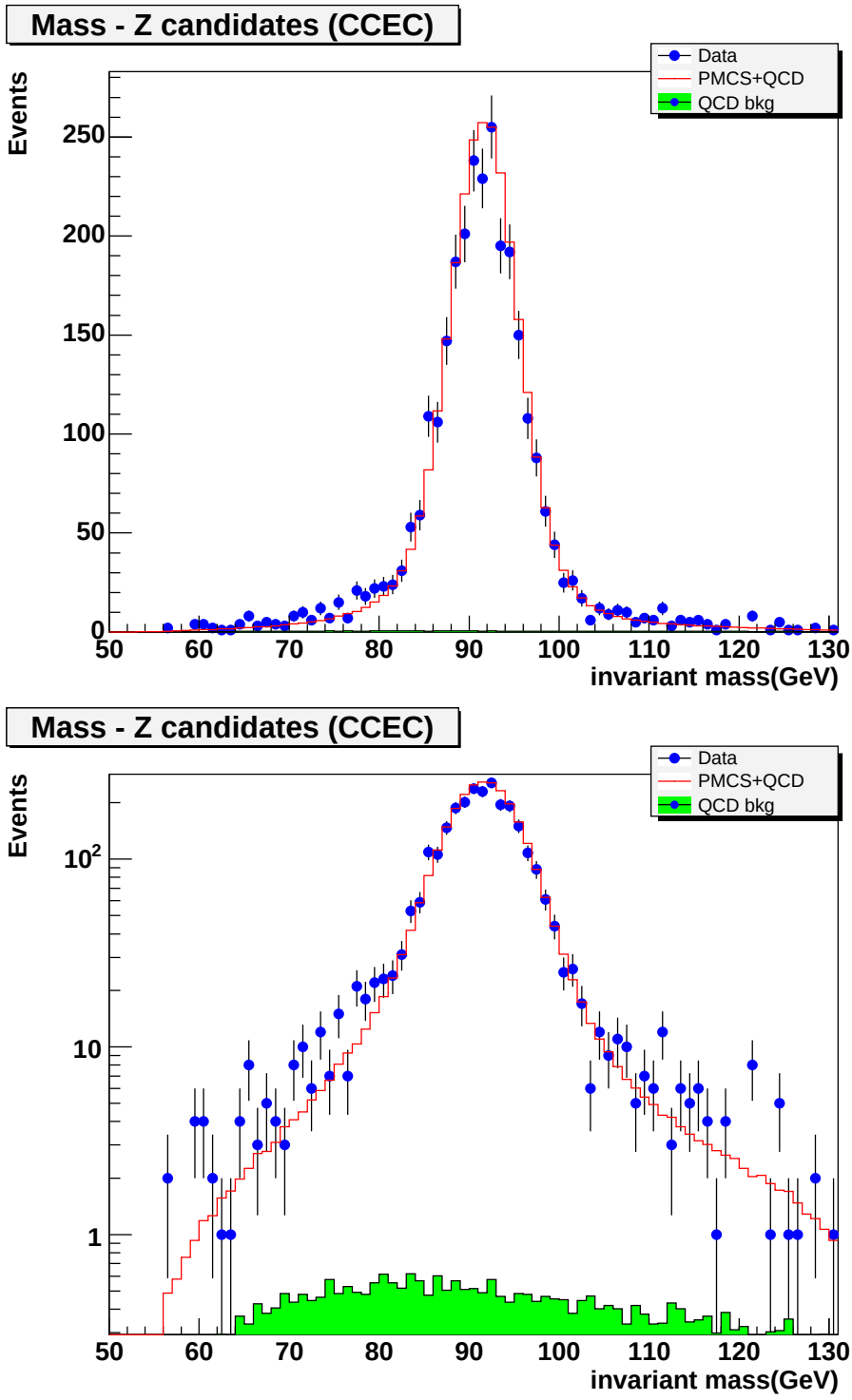

Fig. 6.27: PMCS to data comparison of Z candidate invariant mass for CC-EC events shown with a linear scale (top) and log scale (bottom)

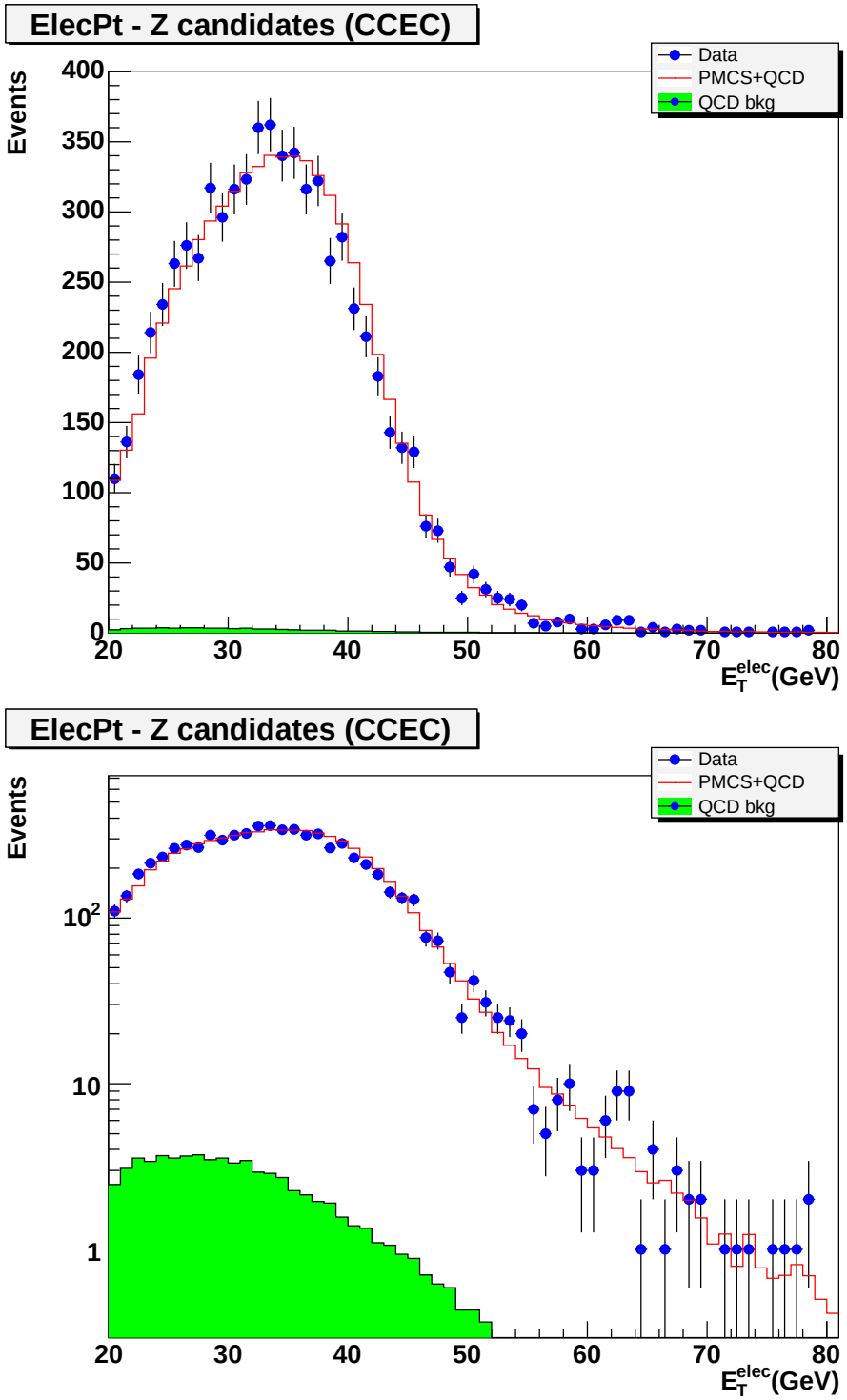

Fig. 6.28: PMCS to data comparison of Z candidate electron E_T for CC-EC events shown with a linear scale (top) and log scale (bottom) The E_T cut is extended down to 20 GeV for this plot only in order to ensure reasonable behavior.

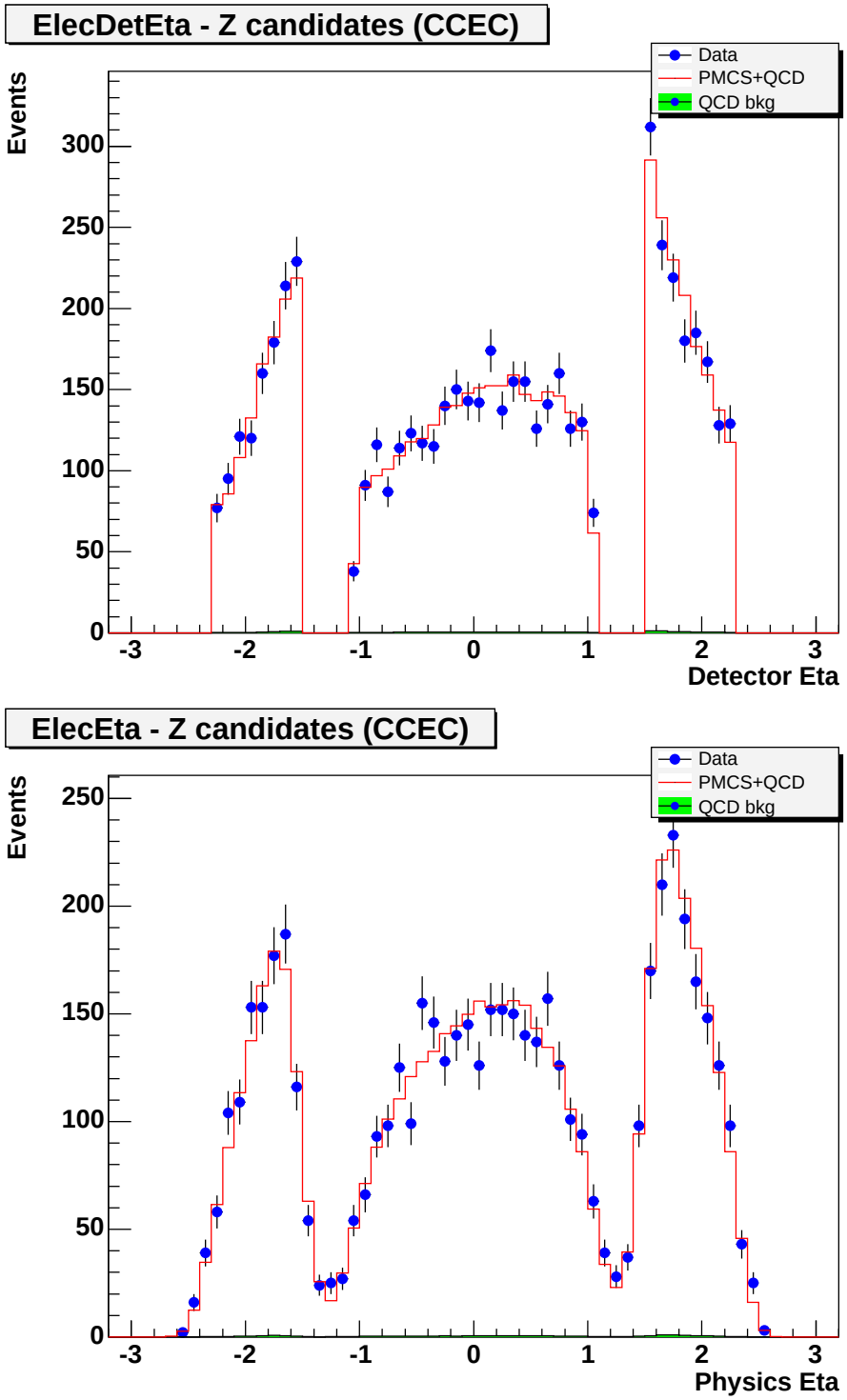

Fig. 6.29: PMCS to data comparison of Z candidate CC-EC electron η_{det} (top) and $\eta_{physics}$ (bottom) .

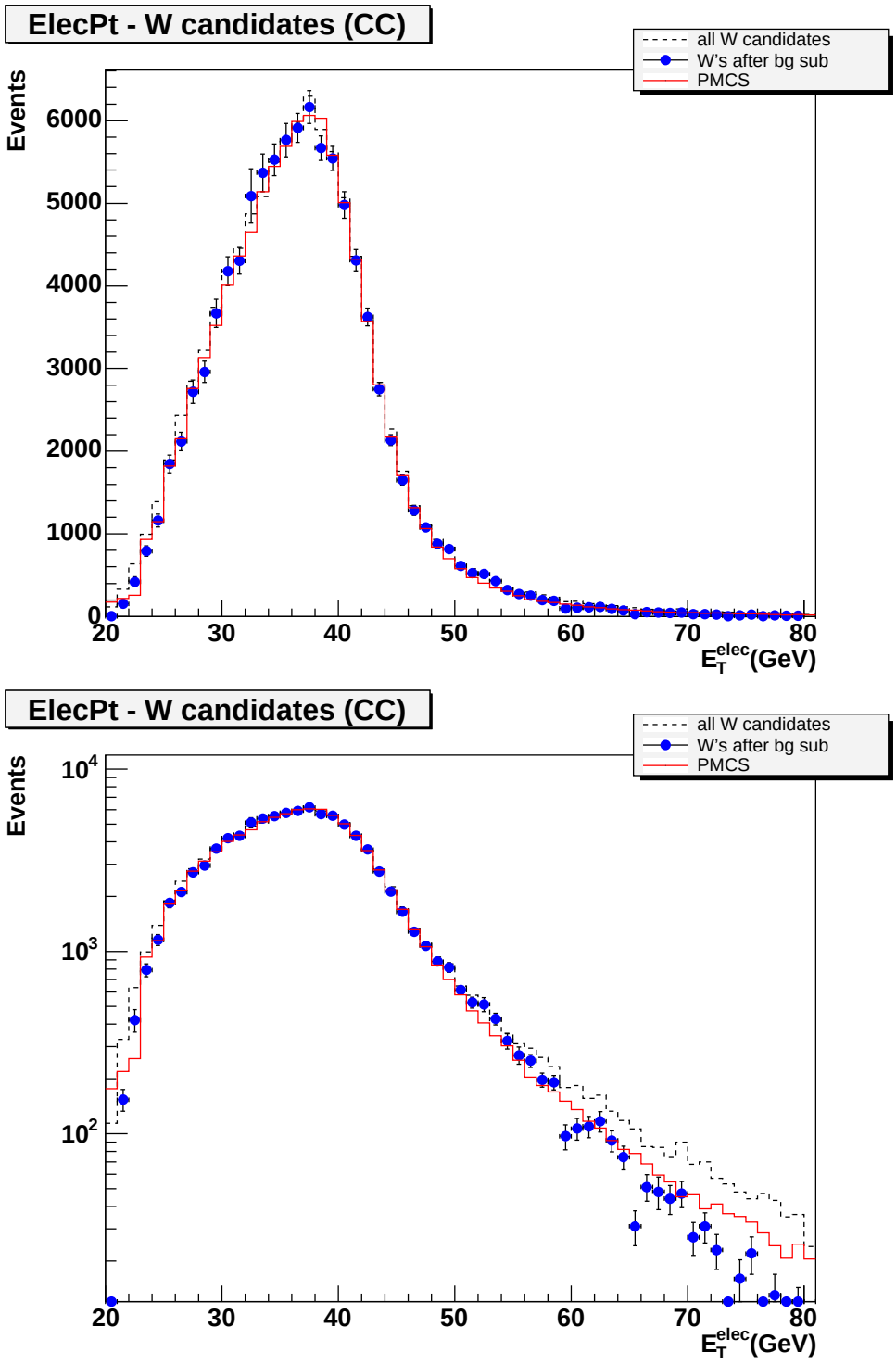

Fig. 6.30: PMCS to data comparison of W background subtracted electron E_T for CC using a linear scale (top) and log scale (bottom). W candidates before background subtraction are represented by the black dashed histogram. The E_T cut is extended down to 20 GeV for this plot only in order to ensure reasonable behavior.

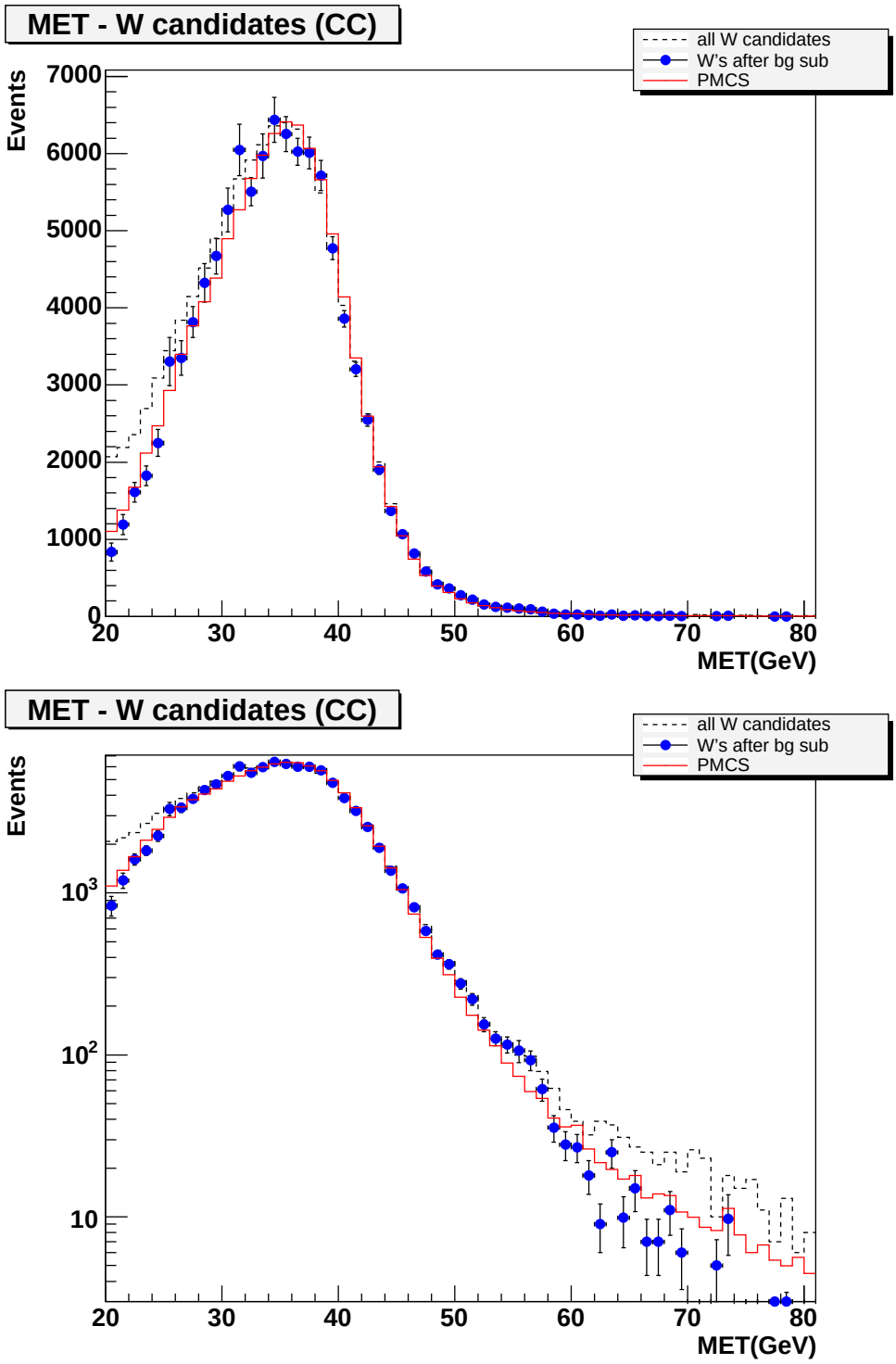

Fig. 6.31: PMCS to data comparison of W background subtracted missing E_T for CC using a linear scale (top) and log scale (bottom). W candidates before background subtraction are represented by the black dashed histogram. The missing E_T cut is extended down to 20 GeV for this plot only in order to ensure reasonable behavior.

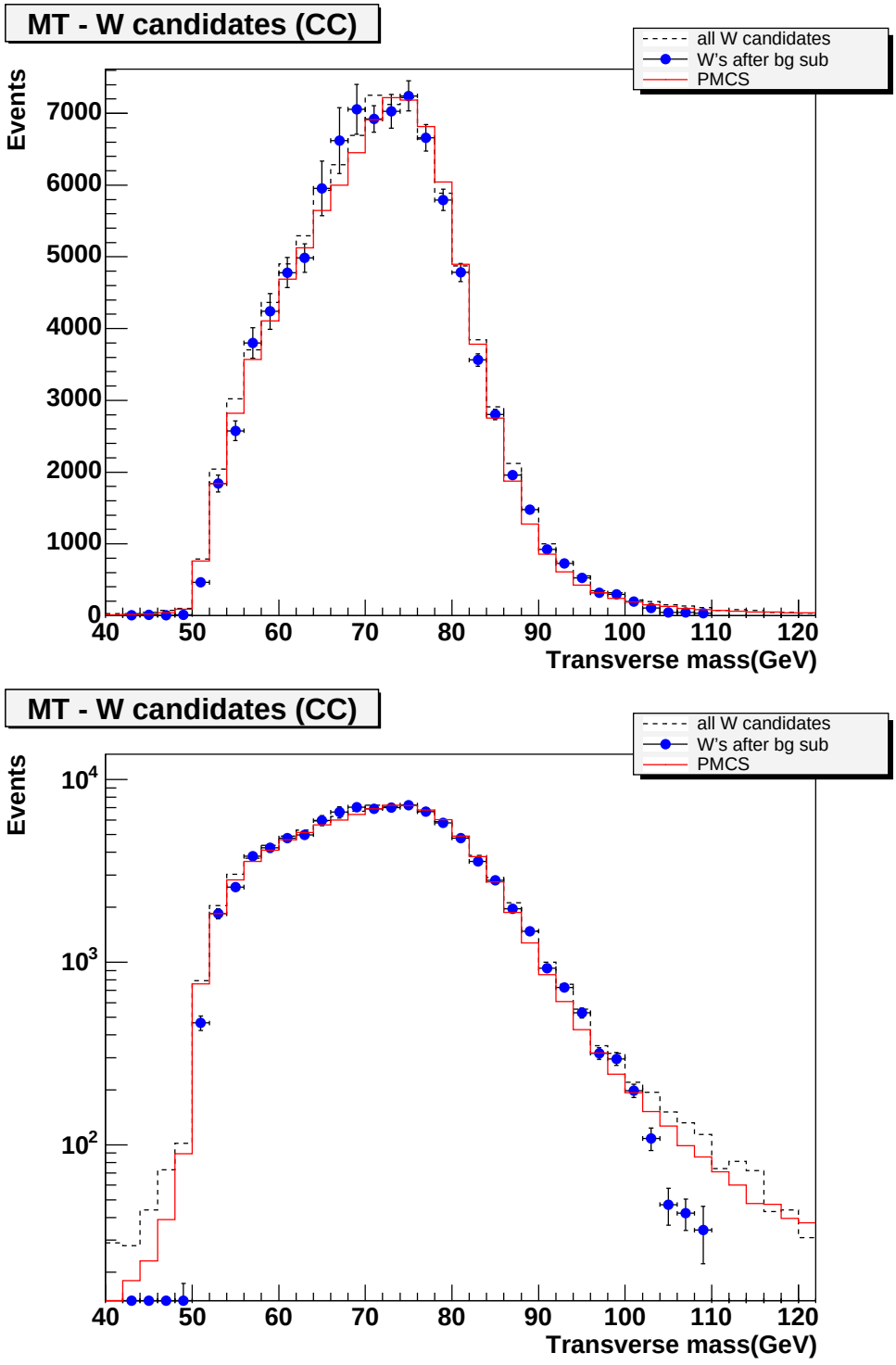

Fig. 6.32: PMCS to data comparison of W background subtracted transverse mass for CC using a linear scale (top) and log scale (bottom). W candidates before background subtraction are represented by the black dashed histogram.

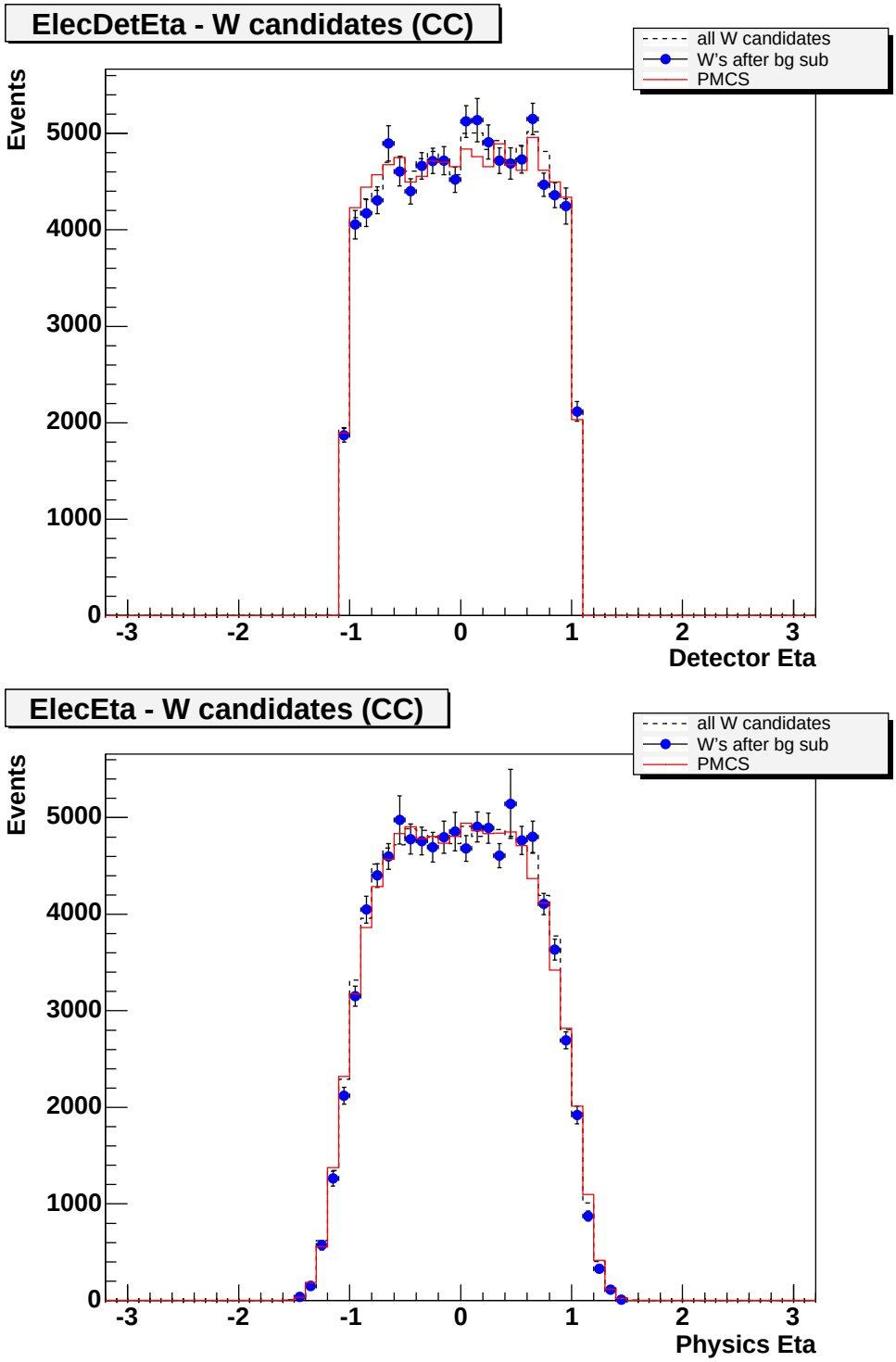

Fig. 6.33: PMCS to data comparison of W background subtracted electron η_{det} (top) and $\eta_{physics}$ (bottom). W candidates before background subtraction are represented by the black dashed histogram.

Acceptance	
$W \to e\nu$ (CC)	0.18254 ± 0.00007
$Z/\gamma^* \to ee$ (CC-CC)	0.10161 ± 0.00008
$Z/\gamma^* \to ee$ (CC-EC)	0.05518 ± 0.00006
$Z/\gamma^* \to ee$ (both)	0.15678 ± 0.00009

Tab. 6.3: Acceptance values calculated with PMCS. The errors shown reflect statistical uncertainties due to the number of generated events used in the sample. A complete accounting of the uncertainty on the acceptance values can be found in Section 6.5.

6.4 Acceptance Results

The acceptance values are summarized in Table 6.3. This is after all event selection criteria including preselection, fiducial, kinematic and additional electron ID requirements are simulated in PMCS.

6.5 Uncertainty Estimates

The uncertainty of the MC acceptance value is assumed to arise solely from the uncertainties of the inputs into the MC simulation. The following sources of uncertainty are considered:

- Positional resolution in η and ϕ (EC only) of the electron, and the *phimod* shift applied to CC electrons.
- Electron energy scale: slope and offset parameters for the CC and EC calorimeter regions.
- Electron energy resolution for the CC and EC calorimeter regions, which is parameterized in three terms: *constant*, *sampling*, and *noise*. The sampling term is considered a fixed value with no error. The noise term is also considered fixed with no error: its contribution to the energy resolution is very small for the electron energy range in this analysis. Therefore only the

uncertainty on the constant term affects the uncertainty on the acceptance value.

- Hadronic energy scale: slope and offset parameters. Only the slope parameter is considered in the uncertainty estimate. As discussed in Section 5.6.5, the offset parameter (and its error) is very close to zero, so it has been set to zero and is considered to have no error.

- Hadronic energy resolution, which is parameterized in three terms: *constant*, *sampling*, and *noise*. The noise term is small relative to the others, and is considered fixed (at zero) with no error.

- Underlying Event

- Electron preselection, electron track-match, electron ID, and electron trigger efficiencies. These have both statistical and systematic uncertainties.

- Parton distribution functions.

6.5.1 Uncertainty from the Smearing Parameters

For the case of the smearing parameters, the uncertainty on the acceptance value due to the uncertainty of each parameter is estimated by independently varying each parameter up and down by one sigma of its estimated uncertainty and noting the effect on the resulting acceptance value. Results are shown in Table 6.4.

By varying the parameters independently, any correlations between parameters have been ignored. Significant correlation is expected only between the electron energy scale slope and offset parameters. Due to the method used to determine these parameters (see Section 5.6), the magnitude of the correlation is difficult to determine. Therefore, to avoid underestimating this source of uncertainty, these two parameters are considered fully correlated and added linearly

together before being added in quadrature with the other results. For each parameter tested, the largest shift in the result between the up and down checks is taken to be the symmetric uncertainty which is used to find the total uncertainty estimate shown in the last row of Table 6.4.

6.5.2 *phimod* Shift

The uncertainty on the final cross section due to the uncertainty of the *phimod* shift (Section 5.6.4) is handled separately from the other input parameters. It is estimated by varying the ϕ-fiducial cut in both data and PMCS by the ϕ resolution, and noting the variation in the cross section. However, the cut cannot be made looser, since this would accept electrons for which the energy scale is not well measured. Therefore, the cut is only made tighter, and the resulting uncertainty estimate is assumed to be symmetric. The result is shown in Table 6.4.

6.5.3 Statistical Uncertainty of the Efficiencies

The uncertainty on the acceptances due to the statistical uncertainties of the electron preselection, track-match, trigger and electron likelihood efficiencies is determined by calculating the acceptance values many times, each time with a different set of input efficiency distributions. Each set of input efficiency distributions is determined by simultaneously varying each nominal efficiency value by a Gaussian distribution of width given by the statistical error. The resulting acceptance values using 500 trials over the entire W and Z candidate samples are shown in Figure 6.34. These are fit to Gaussian distributions with the widths (one standard deviation) determining the uncertainty on the nominal acceptance values. The resulting relative uncertainties are 0.60% and 0.59% for the W and Z candidate acceptances (A_W and A_Z) respectively and 0.45% for the ratio of

	% change in acceptance				
	Z/γ^*			W	R
PMCS parameters	CC-CC	CCEC	both	CC	CC/both
phimod Shift	+0.71	+0.57	+0.64	+0.92	+0.28
EC Position Res ϕ (up)	N/A	+0.04	+0.01	N/A	-0.04
EC Position Res ϕ (down)	N/A	-0.28	-0.10	N/A	+0.10
CC Position Res η (up)	-0.07	+0.12	-0.01	+0.02	+0.02
CC Position Res η (down)	+0.24	-0.21	+0.08	+0.01	-0.07
EC Position Res η (up)	N/A	-0.26	-0.04	N/A	+0.04
EC Position Res η (down)	N/A	-0.12	-0.09	N/A	+0.09
CC EM-Scale Slope (up)	+0.17	+0.29	+0.21	+0.27	+0.05
CC EM-Scale Slope (down)	-0.13	-0.24	-0.17	-0.28	-0.12
EC EM-Scale Slope (up)	N/A	+0.63	+0.22	N/A	-0.22
EC EM-Scale Slope (down)	N/A	-0.56	-0.20	N/A	+0.20
CC EM-Scale Offset (up)	-0.04	+0.01	-0.02	+0.25	+0.28
CC EM-Scale Offset (down)	+0.09	-0.07	+0.03	-0.03	-0.06
EC EM-Scale Offset (up)	N/A	+0.53	+0.19	N/A	-0.19
EC EM-Scale Offset (down)	N/A	-0.25	-0.09	N/A	+0.09
CC EM Resolution (up)	+0.01	-0.06	-0.01	-0.06	-0.04
CC EM Resolution (down)	+0.09	-0.05	+0.04	+0.09	+0.05
EC EM Resolution (up)	N/A	-0.20	-0.07	N/A	+0.07
EC EM Resolution (down)	N/A	-0.06	-0.02	N/A	+0.02
FSR Radius (up)	+0.26	+0.40	+0.31	+0.09	-0.22
FSR Radius (down)	-0.25	-0.59	-0.37	-0.20	+0.17
Had. E-Scale Slope (up)	N/A	N/A	N/A	-0.13	-0.13
Had. E-Scale Slope (down)	N/A	N/A	N/A	+0.33	+0.33
Had E-Res Constant (up)	N/A	N/A	N/A	+0.03	+0.03
Had E-Res Constant (down)	N/A	N/A	N/A	+0.16	+0.16
Had E-Res Sampling (up)	N/A	N/A	N/A	+0.05	+0.05
Had E-Res Sampling (down)	N/A	N/A	N/A	-0.09	-0.09
CC $u_{\parallel}$ (up)	N/A	N/A	N/A	+0.06	+0.06
CC $u_{\parallel}$ (down)	N/A	N/A	N/A	+0.01	+0.01
Total PMCS Uncertainty	0.83	1.49	0.88	1.15	0.78

Tab. 6.4: Relative uncertainty on the MC acceptance value due to uncertainties on the inputs of the MC simulation.

acceptances ($A_R \equiv A_W/A_Z$). The ratio of acceptances corresponds to the statistical uncertainty of the acceptance due to efficiencies for the ratio of cross sections, R.

For the Z cross section, the uncertainty on the cross section due to the statistical uncertainty of the efficiencies is the same as the uncertainty on the acceptance value due to the statistical uncertainty of the measured preselection, track-match, trigger and electron likelihood efficiencies. Thus the relative uncertainty on the cross section is the same as that on the Z acceptance.

For the W cross section, however, the electron likelihood efficiency enters through the matrix method (Section 7.1.2) and not the acceptance. In this case, a similar method is followed with the quantity N_W/A_W determined for the same set of 500 trials specified above, where N_W is the number of W events after matrix method background subtraction. The result is shown in the top plot of Figure 6.35.

The relative uncertainty on the ratio of cross sections, R is determined in a manner similar to the W cross section. This is found by calculating N_W/A_R, where A_R is the ratio of the W and Z acceptances described above. The result is shown in the bottom plot of Figure 6.35.

To summarize, the total uncertainty on the cross sections due to the statistical uncertainty of the efficiencies is 1.03% for W, 0.59% for Z and 0.66% for R.

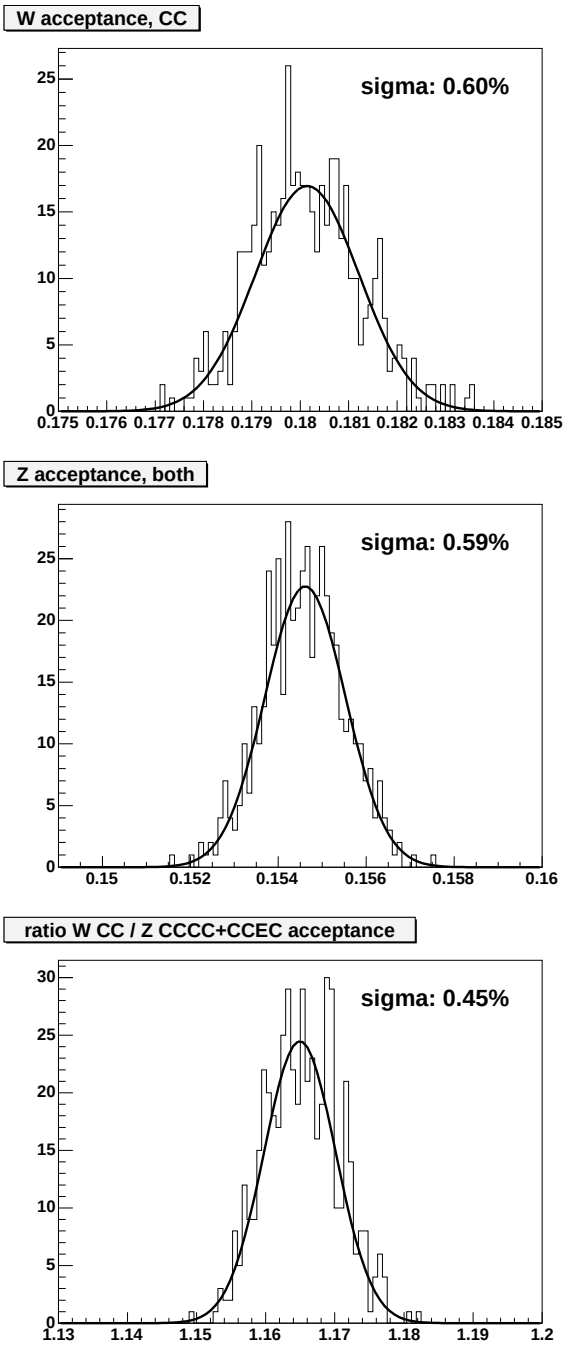

Fig. 6.34: The distribution of acceptance values produced by PMCS that results from simultaneously varying the input efficiency values by their statistical error.

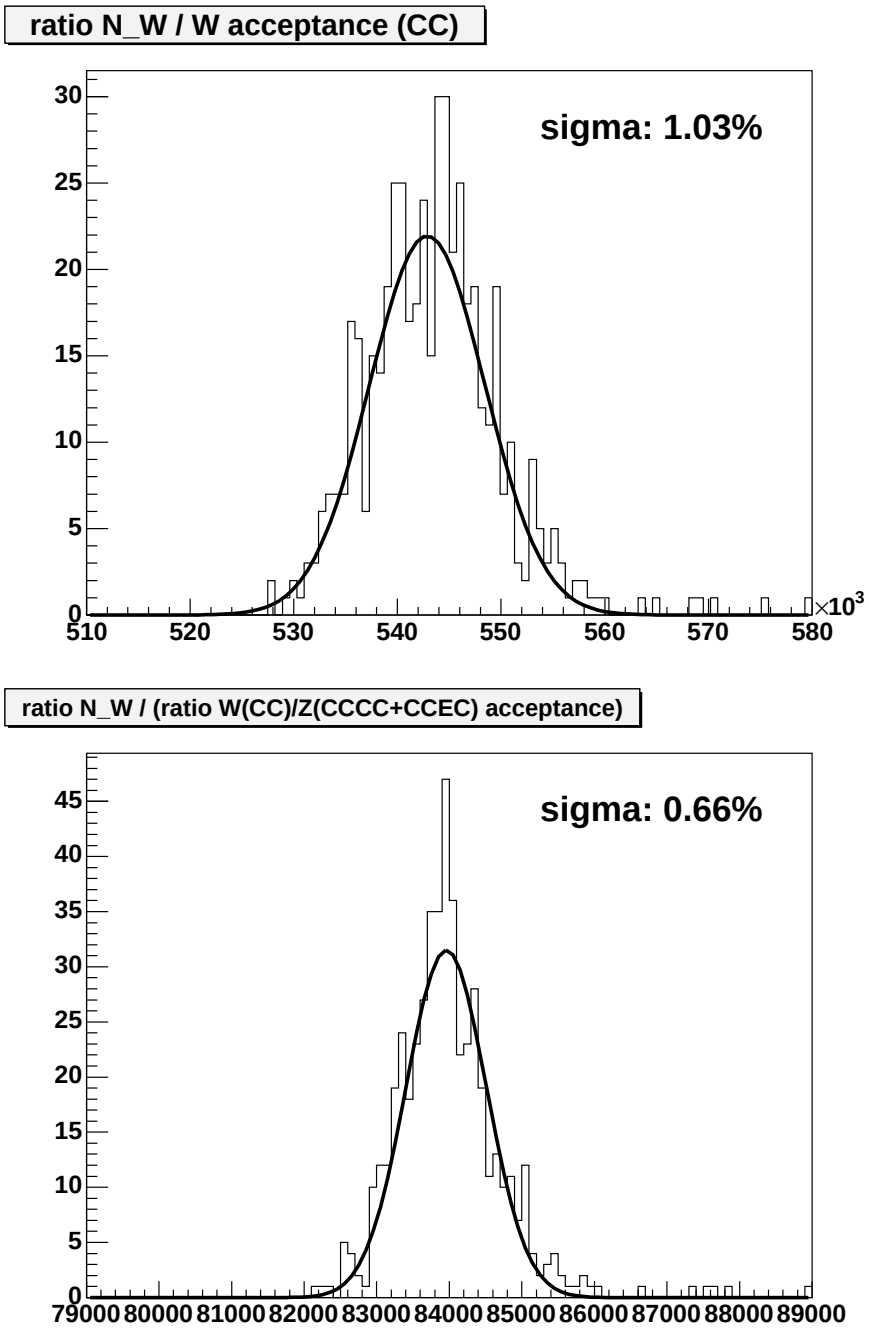

Fig. 6.35: The distribution of N_W/A_W and N_W/A_R values produced by PMCS and the matrix method that results from simultaneously varying the input efficiency values by their statistical error.

6.5.4 Systematic Uncertainty of the Efficiencies

Systematic uncertainties on the cross sections due to efficiencies are found by running separate trials in PMCS increasing(+) and decreasing(-) each efficiency by the systematic error. The uncertainty is conservatively assumed to be symmetric with the larger error used. Since the cross section is inversely proportional to acceptance, shifting the efficiency up is expected to increase acceptances and therefore lower the cross sections. Symmetric errors are summarized in Table 6.5.

- Electron Preselection Efficiency

  As described in Section 6.2.2, there is an approximate 0.7% relative uncertainty on the electron preselection efficiency which will enter once in the W acceptance and twice in the Z acceptance. Uncertainties for Z (CC-CC + CC-EC) are $-0.74\%(+)$ and $+1.22\%(-)$ and for W are $-0.52\%(+)$ and $+0.77\%(-)$.

- Track-Match Efficiency

  As described in Section 6.2.3, there is an approximate 0.5% relative uncertainty on the electron track-match efficiency. Since only one electron must have a track-match for Z events, uncertainties for the Z are expected to be quite small and are found to be $-0.17\%(+)$ and $+0.24\%(-)$ for (CC-CC + CC-EC). Uncertainties for the W are $-0.37\%(+)$ and $+0.40\%(-)$.

- Trigger Efficiency

  The systematic uncertainty for Z (CC-CC + CC-EC) candidates is found by finding the shift in acceptance when the trigger efficiency probe is not required to have a matched track. As was the case for the track-match efficiency, uncertainty for Z events should be very small and a shift of only -0.07% is found. Uncertainties for W events are found from differences in the W cross section using CMT 8 to 11 vs CMT 12 triggers and is found

	Relative Uncertainty on W	Relative Uncertainty on Z	Relative Uncertainty on R
Preselection	0.77%	1.22%	0.46%
Trigger	0.38%	0.07%	0.39%
Track Match	0.40%	0.24%	0.19%
Likelihood	0.64%	0.34%	0.35%

Tab. 6.5: Relative systematic uncertainty on the cross sections based on systematic error of the given input efficiency.

to be 0.38%. Systematic uncertainties for trigger efficiency are described further in Section 6.2.4.

- Electron Likelihood Efficiency

  As described in Section 6.2.5, there is an approximate 0.5% relative uncertainty on the electron likelihood efficiency. As was the case for the track-match efficiency, the Z uncertainties should be very small and are found to be $-0.34\%(+)$ and $+0.29\%(-)$ for (CC-CC + CC-EC). Uncertainties for the W are $-0.63\%(+)$ and $+0.64\%(-)$. Since the likelihood cut is only used in W background subtraction it has no affect on acceptance. This uncertainty is on the number of W events after background subtraction.

	X_-	X_+
$W \to e\nu$ (CC)	0.97%	1.91%
$Z/\gamma^* \to ee$ (CC-CC + CC-EC)	1.22%	1.48%
$R(W(CC)/Z/\gamma^*$ (CC-CC + CC-EC))	0.70%	1.12%

Tab. 6.6: Relative PDF uncertainty on the cross sections.

6.5.5 Acceptance Uncertainty due to PDF

The method for determining the uncertainty on the acceptance due to the choice of PDF is described in Section 5.2.1. PDF uncertainties for the $W \to e\nu$ and $Z \to ee$ cross sections and the ratio, $R \equiv \frac{\sigma_W \times B(W \to e\nu)}{\sigma_{Z/\gamma^*} \times B(Z/\gamma^* \to ee)}$, are found by replacing X in Equation 5.1 by the corresponding acceptances. Calculations are made with 2 million events generated using Pythia and the CTEQ6.1 NLO PDF set for the default and each of the 20 pairs of error PDF's for W and Z/γ^*. The resulting uncertainties are shown in Table 6.6.

CHAPTER 7

BACKGROUNDS

In this chapter the amount of background in the W and Z candidate samples is estimated. Sources of background contamination in the samples can arise either from the misidentification of particles due to detector limitations or from other physical processes with final states similar to that of the $W \rightarrow e\nu$ and $Z \rightarrow ee$ processes.

7.1 QCD Background in the W candidate sample

QCD background comes from multi-jet events where one jet is misidentified as an electron and a large missing E_T is produced from a mis measurement of the E_T of another. This background is estimated using loose and tight samples: the W candidate sample and the tight W candidate sample (electron likelihood added). The method for estimating QCD background also requires efficiencies for real electrons and for fake electrons, from QCD jets, to pass the electron likelihood cut. Real electron likelihood efficiencies are estimated in Section 6.2.5 and fake electron likelihood efficiencies are estimated below in Section 7.1.1.

7.1.1 The Electron Likelihood Fake Rate

After having already passed all loose electron cuts, the fake rate is defined as the probability for a fake electron to then pass the electron likelihood cut. The fake

electron sample is obtained from di-jet events where one fakes an electron.

Events are used in which there is one jet passing cuts defined below and one EM object passing identical electron selection criteria as used to select the W candidate sample. The electron candidate and the jet are required to be back-to-back with $\Delta\phi > \pi - 0.5$. The E_T ratio of the leading jet and the EM object needs to be smaller than 2.0. The jet opposite to the electron candidate is required to pass the following criteria designed to select jets and reject electrons [80]:

- N90 > 1

  This is the number of towers required to comprise $\geq 90\%$ of the total E_T of the jet.

- F90 < 0.65

  This is the ratio of N90 and the total number of towers in the jet.

- $0.05 <$ EM fraction < 0.7

  The jet is expected to have a low energy fraction in the EM layers.

- CHF < 0.25

  This is the fraction of the energy for the jet in the coarse hadronic layers.

- Jet7_hotf $<= 5$

  This is the ratio of the E_T of the leading cell in the jet to the E_T of the second leading cell.

- $E_T > 20$ GeV

  Both objects in the di-jet event should have a large E_T.

- $>= 5$ tracks within $\Delta R_{det} < 0.5$

  Many tracks are expected from the charged particles present in the hadronic shower.

The requirements on the EM fraction of the jet and the F90 variable are more stringent than the general recommendation. This reduces the risk of background contamination in the jet sample. Missing E_T in the event must be smaller than 10 GeV in order to remove W + jet events from the sample. There are 26,305 total probes in the central region where the jet and EM object satisfy the necessary requirements. The electron candidate probe is then required to satisfy the electron likelihood requirement. A total of 4763 of these probes pass this requirement for an average fake rate of 18.1%.

The fake rate values used to determine the background in the W sample are shown in Figure 7.1. Binning is chosen to match that of electron likelihood efficiency. Dependencies are also quite large for the fake rate as a function of E_T and missing E_T as shown in Figures 7.2 and 7.3. Fake rate, with missing $E_T <$ 10 GeV, varies between 15 and 20% for both of these distributions in the central region. For high values of missing E_T the data sample is contaminated by W + jet events causing the apparent increase in fake probability.

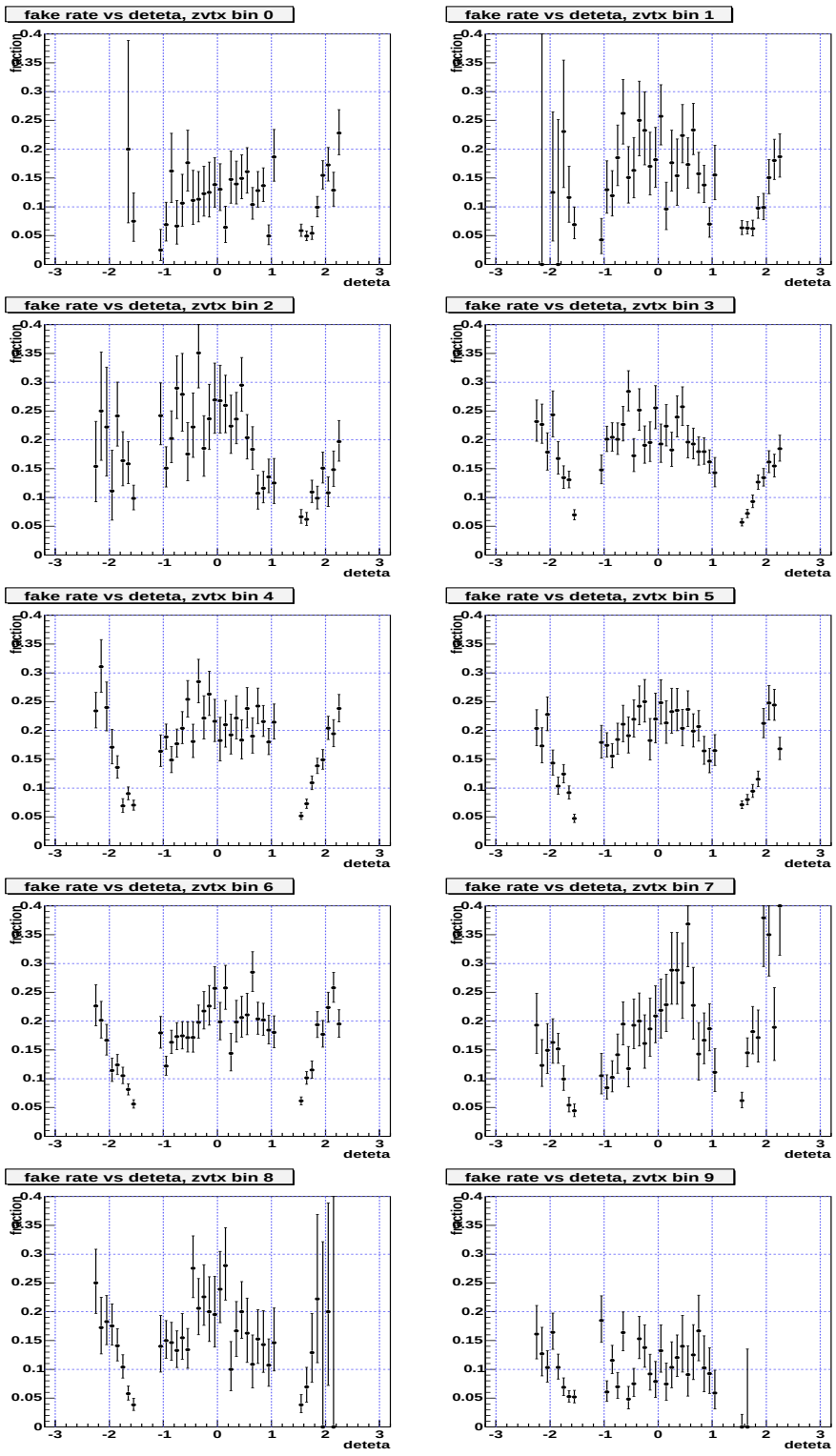

Fig. 7.1: Electron likelihood fake rate as a function of η_{det} in vertex z bins as used for W background subtraction. Z vertex bins are, going left to right from top to bottom: $<$ -39, -39 to -30, -30 to -23, -23 to -10, -10 to 0, 0 to 10, 10 to 23, 23 to 30, 30 to 39, and $>$ 39 cm.

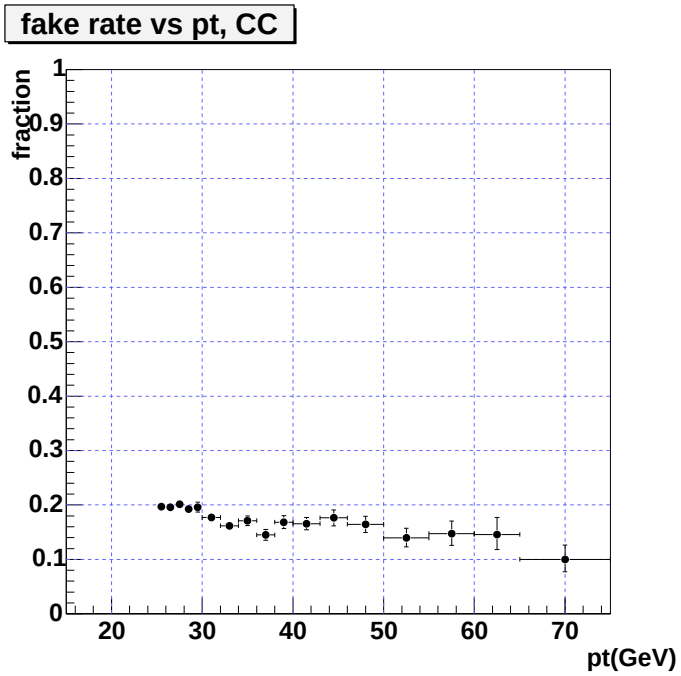

Fig. 7.2: Electron likelihood fake rate as a function of the electron E_T

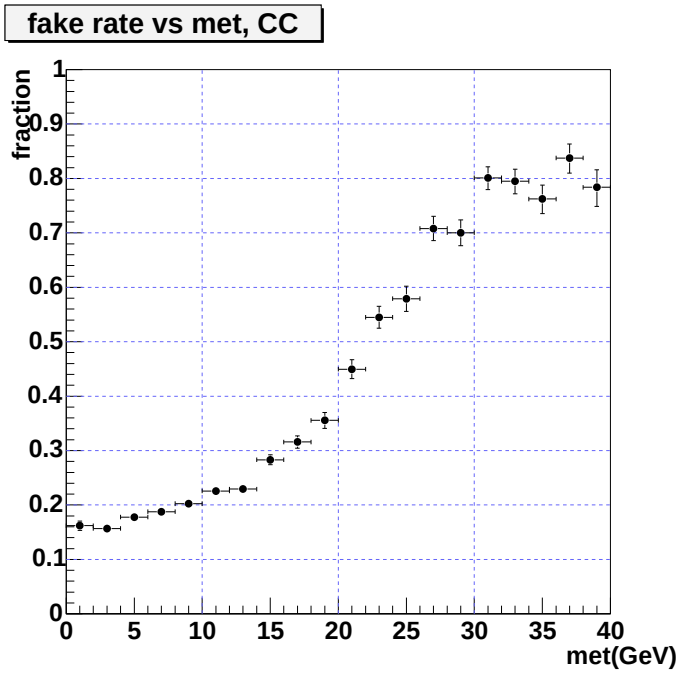

Fig. 7.3: Electron likelihood fake rate as a function of the missing E_T

7.1.2 Matrix Method Background Subtraction

In order to subtract QCD background from W candidates we solve two linear equations using the number of W Candidates with and without the electron likelihood requirement as well as the likelihood efficiency and fake rate. The number of W bosons produced is extracted from the following equations.

$$N_{WCandidates} = N_W + N_{QCD}$$

$$N_{WCandidates}^{likelihood} = \epsilon_{likelihood} N_W + f_{QCD} N_{QCD}$$

Yielding

$$N_W = \frac{N_{WCandidates}^{likelihood} - f_{QCD} N_{WCandidates}}{\epsilon_{likelihood} - f_{QCD}}$$

where N_W is the true number of W bosons, $N_{WCandidates}$ is the number of W candidate events, $N_{WCandidates}^{likelihood}$ is the number of W candidate events passing the likelihood cut, f_{QCD} is the electron likelihood fake rate, and $\epsilon_{likelihood}$ is the likelihood efficiency.

The above equations are applied in bins of η_{det}, and vertex z as shown in Figures 6.15 and 7.1. The result of the matrix method for all bins is shown in Figure 7.4. The number of W events is determined to be

$$N_W^{CC} = 96799 \pm 731 \tag{7.1}$$

The quoted uncertainty includes the statistical uncertainty of the W sample as well as the propagated statistical uncertainties coming from the likelihood efficiency and the fake rate. This indicates a background of $1.0 \pm 0.7\%$ in the W sample.

This method of background subtraction is also used to determine additional properties of the W boson and the electron from W decay. The comparisons to

PMCS shown in Chapter 5.5 are produced this way.

The systematic error arising from the uncertainties in the fake rate is found to be negligible. Variations found in the central region for the E_T and missing E_T distributions suggest a 25% uncertainty in the fake rate to be a rather conservative estimate. However, results are stable under even much larger variations. Setting the fake rate to zero results in a change of -0.03% in the number of background subtracted W candidates and and increasing it by 50% results in a 0.13% change. To first order the uncertainty due to the fake rate goes as

$$\delta N_W = \frac{N_{QCD}}{\epsilon_{likelihood} - f_{QCD}} \times \delta f_{QCD}. \tag{7.2}$$

Therefore, this lack of sensitivity to variation in fake rate is due to the already high purity of the (loose) W candidate sample along with the relatively high efficiency of the likelihood cut.

Crosschecks for the matrix method are carried out using alternate discriminants in place of the nominal likelihood > 0.9 cut and using an alternate fake sample. These checks are described in Sections 7.1.3 and 7.1.4. An additional check tests the consistency of the matrix method with the 'peak fit' method used for Z event QCD background subtraction. This is discussed in Section 7.3.4.

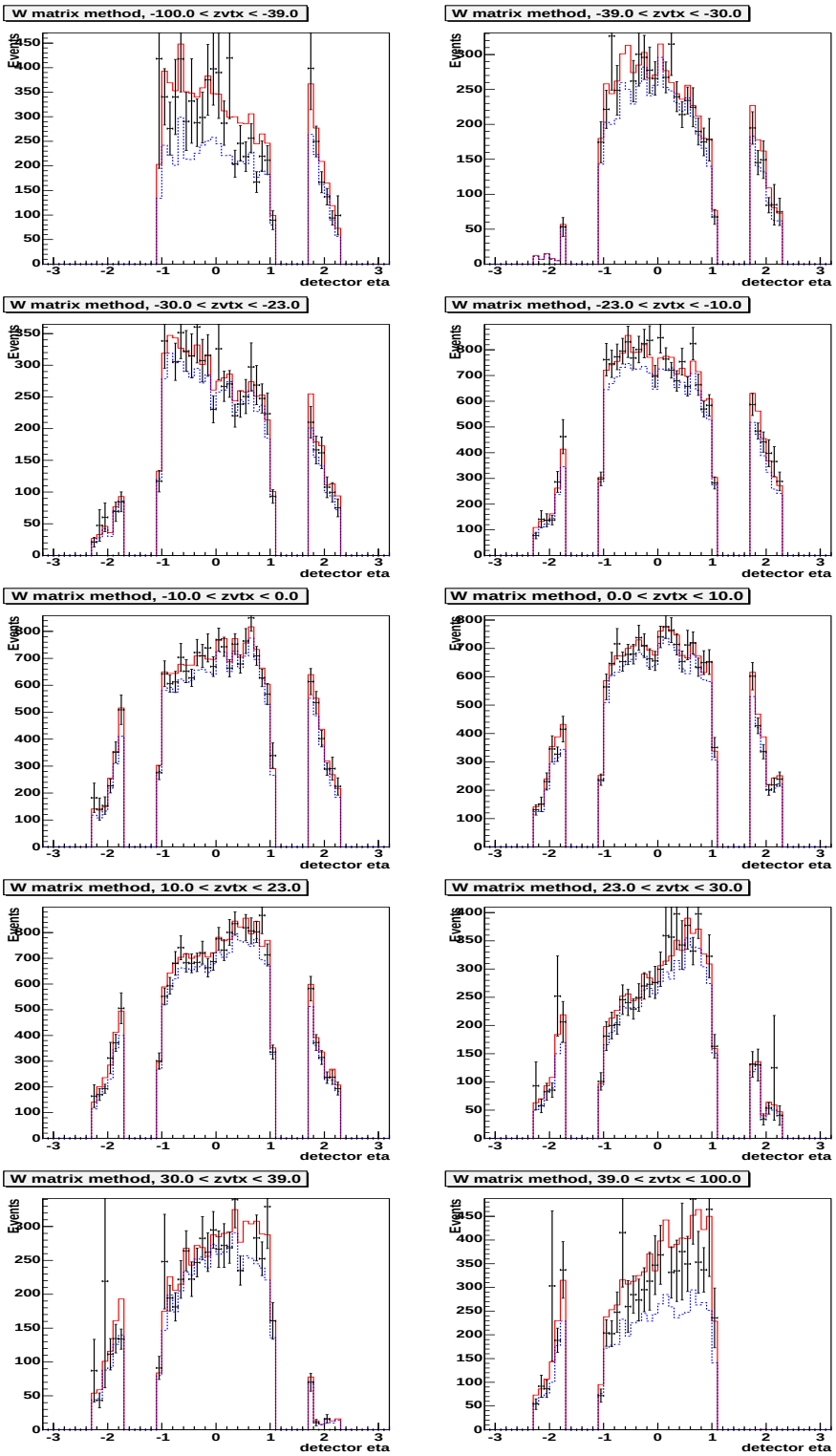

Fig. 7.4: Background subtraction for W candidates as a function of η_{det} and in bins of vertex z. Vertex z bins are, going left to right from top to bottom: $<$ -39, -39 to -30, -30 to -23, -23 to -10, -10 to 0, 0 to 10, 10 to 23, 23 to 30, 30 to 39, and $>$ 39 cm. The measured input variables are (loose) W candidates before the likelihood cut (the solid red histograms) and tight W candidates after the likelihood cut (the dashed blue histograms). The true number of W events is shown at each bin with error bars indicating the uncertainty arising from event statistics and the measured likelihood efficiency and fake rate.

	loose W cand background
nominal	$1.0 \pm 0.7\%$
likelihood > 0.5	$1.3 \pm 0.6\%$
H-Matrix(7) < 12	$1.4 \pm 1.5\%$
H-Matrix(7) < 16	$0.2 \pm 1.1\%$
iso < 0.08, EMfrac > 0.97	$2.1 \pm 0.9\%$
track $P(\chi^2) > 0$	$0.6 \pm 0.9\%$

Tab. 7.1: W background checks using nominal method

7.1.3 Checks Using Alternate Matrix Method Discriminants

Checks are made on the choice of discriminant used in W QCD background estimation by varying definitions for 'loose' and 'tight' cuts placed on the W candidate and fake samples when applying the matrix method described in Section 7.1.2. The nominal 'loose' and 'tight' sample requirements are given in Section 4.9 with the difference being the addition of the electron likelihood > 0.9 cut in the tight sample. The first four checks change the cut added in the tight sample. For the first test, the electron likelihood > 0.9 cut is replaced by electron likelihood > 0.5, for the second H-Matrix(7) < 12, for the third H-Matrix(7) < 16 and for the fourth Isolation < 0.08 and EMFraction > 0.97. In the last check the loose sample uses a relaxed track requirement with $P(\chi^2) > 0$ and the nominal loose sample, with track $P(\chi^2) > 0.01$, becomes the tight sample. Table 7.1 compares the resulting background percentages on the nominal loose W candidate sample.

	loose W cand background (using single EM)
nominal	0.8 ± 0.9%
likelihood > 0.5	1.4 ± 0.6%
H-Matrix(7) < 12	1.6 ± 1.7%
H-Matrix(7) < 16	-1 ± 5%
iso < 0.08, EMfrac > 0.97	2.3 ± 1.1%
track $P(\chi^2) > 0$	1.6 ± 0.7%

Tab. 7.2: W background checks using single EM

7.1.4 Checks Using An Alternate Fake Sample

An alternative 'single EM' fake sample is created by removing the requirement of a jet opposite the fake electron. Doing this removes any possible bias from this requirement, however more signal is allowed into the fake sample which is at least partially responsible for an increased fake rate compared to the nominal method with an opposite jet. This signal is evident by the peak at around 40 GeV in the single EM fake rate vs. E_T plot shown in Figure 7.5 but not in the nominal plot shown in Figure 7.2. One nice feature of this fake sample is a flat fake rate as a function of missing E_T below 10 GeV, as seen in Figure 7.6. Given the increased signal, this method is a good estimate for an upper bound on systematic uncertainty on the fake rate. Its effect on background percentage is negligible, yielding a -0.2% difference from the nominal method. W QCD background percentages are found using the same cuts for 'loose' and 'tight' samples in Section 7.1.3. See Table 7.2 for results.

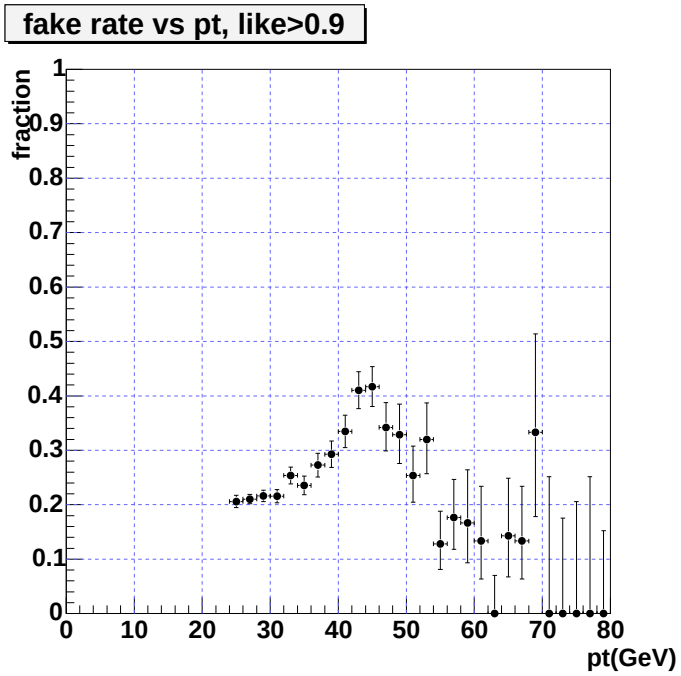

Fig. 7.5: Comparison of CC fake rate as a function of E_T(missing $E_T < 10$ GeV) using the alternate single EM fake rate sample.

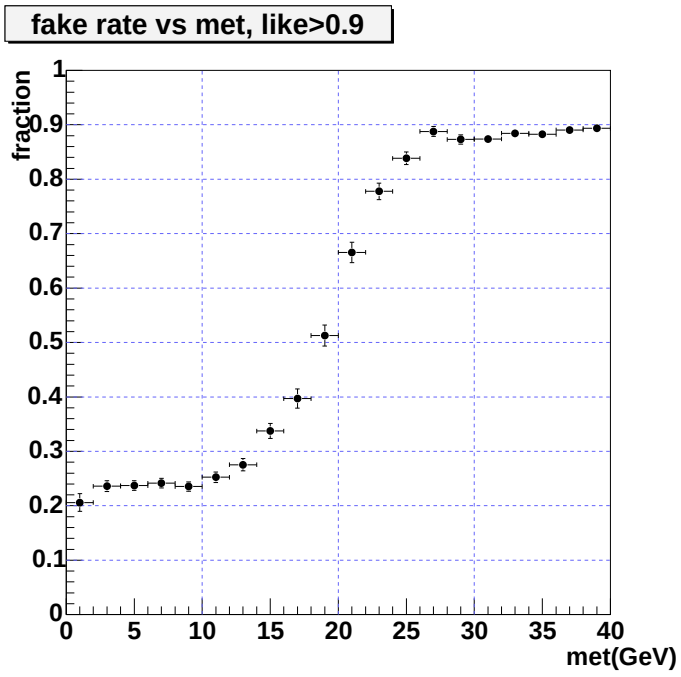

Fig. 7.6: Comparison of CC fake rate as a function of missing E_T using the alternate single EM fake rate sample.

7.2 Other Backgrounds in the W candidate sample

In addition to QCD, two other backgrounds for W candidate events were considered: $W \to \tau\nu$ and $Z \to ee$.

7.2.1 W $\to \tau\nu$ Background

Events from $W \to \tau\nu$ production in which the τ decays to an electron will appear similar to $W \to e\nu$ events except that on average the electron E_T will be lower. One million $W \to \tau\nu$ events are generated using Pythia and the CTEQ6.1 NLO PDF set and then the W candidate selection criteria is applied in PMCS to find an acceptance for $W \to \tau\nu$, $A_{W\to\tau\nu}$, in exactly the same way as for the $W \to e\nu$ acceptance calculation. Assuming the cross section times branching ratio for $W \to e\nu$ and $W \to \tau\nu$ are the same, the $W \to \tau\nu$ background fraction is then $A_{W\to\tau\nu}/A_{W\to e\nu}$. This is found to be $(1.80 \pm 0.36)\%$ for the central region using a relative uncertainty of 20%. This is a conservative value; since relative uncertainty should be approximately the same as for $W \to e\nu$ ($\approx 2\%$), it could be reduced with additional study. However, since its contribution to the W cross section uncertainty is already very small, this is not necessary.

7.2.2 W Candidate background from Z $\to ee$

A $Z \to ee$ can mimic a $W \to e\nu$ event if one electron is lost in a poorly instrumented region of the detector or is misidentified as a jet, and the transverse energy in the event is mis measured, giving rise to a large missing E_T value. A sample of 2M $Z/\gamma^* \to ee$ MC events is generated using Pythia and the CTEQ6.1 NLO PDF set and then W candidate selection criteria are applied in PMCS. This results in 11574 events in the central region surviving the acceptance cuts. The background fraction is then the product of the ratio of this acceptance ($A_{Z\to W}$)

to the W acceptance A_W and the ratio of Z to W inclusive cross sections times branching ratio:

$$f_Z^W(CC) = \frac{\sigma(p\bar{p} \to Z \to ee)}{\sigma(p\bar{p} \to W \to e\nu)} \times \frac{A_{Z\to W}^{CC}}{A_W^{CC}} = \frac{\sigma(p\bar{p} \to Z \to ee)}{\sigma(p\bar{p} \to W \to e\nu)} \times \frac{11574/2000000}{A_W^{CC}} \tag{7.3}$$

The ratio of production cross sections is taken from the theoretical calculations. We have $f_Z^W(CC) = (0.26 \pm 0.05)\%$ using a conservative relative uncertainty of 20%. As with the $W \to \tau\nu$ background estimation, a reduction in estimated relative uncertainty through further study is not necessary.

7.3 Estimation of QCD Background in $Z/\gamma^* \to ee$ Events

The primary source of QCD background comes from multi-jet events where two jets are misidentified as electrons. QCD background subtraction is performed for $Z/\gamma^* \to ee$ events using a 'peak fit' method. This method is used for estimation of background in both the Z candidate sample and in the samples used for tag & probe-based efficiencies.

7.3.1 The Peak Fit Method

The peak fit method refers to the estimation of background in a $Z/\gamma^* \to ee$ based data sample by fitting the peak of its invariant mass distribution to a linear combination of invariant masses for a signal shape obtained from $Z/\gamma^* \to ee$ Monte Carlo and a background shape obtained from data. The linear scale factors for the signal and background shapes are left as free parameters in a χ^2 fit which is performed within a mass range of 40 GeV to 140 GeV.

The invariant mass distribution of the signal is taken from $p\bar{p} \to Z/\gamma^* + X \to e^+e^- + X$ decays simulated with PMCS Monte Carlo that has been tuned to

account for detector effects (see Section 5.5). The QCD background invariant mass shape is described in the next section.

7.3.2 QCD Background Shape

The invariant mass distribution of the QCD background is determined directly from data. QCD background candidates are required to satisfy the following criteria:

- At least two EM objects passing preselection, fiducial and kinematic cuts
- Both EM objects must pass an inverted electron likelihood cut (< 0.1)
- One of the EM objects must have fired the trigger.
- di-EM invariant mass between 70 and 110 GeV.

In this way we select two jets with high electromagnetic energy content in the shower. Inversion of the electron likelihood cut is chosen as it is expected that this quantity has little impact on the kinematic properties of the background selection. The invariant mass distribution is determined separately for CC-CC and CC-EC.

To subtract background from other distributions, QCD background from the di-EM mass distribution within 70 to 110 GeV is also plotted for all variables of interest. This background, scaled by the same amount as in the invariant mass fit, is subtracted from the sample. One additional factor that must be considered is the dependence of track matching on the variable. Although background invariant mass shape has very little dependence on the presence of a track, for other distributions such as pseudorapidity and vertex z the dependence can be large, especially in the end caps. When plotting backgrounds as a function of these variables, separate background distributions must be made for Z candi-

dates where at least one track is required in an event and for the tag & probe sample where each tag must have a track.

7.3.3 Z candidate QCD Background Estimation

Separate signal and background shapes for Z events with electrons in the CC-CC and CC-EC regions have been used for the background subtraction. This fit is shown in Figure 6.24 for CC-CC and Figure 6.27 for CC-EC. See Table 7.3 for statistics after background subtraction.

The systematic uncertainty is estimated based on a combination of the following sources: χ^2 fit errors, variations with alternate background choices and comparisons to matrix method background subtraction.

The uncertainty from the χ^2 fit is $\sqrt{\delta^2_{\chi^2} - \delta^2_{stat}}$ where δ_{χ^2} is the total uncertainty of the fit and δ_{stat} is the uncertainty due to limited numbers of Z events. This is found to be 0.35% for CC-CC and 0.46% for CC-EC and 0.39% combined.

To study the effect on the cross sections due to a systematic uncertainty in the background shape, several alternate background shapes were defined using different cuts. Below are the cut requirements for the six background shapes studied:

- likelihood < 0.1 (nominal)
- H-Matrix(7) > 20 (CC) or H-Matrix(8) > 25 (EC)
- H-Matrix(8) > 35
- H-Matrix(8) > 25
- $25 <$ H-Matrix(7)/H-Matrix(8) < 60
- H-Matrix(7)/H-Matrix(8) > 50

	signal	background
CC-CC	5068 ± 38	106 (2.0%)
CC-EC	2732 ± 13	22 (0.8%)

Tab. 7.3: Z event signal and background statistics

where H-Matrix(7)/H-Matrix(8) means that the H-Matrix(8) value was used in the EC region and twice the H-Matrix(7) value was used in the CC region (see Section 4.6 for a description of the H-Matrix). The track-match efficiency, number of Z events, number of W events and the resulting cross sections were redetermined for each background choice. As a conservative estimate, the largest deviation from the normal cross section value is used. This is found to be -0.24% for CC-CC, 0.11% for CC-EC and -0.15% combined.

For the last check, a matrix method similar to that used for W background subtraction is adapted for Z events. See Section 7.3.4 for a description. For this, electrons with a track in di-EM events are used as probes and the matrix method is applied in a similar way as for W events as described in Section 7.1.2. Compared to the nominal method of fitting to a peak and background shape, the number of background subtracted events predicted using the matrix method differs by 0.62% for CC-CC and -0.11% for CC-EC or 0.40% combined.

Combining these results in quadrature yields a background systematic uncertainty of 0.75% for CC-CC, 0.47% CC-EC and 0.58% combined.

7.3.4 Matrix Method Consistency With The Peak Fit Method

A probe sample, obtained from di-EM events, is used to check the consistency of the matrix and peak fit methods by adapting the matrix method for use with the probe sample and comparing predicted number of background subtracted events in the probe sample to that found using the peak fit method. di-EM events passing the following selection criteria are chosen:

	total	matrix method		peak fit	
	probes	after bgsub	bkg %	after bgsub	bkg %
CC-CC loose probes	9139	8771 ± 116	4.0	8759 ± 98	4.2
CC-CC tight probes	7893	7819 ± 94	0.9	7803 ± 91	1.1
CC-EC loose probes	3195	3065 ± 65	4.1	3088 ± 58	3.3
CC-EC tight probes	2754	2729 ± 55	0.9	2732 ± 54	0.8

Tab. 7.4: Comparison of Z probe sample background subtractions using the matrix and peak fit methods.

- At least two electron candidates passing preselection, fiducial and kinematic cuts
- One of the electron candidates must have fired the trigger.
- di-EM invariant mass between 70 and 110 GeV.

Both electron candidates are considered as possible probes for CC-CC events while only the CC electron is considered for CC-EC events. Electron candidates can be used as probes if they satisfy loose electron criteria. The matrix method is performed on these probe electron candidates in the same manner as the electrons in the loose W candidate sample (see Section 7.1.2). The predicted matrix and peak fit methods are found to agree quite well. See Table 7.4 for results and Figures 7.7 and 7.8 for peak fit plots.

The results for the number of background subtracted probes can be used to obtain predictions for the number of background subtracted Z events. The CC-EC tight probe sample matches exactly the Z CC-EC candidate sample and therefore results can be compared directly yielding a -0.11% difference in the number of predicted background subtracted Z CC-EC candidates using the matrix method. It is not as straightforward for CC-CC events since either electron in a Z candidate can be tight. However, the number of Z CC-CC candidate background events should be approximately equal to the total number of background events in the CC-CC probe sample. This gives a prediction of 74 background

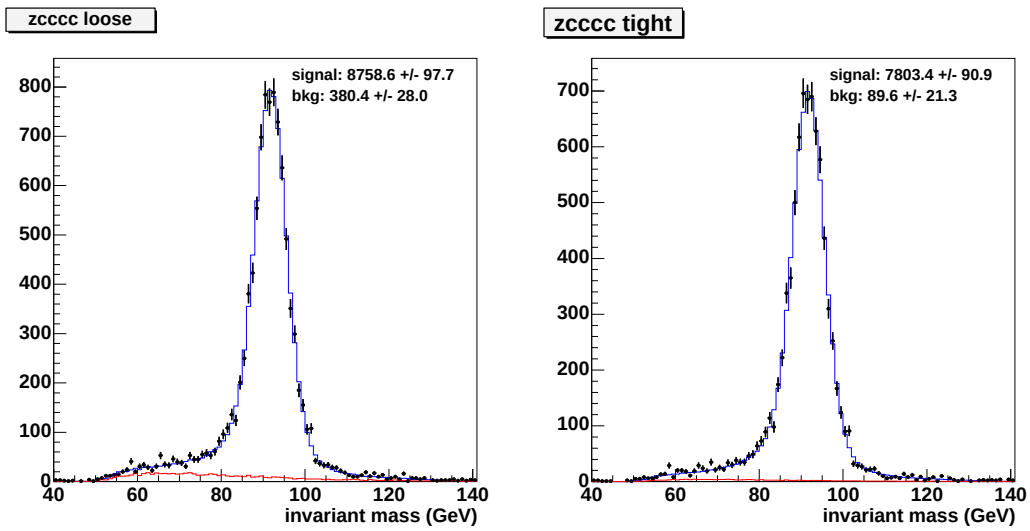

Fig. 7.7: Background subtraction by fitting the Z CC-CC probe data peak to a signal plus background shape. Shown are the invariant mass distributions of the loose probe sample (left) and tight probe sample (right).

events using the matrix method compared to 106 from the peak fit method. Subtracting these numbers from the 5174 total Z CC-CC candidate events yields the number of background subtracted events. This number is found to be +0.62% larger using the matrix method.

7.4 Other Backgrounds in the Z candidate sample

In addition to QCD background, two other backgrounds for $Z \rightarrow ee$ events were considered: physics background from Drell-Yan and $Z \rightarrow \tau\tau$ events.

7.4.1 Correction for Drell-Yan

The production of dielectron pairs is properly described by the Z boson, the off-shell photon propagator, and the interference between the two. To match with data, acceptance is found using full Z/γ^* Monte Carlo. The physical Z/γ^* cross section is then proportional to the number of Z candidates, after QCD

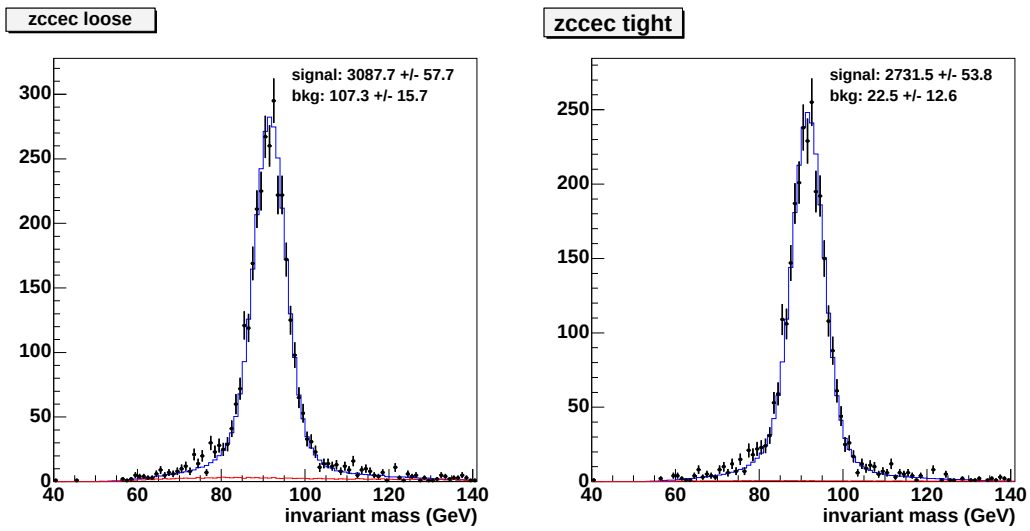

Fig. 7.8: Background subtraction by fitting the Z CC-EC probe data peak to a signal plus background shape. Shown are the invariant mass distributions of the loose probe sample (left) and tight probe sample (right).

background subtraction, over acceptance.

$$\sigma_{Z/\gamma^*} \times B(Z/\gamma^* \rightarrow ee) \propto N_Z / A_{Z/\gamma^*} \tag{7.4}$$

In order to convert to a pure Z cross section, a Drell-Yan correction factor is introduced relating the Z/γ^* cross section to that expected purely from Z boson production:

$$\sigma_Z \times B(Z \rightarrow ee) = R_\sigma \times [\sigma_{Z/\gamma^*} \times B(Z/\gamma^* \rightarrow ee)] \tag{7.5}$$

where $R_\sigma = 0.9547$ is the ratio of the pure Z to Z/γ^* cross sections within the 50 to 130 GeV mass range used in the acceptance calculation.

$$R_\sigma \equiv \frac{\sigma_Z \times B(Z \rightarrow ee)}{\sigma_{Z/\gamma^*} \times B(Z/\gamma^* \rightarrow ee)} \tag{7.6}$$

This ratio is based upon the theoretically predicted cross sections obtained from

	X_-	X_+
$R_\sigma(\ \sigma(Z)/\sigma(Z/\gamma^*)\ )$	0.28%	0.23%

Tab. 7.5: Relative PDF uncertainty on R_σ.

the sample of 20 million pure Z, 2 million Z/γ^* interference, and 2 million pure γ^* events generated using Resbos with the CTEQ6.1 NLO PDF sets.

A systematic error of 0.30% on the cross sections is estimated by comparing to results from Pythia using the CTEQ6.1 error PDF sets. The method for determining the uncertainty on an observable due to the choice of PDF is described in Section 5.2.1. PDF uncertainty is found by replacing X in Equation 5.1 by the ratio of pure Z to Z/γ^* cross sections. Calculations are made with 2 million events generated using Pythia and the CTEQ6.1 NLO PDF set for the default and each of the 20 pairs of error PDF's for Z/γ^* and pure Z. The resulting '+' and '-' uncertainties are shown in Table 7.5. The R_σ uncertainty is small and for simplicity is set to $\pm 0.28\%$, which contributes an uncertainty of 0.30% in the $Z \to ee$ cross section.

7.4.2 Z $\to \tau\tau$ Background

The background from $Z \to \tau\tau$ processes, where both taus decay electronically is considered. However, electrons from τ decays have a softer E_T spectrum and a small branching ratio $B(\tau \to e\nu\nu)^2$, making this background negligible.

CHAPTER 8

RESULTS AND CONCLUSIONS

8.1 The $W \rightarrow e\nu$ Cross Section

The W cross section times branching ratio is calculated using

$$\sigma_W \times B(W \rightarrow e^{\pm}\nu) = \frac{N_W}{\mathcal{L}} \frac{1}{A_W}(1 - f_\tau^W - f_Z^W) \tag{8.1}$$

where N_W is the number of W candidate events after QCD background subtraction and $\mathcal{L}$ is the integrated luminosity for the data sample. A_W is the total acceptance, including efficiency loss from electron selection cuts, for W bosons calculated from the Monte Carlo simulation. The backgrounds, other than QCD, are f_τ^W, the fraction of $W \rightarrow \tau\nu$ events that pass the $W \rightarrow e\nu$ selection criteria, and f_Z^W, the fraction of Z boson events misidentified as W bosons.

N_W	$\mathcal{L}$ (pb^{-1})	A_W	f_τ^W	f_Z^W
96799	177.3	0.18254	1.80%	0.26%

Tab. 8.1: Summary of input parameters for the $W \rightarrow e\nu$ cross section result.

Using the values summarized in Table 8.1 and the uncertainty estimates summarized in Table 8.3, the inclusive W cross section times branching ratio is

$$\sigma_W \times B(W \rightarrow e^{\pm}\nu) = 2929 \ \pm \ 9 \ (stat) \pm 57 \ (sys) \ ^{+\mathbf{56}}_{-\mathbf{28}} \ (pdf) \pm 190 \ (lumi) \text{ pb.}$$

8.2 The $Z \rightarrow ee$ Cross Section

First, a physical Z/γ^* cross section times branching ratio, which includes the contribution from the photon Drell-Yan process, is calculated within the 50 to 130 GeV mass range used in the Monte Carlo simulation:

$$\sigma_{Z/\gamma^*} \times B(Z/\gamma^* \rightarrow e^+e^-) = \frac{N_Z}{\mathcal{L}} \frac{1}{A_{Z/\gamma^*}} \tag{8.2}$$

where N_Z is the number of Z candidate events after QCD background subtraction and $\mathcal{L}$ is the integrated luminosity for the data sample. A_{Z/γ^*} is the total acceptance, including efficiency loss from electron selection cuts, for Z/γ^* within the 50 to 130 GeV mass range.

The Z cross section times branching ratio is then

$$\sigma_Z \times B(Z \rightarrow e^+e^-) = R_\sigma \times [\sigma_{Z/\gamma^*} \times B(Z/\gamma^* \rightarrow e^+e^-)] \tag{8.3}$$

where R_σ is the Drell-Yan correction factor.

Region	N_Z	$\mathcal{L}$ (pb^{-1})	A_{Z/γ^*}	R_σ
CC-CC	5068	177.3	0.10161	0.9547
CC-EC	2725	177.3	0.05518	0.9547
Combined	7793	177.3	0.15678	0.9547

Tab. 8.2: Summary of input parameters for the $Z \rightarrow ee$ cross section results

Using the values summarized in Table 8.2 and the uncertainty estimates sum-

marized in Table 8.3, the physical Z/γ^* cross section times branching ratio is

$\sigma_{Z/\gamma^*} \times B(Z/\gamma^* \to e^+e^-) =$

(CC-CC) 281.3 ± 3.9 $(stat)$

(CC-EC) 278.5 ± 5.3 $(stat)$

(Combined) 280.4 ± 3.1 $(stat) \pm 4.9$ (sys) $^{\mathbf{+4.1}}_{\mathbf{-3.4}}$ $(pdf) \pm 18.2$ $(lumi)$ pb.

Multiplying by R_σ yields the inclusive Z cross section times branching ratio:

$\sigma_Z \times B(Z \to e^+e^-) =$

(CC-CC) 268.6 ± 3.7 $(stat)$

(CC-EC) 265.9 ± 5.1 $(stat)$

(Combined) 267.7 ± 3.0 $(stat) \pm 4.8$ (sys) $^{\mathbf{+4.0}}_{\mathbf{-3.3}}$ $(pdf) \pm 17.4$ $(lumi)$ pb.

8.3 The Ratio of Cross Sections

When finding the ratio of the W and Z cross sections, the integrated luminosity terms cancel out:

$$R = \frac{\sigma_W \times B(W \to e^{\pm} \overset{(-)}{\nu})}{\sigma_Z \times B(Z \to e^+e^-)} = \frac{N_W}{N_Z} \times \frac{A_{Z/\gamma^*}}{A_W} \times \frac{1 - f_\tau^W - f_Z^W}{R_\sigma}. \tag{8.4}$$

Using the values summarized in Tables 8.1 and 8.2 and the uncertainty estimates summarized in Table 8.3 , with combined statistics for Z, the ratio of cross sections is found to be

$R = 10.94 \pm 0.13$ $(stat) \pm 0.16$ (sys) $^{\mathbf{+0.12}}_{\mathbf{-0.08}}$ (pdf).

8.4 $Br(W \to e^{\pm}\nu)$ and Γ_W

The electron channel branching ratio of the W boson, $Br(W \to e\nu)$, and the W total width, Γ_W, can be determined using the result for the ratio of cross sections, R:

$$Br(W \to e\nu) = R \times \frac{[Br(Z \to ee)]}{[\sigma_W/\sigma_Z]} \tag{8.5}$$

and

$$\Gamma_W = \frac{1}{R} \times \frac{[\Gamma(W \to e\nu)] \times [\sigma_W/\sigma_Z]}{[Br(Z \to ee)]} \tag{8.6}$$

where the externally determined parameters, based on Standard Model predictions, are

$Br(Z \to ee) = (3.3655 \pm 0.0022)\%$ [1],

$\sigma_W/\sigma_Z = 3.381 \pm 0.051$ (Section 5.3), and

$\Gamma(W \to e\nu) = 0.22656 \pm 0.00024$ GeV [1].

The results are

$Br(W \to e^{\pm}\nu) = (10.89 \pm 0.13\ (stat) \pm 0.16\ (sys)\ ^{+\mathbf{0.12}}_{-\mathbf{0.08}}\ (pdf) \pm 0.16\ (ext)\ )\%$

and

$\Gamma_W = 2.080 \pm 0.024\ (stat) \pm 0.030\ (sys)\ ^{+\mathbf{0.023}}_{-\mathbf{0.015}}\ (pdf) \pm 0.031\ (ext)$ GeV

where the last source of uncertainty is from the external parameters.

8.5 Uncertainties

The uncertainties on the cross sections and the ratio are summarized in Table 8.3 and are divided into the four categories described below.

Source	Relative Uncertainty (%) σ_W	σ_Z	R
stat			
Number of Events	0.32	1.12	1.17
sys			
Stat Error on Efficiencies	1.03	0.59	0.66
$W \to \tau\nu$ and $Z \to ee$ Background	0.36	n/a	0.36
Drell Yan Correction	n/a	0.30	0.30
QCD Background Subtraction	nil	0.58	0.58
PMCS Parameters	1.15	0.88	0.78
Preselection Eff	0.77	1.22	0.46
Trigger Eff	0.38	0.07	0.39
Track-match Eff	0.40	0.24	0.19
Likelihood Eff	0.64	0.34	0.35
Total **sys**	1.66	1.69	1.30
pdf			
Acceptance	$^{+\mathbf{1.91}}_{-\mathbf{0.97}}$	$^{+\mathbf{1.48}}_{-\mathbf{1.22}}$	$^{+\mathbf{1.12}}_{-\mathbf{0.70}}$
lumi			
Luminosity	6.5	6.5	n/a

Tab. 8.3: A summary of percent relative uncertainties for the cross sections measurements.

8.5.1 stat

- Number of Events

  The statistical uncertainty is based on the number of W and Z candidate events before background subtraction.

8.5.2 sys

- Stat Error on Efficiencies

  This uncertainty results from statistical uncertainty of the measured preselection, track-match, trigger and electron likelihood efficiencies. This uncertainty is directly related to the size of the Z event sample that was used to determine the efficiencies. See Section 6.5.3 for details.

- Drell Yan Correction

  The uncertainty from the Drell-Yan correction factor is described in Section 7.4.1. The Z/γ^* systematic does not include the Drell Yan correction.

- $W \to \tau\nu$ and $Z \to ee$ Background

  A conservative uncertainty of 20% is assigned to the background in the $W \to e\nu$ sample from the $W \to \tau\nu$ and $Z \to ee$ backgrounds.

- QCD Background Subtraction

  The number of Z events and the track-match efficiency calculation rely on the background subtraction technique described in Section 7.3.3. Uncertainties are estimated based on χ^2 fit errors, variations with alternate background choices and comparisons to matrix method background subtraction. See Section 7.3.3 for more details.

- PMCS Parameters

  This is the uncertainty on the cross section due to the uncertainty on the in-

put parameters to PMCS, which affect the acceptance values as determined in Section 6.5.1.

- Preselection, Trigger and Track-Match Eff

  This is the uncertainty on the cross section due to the systematic uncertainty of the trigger, preselection, and track-match efficiencies, which affect the acceptance values as determined in Section 6.5.4.

- Likelihood Eff

  This is the uncertainty on the cross section due to the systematic uncertainty of the electron likelihood efficiency determined in Section 6.2.5. It affects the Z cross section via the acceptance value as determined in Section 6.5.4. It affects the W cross section via the matrix method (Section 7.1.2).

- Total sys

  All **sys** uncertainties are added in quadrature.

8.5.3 pdf

- Acceptance

  The PDF uncertainty is based on variations in acceptance calculated when using the error PDF sets as described in Section 6.5.5.

8.5.4 lumi

- Luminosity

  This is the uncertainty on the integrated luminosity which is estimated to be 6.5% (see Section 3.1).

8.6 Stability Checks

In Figure 8.1 the W cross section as a function of run number, η_{det} and ϕ is plotted as a check on the stability of the measurement as a function of position and time.

8.7 Conclusions

A total of 97757 W and 7928 Z candidate events were obtained from the 177 pb^{-1} data sample collected between September 2002 and September 2003 at the DØ Detector. All sources of uncertainty are combined below and the results compared to Standard Model predictions and also, for the W branching ratio and total width, to the experimental world averages.

The inclusive W and Z electron channel production cross sections, at a center-of-mass energy of 1.96 TeV, are

$\sigma_W \times B(W \to e^{\pm}\nu) = 2929 \pm 206$ pb and
$\sigma_Z \times B(Z \to e^+e^-) = 268 \pm 19$ pb.

These results are somewhat larger than the Standard Model predictions, with the significance of this difference just under 1.3 σ's:

(SM) $\sigma_W \times B(W \to e^{\pm}\nu) = 2627 \pm 109$ pb and
(SM) $\sigma_Z \times B(Z \to e^+e^-) = 242 \pm 10$ pb.

The largest source of uncertainty in the cross sections measurement, integrated luminosity, cancels out for the ratio of cross sections,

$R = 10.94 \pm 0.24$.

This is in good agreement with the Standard Model prediction,

(SM) $R = 10.87 \pm 0.16$.

From the measured value of R, the W branching ratio and total W width are extracted:

$Br(W \to e^{\pm}\nu) = (10.89 \pm 0.29)\%$ and
$\Gamma_W = 2.080 \pm 0.054$ GeV.

These are in good agreement with the Standard Model predictions [1]:

(SM) $Br(W \to e^{\pm}\nu) = (10.822 \pm 0.016)\%$ and
(SM) $\Gamma_W = 2.0936 \pm 0.0022$ GeV,

and are also consistent with the world averages [81]:

(WA) $Br(W \to e^{\pm}\nu) = (10.72 \pm 0.16)\%$ and
(WA) $\Gamma_W = 2.124 \pm 0.041$ GeV.

All results are consistent with the Standard Model and therefore no evidence of new physics is observed.

Integrated luminosity is by far the largest uncertainty for the cross sections and is unlikely to become much smaller in the near future. For R, however, this uncertainty cancels and future measurements can make significant improvements over this result. Increased statistics will not only improve the statistical uncertainty, but also allow more precise estimates of the effects of many sources of systematic error. Additionally, the understanding of the detector has improved greatly since this data sample was collected. An improved calibration of the calorimeter and the addition of the preshower detectors should enable more ac-

curate measurements and reduce systematics. This is especially true of the EC calorimeters where a number of problematic regions have been fixed. The resulting inclusion of more high pseudorapidity bosons in the candidate samples should significantly reduce PDF uncertainty. Of the external Standard Model based parameters needed for the extraction of the W branching ratio and total width, the uncertainty from the ratio of total cross sections, σ_W/σ_Z, is by far the largest at 1.4%. If this is not reduced, it is likely to become the dominate source of uncertainty in future measurements.

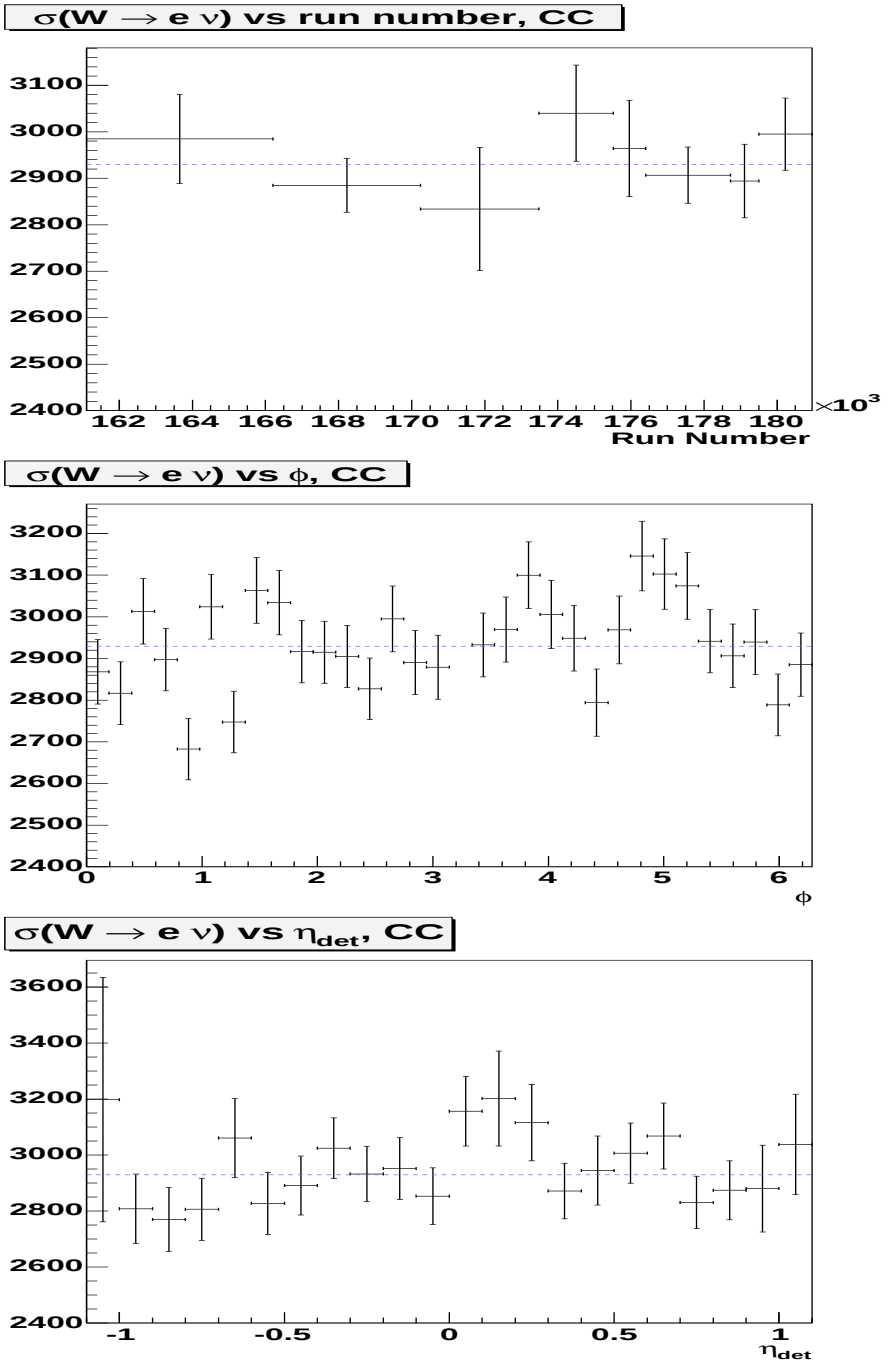

Fig. 8.1: A comparison of the W cross sections as a function of Run Number(top), ϕ_{det}(middle) and η_{det}(bottom). Error bars include only statistical uncertainty. The dashed line indicates the mean W cross section.

BIBLIOGRAPHY

[1] Particle Data Group; S. Eidelman et al., *Electroweak model and constraints on new physics*, Phys. Lett. B 592, 1 (2004).

[2] Particle Data Group; S. Eidelman et al., *Quantum chromodynamics*, Phys. Lett. B 592, 1 (2004).

[3] S.I. Glashow, Nucl. Phys. 22, 579 (1961).
S. Weinberg, Phys. Lett. 19, 1264 (1967).
A. Salam, *Elementary Particle Physics, Nobel Symp. no. 8*, N. Svartholm, 367 (1968).

[4] Super-Kamiokande, *Evidence for oscillation of atmospheric neutrinos*, Phys. Rev. Lett. 81, 1562-1567 (1998).

[5] Particle Data Group; S. Eidelman et al., *Summary tables of particle properties*, Phys. Lett. B 592, 1 (2004).

[6] Particle Data Group; S. Eidelman et al., *The Cabibbo-Kobayashi-Maskawa Quark-Mixing Matrix*, Phys. Lett. B 592, 1 (2004).

[7] The UA1 Collaboration; G. Arnison et al., *Experimental observation of isolated large transverse energy electrons with associated missing energy at s**(1/2) = 540-GeV*, Phys. Lett. B122, 103 (1983).
The UA2 Collaboration; M. Banner et al., *Observation of single isolated electrons of high transverse momentum in events with missing transverse energy at the CERN anti-p p collider*, Phys. Lett. B122, 476 (1983).

[8] V. Barger and R. Phillips, *Collider Physics*, Addison-Wesley Publishing Company (1997).

[9] J. L. Rosner, M. P. Worah and T. Takeushi, *Oblique Corrections to the W Width* , Phys. Rev. D49, 1363 (1994).

[10] CLEO Collaboration, *Experimental Tests of Lepton Universality in Tau Decay* , Phys. Rev. D55, 2559 (1997).

[11] The DØ Collaboration; B. Abbott et al., *Extraction of the width of the W boson from measurements of* $\sigma(p\bar{p} \rightarrow W + X) \times B(W \rightarrow e\nu)$ *and* $\sigma(p\bar{p} \rightarrow Z + X) \times B(Z \rightarrow ee)$ *and their ratio*, Phys. Rev. D61, 072001 (2000).

[12] The CDF Collaboration; F. Abe et al., *Measurement of sigma B(W -> e nu) and sigma B(Z0 -> e+ e-) in p anti-p Collisions at s**(1/2) = 1.8 TeV*, Phys. Rev. Lett. 76, 3070 (1996).

[13] The DØ Collaboration; B. Abbott et al., *Measurement of W and Z boson production cross sections in* $p\bar{p}$ *collisions at* $\sqrt{s} = 1.8$ *TeV*, Phys. Rev. D60, 052003 (1999).

[14] The CDF Collaboration; F. Abe et al., *Measurement of the production and muonic decay rate of W and Z bosons in p anti-p collisions at s**(1/2) = 1.8 TeV*, Phys Rev. Lett. 69, 28 (1992).

[15] The CDF Collaboration; D. Acosta et al., *First Measurements of Inclusive W and Z Cross Sections from Run II of the Tevatron Collider*, Phys Rev. Lett. 94, 091803 (2005).

[16] The CDF Collaboration; D. Acosta et al., *Physics with Taus at CDF*, Nucl. Phys. Proc. Suppl. 144, 323-332 (2005).

[17] The DØ Collaboration; V. M. Abazov et al., *First measurement of* $\sigma(p\bar{p}) \rightarrow Z) \cdot Br(Z \rightarrow \tau\tau)$ *at* $\sqrt{s} = 1.96$ *TeV*, Phys. Rev. D71, 072004 (2005).

[18] A. Kotwal et al. (The Tevatron Electroweak Working Group), *Combination of CDF and DØ Results on W Boson Mass and Width*, Fermilab-FN-716.

[19] J. Zhu, *Direct Measurement of the W width in Proton-Antiproton Collisions at* $\sqrt{s} = 1.96\ TeV$, D0 Note 4650.

[20] The LEP Collaborations ALEPH, DELPHI, L3, OPAL, and the LEP WW Working Group, *Combined preliminary results on the mass and width of the W boson measured by the LEP experiments*, LEPEWWG/MASS/2003-01, ALEPH 2003-007 PHYSIC 2003-004, DELPHI 2003-007-CONF-629, L3 Note 2794, Opal TN-734 (2003).

[21] UA1 Collaboration; C. Albajar et al., *Measurement of the Ratio* $R \equiv \sigma_W Br(W \rightarrow \mu\nu)/\sigma_Z Br(Z \rightarrow \mu\mu)$ *and* $\Gamma_{tot}(W)$ *at the CERN proton-antiproton Collider*, Phys. Lett. B253, 503 (1991).

[22] UA2 Collaboration; J. Alitti et al., *A measurement of the W and Z production cross sections and a determination of* $Gamma_W$ *at the CERN* $\bar{p}p$ *collider*, Phys. Lett. B276, 365 (1992).

[23] The DØ Collaboration; S. Abachi et al., *Observation of the Top Quark*, Phys. Rev. Lett. 74, 2632 (1995).

[24] The CDF Collaboration; F. Abe et al., *Observation of Top Quark Production in* $p\bar{p}$ *Collisions with the Collider Detector at Fermilab* , Phys. Rev. Lett. 74, 2626 (1995).

[25] *The Run II Handbook*,
www-bd.fnal.gov/runII/index.html

[26] *The DØ Upgrade*.
http://www-d0.fnal.gov/hardware/upgrade/pac0495/d0toc.html

[27] The DØ Collaboration; S. Abachi et al., *The DØ Detector*, Fermilab-Pub-93/179-E (2005)

[28] The DØ Collaboration; V. M. Abazov et al., *The Upgraded DØ Detector*, Fermilab-Pub-05/341-E (2005)

[29] DØ Production Testing Group, *Electrical Production Testing of the DØ Silicon Microstrip Tracker Detector Modules*, D0 Note 3841.

[30] J. Gardner et al., *Results From Irradiation Tests on D0 Run2a Silicon Detectors at the Radiation Damage Facility at Fermilab*, D0 Note 3962.

[31] A. Bean et al., *Studies on the Radiation Damage to Silicon Detectors For Use in the D0 Run2b Experiment* , D0 Note 3958.

[32] P. Baringer, D. Coppage, J Gardner, C. Hebert and A. Turcot, *CPSReco: the cluster reconstruction package for the central preshower detector*, D0 Note 3922.

[33] P. Baringer, D. Coppage and J. Gardner, *CPSReco: An Initial Study of Performance Versus RCP Parameters* , D0 Note 3922.

[34] J. Kotcher, *Design, Performance, and Upgrade of the DØ Calorimeter*, FERMILAB-Conf-95/007-E.
http://www-d0.fnal.gov/hardware/cal/notes/d0-note2417.pdf

[35] SVXII Design Group; R. Yarema et al., *A Beginner's Guide to the SVXII*, FERMILAB-TM-1892 (1994).

[36] D. Bauer and R. Illingworth, *Level 3 Trigger: Clustering in the SMT*, D0 Note 3822.

[37] DØ Upgrade Collaboration, *DØ Silicon Tracker Technical Design Report*,

D0 Note 2169.
http://www-d0.fnal.gov/trigger/stt/smt/smt_tdr.ps

[38] M. Roco, *The Silicon Microstrip Tracker for the DØ Upgrade*, D0 Note 3553.

[39] D. Adams et al., *The DØ Upgrade: Central Fiber Tracker, Technical Design Report*, D0 Note 4164.

[40] *DØ Central Fiber Tracker Description Page.*
http://d0server1.fnal.gov/projects/SciFi/cft_description.html

[41] B. Squires et al., *Design of the 2 Tesla Superconducting Solenoid for the Fermilab DØ Detector Upgrade*, FERMILAB-Pub-098/047-E (1994).

[42] M. Adams et al., *Design Report of the Central Preshower Detector for the DØ Upgrade.*
http://www-d0.fnal.gov/∼qianj/dn3104.pdf

[43] A. Gordeev et al., *Technical Design Report of the Forward Preshower Detector for the DØ Upgrade*, D0 Note 3445.

[44] *Calorimeter Electronics Upgrade for Run II, Technical Design Report.*
http://www-d0.fnal.gov/∼d0upgrad/calelec/intro/tdr/tdr17.pdf

[45] K. De et al., *Technical Design Report for the Upgrade of the ICD for DØ Run II*, D0 Note 2686.

[46] B. S. Acharya et al., *Technical Design of the Central Muon System*, D0 Note 3365.

[47] G. Alexeev et al., *Technical Design Report for the DØ Forward Muon Tracking Based on Mini-drift Tubes*, D0 Note 3366.

[48] V. Abramov et al., *Technical Design Report for the DØ Forward Trigger Scintillation Counters*, D0 Note 3237.

[49] G. Alexeev et al., *The DØ Muon System Upgrade*, DO Note 2780.

[50] A. Brandt et al., *A Forward Proton Detector at DØ*, FERMILAB-Pub-97/377 (1997).

[51] M. Martens and P. Bagley, *Luminosity Distribution During Collider Run II*, D0 Note 3515.

[52] *Luminosity Monitor Detector Homepage*.
http://www-d0online.fnal.gov/www/groups/lum/index.html

[53] *JETMET Run & Lumi-Block Selection*.
http://www-d0.fnal.gov/computing/algorithms/calgo/jet_met/runsel.html

[54] T. Edwards et al., *The Updated DØ Luminosity Determination - Short Summary*, D0 Note 4328.

[55] *D0Reco Webpage*.
http://www-d0.fnal.gov/computing/algorithms/#intro

[56] F. Fleuret, *The D0 Electron/Photon Analysis Package EMAnalyze*, D0 Note 3888.

[57] D. Adams, *Finding Tracks*, DØ Note 2958.

[58] G. Hesketh, *Central Track Extrapolation Through the DØ Detector*, DØ Note 4079.

[59] A. Garcia-Bellido, S. Lager, F. Rizatdinova, A. Schwartzman and G. Watts, *Primary Vertex Certification in p14*, DØ Note 4320.

[60] *MET Certification Version 5.0 for p14*.
http://www-d0.fnal.gov/computing/algorithms/calgo/met/metdoc.html

[61] *PMCS Home Page*
http://www-d0.fnal.gov/computing/MonteCarlo/pmcs/pmcs_doc/pmcs.html

[62] J. Stark, *Correction of the tower two problem in the calorimeter data*, D0 Note 4268.

[63] S. Baffioni, E. Nagy and S. Protopopescu, *Thumbnail: a compact data format*, D0 Note 3979.

[64] R. Brun and F. Rademakers, *ROOT: An Object-Oriented Data Analysis Framework.*
http://root.cern.ch

[65] J. Kozminski et al., *Electron Likelihood in p14* , D0 Note 4449.

[66] A. Abdesselam, *Comparison of H-Matrices for electron identification in DØ Run II*, D0 Note 3745.

[67] F. Touze, M. Jaffré, *Construction of EM Hmatrices and chi2 package.*
http://www-d0.fnal.gov/d0dist/dist/releases/development/hmreco/doc/

[68] C. Balazs, C.-P.Yuan, *Resbos: The Monte Carlo for Resummed Boson Production and Decay.*
http://www.pa.msu.edu/people/balazs/ResBos/

[69] Golonka, Piotr, Was, Zbigniew, *PHOTOS Monte Carlo: a precision tool for QED corrections in Z and W decays*, hep-ph/0506026.

[70] T. Sjöstrand, P. Edén, C. Friberg, L. Lönnblad, G. Miu, S. Mrenna and E. Norrbin, *High-Energy-Physics Event Generation with PYTHIA 6.1*, hep-ph/0010017 (2000).

[71] *Official Webpage for TAUOLA*
http://wasm.home.cern.ch/wasm/goodies.html

[72] J. Pumplin et al., *New Generation of Parton Distributions with Uncertainties from Global QCD Analysis* , hep-ph/0201195.

[73] A.D. Martin et al., *Uncertainties of Predictions From Parton Distribution I: Experimental Errors* , hep-ph/0211080.

[74] R. Hamberg, W.L. van Neerven and T. Matsuura, *A complete calculation of the order α_S^2 correction to the Drell-Yan K-factor*, Nucl. Phys. B359, 343 (1991).

[75] S. Eno et al., *Combining the CDF and DØ R Measurement*, D0 Note 3693.

[76] Y. Fisyak and J. Womersley, *D0gstar D0 Geant Simulation of the Total Apparatus Response*, D0 Note 3191.

[77] J. Zhu, *Determination of Electron Energy Scale and Energy Resolution using P14 zee data* , D0 Note 4323.

[78] S. Fatakia et al., *Jet Energy Scale and Resolution for p13 Data and Monte Carlo.*
http://www-d0.fnal.gov/phys_id/jes/d0_private/certified/v4.2/note.ps

[79] J. Gardner, *Single EM Trigger Efficiency Using a Diem Tag and Probe Method* , D0 Note 4338.

[80] *Jet-ID Certification Results Webpage.*
http://www-d0.fnal.gov/phys_id/jets/jetid-certification.html

[81] Particle Data Group; S. Eidelman et al., *Gauge and Higgs Boson Particle Listings*, Phys. Lett. B 592, 1 (2004).